12-5-2018

Optimal Selection of Test Designs and Sensor Sets for Active Fault Diagnosis

Kyle Palmer
University of Connecticut - Storrs, kyle.palmer@uconn.edu

Optimal Selection of Test Designs and Sensors Sets for Active Fault Diagnosis

Kyle Palmer, Ph.D.

University of Connecticut, 2018

Fault detection and isolation (FDI) is crucial to identifying problems that can occur in complex systems. Many industrial systems require the implementation of model-based FDI to reduce the risk of system failure and increase good performance while minimizing the use of additional hardware. Active FDI has become increasingly popular as it uses auxiliary tests to reduce the impact of uncertainty and improve fault diagnosis. A methodical approach is needed to consistently generate feasible test designs for the optimal detectability and isolability of faults in targeted systems.

The focus of this dissertation is to design a general framework that improves the identifiability of faults based on methods of active fault diagnosis and optimal sensor selection and placement. The proposed standard work and corresponding methods treat fault detection and isolation as a series of constrained optimization problems. The issues of uncertainty caused by system operations and modeling error are addressed through the formulation of

mathematical problems to minimize their impact on fault detection and isolation procedures. This method is based on optimal experimental design (OED) techniques that reduce correlations between targeted model parameters.

The objective was to select optimal test designs that improve the detection and isolation of faults by maximizing available information with respect to faults, with the information represented as sensitivities of selected system outputs. FDI was treated in this dissertation as a series of constrained optimization problems. After the optimal test design was determined, the system of interest was evaluated at the optimal operating conditions to assess the success rate of the proposed fault diagnosis. Simultaneous test design and sensor selection is presented as a mixed-integer nonlinear optimization problem, and novel approaches were implemented to select the most effective FDI test from available sensors and inputs. The methodology presented in this dissertation is intended to refine system design and maintenance schedules to mitigate costs associated with anticipated faults. The resulting FDI test designs are shown to consistently reduce false alarms and nondetections with implementation. Verification of the improved fault diagnosis through the proposed techniques was done with benchmark virtual systems of various levels of scale and complexity.

Optimal Selection of Test Designs and Sensors Sets for Active Fault Diagnosis

Kyle Palmer

B.S., Montana State University - Bozeman, 2013

A Dissertation

Submitted in Partial Fulfillment of the

Requirements for the Degree of

Doctor of Philosophy

at the

University of Connecticut

2018

APPROVAL PAGE

Doctor of Philosophy Dissertation

Optimal Selection of Test Designs and Sensors Sets for Active Fault Diagnosis

Presented by

Kyle Palmer, B.S.

Major Advisor

Dr. George Bollas

Associate Advisor

Dr. Matthew Stuber

Associate Advisor

Dr. Ranjan Srivastava

Associate Advisor

Dr. Douglas Cooper

Associate Advisor

Dr. Peter Luh

University of Connecticut

2018

Dedicated to my family for always believing in me ...

and to Francesca for being my unwavering support ...

ACKNOWLEDGEMENTS

First, I would like to express my gratitude to my advisor, Prof. George Bollas for the continuous support in the pursuit of my Ph.D. studies and related research. His patience, guidance and knowledge were immensely valuable throughout my time in research and the development of this thesis. The experiences I have learned under his mentorship are invaluable and I sincerely thank him for the lessons I have gained as a Ph.D. student.

I would also like to thank the rest of the thesis committee: Prof. Ranjan Srivastava, Prof. Douglas Cooper, Prof. Matthew Stuber, and Prof. Peter Luh, for their insightful feedback and support, and for their difficult questions which encouraged me to broaden my perspectives on the related areas of my research.

My thanks as well to current and past members of this research group, Dr. Lu Han, Dr. Zhiquan Zhou, Dr. Shoucheng Du, William Hale, Brian Baillie, Chunxiang Zhu, Chen Chen, Xi Yang, and Evangelos Stefanidis. I would also like to thank the undergraduate students that I have mentored, Kyle Such and Anh Nguyen, and the administrative support provided by Michelle Morse and her team.

Finally, I would like to thank my family for their incredible support in my pursuance of a Ph.D. in Chemical Engineering. Their continual encouragement despite the travel distance between us was appreciated beyond words. And last and most of all I thank my wife, who

has been my foundation throughout my studies; because of her support was I able to complete this stage of our lives. This work was sponsored by the UTC Institute for Advanced Systems Engineering (UTC-IASE) of the University of Connecticut and the United Technologies Corporation. Any opinions expressed herein are those of the authors and do not represent those of the sponsor.

TABLE OF CONTENTS

LIST OF FIGURES

LIST OF TABLES

Chapter 1

Introduction

1.1 Motivation

Industrial systems and processes have become steadily more intricate over the years. In particular, systems in automotive, aerospace and other industries have become increasingly complex due to the addition of actuators, sensors, control functions and embedded software to improve process safety and effectiveness. However, the increasing complexity of these systems also results in a growing need for effective methods of system troubleshooting and health monitoring. The latter is accomplished with methods that detect impermissible deviations from standard operating conditions and determine likely causes. These deviations represented as system parameters or properties are linked to system faults [10]. However, advanced techniques are needed to diagnose faults in complex systems that are subject to uncertainty related to environmental and process conditions. This dissertation aims to optimize the design of tests for fault diagnosis, actively reconfiguring input trajectories for a limited period of time to improve the sensitivity of outputs with respect to faults and

improve the capability of health monitoring systems.

1.2 Overview of fault detection and diagnosis methods

Fault diagnosis methods can be divided into three main types, model-based, knowledge-based and history-based fault diagnosis [11, 12, 13]. Model-based approaches use mathematical representations of the system of interest. These models can be physics-based or empirically correlated, relying on input and output signals at steady-state or dynamic conditions to evaluate system health. An effective FDI test is one that maximizes the inconsistencies between expected outputs for faulty and healthy systems such that the effects of faults are distinguishable from the effects of uncertainty. The most common approaches to FDI with models involve some form of parameter estimation [14, 15], observers such as sliding mode or Kalman filter [16, 17], or parity equations [18]. Model-based FDI is appropriate when mathematical models are available, if they are sufficiently accurate representations of the system at fault and fault-free conditions. When a system model is not available, or inapplicable to FDI, knowledge-based or data-driven approaches are used. Knowledge or heuristic-based FDI is dependent on the system of interest; thus, acquiring and maintaining useful knowledge for FDI is difficult outside of standard operating conditions. Data-driven approaches such as neural networks [19] and classification methods [20] are applicable when the system can be monitored at anticipated fault and fault-free conditions. Unlike the previous two approaches, data-driven FDI does not require extensive knowledge of the system, though a

significant amount of data is often required.

The approaches to FDI mentioned above are considered passive techniques, in that the system data is collected at nominal operating conditions, or is otherwise unaffected by the implementation of fault detection and diagnosis. Until recently, the majority of FDI research has focused on passive methods. However, active FDI has steadily become more popular for its ability to select input signals or trajectories that improve the success rate of fault diagnosis [21]. Active FDI can be implemented on-line with standard process-related activities, or off-line depending on system requirements. It is crucial to know which active FDI technique is appropriate for a particular system to minimize false alarms, nondetections and misdiagnoses. In many cases, active FDI is used to search for conditions where there is no overlap between fault and fault-free conditions [22, 23], which may not be possible depending on the system and the severity of faults and uncertainty present. Other methods strive to improve active FDI while weighing in energy costs via optimal control [24, 25] that requires on-site, real-time computations that satisfies the requirements for successful FDI. The presence of uncertainty caused by environmental or system variability can significantly hinder the success of such applications.

Research has also been conducted to reduce the impact of uncertainty on fault detection and diagnosis. When designing an FDI test, a trade-off is usually made between sensitivity to faults and robustness against uncertainty [26]. Techniques such as unknown input observers [27, 28], and polynomial chaos expansion [7, 29] have been used to either

minimize the effect of uncertainty on generated residuals, or to anticipate the range of effects caused by disturbances and noise at anticipated fault scenarios. While active FDI methods have been developed to minimize the impact of uncertainty, there is difficulty in implementing on-line methods for nonlinear, complex systems as these systems often contain multiple inputs and outputs. The method for selecting external input trajectories for active FDI must be computationally feasible. By implementing active fault diagnosis when off-line, the optimal selection of the active test design is feasible to calculate off-site prior to implementation, improving FDI performance in complex systems while off-line or at predetermined maintenance schedules.

1.3 Active fault diagnosis test design framework

Selecting admissible input trajectories for fault diagnosis prior to implementation can significantly improve the rate of successful fault detection and identification. The effects of faults and uncertainty can be predicted and classified with available mathematical models, provided that they are sufficiently accurate in representing the system at fault and fault-free conditions. If faults and system uncertainty remain invariant for a specified period of time, then these elements can be classified either as parameters or invariant inputs. Techniques are available in the literature for the optimal design of process conditions for identifying system properties. A widely-used approach in statistics that is used to improve parameter estimation is known as the Optimal Design of Experiments, or Optimal Experimental

Design (OED) [30, 31, 32]. In OED, available information from a system model is used to improve the confidence in the estimation and identification of uncertain or unknown parameters based on the appropriate criteria. Fisher information is often used as a metric due to its connection with estimation covariance. By selecting system conditions and settings based on optimization formulations of OED and Fisher information, fault diagnosis can be improved in the detectability and isolability of faults, reducing false alarms and nondetections.

The author of this thesis introduces a comprehensive methodology for the selection and implementation of optimal tests for active FDI. An illustration of the general workflow of the proposed approach to fault diagnosis is presented in Figure 1.1. There are two main phases in the implementation of the proposed methodology: the design phase and the execution phase. In the design phase, the system requirements and system model are used to determined the feasibility of FDI as well as the range of admissibility in the test design space. Once the capabilities and limitations are known, the best feasible test design is determined, treating the design selection as a constrained optimization problem with the objective to maximize output sensitivities to faults; the system model is used to determine the extractable information at any given test design. After the test design is calculated, the test design is evaluated for anticipated rates of successful detection and isolations. If the proposed test does not meet available system requirements, then the test requires further evaluation and other aspects of the FDI may need to be adjusted. If the proposed test is considered to achieve the necessary diagnostic criteria, then the design is implemented in the execution phase. The method

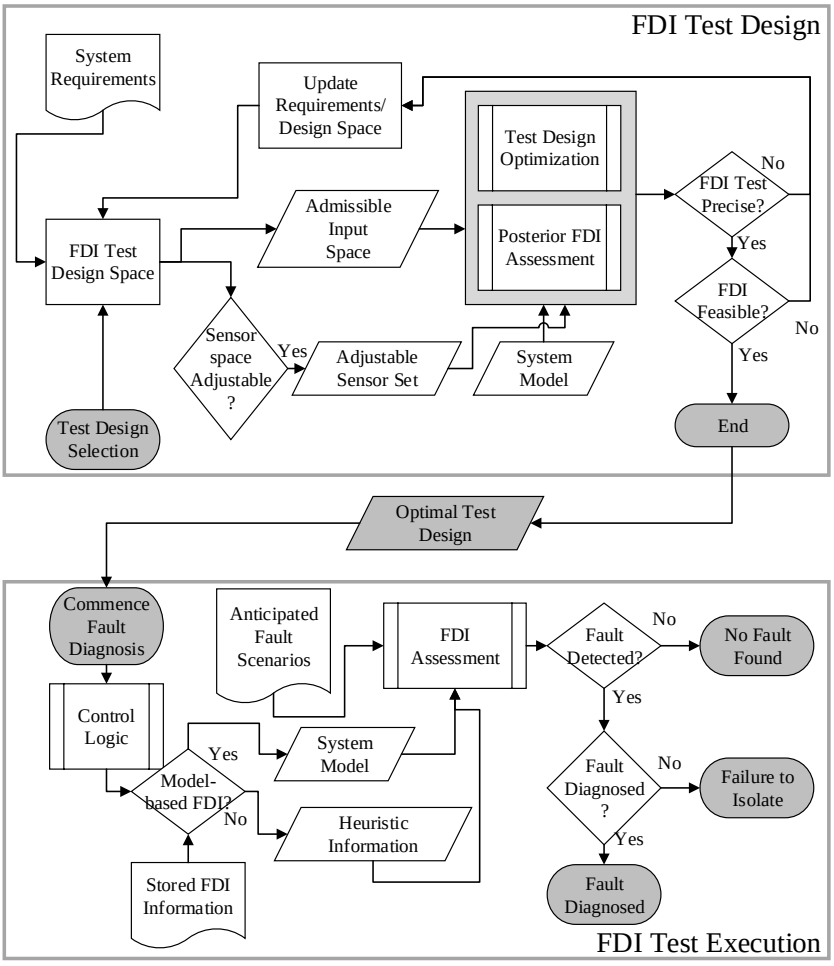

Fig. 1.1: The general flowchart for optimal design (top) and execution (bottom) of active FDI tests. The design phase involves the selection of test conditions from an admissible design space with posterior assessment of FDI precision. The execution phase involves the implementation of on-line FDI techniques to detect and diagnose anticipated faults.

considered for fault diagnosis, whether model-based or data-driven, is then used to determine which fault scenario the system most likely exhibits based on available output information. The following chapters in this document expand on various aspects of this methodology, particularly in the design phase; these aspects include the selection of test design criteria, utilization of steady-state and dynamic information, and approaches to evaluating success of fault diagnosis.

A significant benefit to the selection of test designs for active FDI prior to implementation is the incorporation of sensor selection into the FDI test design. Sensor selection has been used in various fields to improve confidence in the estimation and identification of system properties [33, 34], typically in linear systems. However, few reports are publicly available that consider the simultaneous selection of sensors and input trajectories for the intended use of active FDI. Patan and Ucinski [35] treated the sensor problem as a discrete optimization problem, while also considering a finite number of test conditions as other discrete variables that were adjustable. The selection of optimal sensors and test conditions for active FDI is treated as a constrained, mixed-integer non-linear optimization problem that maximizes sensed information of the system with respect to faults, with input trajectories as bounded continuous variables. By including sensor selection in the FDI test design optimization, the quality of information provided by each sensor can be evaluated to determine which combination of sensors provide the most useful information for fault diagnosis.

1.4 Objectives and organization of chapters

The objective of this dissertation is to introduce a methodology that improves the overall performance of fault diagnosis based on the selection of controllable inputs and available outputs from within the allowable design space of a system. The key ideas in this dissertation are to utilize model-based optimal design of experiments with understanding of process-based faults and system or environmental uncertainty, incorporate an *a posteriori* analysis for evaluating the rate of successful fault diagnosis to verify the FDI test precision, and the inclusion of sensor selection for a concurrent optimization of input trajectories and sensor subset for FDI test designs. The key research activities in this dissertation are the application of design selection based on optimal experimental design for the detection and identification of fouling in a plate-fin heat exchanger with environmental uncertainties present (Chapter 2), with an assessment of conventional FDI implementations utilizing transient information (Chapter 3); the development of a comprehensive model-based FDI framework for maintenance testing that includes an *a posteriori* analysis on the possibility of false alarms (Chapter 4); an analysis of optimal test design criteria for active fault diagnosis in uncertain systems (Chapter 5); and the incorporation and assessment of sensor selection methods in optimal active FDI that accept or reject sensors based on their relative quality of information (Chapter 6).

The aforementioned research activities are organized in the next six chapters of this dissertation as follows:

Chapter 2: Optimal Design of Tests for Heat Exchanger Fouling Identification.

A methodology is presented to generate a test design for the identification of particular fouling in a plate-fin heat exchanger. The proposed method is applicable for off-line maintenance scheduling, where the range of admissible conditions is within safe operations in an environmental control system (ECS). A model was developed for the plate-fin heat exchanger based on first principles and empirical correlations, and the model was used to infer sensitivities of the selected outputs with respect to parameters representing fouling and other sources of uncertainty. Input trajectories were manipulated to maximize these sensitivities and improve the accuracy of the FDI test design. D-optimality was selected as a criterion to the reduce the joint confidence region between fouling and uncertain parameters. A series of case studies were performed that shows the improvement in estimation confidence in thermal fouling resistance at uncertain conditions from the proposed test design optimization.

Chapter 3: Analysis of Transient Data in Test Designs for Active Fault Detection and Identification.

Active FDI methods generally select from system states that results in successful diagnosis. Although the understanding of process dynamics are of interest in complex systems and control design, an evaluation of steady state vs dynamic test designs for FDI has not been explicitly performed in the open literature. The use of transient information in active FDI tests is shown in this chapter to improve the identifiability of faults compared to steady-state tests. A series of case studies were performed using the virtual heat exchanger developed in Chapter 2. Two methods based on conventional FDI implementations were used in these case

studies: an extended Kalman filtering technique with dual state and parameter estimation for on-line FDI, and a moving horizon estimation technique that is performed at specific intervals throughout the test duration.

Chapter 4: Active Fault Identification by Optimization of Test Designs.

This chapter includes a comprehensive model-based framework to improve fault diagnosis and reduce false alarms for maintenance testing. In addition to test design optimization a false alarm analysis is performed, where the system model is used to explore whether false alarms are plausible within the expected parameter space and measurement noise. The distance between parameter sets is maximized while considering likelihood ratios calculated from the system outputs at fault and fault-free conditions. The analysis is based on structural global identifiability analysis, which is performed on system models to ensure they are structurally identifiable. The framework is tested in two case studies. The first case study is a plate fin heat exchanger that is subject to particulate fouling. The second case study focuses on a similar fault scenario but the system is expanded to an aircraft environmental control system with multiple sources of uncertainty.

Chapter 5: Active Fault Diagnosis for Uncertain Systems using Optimal Test Designs and Detection through Classification.

The test design optimization techniques from Chapter 2 are used to explore the viability of multiple design criteria for the purpose of fault diagnosis. In addition, a robust deployment method for assessing the success rate of fault diagnosis is included in the FDI

design framework, based on principal component analysis and k-nearest neighbor classification algorithms. Two virtual case studies are shown in this chapter to verify the updated methodology, a three-tank system and a diesel engine. Results show that D_s-optimal criterion, a subset-based D-optimal criterion, is the most suitable criterion for fault diagnosis in uncertainty systems, by reducing joint confidence region between faults and uncertainty while maximizing sensitivity of outputs with respect to faults. The performance of each design criterion in active fault diagnosis is presented in the form of confusion matrices and receiver operating characteristic plots generated from the optimal test designs.

Chapter 6: Sensor Selection for Active Fault Diagnosis.

The methodology presented in Chapter 5 is expanded to include optimal selection of sensor sets for improved active fault diagnosis in uncertain systems. In this chapter, a finite number of sensors is considered for use in an FDI test design, along with a range of admissible input trajectories. Prior to this work, sensor selection was typically performed with a fixed number of sensors considered for FDI. Two methodologies are presented that maximize the success rate of fault diagnosis by accepting or rejecting sensors based on their relative quality of information in regards to FDI, based on normalized Fisher information and measures of discrepancy such as Kullback-Leibler divergence and Hellinger distance, respectively. A simulated three-tank system was used to verify these approaches to optimal sensor selection and test design. It is shown that when prior information is available and the range of parameter distributions is large, the approach that measures the divergence between fault

scenarios is more accurate, otherwise the first approach is recommended for its computational efficiency.

Chapter 7: Conclusions and Recommendations.

A general conclusion of the research performed is presented in this chapter, along with a brief list of possible opportunities for future work.

Chapter 2

Optimal Design of Tests for Heat Exchanger Fouling Identification

Abstract

Particulate fouling in plate-fin heat exchangers of aircraft environmental control systems is a recurring issue in environments rich in foreign object debris. Heat exchanger fouling detection, in terms of quantification of its severity, is critical for aircraft maintenance scheduling and safe operation. In this work, we focus on methods for off-line fouling detection during aircraft ground handling, where the allowable variability range of admissible inputs is wider. We explore methods of optimal experimental design to estimate heat exchanger inputs and input trajectories that maximize the identifiability of fouling. In particular, we present a methodology in which D-optimality is used as a criterion for statistically significant inference of heat exchanger fouling in uncertain environments. The optimal tests are designed on the basis of a heat exchanger model of the inherent mass, energy and momentum balances, validated against literature data. The model is then used to infer sensitivities of the heat exchanger outputs with respect to fouling metrics and maximize them by manipulating input trajectories; thus enhancing the accuracy in quantifying the fouling extent. The proposed

methodology is evaluated with statistical indices of the confidence in estimating thermal fouling resistance at uncertain operating conditions, explored in a series of case studies.

2.1 Introduction

The primary objective of an aircraft environmental control system (ECS) is to provide fresh air at appropriate conditions for the passengers and crew, while performing secondary heating and cooling to various aircraft components [36]. ECSs are required to control the temperature of hot bleed air stream after compression, using cross-flow plate-fin heat exchangers because of their small weight and volume relative to their heat transfer efficiency [37]. As shown in Fig.2.1, the ECS primary heat exchanger uses ambient ram air as the cold fluid side to decrease the temperature of the compressed bleed stream. As a result, aircraft operations expose the ECS, and in particular its cold side, to fouling from contaminants such as sand, dust, and salt [38, 39].

Fouling in aircraft ECSs is caused by deposition of dust particles suspended in the inlet airflow. Particulate accumulation is a function of air flow rate, concentration of contaminants, and system temperature and pressure [40, 41]. The accumulation of contaminants on the ECS heat exchanger surface significantly reduces its heat transfer efficiency and performance over time while also increasing pressure drop, leading to significant costs from maintenance and component failures [39, 42]. Therefore, the prediction, identification and isolation of ECS fouling have been the subject of several studies [4, 43, 44].

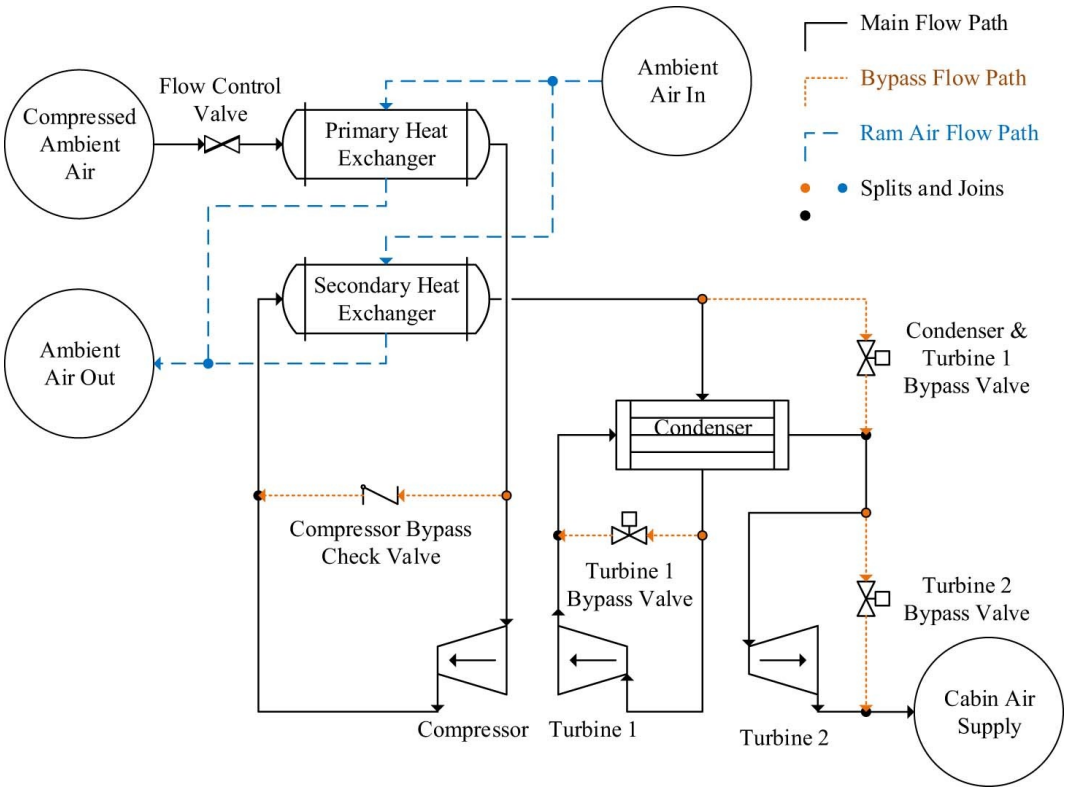

Fig. 2.1: Typical aircraft ECS piping and instrumentation diagram [1].

The physical phenomenon of particulate fouling is currently not well understood, making fouling behavior difficult to predict. Therefore, fouling detection methods are the primary means in monitoring fouling and its impact on aircraft operation [45]. Typically, on-line detection methods are applicable to estimate system states and predict deviations in heat transfer effectiveness [46]. Jonsson et al. [47] presented a fault detection method that uses an extended Kalman filter, designed for nonlinear state estimation and filtering of process and measurement noise. Kobayashi and Simon [48] employed a hybrid Kalman filter approach specifically for aircraft-related fouling detection that uses a continuous model combined with discrete-time measurements. Lalot and Pálsson [19] presented an approach for fouling detection that uses artificial neural networks to update weighted biases into system networked layers. Delmotte et al. [49] implemented weighted uncertainty into a heat exchanger model using a fuzzy polynomial approach. A black-box method was developed by Lalot and Mercère [50] for performing model reduction using recursive subspace model identification. Ingimundardóttir and Lalot [51] used wavelet functions for fault detection by applying wavelet transforms onto continuous or discrete measurements to reduce output noise. All these detection methods treat fouling as a state that increases gradually over time. They are less effective at lower accumulation rates, as it becomes increasingly difficult to discern between system deviation, noise and uncertainty. Moreover, classic methods such as the Kalman filter are difficult to use during off-line analysis, as the duration is very small compared to most on-line applications.

In the particular case of aircraft ECS heat exchanger fouling detection, when aircraft operations are on the ground and prior to flight, a manually initiated built-in test, called iBIT, is used for fault detection [52]. iBIT generally lasts minutes, whereas fouling typically occurs over hundreds of hours, a significant difference in time scales between the fouling process and the time available for its offline detection. This separation of time scales allows fouling affected properties, such as deposit thickness and thermal fouling resistance, to be treated as parameters. Correspondingly, an alternative approach for fouling detection can be applied on the basis of parameter estimation. Here, we propose a method that calculates a set of system inputs that minimize fouling identification uncertainty in iBIT. This technique is based on Optimal Experimental Design (OED) methods [53].

OED is a model-based method that combines a system model with measurements and their variance to decrease the uncertainty of estimated model parameters [54, 55]. The framework for OED is well known in the field of statistics of experiments and is commonly applied in precision-based estimation [56, 57]. Generally, the objective of design of experiments (DOE) is to minimize uncertainty and maximize the information that can be extracted from a series of experiments [31, 32]. Model-based DOE, or OED, relies on the explicit use of a mathematical model with uncertainty in its parameters, cast as an optimization problem that maximizes the information extractable from future experiments. Model equations reflect our current state of understanding of a system, whereas unknown parameters express our lack of fundamental knowledge. Model-based experimental design applications are

abundant across all engineering disciplines and can be applied to any system (linear, non-linear, steady-state or dynamic). The requirement of this approach is a model that captures the physical phenomena of the process through first principles/fundamental equations and empirical correlations, of which the uncertainty is known or relatively well anticipated and understood.

Therefore, in this work we first present a comprehensive model for plate-fin heat exchangers, in which the empirical correlations and model parameters are identified and model input uncertainty is taken into consideration. The fouling detection method is based on a framework inspired by OED for dynamic heat transfer analysis, while considering operating constraints and uncertainty of a realistic iBIT. A cross-flow plate-fin heat exchanger model is first formulated to assess the effects of fouling and the implications of its detection. The plate-fin heat exchanger model is validated with experimental data obtained from the literature. The iBIT OED problem is then formulated to explore sensitivities of the measured heat exchanger outputs with respect to fouling-related model parameters. System inputs are optimized to maximize these sensitivities, using the heat exchanger model employed in a D-optimal experimental design framework that reduces the joint confidence regions of the estimated parameters [58, 59]. Therefore, fouling is dissociated from system noise and input uncertainty in the heat exchanger, which is illustrated through a series of case studies.

2.2 Heat exchanger model and validation

2.2.1 Mass, energy and momentum balances

The heat exchanger model was developed on the basis of mass, energy and momentum conservation equations. As shown in Fig.2.2, each stream in the plate-fin heat exchanger was considered to have temperature gradients solely along the direction of fluid flow, as the flow length is significantly larger than the fin spacing. The fluid flow was considered one-dimensional along each fluid flow direction, whereas the crossflow plate walls that separate the two fluid streams were modeled in two dimensions. The fins have uniform thickness and were assumed to have negligible thermal resistance compared to the plate walls. The fluids were treated as ideal gases, and the thermal conductivity, dynamic viscosity, and specific heat capacity for each fluid were calculated using the correlations presented in Appendix B. These properties were considered to be unaffected by small foulant concentrations. Fig.2.2 illustrates the grid adaptation applied to the plate-fin heat exchanger model. This grid formulation was used to discretize the heat exchanger into a series of sequential cells. The mass, energy and momentum balances were therefore simplified to discrete axial profiles using the method of lines, with axial derivatives approximated by finite differences. The temperature, velocity, and foulant concentration axial profiles within the heat exchanger are not shown here, as the iBIT only has access to input/output measurements of the temperature of the system.

In the discretization scheme of Fig.2.2, the 1-D continuity equation in each direction

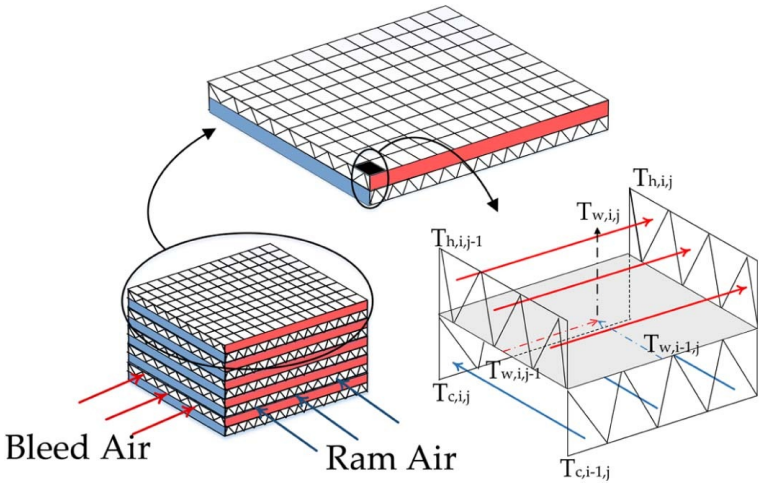

Fig. 2.2: General scheme for the cross-flow plate-fin heat exchanger model discretization.

reads:

$$\frac{\partial \rho_g}{\partial t} + \frac{\partial \left(\rho_g u_g\right)}{\partial x} = 0, \tag{2.1}$$

where ρ_g is the fluid density, and u_g is the fluid velocity. The heat flux in and out of each gas stream depends primarily on advection in the fluid and convective solidgas heat transfer. The axial heat conduction along the fluid is considered negligible, which is reasonable for when the Peclet number, the ratio of thermal energy convected in the fluid over the thermal energy conducted in the fluid, is less than 55 ((B.4-B.6)) [60]. Applying the advective and convective terms into a transient energy balance for an adiabatic heat exchanger yields [61]:

$$\rho_g V_g C_{p,g} \left(\frac{\partial T_g}{\partial t} + u_g \frac{\partial T_g}{\partial x}\right) = A_{s,g} h_g \left(T_w - T_g\right), \tag{2.2}$$

where T_g is the fluid temperature, T_w is the heat exchanger wall temperature, V_g is the

total volume of the gas in the heat exchanger, A_s is the effective heat transfer area (see Supplementary Information), and h_g is the convective heat transfer coefficient.

The wall energy balance includes the terms of convective heat transfer from the fluids and conduction along the plate surface.

$$\begin{aligned} m_w C_{p,w} \frac{\partial T_w}{\partial t} = k_w V_w \left(\frac{\partial^2 T_w}{\partial x^2} + \frac{\partial^2 T_w}{\partial y^2} \right) \\ - A_{s,c} h_c \left(T_w - T_c \right) - A_{s,h} h_h \left(T_w - T_h \right), \end{aligned} \tag{2.3}$$

where m_w is the total mass of the heat exchanger plate, k_w is the uniform thermal conductivity, and V_w is the volume of the plate. The convective heat transfer coefficient can be determined by the fluid properties and Colburn factor (B.7-B.12):

$$h_g = \frac{j C_{p,g} G}{\mathrm{Pr}^{2/3}}, \tag{2.4}$$

where j is the Colburn factor, Pr is the Prandtl number, and G is the fluid mass velocity. It is considered that the Colburn factor correlations used for plain and offset configurations are adequate for the level of model fidelity required for the design of iBIT [62, 63]. Colburn factors and friction factors use different correlations depending on the occurrence of laminar or turbulent conditions as determined by the corresponding Reynolds numbers. In the majority of case studies of this work, the flow was laminar with Reynolds numbers in the range of 100 to 800. The total pressure loss from the heat exchanger is expressed as reported in Shah [64]:

$$\Delta p_{total} = \Delta p_{entrance} + \Delta p_{core} + \Delta p_{exit}, \tag{2.5}$$

where the three types of pressure loss are:

$$\Delta p_{core} = \int_0^x \frac{\partial p_g}{\partial x} dx, \tag{2.6}$$

$$\Delta p_{entrance} = K_c \left(\frac{\rho_g u_g^2}{2} \right), \tag{2.7}$$

$$\Delta p_{exit} = K_e \left(\frac{\rho_g u_g^2}{2} \right). \tag{2.8}$$

The entrance and exit loss coefficients K_c and K_e are 0.2 and 0.4, according to the correlations proposed by Kays and London for typical plate-fin heat exchanger construction [37]. Frictional pressure drop is prominent in plate-fin heat exchangers. The diffusive transport is negligible compared to the convective transport, due to high fluid velocities. Thus, the pressure balance is expressed as:

$$\frac{\partial p_g}{\partial x} = F_w - \rho_g \left(\frac{\partial u_g}{\partial t} + u_g \frac{\partial u_g}{\partial x} \right), \tag{2.9}$$

$$F_w = \frac{2 f \rho_g u_g^2}{d}, \tag{2.10}$$

$$d = \frac{2 \left(H_f - t_f \right) \left(s_f - t_f \right)}{H_f - s_f - 2 t_f}, \tag{2.11}$$

where F_w is the friction loss and d is the hydraulic diameter of the fins [65]. Friction factor correlations for plain fins and offset fins are shown in the Appendix B ((B.7-B.12)) [62, 63].

2.2.2 Particulate fouling

The bulk phase fouling concentration is presented as a transient mass balance with particulates attaching to the heat exchanger surface:

$$\frac{\partial c_f}{\partial t} = -\frac{\partial \left(c_f u_g\right)}{\partial x} + \frac{A_s}{V}\frac{dM_f}{dt}, \tag{2.12}$$

where c_f is the foulant concentration in the bulk fluid, V is the void volume in the heat exchanger, and M_f is the foulant mass per unit area attached to or removed from the heat exchanger wall. The process of particulate fouling was simulated, following the model by Kern and Seaton [3]:

$$\frac{dM_f}{dt} = \alpha u_g c_f - \beta \tau_s m_f, \tag{2.13}$$

where $\frac{dM_f}{dt}$ is the foulant mass flux, and α and β are empirically determined deposition and removal rate constants. The shear rate, τ_s, is equal to $\frac{f\rho_g u_g}{\mu}$. The thermal fouling resistance is directly correlated to the deposited foulant mass:

$$R_f = \frac{M_f}{\rho_f k_f}, \tag{2.14}$$

where k_f is the foulant thermal conductivity, and ρ_f its density. The corresponding convective heat transfer coefficient of the fouled heat exchanger then becomes [6]:

$$h_f = \frac{1}{1/h_g + R_f}. \tag{2.15}$$

The deposit thickness, $\delta_f = R_f k_f$, impacts the fluid velocity in plate-fin heat exchangers by decreasing the available fluid flow area, subtracting the thickness from the fin height and spacing.

Use of the Kern and Seaton model requires the empirical parameters α and β of (2.13) to be estimated from experimental observations. In this work, the data reported by Abd-Elhady et al. [2] were used to generate realistic fouling profiles with the heat exchanger model, which are then to be identified and estimated. Abd-Elhady et al. [2] studied an exhaust gas recirculation cooler, found in diesel engines (a shell-and-tube heat exchanger), in terms of the asymptotic behavior of particulate fouling, as it accumulates along surface walls. They used a soot generator to produce particulates in order to deliberately foul the exhaust cooler using gas velocities of 30 m/s, 52 m/s and 130 m/s. We employed the heat exchanger model of Section 2.2.1 and estimated values for the empirical parameters and of the Kern and Seaton model, to match the data reported by Abd-Elhady et al. [2]. For the purposes of this research, it was assumed that the rate of fouling was unaffected by the geometry of the heat exchanger. In other words, the use of the model by Kern and Seaton with parameters estimated by the data of Abd-Elhady et al. [2] serves the purpose of performing simulations of relatively realistic scenarios of particulate fouling, with no expectations or requirements for the fouling prediction to be accurate for the particular plate-fin heat exchangers studied here. The model was compared to the data reported by Abd-Elhady et al. [2] at 52 m/s gas velocity because of the notable thermal fouling resistance and clear asymptotic behavior. The soot density was reported to be at 1.2 g/cm^3 in [2], the thermal conductivity at 0.1 W/(m K), and the particulate concentration at 100 mg/m^3. Fig. 2.3 shows the fouling data from Abd-Elhady et al. [2] and the simulation results after adjustment of the deposition

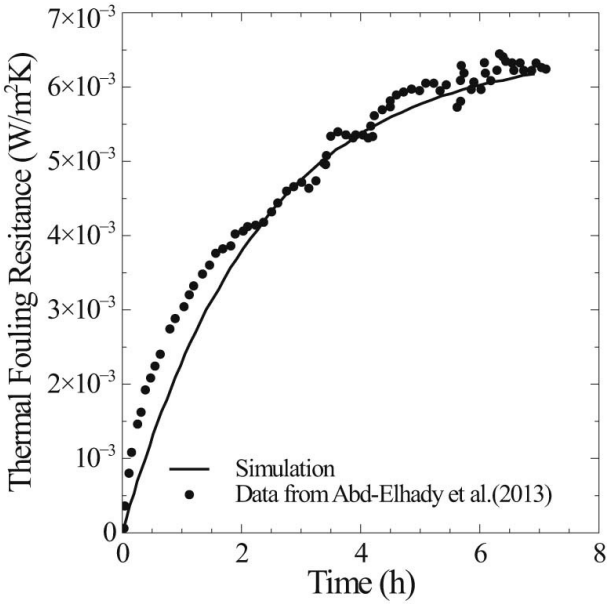

Fig. 2.3: Thermal fouling resistance comparison between data by [2] and simulations using the Kern and Seaton model [3], with α and β at 4.2 and 1.3 s/kg m, respectively. Foulant density is 1.2 g/cm^3, thermal conductivity 0.1 W/m K, inlet particulate concentration 100 mg/m^3, and gas velocity of 52 m/s.

and removal rate coefficients, α and β of (2.13). The empirical parameters α and β were estimated at 4.2 and 1.3 s/kg m, respectively. During the first two hours, the thermal fouling resistance exhibits nearly linear behavior. As time progresses, the accumulation rate slows considerably until it reaches equilibrium at t $\approx$ 7 hours. This final thermal resistance of approximately 6.2×10^3 m^2 K/W is used in the following sections as the unknown thermal fouling resistance that needs to be estimated.

2.2.3 Model validation

Heat transfer effectiveness

The heat exchanger model was validated with literature data of steady-state and dynamic heat transfer experiments in a bench-scale plate-fin heat exchanger. Specifically, the cross-flow, plate-fin heat exchanger experimental data reported by Shah et al. [42] were used for validation of the mass and energy balances of the model. The geometry of the heat exchanger apparatus of Shah et al. [42] is shown in Table 2.1. This small-scale heat exchanger was tested in experiments of varying temperatures and flow rates of the bleed and ram side air, wherein steady-state and transient heat transfer was recorded. Shah et al. [42] reported four steady-state tests, A-D as shown in Table 2.2, in which the flow rates of the bleed and ram inlet streams were varied. The bleed outlet temperature was recorded at steady-state. They also performed transient step tests, as shown in the case studies E-H of Table 2.3. For each transient test, the heat exchanger was configured to reach steady-state with the inlet conditions of Table 2.3, and then a step change of +22 °C was applied at the inlet bleed temperature set point and exit temperatures were recorded.

The model described in Section 2.2.1 with Colburn factors corresponding to plain fin geometry (B.8) was validated with steady-state and transient simulations of the experimental tests reported in Table 2.2, Table 2.3. The results of the simulations of the steady-state tests are shown in Table 2.2. The bleed outlet temperatures of the heat exchanger model match the reported experimental values of each test within ±2.6 °C, without any parameter fitting.

Table 2.1: Core geometry and operating conditions of the heat exchanger apparatus used by Shah [4] for tests A-H.

Bleed flow length (cm)	15.24	Inlet bleed pressure (kPa)	240
Ram flow length (cm)	7.67	Inlet ram pressure (kPa)	100
Bleed fin height (mm)	6.15	Geometry fin type	Plain
Ram fin height (mm)	2.64	Number of cells (for both axes)	5
Plate thickness (mm)	0.599	Number of channels	4
Fin thickness (mm)	0.102	Heat exchanger material	Al

Table 2.2: Comparison of bleed outlet temperatures between simulations and data reported by Shah [4] for steady-state heat transfer.

Test	A	B	C	D
Inlet bleed temperature (°C)	72.8	66.7	78.2	74.6
Inlet ram temperature (°C)	20	20	20	20
Inlet bleed mass flow (g/s)	5.22	4.85	20.41	18.33
Inlet ram mass flow (g/s)	4.99	23.13	4.31	23.36
Outlet bleed temperature, experiment (°C)	37.4	23.4	62.9	34.8
Outlet ram temperature, model (°C)	38.0	23.9	64.6	37.4

Table 2.3: Initial inlet flow conditions for transient heat transfer tests EH, reported by Shah [4].

Test	E	F	G	H
Inlet bleed temperature (°C)	49.3	47	49.8	51.4
Inlet ram temperature (°C)	20	20	20	20
Inlet bleed mass flow (g/s)	4.99	4.72	20.82	18.55
Inlet ram mass flow (g/s)	4.49	23.81	4.41	22.63

The transient tests were also simulated using the model, by comparing the estimates of initial steady-states corresponding to the inputs of Table 2.3 and the transient responses to the set point step changes at the inlet bleed temperature. Fig. 2.4 shows the dynamic responses of the model and the corresponding measurements reported by Shah [4]. Very good agreement between simulations and experiments was accomplished. Tests E and F have lower mass flow rates on the bleed side, so changes in the bleed side temperature produce slower responses. Test G has the highest increase in bleed temperature due to significantly higher inlet mass flow. The simulated responses to the inlet disturbances were slightly faster than their experimental counterpart. This is likely caused by heat loss to the environment and transient sensor delays which were not modeled [4]. Overall, the model provides an accurate representation of the transient heat transfer phenomena in plate-fin heat exchangers.

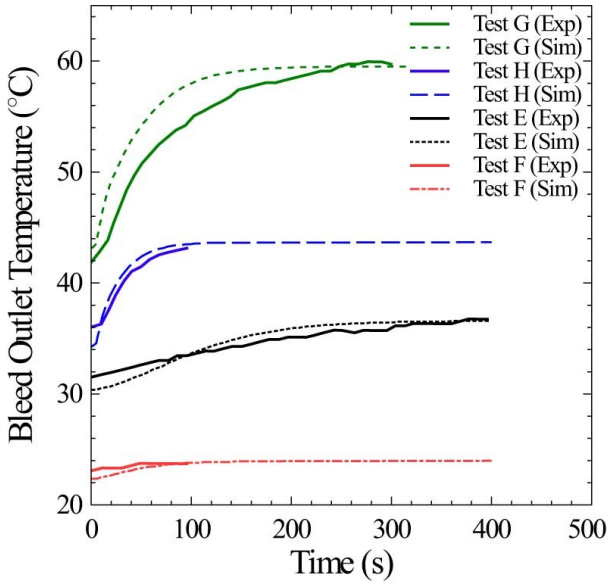

Fig. 2.4: Comparison of predicted bleed outlet temperatures for the transient tests EH of Table 2.3 with the corresponding literature data [4].

Pressure drop and heat transfer coefficient

The heat exchanger model was also validated against frictional pressure drop measurements and heat transfer coefficient estimates for a series of reported heat exchanger geometries. Dong et al. [63] tested multiple fin-and-tube heat exchangers to determine the effects of heat exchanger geometry on pressure drop and heat transfer. The frictional pressure drop and the heat transfer coefficient for the fin side of these heat exchangers were determined by observing the inlet and exit temperatures and pressures. For brevity, only three heat exchanger configurations tested by Dong et al. are reported here. These heat exchangers had identical properties with the exception of fin spacing as shown in Table 2.4. The model

Table 2.4: Geometry and operating conditions of the heat exchangers studied by Dong et al.[35].

Flow length (mm)	65	Geometry fin type	Offset
Fin height (mm)	7.8	Offset fin length (mm)	5.0
Fin thickness (mm)	0.2	Number of cells (both axes)	5
Fin spacing 1 (mm)	1.8	Number of channels	1
Fin spacing 2 (mm)	2.1	Heat exchanger material	Al
Fin spacing 3 (mm)	12.35	Inlet water side temp (°C)	190

was modified to match the geometry of each heat exchanger, as detailed in Table 2.4.

Fig. 2.5 shows the relationship between the inlet fluid velocity and the pressure drop and heat transfer coefficient for the fin spacing lengths listed in Table 2.4. The model predictions are in very good agreement with the reported data. These results validate the momentum balance expressions and the heat transfer coefficient correlations of (2.4-2.11), as well as (B.12) for the estimation of the offset fin Colburn factor. As the number of fins increases, the overall effectiveness of the heat exchanger increases, but at the cost of higher pressure drop. Dong et al. [63] reported that the experimental results contained an uncertainty of ±8.4% for pressure drop, and ±9.4% for heat transfer coefficient estimates, due to medium property uncertainties and sensor errors.

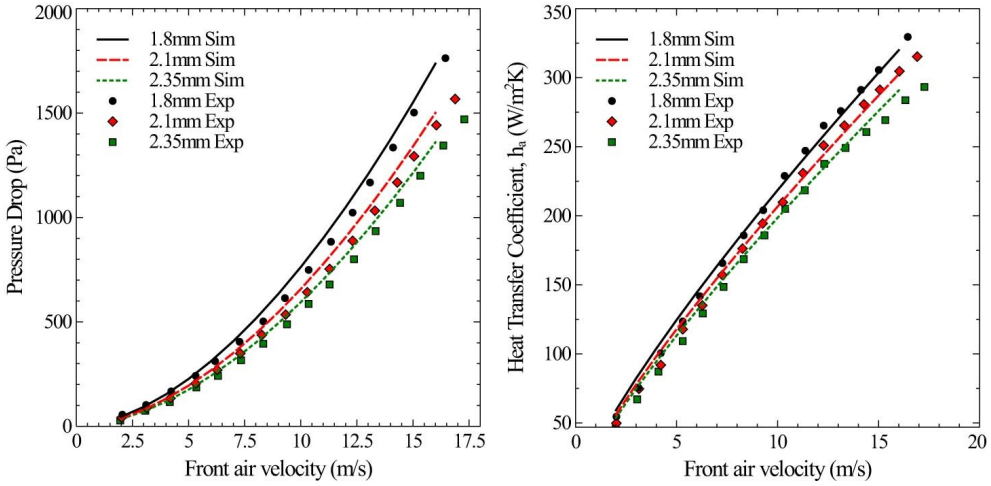

Fig. 2.5: Comparison of predicted heat exchanger fin side pressure drop (left) and heat transfer coefficient (right) with reported results from Shah [4] over a range of fluid velocities. The legend indicates the fin spacing used in each heat exchanger configuration.

2.3 Fouling detection

As discussed in the Introduction, the focus of this work is on a methodology for iBIT of aircraft ECS; in particular, for plate-fin heat exchanger fouling identification. In this section, we formulate the mathematical problem of fouling identification in iBIT. The rationale of this formulation follows the input variables available in the real system, the measurements that are or can be available in an aircraft ECS, and realistic constraints for all the inputs and time scales. It is noted that iBIT in this work is cast as a test (experiment) or series of tests that need to be performed for the identification of fouling and its isolation from

other system uncertainties. The identification of the fault is improved by maximizing the information that can be extracted from a test, relative to this fault. This information can be steady state or transient, which are both explored in the following. The model-based methodology discussed in the following makes use of the model described in Section 2.2, of which parametric sensitivities with respect to fouling indicators (parameters) are maximized in designing an optimal iBIT. Each optimal iBIT (which may consist of a series of tests) is then compared to a nominal iBIT comprising a set of tests performed at normal or standard ECS conditions.

2.3.1 Method formulation

In the model, heat exchanger fouling is expressed as thermal fouling resistance, R_f, and treated as a parameter during iBIT. Fouling resistance affects the measured (at the system level) exit temperatures and pressures by reducing the overall heat transfer coefficient and decreasing the cross-sectional area of the heat exchanger, as detailed in Section 2.2. However, the same measured variables are affected by other input or state variables, such as flow rates, inlet pressure, temperature, etc. Therefore, it is possible (and likely) that uncertainty and noise in the inlet conditions or system states are misinterpreted as fouling in certain situations. Overall, the objective of iBIT in this analysis is to estimate the thermal fouling resistance as accurately as possible in aircraft ECS with uncertainty in its states or inputs and other system parameters.

The uncertainties explored here include all the conditions that affect heat transfer effectiveness. Specifically, the moisture content, w_{H_2O}, increases the fluid heat capacity (B.3) for gas heat exchangers, affecting the outlet temperature. The inlet pressure and mass flow in the bleed stream, p_{hi}, $\dot{m}_{hi}$, and ram stream, p_{ci}, $\dot{m}_{ci}$, control the density and velocity of each fluid, which impact heat transfer and pressure drop. The inlet ram temperature, T_{ci}, has a significant effect on the exit temperature as shown in Section 2.2. These system conditions or parameters are considered uncertain and are estimated along with the thermal fouling resistance through a series of case studies (detailed in Section 2.4) to showcase the strengths and capabilities of the method proposed here. It should be noted that uncertainty is expressed in this work as a variance interval for each one of the variables considered. Depending on the level of confidence we have on the system measurements or on the accuracy of inferred variables, the intervals of each variable are expressed as wide or narrow bounds in their estimation. As such, even system inputs are considered unknown, and the level of accuracy in their value in the system is expressed by their upper and lower bounds. In summary, the unknown fouling resistance and uncertain inlet conditions were compiled together as a vector of estimated system parameters and inputs:

$$\begin{aligned} \boldsymbol{\xi} =& [\boldsymbol{\theta}, \mathbf{u}], \\ =& [R_f, w_{H_2O}, \dot{m}_{hi}, \dot{m}_{ci}, p_{hi}, p_{ci}, T_{ci}]. \end{aligned} \tag{2.16}$$

Equation (2.16) does not describe a complete iBIT input set for aircraft ECS. The bleed stream is typically controlled and conditioned by the bleed system before entering the

primary heat exchanger. Here, the ECS iBIT problem is simplified by adjusting the inlet bleed temperature directly as an input for optimal fouling detection, without considering the implications upstream to the bleed source. Moreover, the iBIT considered here changes the inlet bleed temperature in a series of discrete steps over time. The number of discrete step changes, n_s, and their duration, $\mathbf{t}_s$, were also optimized to find a balance between estimation confidence, complexity and duration of the design. The duration of each step was constrained to a minimum of twenty seconds to allow for utilization of steady-state information when applicable. The initial conditions, $\mathbf{y}_0$, were optimized as well. In iBIT, the optimality of $\mathbf{y}_0$ corresponds to finding optimal system inputs for the initial system steady-state. The timespan of the iBIT analysis in an aircraft is relatively small to ensure all tests are completed within the aircraft ground handling time. Most iBITs run for less than ten minutes for aircraft diagnostics [66], so for this analysis the maximum test duration, τ, was set to five minutes. The inlet temperature, number of step changes, steps duration, and overall timespan are included in the test design vector, $\boldsymbol{\varphi}$:

$$\boldsymbol{\varphi} = [T_{hi}(t), \mathbf{t}_s, n_s, \mathbf{y}_0, \tau]' \in \Phi \tag{2.17}$$

The variables of the test design vector of (2.17) were restricted to a design space Φ, assigning upper and lower bounds to each component. To formulate the iBIT design problem, within the allowable design space of the ECS, the model equations described in Section 2.2 were expressed as an implicit system of differential equations:

$$\mathbf{f}\left(\dot{\mathbf{x}}(t), \mathbf{x}(t), \mathbf{u}(t), \boldsymbol{\theta}, t\right) = \mathbf{0}, \tag{2.18}$$

where $\mathbf{f}(\cdot)$ is the system governing equations, $\mathbf{x}(t) \in \mathbb{R}^{N_x}$ is the $N_x \times 1$ vector of system states (temperature and pressure), $\mathbf{u}(t) \in \mathbb{R}^{N_u}$ is the $N_u \times 1$ vector of system inputs (inlet bleed temperature), and t is time. It was assumed that sensors exist at the outlet bleed and ram channels to measure the exit temperatures and pressures, regardless of whether they exist in all ECSs. Estimates of the $N_y \times 1$ vector of measured outputs, $\hat{\mathbf{y}}(t) \in \mathbb{R}^{N_y}$, are then expressed as:

$$\hat{\mathbf{y}}(t) = \mathbf{h}\left(\mathbf{x}(t), \mathbf{u}(t), \boldsymbol{\theta}, t\right) \tag{2.19}$$

where $\mathbf{h}(\cdot)$ is the function of the relationship between the states, inputs and parameters to the estimated outputs at time t. The initial conditions, $\mathbf{y}_0$, were arranged for the defined system as:

$$\mathbf{y}_0 = \begin{cases} \mathbf{f}\left(\dot{\mathbf{x}}(t_0), \mathbf{x}(t_0), \boldsymbol{\theta}, \mathbf{u}(t_0), t_0\right) = \mathbf{0}, \\ \hat{\mathbf{y}}(t_0) = \mathbf{h}\left(\mathbf{x}(t_0), \boldsymbol{\theta}, \mathbf{u}(t_0)(t_0)\right), \end{cases} \tag{2.20}$$

where $\mathbf{y}_0$ is a set of $\mathbf{x}$, $\dot{\mathbf{x}}$ sufficient to establish the system initial conditions, not to be confused with $\mathbf{y}$ or $\hat{\mathbf{y}}$.

An optimal iBIT should provide maximum information on thermal fouling resistance, even at uncertain inlet conditions. This information is acquired through the sensitivities of measured outputs with respect to the anticipated values of $\boldsymbol{\xi}$, $\tilde{\boldsymbol{\xi}}$ for all sampling times within τ. These sensitivities were compiled into a series of matrices, $\mathbf{Q}_i$, for each output, y_i, and weighed by the experimental variance to produce the variance covariance matrix and Fisher

information matrix at the anticipated vector, $\tilde{\boldsymbol{\xi}}$:

$$\mathbf{V}_{\xi}\left(\tilde{\boldsymbol{\xi}},\boldsymbol{\varphi}\right)=\mathbf{H}_{\xi}^{-1}\left(\tilde{\boldsymbol{\xi}},\boldsymbol{\varphi}\right)=\left[\sum_{i=1}^{N_y}\sum_{j=1}^{N_y}\sigma_{ij}^{-2}\mathbf{Q}_i^T\mathbf{Q}_j\right]^{-1} \tag{2.21}$$

where σ_{ij}^{-2} is the ij-th element of the experimental variance matrix [56], and is the total number of measured outputs. The D-optimal design criterion was chosen for the iBIT case studies in the following, to minimize the correlation between estimated parameters from the extracted information, and thus isolate fouling from all other system uncertainty:

$$\begin{aligned}
&\boldsymbol{\varphi}_D^* \in \arg\min_{\boldsymbol{\varphi}\in\Phi} \det\left[\mathbf{H}_{\xi}^{-1}\left(\tilde{\boldsymbol{\xi}},\boldsymbol{\varphi}\right)\right]\\
&\quad \text{s.t.}\\
&\quad \mathbf{f}(\dot{\mathbf{x}}(t),\mathbf{x}(t),\mathbf{u}(t),\boldsymbol{\theta},t)=\mathbf{0},\\
&\quad \hat{\mathbf{y}}(t)=\mathbf{h}(\mathbf{x}(t),\mathbf{u}_p(t),\boldsymbol{\theta},t),\\
&\quad \mathbf{y}_0=\begin{cases}\mathbf{f}(\dot{\mathbf{x}}(t_0),\mathbf{x}(t_0),\mathbf{u}_p(t_0),\boldsymbol{\theta}_p,\tilde{\boldsymbol{\xi}},t_0)=\mathbf{0},\\ \hat{\mathbf{y}}(t_0)=\mathbf{h}(\mathbf{x}(t_0),\mathbf{u}_p(t_0),\boldsymbol{\theta}_p,\tilde{\boldsymbol{\xi}},t_0),\end{cases}\\
&\quad \mathbf{u}^L\le\mathbf{u}(t)\le\mathbf{u}^U,\quad \forall t\in[0,\tau],\\
&\quad \mathbf{x}^L\le\mathbf{x}(t)\le\mathbf{x}^U,\quad \forall t\in[0,\tau].
\end{aligned} \tag{2.22}$$

The optimal iBIT test design vector, $\boldsymbol{\varphi}_D^*$, of (2.22) is then applied to several fouling identification and isolation scenarios (Section 2.4) and compared to iBIT effectiveness at nominal conditions.

2.3.2 Tool chain

The plate-fin heat exchanger model was formulated with the object-oriented language Modelica [67], in the commercial software Dymola [68]. The governing equations for the heat exchanger model were written as a series of differential and algebraic equations. The bleed, ram, and wall temperatures leaving each volume segment of the heat exchanger model were defined as states. The densities of the fluids were also treated as states, as their time derivatives constitute the conservation of mass equations. The total number of states was, thus, the number of states per cell times the number of cells of the heat exchanger model grid formulation. Algebraic variables were defined to calculate heat transfer coefficients, flow areas, thermal properties for each fluid, and frictional pressure loss. These correlations can be found in Appendix B. The parameters of this model were the dimensions of the plate-fin geometry, the constants used to compute thermal properties, the constants used to compute various empirical formulas, and the uncertain conditions, such as the thermal fouling resistance and fluid moisture content. The resulting Modelica code was flattened to its non-object-oriented equivalent to simplify computations. The flattened model was exported using the Functional Mockup Interface (FMI), a tool-independent standard for configuring dynamic models [69]. The code was converted to a Functional Mockup Unit to be transferred to MATLAB [70] using the Modelon FMI-Toolbox [71]. Dynamic and steady state parametric sensitivities were calculated with the solver CVODES [72], a C-coded ODE solver capable of sensitivity analysis, using finite differences or adjoints. In this work, the parametric sensitivities were

defined as the variability of exit temperatures of the plate-fin heat exchanger with respect to fouling-related parameters at each sampling time. This was done to represent a real system with temperature sensors at heat exchanger exits. As stated previously, these sensitivities were compiled into a variancecovariance matrix, and the determinant of this covariance matrix was calculated and optimized in MATLAB. The optimal design was calculated with the Mesh Adaptive Direct Search algorithm, NOMAD [73], and was verified with an exhaustive search of test design within the design space.

2.4 Results and discussion

In this section, the models and methodologies presented previously are applied to the heat exchanger design reported by Shah et al. [42]. Validation of the model for this particular heat exchanger was performed but is not presented here, because the conditions in Shah and Sekulic [40] are outside of the range of normal ECSs. Nonetheless, the size, flow rates and Re numbers of this heat exchanger are in much better agreement with those found in ECSs, whereas the experimental apparatus by [42] operates at a different regime, giving rise to considerably different sensitivities and dynamics for the heat transfer process. Here, we focus on the effectiveness of the methodology presented, rather than absolute values for the conditions estimated. The effectiveness of the proposed iBIT method is studied in case studies, in which the heat exchanger model presented in Section 2.2.1 is studied under heavy foulant accumulation conditions, using the fouling model of Section 2.2.2. This is

accomplished by running the heat exchanger and the fouling models for 7 hrs (real process time) with a high inlet foulant concentration of 100 mg/m^3 until the overall thermal fouling resistance reaches 6.2×10^{-3}m^2 K/W, based on the fouling simulations shown in Fig. 2.3. At this point, it is postulated that fouling is significant and must be identified from an iBIT, which is ran at nominal and optimal conditions and the capability of the iBIT to identify fouling with certainty is explored. We thus have a model representing noisy responses of a heat exchanger at significant fouling conditions, which we will call "virtual system" and a model with no noise in its predictions and void of any foulant deposition, which we will call "system model." The responses of the virtual system are used in a computational framework for parameter estimation to estimate the thermal fouling resistance and uncertain inputs of the system model.

2.4.1 Basis for heat exchanger fouling analysis

The flow conditions in the ECS heat exchanger were set to nominal conditions typical for ECS heat exchanger operations, detailed in Table 2.5. The bleed inlet temperature was constrained between 100 °C and 250 °C, assuming that it is controlled upstream, but with significant uncertainty. The inlet ram temperature was set according to the international standard atmospheric values at ground level determined by the International Civil Aviation Organization [74].

To evaluate the effectiveness of the proposed method for fouling detection, the thermal

Table 2.5: Conditions applied in the ECS heat exchanger case studies of fouling estimation.

Flow condition	Nominal setting
T_{hi} (°C)	175
T_{ci} (°C)	15
$\dot{m}_{hi}$ (kg/s)	0.30
$\dot{m}_{ci}$ (kg/s)	1.00
p_{hi} (kPa)	250
p_{ci} (kPa)	100

fouling resistance and uncertain flow conditions were estimated in several case studies, and their 95% confidence intervals at nominal and optimal conditions are reported and compared. Measurement noise was added to the heat exchanger model outputs to provide virtual experimental data for analysis. The measurement standard deviation of the system was assigned zero-mean white measurement noise typical for each outlet (0.5 °C for outlet temperatures, and 100 Pa for outlet pressures). Thereafter, noiseless model simulations (from the system model) were matched to the experimental data (from the virtual system) by adjusting $\boldsymbol{\xi}$, the estimated parameters and system uncertain inlets. The robustness of fouling detection was then determined as the capability of the parameter estimation to minimize deviations between the noiseless simulations of a model with zero initial fouling and noisy model responses

of the model with heat exchanger fouling:

$$\begin{aligned} &\min_{\boldsymbol{\xi}} \sum_{i=1}^{N_{sp}} \left(\left(T^i_{c,o,sim} - T^i_{c,o,exp}\right)^2 + \left(T^i_{h,o,sim} - T^i_{h,o,exp}\right)^2 \right) \\ &0.75\tilde{\boldsymbol{\xi}} \leq \boldsymbol{\xi} \leq 1.25\tilde{\boldsymbol{\xi}}. \end{aligned} \tag{2.23}$$

Only temperature measurements were compared for these studies, as it is more common to have temperature sensors available in ECS, and not pressure transducers. All uncertain inlet conditions were subject to bounds that were ±25% of their nominal value, $\tilde{\boldsymbol{\xi}}$.

2.4.2 Identification of fouling in an uncertainty-free system

As a first step, we explored the robustness of the proposed method to identify heat exchanger fouling as a parametric fault in an ideal system with no uncertainty. Thus, the task here is to find optimal system conditions for estimating thermal fouling resistance, with all other system inputs known accurately. In the virtual system, thermal fouling resistance was set to 6.2×10^{-3} m^2 K/W, to represent realistic equilibrated fouling, as shown in Fig. 2.3. For the optimal iBIT design, calculated by (2.22), the inlet temperature was found at the upper bound of its allowable range (250 °C). Only one temperature step was required (n_s=1) throughout the entire iBIT duration, τ. Adding more input steps did not increase the estimation accuracy of fouling resistance in iBIT.

To better illustrate the effect of system inlet conditions on fouling detection, Fig. 2.6 shows the difference between clean and fouled heat exchanger operation, at nominal and optimal conditions. The inlet bleed temperature is also shown in Fig.2.6, to illustrate

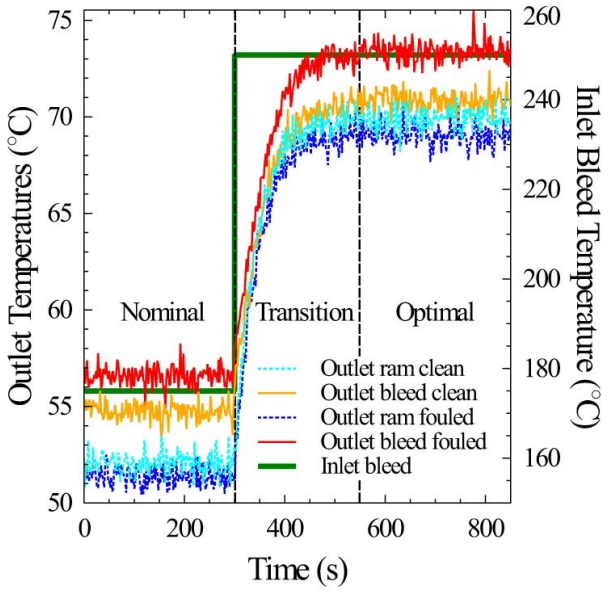

Fig. 2.6: Inlet bleed temperature and predicted outlet ram and bleed temperatures of clean and fouled heat exchanger. The heat exchanger is initially set to steady-state at nominal conditions for 300 s and then transitioned to the steady-state of the optimal iBIT settings. The optimal test is simulated for 300 s.

the distance between nominal iBIT conditions and the conditions estimated by (2.23). To generate Fig. 2.6, the virtual system (fouled and noisy heat exchanger model) was initialized at a nominal steady-state and simulated at steady state for 300 s. Then the inlet bleed temperature was set to the value estimated by (2.23) (250 °C), and the virtual system was run for another 600 s. The transient response of the virtual system in Fig. 2.6 indicates a smooth transitioning to the iBIT optimal steady-state. The solution of the D-optimal iBIT design, (2.22), in this case is trivial and easy to understand. The inlet bleed temperature

is higher at the D-optimal experiment, which causes the heat transfer rate to rise up as well. Fouling identifiability is enhanced at the higher heat transfer rate due to the improved observability of effects on the heat exchanger thermal effectiveness. In particular, it is clear in Fig. 2.6 that the absolute temperature difference (between fouled and clean heat exchanger responses) at the outlet bleed stream is much larger for the higher bleed inlet stream temperature. The heat transfer effectiveness of the heat exchanger is deteriorated because of fouling and this is more evident when the heat transfer requirement is higher.

The fitting of the heat transfer resistance of the system model to the virtual system data produced thermal fouling resistance estimates of $6.26\pm0.40\times10^{-3}$ and $6.19\pm0.34\times10^{-3}$ m^2 K/W at nominal and optimal conditions, respectively. In real systems, the inlet ram temperature depends on day time and location of the aircraft. The atmospheric conditions influence the rate of heat transfer, and therefore the fouling identifiability. To account for this, the thermal fouling resistance was also estimated with inlet ram temperatures of -50 °C and 40 °C to represent cold and hot atmospheric conditions. The corresponding estimates of thermal fouling resistance were nearly identical to the values listed for the standard inlet ram temperature. The estimated value of thermal fouling resistance and its confidence intervals were slightly improved through optimal design of the iBIT inlet bleed temperature, regardless of the temperature of the atmosphere surrounding the aircraft.

2.4.3 Heat exchanger fouling with uncertainty in the air moisture content

One common uncertainty in ECS is the moisture of the ambient air. The aircraft surrounding atmosphere has different moisture levels depending on location, time, and the particular location in the airport. Therefore, it is of interest to consider uncertainty in the moisture content of air and explore its impact on the robustness of fouling identification using nominal and iBIT optimal inlets. For simplicity, the moisture content was considered to affect only the heat capacity of each fluid in the system (B.4). From psychrometric charts [75], the maximum atmospheric humidity at 15 °C is 1.2 wt%, or 0.012 kg water/kg air, assuming there is no precipitation, while the minimum atmospheric humidity is roughly 0.1 wt%. This variability corresponds to a heat capacity range of 1040 to 1078 J/(kg s). Thus, the heat capacity of air was treated as an unknown in the optimal iBIT problem, with range as indicated above.

Fig. 2.7 shows the virtual system temperature of the bleed and ram outlets at the maximum humidity level for nominal and optimal conditions, in a similar format to what was presented in Fig. 2.6. The minimum humidity level was also assessed, with similar overall conclusions. The optimal iBIT was found with two control actions (n_s=2), signifying that two very different temperatures are needed for the separation of the effects of unknown moisture and fouling thermal resistance, when only outlet temperature measurements are available. In the optimal iBIT design, the bleed temperature was set initially to the lower bound for 20 s, and then was set to the upper bound for the remaining test duration. This

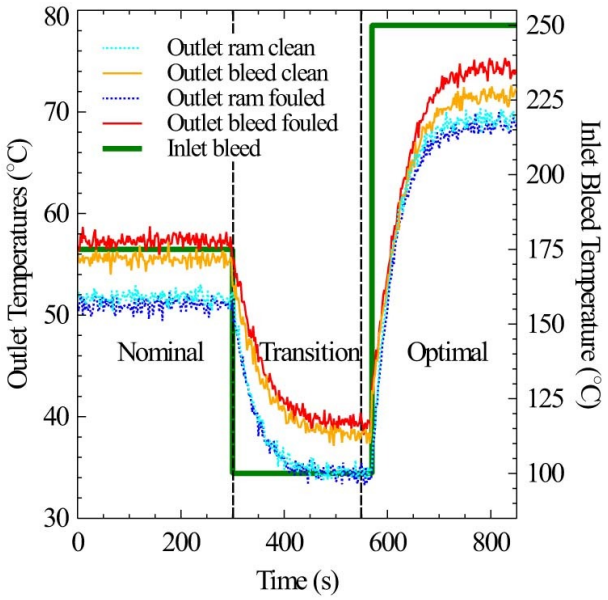

Fig. 2.7: Inlet bleed temperature and predicted outlet ram and bleed temperatures of clean and fouled heat exchanger with a moisture content of 1.2 wt%. The heat exchanger is initially set to steady-state at nominal conditions for 300 s and then transitioned to the steady-states of the optimal iBIT settings (100 to 250°C). The optimal final test is simulated for 300 s.

design improves the estimation precision for the advective and convective aspects of heat transfer, both of which are affected by the specific heat capacity. A transitional period between the nominal and optimal settings was required in order to reach the optimum steady-state outlet temperature for the first control step. The estimates of moisture and fouling thermal resistance were acquired using the entire transient response exhibited by the system from the second input step change.

Fitting of the thermal fouling resistance and moisture content to the steady state data at nominal conditions (t=0 to 300 s in Fig. 2.7) produced estimates of $5.90\pm8.71\times10^{-3}$ m^2K/W and 1.21±3.67 wt%, respectively. At optimal iBIT conditions, the estimates for R_f and were at $6.03\pm0.81\times10^{-3}$ m^2 K/W and 1.27±0.28 wt%. At minimum humidity levels, the confidence intervals of the parameter estimates from nominal and optimal iBIT designs were similar, indicating that the optimal iBITs are useful for estimating fouling regardless of the humidity levels. The 95% confidence region was notably large for the nominal design, to the degree that negative values for thermal fouling resistance and moisture content were deemed statistically feasible. Fouling estimation at uncertain moisture levels was ineffective at the default settings, emphasizing the importance of applying a structured iBIT design strategy to improve the confidence and precision of fouling detection and isolation.

This case study provides the opportunity to enumerate the objective function of (2.23) over the entire allowable space of thermal fouling resistance and moisture content values. Therefore, we can visualize the benefits of the proposed methodology for iBIT in terms of the corresponding capability to determine the unknown and uncertain system variables and parameters. Fig. 2.8 shows how the objective function of (2.23), used for parameter estimation and thus fouling identification, is affected by the system model moisture content and thermal fouling resistance at nominal and optimal iBIT settings. At nominal iBIT, the objective function presents a valley of similar values neighboring the true values of R_f and w_{H_2O}. Thus, the corresponding parameter estimation problem is applied to a system that

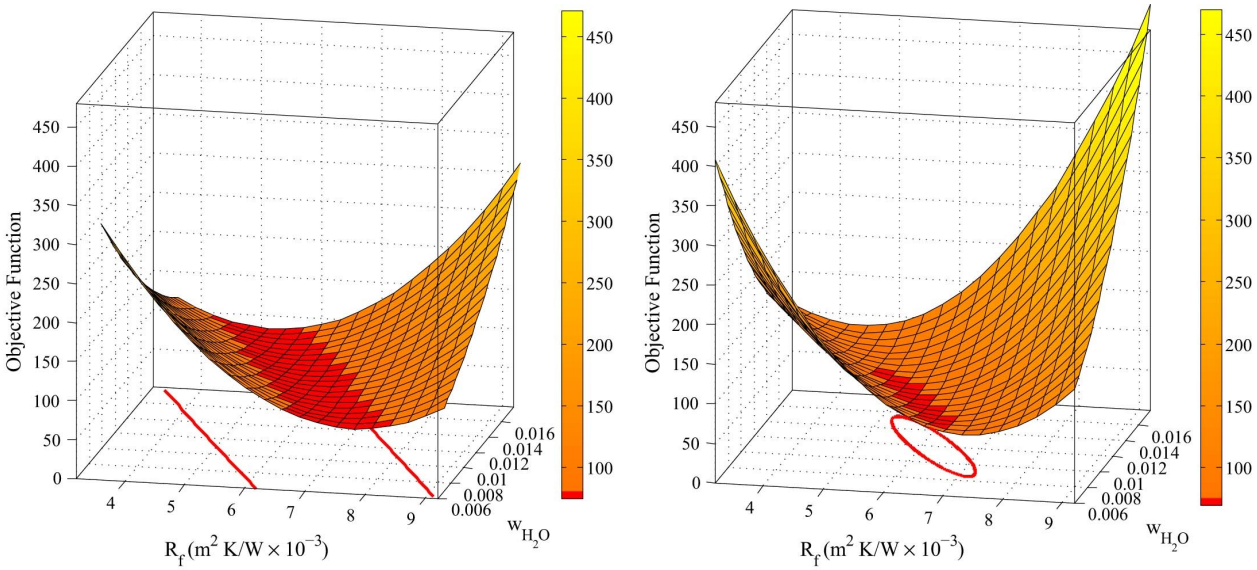

Fig. 2.8: Objective function values of the parameter estimation problem of (2.23) over a range of system model thermal fouling resistance and moisture content values using nominal (left) and optimal (right) iBIT settings. The true values of the virtual system were at 6.2×10^{-3} m^2 K/W and 1.2 wt%, respectively. The dark squares represent the estimated parameters that correspond to the correct system output (the minimum objective function), and the contour plot shows the 95% confidence ellipses.

is not identifiable. The range of R_f and w_{H_2O} yielding closely neighboring estimates for the objective function of (2.23) is significantly reduced in the optimal iBIT, thus the likelihood that parameters are estimated at their true values is significantly improved.

2.4.4 Heat exchanger fouling with uncertainty in the inlet pressures

In certain ECSs, the pressure and temperature of the inlet bleed stream are controlled by a compression system. Depending on the state of the compressors and downstream pressure impedance, the pressure of the inlet bleed stream in the ECS heat exchanger might contain significant uncertainty. Therefore, in this case study, we explored the impact of uncertain inlet pressure for the bleed side on iBIT fouling detection. As an exercise, uncertainty was also considered for the ram flow. The sensitivities obtained in this case study produced Fisher information matrices that were nearly singular for all available input configurations. At constant mass flow, the velocity and density of the fluid are inversely proportional, so the inlet pressure has little impact on the Reynolds number. At nominal ECS flow conditions, the system pressure does not affect the intrinsic fluid flow properties enough to provide useful information. No experimental evidence was found to validate this finding, as most studies that examine heat exchanger pressure focus on pressure drop analysis. Nonetheless, this case study indicates that uncertainty in inlet pressure should not affect a model-based iBIT process of fouling identification.

2.4.5 Heat exchanger fouling with uncertainty in the inlet mass flows

Inefficient operation of the ECS compressors may lead to uncertain flow rates for the bleed stream of the ECS. Similarly, the ram flow is controlled by a fan and other upstream system components that might bring uncertainty to the mass flow rate of that side of the heat

Table 2.6: Estimated values and 95% confidence intervals of mass flow rates and thermal fouling resistance.

iBIT settings, $\boldsymbol{\varphi}$	Nominal		
	T_{hi}=175 °C, n_s=1, τ=300 s		
	$\dot{m}_{ci}$ (kg/s)	$\dot{m}_{hi}$ (kg/s $\times 10^1$)	R_f (m^2 K/W $\times 10^3$)
Ram flow	1.00±0.003	-	5.94±0.42
Bleed flow	-	3.00±0.010	5.90±0.42
Ram and Bleed flow	1.00±1.36	3.00±4.12	5.91±16.4
iBIT settings, $\boldsymbol{\varphi}$	Optimal		
	T_{hi}=[100 °C, 250 °C], n_s=2, τ=300 s		
	$\dot{m}_{ci}$ (kg/s)	$\dot{m}_{hi}$ (kg/s $\times 10^1$)	R_f (m^2 K/W $\times 10^3$)
Ram flow	1.00±0.003	-	6.27±0.34
Bleed flow	-	3.00±0.007	6.12±1.05
Ram and Bleed flow	1.00±0.010	3.00±0.023	6.12±1.05

exchanger. Thus, here the ram and bleed mass flows were considered uncertain during the iBIT for fouling estimation. Three iBIT scenarios were studied to explore the impact of uncertainty in the flow rates: the first and second tests focused on uncertain bleed side and ram side flows rates, respectively, and a third test analyzed uncertain bleed side and ram side flow rates simultaneously. The results of these case studies for nominal and optimal iBITs are presented in Table 2.6, along with the design vector for the optimal iBIT. Similar to the case of uncertain medium heat capacity, the mass flow rate affects the convective and advective heat transfer of the system and, thus, the overall thermal effectiveness of the heat exchanger. The 95% confidence intervals for the estimates of all the uncertain system inputs were obtained at nominal and optimal conditions as shown in Table 2.6.

Fouling identifiability decreased when applying uncertain flow rates, as expressed by the lack of accuracy in the estimates at nominal conditions and their wide confidence inter-

vals. As expected, the system flow rates have a significant impact on fouling detection due to their influence on the heat transfer effectiveness. Nonetheless, a vast improvement was feasible with the optimal iBIT strategy.

2.4.6 Heat exchanger fouling with multiple uncertain conditions

With multiple unknown/uncertain system parameters, inputs and states, the task of using iBIT to estimate system fouling becomes a large-scale multi-variable optimization problem. It is clearly evident from the previous analyses that when fouling, air moisture and flow rates are simultaneously unknown or uncertain there is little chance in identifying fouling at nominal conditions with only one steady state test. Thus, the task here is to optimize a number of tests determined by D-optimal experimental designs, which by definition seek to separate parametric correlations, within an assigned design space. To confirm the robustness of the iBIT design methodology proposed here, a case study was explored, in which ram inlet temperature, ram flow rate, moisture content, and thermal fouling resistance are considered unknown or uncertain. Fig. 2.9 shows the virtual system temperature of the bleed and ram outlets of the nominal and optimal iBITs for multiple uncertain inlet conditions.

In the iBIT of Fig. 2.9, both steady state and transient information are used for fouling detection and isolation. These conditions provide the highest heat transfer rates and substantial system dynamic responses. The confidence intervals of the estimated parameters and system at the nominal and optimal iBIT settings are shown in Table 2.7. It is clear that

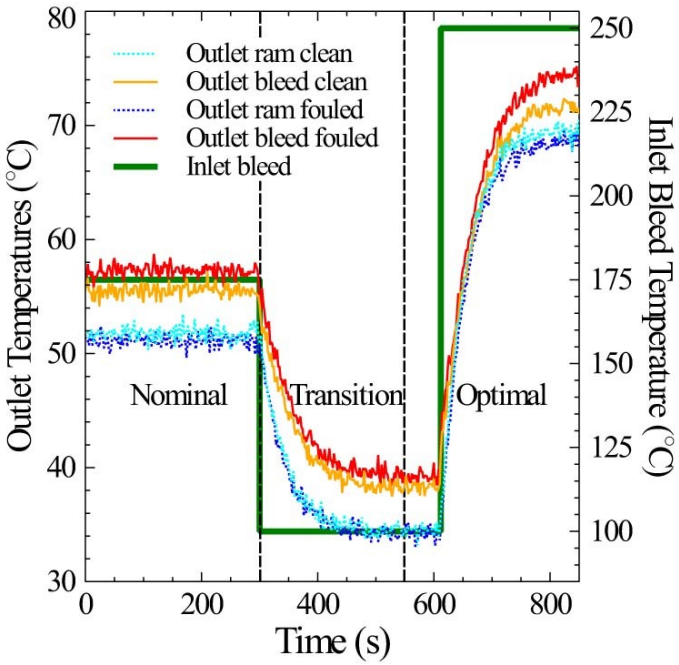

Fig. 2.9: Inlet bleed temperature and predicted outlet ram and bleed temperatures of clean and fouled heat exchanger using the true values detailed in Table 2.7. The heat exchanger is initially set to steady-state at nominal conditions for 300 s and then transitioned to the steady-states of the optimal iBIT settings (100 to 250 °C).

for a heat exchanger operating in a system with significant uncertainty in a large number of its variables or parameters or inputs, only optimal iBITs, as shown in Table 2.7, are capable of identifying and quantifying fouling accurately and with confidence.

Table 2.7: Estimated values and 95% confidence intervals of mass flow rates and thermal fouling resistance.

Uncertain condition	Nominal	Optimal	True values
R_f (m^2 K/W $\times 10^3$)	5.44±133.5	6.50±0.98	6.20
w_{H_2O} ($\times 10^2$)	1.03±65.50	1.13±0.33	1.20
T_{ci} (°C)	15.85±54.45	15.05±0.33	15.00
$\dot{m}_{ci}$ (kg/s)	1.03±1.65	1.00±0.008	1.00

2.5 Conclusions

We proposed an iBIT method for aircraft ECS heat exchanger fouling quantification, in which the extractable test information is maximized on the basis of a system model. The presented methodology involves the development of a plate-fin heat exchanger model, validation of the model using relevant experimental data, and utilization of the model in a D-optimal experimental design framework, to determine optimal iBIT operational settings. The unknown thermal fouling resistance was treated as a parameter and analyzed along with a combination of uncertain system inputs, such as inlet temperatures, moisture content, and mass flows. The iBIT design vector, i.e. the system admissible inputs at which fouling is to be estimated, was manipulated to optimize experimental information, and expressed via the Fisher information matrix. Nominal and optimal iBITs were compared with respect to their capability to identify fouling, through parameter estimation, using the corresponding

heat exchanger measurements. It was shown that the proposed iBIT methodology for heat exchanger fouling identification allows for accurate and precise estimation of the heat exchanger fouling, when this would have been infeasible with current conventional methods and without the addition of extra measurement devices or other BIT equipment.

Chapter 3

Analysis of Transient Data in Test Designs for Active Fault Detection and Identification

Abstract

Active model-based FDI methods are of increasing importance in modern cyber-physical systems due to their ability to generate detections as residuals between anticipated and observed information, and, thus, isolate and identify causes of faults with greater confidence than conventional passive FDI techniques. This work focuses on evaluating the effectiveness of active FDI tests which use either steady-state or dynamic information. It is shown that transient information from active FDI tests can improve the identifiability of faults compared to steady-state testing. These tests are designed by casting FDI as an optimization problem that maximizes the Fisher Information Matrix of a system sensed outputs with respect to faults. The identifiability of faults is examined at steady-state and transient FDI tests in a plate-fin heat exchanger of an aircraft environmental control system. In this system particulate fouling needs to be detected, which is challenged by multiple sources of system uncertainty. It is shown that the inclusion of transient information during fault diagnosis

increases the confidence in fault identification when using optimal test designs.

3.1 Introduction

The objective of traditional model-based FDI is to determine system faults by evaluating deviations from anticipated system behavior. These methods must be accurate, decisive, reliable and quick to execute in order to prevent fault propagation to downstream systems [76]. The increasing uncertainty (in system boundaries, components and system models) and complexity (in system size, number of components and heterogeneity of data generated) lead to failure in fault detection and identification in the form of false alarms and events called No-Fault-Founds (NFFs) [77]. False alarms and NFFs are increasingly challenging in the FDI of systems in the automotive and aerospace industries [78, 79]. Therefore, aircraft system operators deploy built-in tests (BIT) in their maintenance testing to improve FDI capability and reduce maintenance costs [80].

In the previous chapter, an active FDI approach was proposed that generates residuals sensitive to faults, is robust to uncertainty, and examines the impact of transient data in FDI tests. Active FDI was implemented so that the admissible input trajectories are manipulated to create optimal tests for fault detection and identification. Calculation of the FDI test design prior to execution, reduces significantly the on-line computational cost of FDI implementation. The inputs are not updated with new test information, thus a test design is required that improves the identifiability of all faults that can occur beforehand.

The reason for this is that the test design can be computationally cumbersome for on-line FDI, while the differences between sequential (frequentist) and parallel design approaches are often minimal to justify the introduced on-line computational complexity [32]. Thus, the FDI test design was treated as a set of constrained optimization problems that maximize metrics of the information generated from the test with respect to faults, and, in particular, the Fisher Information Matrix. System inputs were manipulated to improve the identifiability of system faults and uncertain conditions by maximizing information with respect to faults in the form of sensitivities of system outputs. This method of FDI test selection is based on a statistical approach known as Optimal Experiment Design [53], which is used to extract available information from system models to improve parameter identifiability. In this classical model-based design of experiments approach [31, 32, 56, 81], steady-state or dynamic tests are designed to maximize the identifiability of fault(s), expressed in the system model as parameter(s). For a given number of system sensors, the system uncertainty is also estimated (if identifiable). The tests designed can be steady-state or transient, depending on the model structure and the accuracy of the system actuators. The objective of the FDI test optimization is to minimize the correlation between faults and uncertain conditions that affect sensor outputs. The D-optimal criterion is selected for test designs that aim to reduce the joint confidence regions of the faults, uncertain parameters and inputs [59]. The tests designed can be steady-state or transient, depending on model structure and accuracy. Although the understanding of process dynamics has been of interest in complex systems and

control [82], quantification of the value proposition of steady-state vs. dynamic FDI tests is relatively vague in the open literature and is the objective of this work.

This chapter is organized as follows: Section 3.2 presents the mathematical formulation for transient and steady-state FDI tests cast as optimization problems. The calculation of optimal test designs is presented in detail, focusing on the differences between steady state and dynamic tests. The mathematical formulation of fault severity estimation using an extended Kalman filter is provided in accordance with [83, 84] followed by another FDI test approach based on well-known moving horizon estimation techniques [85, 86]. Section 3.3 presents the effectiveness of these methods is tested in two case studies. In each case study, a heat exchanger model that was developed and validated earlier [5] is used to simulate particulate fouling in an aircraft environmental control system. Maintenance tests are common in heat exchanger fouling detection [80, 87] and the increased range of control inputs, while the system is off-line, can be used for active fouling identification. In the first case study, system uncertainty is represented by moisture levels in the flow streams. In the second case study, the system uncertainty is extended to include the mass flow rate and inlet temperature of one of the streams. The fault in these cases is assumed to be deterministic in that it can be quantified as a parameter in the system model, and it is present and persistent for the entirety of the FDI test. Although in the applications demonstrated here only one fault is considered (for brevity and illustration purposes), the method presented can handle multiple faults and uncertain conditions. We show the effect of uncertainty at nominal and

optimal test conditions as well as the quantifiable change when steady-state and transient information is used in fault diagnosis.

3.2 Methods

This section introduces the methodology for improving active FDI with high-fidelity models, as well as the terminology and notation used throughout this paper. The workflow of this framework has been discussed in [88]. The first step is to formulate a model that sufficiently represents the system with and without anticipated faults, which are cast as model parameters. The system admissible inputs and the number of tests are considered to be optimization variables for the FDI test design and are compiled into the test design vector. The test design space contains the allowable ranges of each element in the design vector. The uncertain parameters and inputs are assessed prior to test design optimization and assigned fixed upper and lower bounds. The test design vector is then manipulated to determine the test design that maximizes the evidence (impact) of faults on outputs and minimizes correlations between faults and uncertainty. Posterior analysis for parametric identifiability, false alarm rates and threshold design, discussed in [88], are not the focus of this work but can be applied as instructed previously.

The first part of this section introduces the mathematical formulation of the system models selected for FDI. The second part presents the steady-state and dynamic optimization problems, used to determine the D-optimal FDI test designs. Model formulations and

optimization problems for the steady state and transient FDI tests considered are collectively presented in Table 3.1. The last subsection describes the two methods used to compare system measurements with anticipated outputs and determine whether faults are present. The first approach is utilizing an Extended Kalman Filter augmented for state and parameter estimation, while the second method is based on Moving Horizon Estimation.

3.2.1 System model formulation

Following the work from Chapter 2, the mathematical models are written as a series of implicit differential algebraic equations, shown in (3.1a,3.2a). When the system is only considered at steady-state, (3.1a-3.1g), t and $\dot{\mathbf{x}}$ are omitted.

Each system fault is expressed as a parameter with an anticipated value or range of values for when the fault is present in the system, and a known value for the healthy system. For clarity, the model parameters are split into three subsets, as shown in (3.1c) and (3.2c). These subsets represent the $N_{\theta_f} \times 1$ vector of system faults, $\boldsymbol{\theta}_f \in \mathbb{R}^{N_{\theta_f}}$, the $N_{\theta_u} \times 1$ vector of system uncertainty-based parameters, $\boldsymbol{\theta}_u \in \mathbb{R}^{N_{\theta_u}}$, and the $N_{\theta_p} \times 1$ vector of known design parameters, $\boldsymbol{\theta}_p \in \mathbb{R}^{N_{\theta_p}}$. System inputs are similarly divided into two subvectors shown in (3.1d,3.2d) that represent the $N_{u_p} \times 1$ vector of controllable system inputs, $\mathbf{u}_p \in \mathbb{R}^{N_{u_p}}$ at time t, and the $N_{u_u} \times 1$ vector of uncertain inputs, $\mathbf{u}_u \in \mathbb{R}^{N_{u_u}}$. System uncertainty represented as $\boldsymbol{\theta}_u$ and $\mathbf{u}_u$ is assumed to lie within anticipated distributions determined prior to FDI test optimization or execution. These system uncertainties are compiled together with the

Table 3.1: Equations used of steady-state and dynamic FDI methodologies

Steady-State FDI		Dynamic FDI	
$\mathbf{f}(\mathbf{x},\mathbf{u},\boldsymbol{\theta})=\mathbf{0}$	(3.1a)	$\mathbf{f}(\dot{\mathbf{x}}(t),\mathbf{x}(t),\mathbf{u}(t),\boldsymbol{\theta},t)=\mathbf{0}$	(3.2a)
$\hat{\mathbf{y}}=\mathbf{h}(\mathbf{x},\mathbf{u},\boldsymbol{\theta})$	(3.1b)	$\hat{\mathbf{y}}(t)=\mathbf{h}(\mathbf{x}(t),\mathbf{u}(t),\boldsymbol{\theta},t)$	(3.2b)
$\boldsymbol{\theta}=[\boldsymbol{\theta}_f,\boldsymbol{\theta}_u,\boldsymbol{\theta}_p]$	(3.1c)	$\boldsymbol{\theta}=[\boldsymbol{\theta}_f,\boldsymbol{\theta}_u,\boldsymbol{\theta}_p]$	(3.2c)
$\mathbf{u}=[\mathbf{u}_u,\mathbf{u}_p]$	(3.1d)	$\mathbf{u}=[\mathbf{u}_u,\mathbf{u}_p]$	(3.2d)
$\boldsymbol{\xi}=[\boldsymbol{\theta}_f,\boldsymbol{\theta}_u,\mathbf{u}_u]$	(3.1e)	$\boldsymbol{\xi}=[\boldsymbol{\theta}_f,\boldsymbol{\theta}_u,\mathbf{u}_u]$	(3.2e)
$\boldsymbol{\varphi}'=[\mathbf{u}_p,N_{test},\mathbf{y}_0,\tau]\in\boldsymbol{\Phi}'$	(3.1f)	$\boldsymbol{\varphi}'=[\mathbf{u}_p(t),\mathbf{t}_{sp},N_{test},\mathbf{y}_0,\tau]\in\boldsymbol{\Phi}'$	(3.2f)
$\boldsymbol{\varphi}=[\mathbf{u}_p,N_{test}]\in\boldsymbol{\Phi}$	(3.1g)	$\boldsymbol{\varphi}=[\mathbf{u}_p(t),N_{test}]\in\boldsymbol{\Phi}$	(3.2g)
$\mathbf{Q}_{StS,i}=\begin{bmatrix}\frac{\partial\hat{y}_i}{\partial\xi_1}\Big\vert_{\tilde{\boldsymbol{\xi}},n=1} & \cdots & \frac{\partial\hat{y}_i}{\partial\xi_{N_\xi}}\Big\vert_{\tilde{\boldsymbol{\xi}},n=1}\\ \vdots & \ddots & \vdots\\ \frac{\partial\hat{y}_i}{\partial\xi_1}\Big\vert_{\tilde{\boldsymbol{\xi}},n=N_{test}} & \cdots & \frac{\partial\hat{y}_i}{\partial\xi_{N_\xi}}\Big\vert_{\tilde{\boldsymbol{\xi}},n=N_{test}}\end{bmatrix}$	(3.1h)	$\mathbf{Q}_{Dyn,i}=\begin{bmatrix}\frac{\partial\hat{y}_i}{\partial\xi_1}\Big\vert_{\tilde{\boldsymbol{\xi}},t_1} & \cdots & \frac{\partial\hat{y}_i}{\partial\xi_{N_\xi}}\Big\vert_{\tilde{\boldsymbol{\xi}},t_1}\\ \vdots & \ddots & \vdots\\ \frac{\partial\hat{y}_i}{\partial\xi_1}\Big\vert_{\tilde{\boldsymbol{\xi}},t_{N_{sp}}} & \cdots & \frac{\partial\hat{y}_i}{\partial\xi_{N_\xi}}\Big\vert_{\tilde{\boldsymbol{\xi}},t_{N_{sp}}}\end{bmatrix}$	(3.2h)
$\mathbf{H}_\xi(\tilde{\boldsymbol{\xi}},\boldsymbol{\varphi})=\sum_{i=1}^{N_y}\sum_{j=1}^{N_y}\sigma_{ij}^{-2}\mathbf{Q}_i^T\mathbf{Q}_j$	(3.1i)	$\mathbf{H}_\xi(\tilde{\boldsymbol{\xi}},\boldsymbol{\varphi})=\sum_{i=1}^{N_y}\sum_{j=1}^{N_y}\sigma_{ij}^{-2}\mathbf{Q}_i^T\mathbf{Q}_j$	(3.2i)

faults considered, $\boldsymbol{\theta}_f$, into a $N_\xi\times 1$ vector, $\boldsymbol{\xi}\in\mathbb{R}^{N_\xi}$, that is the target of FDI test design optimization, as shown in (3.1e,3.2e). The vector, $\boldsymbol{\xi}$, is considered to have an anticipated

Table 3.2: Test design optimization problems for steady-state and dynamic FDI

Steady-State FDI	Dynamic FDI
$\boldsymbol{\varphi}^*_{StS} \in \left[\mathbf{u}^*_{p,1}, ..., \mathbf{u}^*_{p,N^*_{test}}, \quad N^*_{test} \geq 1\right]$	$\boldsymbol{\varphi}^*_{Dyn} \in \left[\mathbf{u}^*_p(t_1, \ldots, t_{N^*_{test}}), \quad N^*_{test} \geq 1\right]$
(3.3)	(3.4)
$= \arg\min_{\boldsymbol{\varphi}\in\Phi} \det\left[\mathbf{H}^{-1}_{\xi}\left(\tilde{\boldsymbol{\xi}}, \boldsymbol{\varphi}\right)\right]$	$= \arg\min_{\boldsymbol{\varphi}\in\Phi} \det\left[\mathbf{H}^{-1}_{\xi}\left(\tilde{\boldsymbol{\xi}}, \boldsymbol{\varphi}\right)\right]$
s.t.	s.t.
$\mathbf{f}(\mathbf{x}, \mathbf{u}_p, \boldsymbol{\theta}_p, \tilde{\boldsymbol{\xi}}) = \mathbf{0},$	$\mathbf{f}(\dot{\mathbf{x}}(t), \mathbf{x}(t), \mathbf{u}_p(t), \boldsymbol{\theta}_p, \tilde{\boldsymbol{\xi}}, t) = \mathbf{0},$
$\hat{\mathbf{y}} = \mathbf{h}(\mathbf{x}, \mathbf{u}_p, \boldsymbol{\theta}_p, \tilde{\boldsymbol{\xi}}),$	$\hat{\mathbf{y}}(t) = \mathbf{h}(\mathbf{x}(t), \mathbf{u}_p(t), \boldsymbol{\theta}_p, \tilde{\boldsymbol{\xi}}, t),$
$\mathbf{u}^L_p \leq \mathbf{u}_p \leq \mathbf{u}^U_p,$	$\mathbf{y}_0 = \begin{cases} \mathbf{f}(\dot{\mathbf{x}}(t_0), \mathbf{x}(t_0), \mathbf{u}_p(t_0), \boldsymbol{\theta}_p, \tilde{\boldsymbol{\xi}}, t_0) = \mathbf{0}, \\ \hat{\mathbf{y}}(t_0) = \mathbf{h}(\mathbf{x}(t_0), \mathbf{u}_p(t_0), \boldsymbol{\theta}_p, \tilde{\boldsymbol{\xi}}, t_0), \end{cases}$
$\mathbf{x}^L \leq \mathbf{x} \leq \mathbf{x}^U$	$\mathbf{u}^L_p \leq \mathbf{u}_p(t) \leq \mathbf{u}^U_p, \quad \forall t \in [0, \tau],$
	$\mathbf{x}^L \leq \mathbf{x}(t) \leq \mathbf{x}^U, \quad \forall t \in [0, \tau]$

set of values, $\tilde{\boldsymbol{\xi}}$, that represent most likely values of the faults and uncertain inputs and parameters. After the system model has been formulated, the next step is to formulate the method for optimizing the active FDI test design.

3.2.2 FDI test design optimization

System inputs are manipulated by the FDI tests (steady-state or dynamic) resulting in transient system outputs (around the steady state value due to noise, or dynamically as imposed by system dynamics and noise). In the steady-state test, measurements are obtained when the system has reached steady-state. In the dynamic test, the system starts from a steady-state condition, and then measurements are collected while the system is at transient. The admissible system inputs, $\mathbf{u}_p$, are manipulated as a series of discrete steps to generate the optimal test design for fault detection and isolation. The time duration of the FDI test, τ, and allowable number of tests, N_{test} need to be accounted for in FDI design. The selection of steady-state or dynamic test designs can impact the allowable range of each variable. The input trajectories, $\mathbf{u}_p(t)$, number of tests, N_{test}, sampling times, $\mathbf{t}_{sp}$, overall timespan, τ, and initial system states, $\mathbf{y}_0$, are compiled into the test design vector, $\boldsymbol{\varphi}'$, which is constrained within the test design space, $\boldsymbol{\Phi}'$, as shown in (3.1f,3.2f) for steady-state and dynamic tests, respectively.

In this work, the design vector of (3.1f) and (3.2f) was simplified. The sampling times and the overall test duration were constant, and the initial system states were set so that the test design initiates when the system has reached a nominal steady-state. These variables were fixed and the test design vector was reduced to (3.1g,3.2g), where $\mathbf{u}_p(t)$ has the size $N_p \times N_{test}$, the number of admissible inputs used for FDI times the number of tests (which in this context relates to frequency by which admissible inputs are changed during the FDI

test). The input trajectories are cast as piecewise constant functions of time, with each test in N_{test} corresponding to a time period that the process inputs are constant. The design vector, $\boldsymbol{\varphi}$, can represent an FDI test design with a single continuous test, or several separate tests. We assume that $\boldsymbol{\varphi}$ can contain inputs from a series of discrete steady-state tests, or a single continuous dynamic test with transient measurements. The test design space, $\boldsymbol{\Phi}$, specifies the lower and upper bounds of each variable listed in the test design vector.

The objective of the optimization is to maximize the extractable test information with respect to faults and uncertainty by adjusting the test design vector, $\boldsymbol{\varphi}$, thereby generating optimal information for estimating the system values of $\boldsymbol{\xi}$. Local sensitivities of available measurements with respect to targeted parameters (i.e. faults and uncertainty) are determined and compiled to generate the test information. In this work, the local sensitivities are obtained using normalized parametric derivatives that are approximated within the neighborhood of $\tilde{\boldsymbol{\xi}}$ using central finite differences with the system model. A prior analysis was done to ensure that numerical error generated from calculating sensitivities in this manner was negligible. The steady-state test sensitivities are calculated after each test, n_{test}, and compiled into a $N_{test} \times N_{\xi}$ sensitivity matrix, $\mathbf{Q}_{StS,i}$, for each output y_i as shown in (3.1h), where N_{test} is the number of steady-states at which each output, y_i, is observed and N_{ξ} is the number of variables and parameters representing faults and uncertainty in $\boldsymbol{\xi}$. In (3.2h), the sensitivity matrix for dynamic tests, $\mathbf{Q}_{Dyn,i}$, has size $N_{sp} \times N_{\xi}$, with each sensitivity row sampled at time $t_k (k = 1, ..., N_{sp})$, and N_{sp} being the number of discrete measurements

taken from each measurement y_i.

Fisher information is commonly employed in system analysis because of its usefulness in statistical inference [56]. The sensitivity matrix from (3.1h) or (3.2h), depending on the selected type of FDI test, is used to calculate the Fisher Information Matrix (FIM), $\mathbf{H}_\xi$, as shown in (3.1i,3.2i), where σ_{ij} is the inverse of the expected variance of the ij-th measurement. The measurements taken were assumed to have zero-mean normal distributions with known standard deviations that are reflected in σ_{ij}. In (3.3,3.4), the objective is to minimize the correlations between faults and uncertainty that can be determined from test samples of the system measurements. To satisfy this objective, the D-optimal design criterion was used to determine the best FDI test design. Subsequently, the optimal test design vector was calculated by minimizing the determinant of the variance-covariance matrix. In this work, the inverse of $\mathbf{H}_\xi$ in (3.1i,3.2i) is used as it is equivalent to the Cramer-Ráo lower bound of the variance-covariance matrix [89]. The optimization of a steady-state test design is formulated as shown in (3.3). Similarly, the dynamic optimal test design is calculated according to (3.4). After the optimal test designs are selected, an identifiability analysis can be performed prior to FDI implementation as detailed in [88], by examining the confidence regions of the uncertain parameters or by solving optimizations problems that search for a different set of parameters capable of producing nearly identical system outputs. In the case studies presented here, the models were found to be structurally and practically identifiable with respect to their unknown parameters for at least one feasible FDI test design.

3.2.3 Fault severity assessment

After the test design for fault identification has been calculated it is explored in a virtual active FDI test to determine if the anticipated faults are identifiable. In this section, two models are used to determine the severity of faults: a noise-free "system model" with anticipated outputs measured at fault-free conditions and a "virtual system" that is injected with a fault and specific values for uncertainty, $\boldsymbol{\xi}^*$. The model of the virtual system is used to collect "observed" outputs as shown in (3.5):

$$\begin{aligned} y_i(\boldsymbol{\xi}^*, t_k) &= \hat{y}_i(\boldsymbol{\xi}^*, t_k) + w_{ik}; \\ k &= 1, \ldots, N_{sp}, \quad i = 1, \ldots, N_y, \end{aligned} \tag{3.5}$$

where w_{ik} is the normally distributed measurement noise ($\sim \mathcal{N}(0, \sigma_{ik}^2)\ \forall i, k$). Faults are then estimated through the use of two fault identification approaches to provide a more complete assessment of fault diagnosis with transient and steady-state information. In the case studies presented in the Results section, the effectiveness of each method with or without transient information is tested by comparing the fault estimates obtained at nominal and optimal test designs using Monte Carlo simulations. In each run, the measurement noise w_{ik} is randomly generated for all outputs and time points.

Extended Kalman filter

The first approach of fault identification used in this work is the extended Kalman filter, commonly applied to dual state and parameter estimation. The Kalman filter was developed to

estimate non-measurable states in linear systems [84], and the extended Kalman filter (EKF) is applicable to nonlinear systems by linearizing the state equations at each time step [90]. A well-known EKF implementation is the dual state and parameter estimation conducted after each measurement sample is collected a shown in Sun et al. [83], Li et al. [91]. This method allows for simultaneous state tracking and impact reduction of measurement noise, and is suitable for on-line fault diagnosis because of its small computational footprint. The mathematical formulation of the EKF for dual state and parameter estimation is provided in Appendix C. The EKF is applied with the system model linearized with updated $\boldsymbol{\xi}$ values at each time step, until all sampling time points have been collected and the unknown or uncertain parameters and states are estimated. In the steady-state test, the EKF is instigated when the system is at steady-state, and no data is collected while the system transitions to the next steady-state condition. When the system reaches steady-state again, the EKF is reactivated. In the dynamic FDI test, the EKF is implemented throughout the test duration. The formulation of the EKF for the purpose of FDI is provided in Appendix C of this document.

Moving horizon estimation

While the EKF can be implemented for FDI, its applicability for state and parameter estimation is diminished with increasing system complexity and non-linearity. Moving horizon estimation (MHE) is another optimization approach that unlike the Kalman filter allows for

nonlinear programming to be used for state and parameter estimation. MHE techniques have been shown to consistently improve estimation performance compared to EKF, with the drawback of their higher computational requirements [86]. The scheme for the simultaneous estimation of parameters and states through MHE was obtained from the method formulation reported in Küpper et al. [85], Kühl et al. [92], which was designed for dynamic nonlinear systems.

In each iteration of the MHE, states and parameters are estimated for a specific range of time points located in the horizon time $T_N = t_K - t_L$, where t_L is the time at the beginning of the horizon and t_K is the most recent time point in the horizon. The differences between the measured and predicted outputs during the horizon are minimized, as well as the estimated states and parameters from their corresponding predicted values as shown in (3.6). The MHE optimization problem is formulated as follows:

$$\min_{\mathbf{x}(t_L),\boldsymbol{\xi}} \left\{ \left|\left|\left[\begin{array}{c} \mathbf{x}(t_L) - \bar{\mathbf{x}}_L \\ \\ \boldsymbol{\xi} - \bar{\boldsymbol{\xi}}_L \end{array}\right]\right|\right|^2_{\mathbf{P}^{-\frac{1}{2}}_{L|L}} + \sum_{k=L}^{K} \left|\left|\left[\ \mathbf{y}(t_k) - \mathbf{h}(\mathbf{x}(t_k), \mathbf{u}(t_k), \boldsymbol{\theta}_p, \boldsymbol{\xi}, t_k)\ \right]\right|\right|^2_{\mathbf{R}^{-\frac{1}{2}}} \right\}$$

s.t.

$$\begin{aligned} &\mathbf{f}(\dot{\mathbf{x}}(t), \mathbf{x}(t), \mathbf{u}_p(t), \boldsymbol{\theta}_p, \boldsymbol{\xi}, t) = \mathbf{0}, \\ &\hat{\mathbf{y}}(t) = \mathbf{h}(\mathbf{x}(t), \mathbf{u}_p(t), \boldsymbol{\theta}_p, \boldsymbol{\xi}, t), \\ &\mathbf{x}^L \leq \mathbf{x}(t) \leq \mathbf{x}^U, \quad \forall t \in [t_L, t_K] \\ &\boldsymbol{\xi}^L \leq \boldsymbol{\xi} \leq \boldsymbol{\xi}^U, \quad \forall t \in [t_L, t_K] \end{aligned} \tag{3.6}$$

where $\bar{\mathbf{x}}_L$ and $\bar{\boldsymbol{\xi}}_L$ are the expected states vector and uncertain parameters and inputs vector

at time t_L, respectively, and the expression $||\mathbf{x}||^2_{A^{-\frac{1}{2}}} = \mathbf{x}^T\mathbf{A}^{-1}\mathbf{x}$, where $\mathbf{A}$ is the covariance matrix of $\mathbf{x}$. For simplicity, the expected values of the states and parameters were set to those obtained in the previous MHE iteration. The estimation error covariance matrix, $\mathbf{P}_{L|L}$, is updated at time t_L, as shown in Appendix C of this manuscript. The set of predicted outputs, $\mathbf{h}$, is obtained after simulating the system model starting from an initial state, $\mathbf{x}(t_L)$. Only the initial values of the states and parameters at time t_L are considered to be free variables because it is assumed that no process noise occurs within the horizon, as reported in Küpper et al. [85]. In the MHE approach to the fault severity assessment, (3.6) is repeatedly solved until the states and uncertain parameters and inputs have been estimated throughout the FDI test duration. The method of collecting data for use in the MHE is identical to the one implemented for the EKF approach.

3.3 Results and discussion

3.3.1 Heat exchanger system testbed

A heat exchanger model of an aircraft environmental control systems was used in a series of case studies to test the effectiveness of transient information in fault identification. Plate-fin heat exchangers are essential components in the aircraft ECS. The loss in heat transfer caused by fouling degrades ECS performance, thereby increasing the energy needed to provide air to the aircraft cabin at appropriate conditions. Two case studies were considered where the plate-fin heat exchanger from an aircraft ECS experiences particulate fouling, considered in

this context to be a fault that needs quantification. This fault is often the cause of false alarms because of multiple sources of uncertainty in the ECS. The number of uncertain parameters is different in each case study in order to determine the impact of uncertainty on the ability to detect and quantify the heat exchanger fouling with uncertainty.

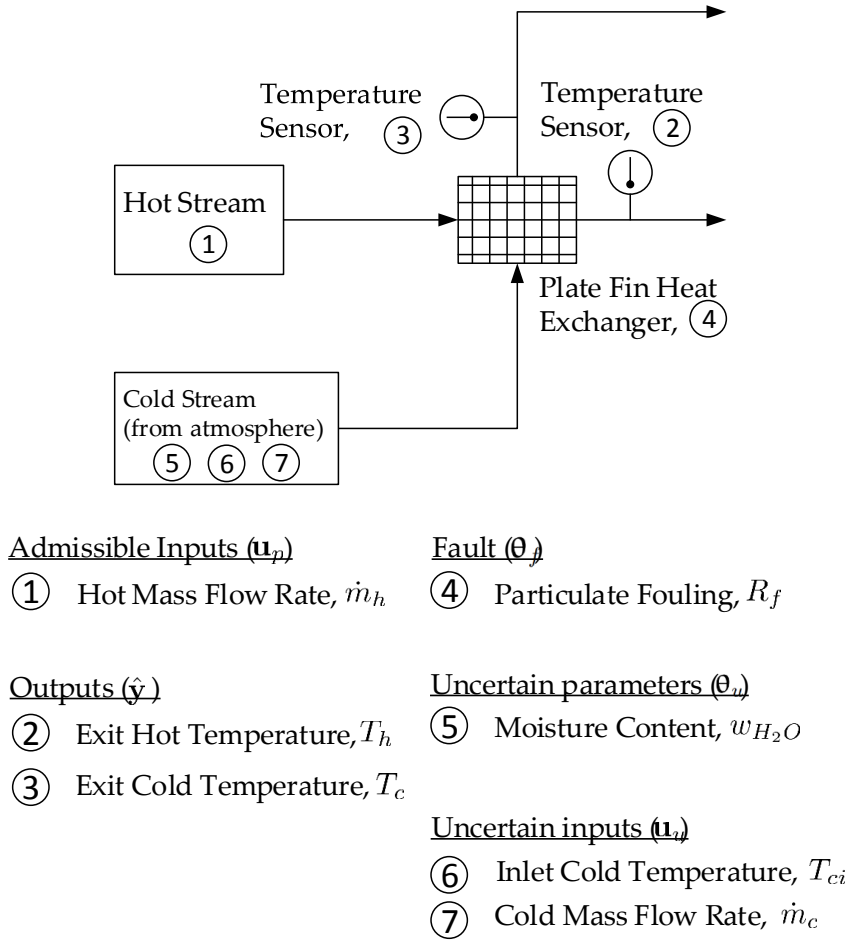

Fig. 3.1: Input-Output architecture of the ECS cross-flow plate-fin heat exchanger.

Figure 3.1 illustrates the inputs and outputs of the plate-fin heat exchanger model. In the studied implementation, the heat exchanger has one admissible input, two measured outputs, one fault and three uncertain variables. For the purpose of the case studies presented here, only the hot mass flow rate was considered admissible for the FDI test design. The mass flow of the hot stream was assumed to be perfectly controlled by upstream ECS components [93]. The hot stream mass flow rate was constrained to 0.1-1.0 kg/s, an acceptable range for the chosen heat exchanger geometry. The total duration for sample collection, τ, was set to 300 s to provide sufficient time for other necessary system diagnostics [66]. During the test implementation, up to one stepwise admissible input change was allowed, i.e. a maximum of two input settings could be used for FDI. Samples were taken at the same sampling frequency of 1 s^{-1}, with variable noise during each test. In the steady-state analysis, each steady-state test had a fixed duration of 150 s. The exit temperature sensors were used to collect measurements for fault identification. Each sensor was assumed to have white measurement noise with standard deviation of 0.5 °C.

3.3.2 Heat exchanger model and fouling identification

The cross-flow heat exchanger model was formulated with mass, energy and momentum conservation equations, as discussed in Chapter 2. Fluid flow was treated as one-dimensional along each fluid direction, whereas the cross-flow plate walls that separate them were modeled as 2D. The heat exchanger model was discretized as a series of sequential cells so the mass and

Table 3.3: Description of model variables for FDI executed with EKF and MHE

Variable	Size	Nominal Setting
$\mathbf{H}_{\xi}$	4×4	-
$\mathbf{Q}_{StS}$	$N_{test} \times 4$	-
$\mathbf{Q}_{Dyn}$	$N_{sp} \times 4$	-
$\boldsymbol{\xi} = [R_f, w_{H_2O}, T_{ci}, \dot{m}_c]$	4×1	[0 m^2K/W, 1.20%, 40 °C, 1.00 kg/s]
$\boldsymbol{\varphi}$	$N_{test} \times 1$	[0.30 kg/s,0.30 kg/s]*
$\mathbf{y}$	$N_{sp} \times 2$	-
$\mathbf{x}$	$N_{sp} \times 48$	-

* Anticipated values for the faults and uncertain parameters are provided in Table 3.4.

energy balances could be simplified into discrete axial profiles, formulated using MATLAB [70] for steady-state and dynamic simulation. The dimensionality of the FDI problem for the heat exchanger is summarized in Table 3.3. The FIM and sensitivity matrices depend on the number of faults and uncertain parameters in $\boldsymbol{\xi}$ (with N_{ξ}=4 in this particular problem). The sensitivity matrix for steady-state FDI had $N_{test} = 2$ rows, and for dynamic FDI the sensitivity matrix contained $N_{sp} = 300$ rows. The size of the vectors of system outputs and states depend on the number of discrete measurements used in the optimization ($N_{sp} = 300$), for both steady state and transient FDI. The system states include the hot and cold stream

temperatures within and exiting the heat exchanger, and the temperature of the plates separating the fluids. In the cases studied, the heat exchanger geometry was discretized into a 4×4 grid (see in Chapter 2 for more details on the discretization), thus 48 states were generated in the model at any time point.

The heat exchanger model was validated with steady-state and transient experimental data obtained from a testbed plate-fin heat exchanger detailed in Shah et al. [42]. Steady-state tests and transient step tests were implemented onto the virtual plate-fin heat exchanger with plain fin geometry, and the output responses generated from these tests were compared with the benchmark heat exchanger reported in Shah et al. [42]. Heat transfer coefficients and estimated pressure drop were also validated using data reported in Dong et al. [63] with various system geometries. The values of $\boldsymbol{\theta}_p$ and $\boldsymbol{\theta}_u$ reported in this document were derived from model validation tests performed using literature-reported data [42, 63, 75]. Model error is expressed as uncertainty in the design parameters, $\boldsymbol{\theta}_p$. As discussed in Palmer et al. [5], system dynamics were accurately captured by the model, which is, thus, considered suitable for dynamic FDI test design and a good computational testbed for FDI execution. The validated model was then used to calculate optimal tests for FDI in systems with 80% of the heat exchanger channel cross-sectional area blocked by particulate fouling. The target of FDI is to quantify the extent of the fault (fouling) in lieu of the uncertainty in system inputs.

The faults and uncertain inputs considered in this analysis are listed in Table 3.4, along

Table 3.4: Lower ($\boldsymbol{\xi}^L$) and upper ($\boldsymbol{\xi}^U$) bounds of the faults and uncertain conditions in the heat exchanger and the anticipated values ($\tilde{\boldsymbol{\xi}}$) of a fouled system.

Uncertain Parameter	Lower Bound	Set of $\tilde{\boldsymbol{\xi}}$	Upper Bound
R_f ($m^2K/W \times 10^3$)	0.00	6.40	8.00
w_{H_2O} (%)	0.10	1.20	5.00
T_{ci} (°C)	15.0	40.0	50.0
$\dot{m}_c$ (kg/s)	0.75	1.00	1.25

with their anticipated values, lower and upper bounds. Fouling is expressed as thermal fouling resistance, R_f, and the range of thermal fouling resistance values corresponds to the percentage of cross-sectional area covered by particulates. The lower bound ($R_f = 0$ m^2K/W) indicates that the heat exchanger is completely clean and free of fouling, and the upper bound ($R_f = 0.008$ m^2K/W) indicates that the system is completely fouled. System uncertainty exists in the air moisture, cold stream flow rate and cold inlet temperature. The range of moisture content in the case studies considered was set to the minimum and maximum expected percentage of moisture in ambient air [75]. The cold stream flow depends on the settings of downstream ECS components e.g. the ram fan, and its rate was assumed in the range of ±25% of its anticipated value, 1.0 kg/s. The cold inlet temperature was assigned the range of expected temperatures shown in Table 3.4, with the nominal inlet temperature for maintenance testing set to 40 °C. In the first case study, only the thermal

fouling resistance and moisture content were considered to be uncertain, and the cold flow rate and inlet temperatures are fixed at their anticipated values, $\tilde{\boldsymbol{\xi}}$. The second case study examines the heat exchanger with all the elements of $\boldsymbol{\xi}$ considered to be uncertain. The sample size collected in the steady-state and dynamic FDI tests was the same.

3.3.3 Case study I: Identification of heat exchanger fouling with uncertainty in one input

Figure 3.2 presents the inputs and outputs generated from steady state and dynamic FDI tests and the corresponding fouling severity assessment as a function of time. First, 300 s of nominal operation were simulated with the virtual heat exchanger and were used to illustrate FDI capability at nominal conditions (within the 300 s test duration constraint). The shaded areas of Figure 3.2 illustrate the period during which data was collected from the steady state and dynamic tests. The optimal *steady-state FDI test design* was calculated from (3.3). In this design, the hot mass flow rate was first set to 0.43 kg/s and data was collected for 150 s of the corresponding steady state. The second optimal mass flow rate setting was at 1 kg/s (the upper bound) with data collected at that steady state for another 150 s. No information was collected during the transition between steady-states (indicated in Figure 3.2a by the shaded regions). The optimal *dynamic FDI test design* was calculated using (3.4). The hot stream was set to the first optimal mass flow rate setting of 0.1 kg/s (lower bound), followed by a step change to the upper bound at 1 kg/s. Dynamic system

responses were recorded for 300 s, which include data from the first optimal steady state, the system transient and the second steady state of this test. The step change of the admissible input from its lower to its upper bound allowed for the greatest dynamic response within the assigned constraints.

Figures 3.2a and 3.2c show the hot stream flow rate and the measured outputs from steady-state and dynamic FDI tests, respectively. The transition from the nominal test conditions are presented in Figure 3.2 only to show that there were no system constraint violations. The anticipated hot and cold exit temperatures of the clean heat exchanger are also presented to compare with the measured outputs obtained from the heat exchanger when it is fouled. The distance between the outputs at clean and fouled conditions is greater at higher hot stream flow rates, which is why all optimal test designs had one input setting at the upper bound. However, an additional test was required in both cases. This input setting (shown first in time in Figure 3.2) was different between the S.S. and dynamic FDI, which is discussed further in the following text. As mentioned, assessment of the fault severity was performed with the EKF and MHE, with a sample of the MHE results illustrated in Figures 3.2b and 3.2d. In these figures, the estimated states and parameters were updated after every new set of data was acquired, which illustrates the value of new information to the test. Overall, the R_f estimates from the tests show significant improvement after information from the second test becomes available, which is particularly clear in the dynamic case (3.2d).

The validity and quality of the optimal test designs were evaluated using the FIM plots

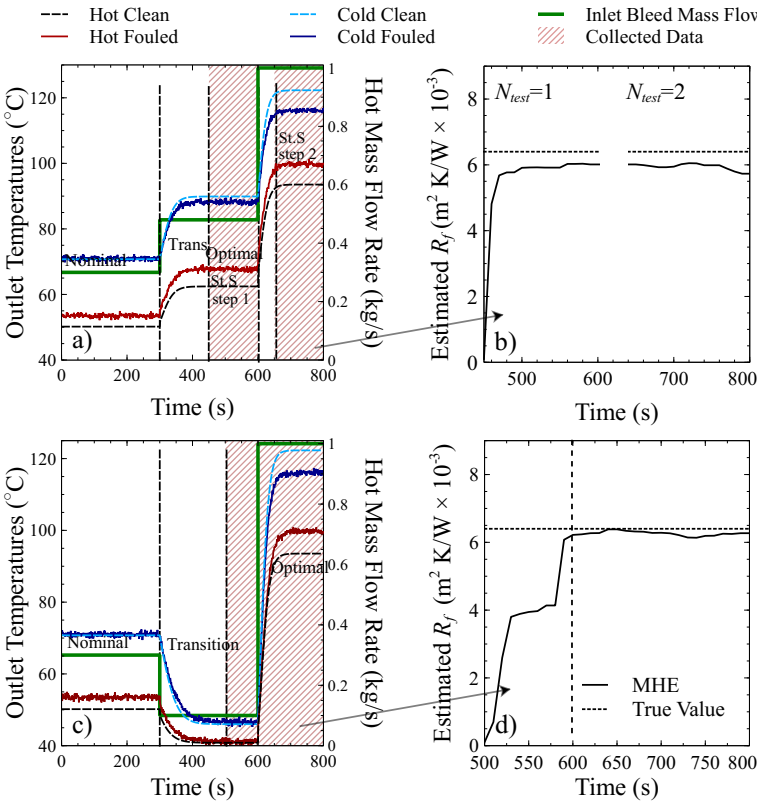

Fig. 3.2: FDI test data and example estimates of fouling identification using steady-state (plots a,b) and dynamic (plots c,d) test designs. The heat exchanger was set to steady-state at nominal conditions for 300 s. and then transitioned to optimal conditions. In the optimal steady-state test, two steady-state conditions were set to 150 s each, with a 50 s transition period between states. The dynamic optimal test was simulated for 300 s. The dynamic responses of the transition to the optimal conditions are presented to show that there were no violations of constraints.

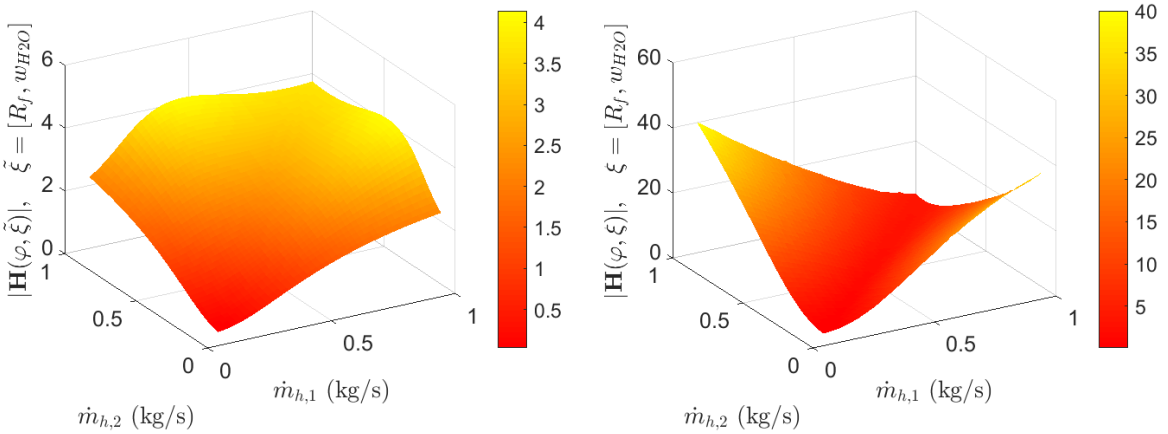

Fig. 3.3: Determinant of the Fisher Information Matrix for the heat exchanger FDI test over a range of admissible hot mass flow rates, with two inputs settings in the test design at steady-state (left, $\boldsymbol{\varphi}^*_{St.S.} = [\dot{m}_h = [0.43kg/s, 1.0kg/s], N_{test} = 2]$) or with transient response (right, $\boldsymbol{\varphi}_{Dyn} = [\dot{m}_h = [0.1kg/s, 1.0kg/s], N_{test} = 1]$). The uncertain parameters were the thermal fouling resistance and the moisture content, with anticipated values listed in Table 3.4.

of Figure 3. This also ensured that the designs for the steady-state and dynamic FDI tests were global solutions to (3.3) and (3.4), respectively. Figure 3.3 presents the determinant of the Fisher Information Matrix as a function of the hot mass flow rate with two input settings using steady-state (left) and dynamic (right) outputs. The two input settings for the hot stream flow rate, $\dot{m}_{h,1}$ and $\dot{m}_{h21}$, were varied within their allowable range of 0.1-1 kg/s, and the FIM was calculated iteratively for steady-state and dynamic FDI using (3.1i,3.2i), respectively. Essentially, the determinant values of the FIM are a metric of the quality of information obtained from each test. The left hand side plot of Figure 3.3 shows that the steady-state test generates the most information when the mass flow rate of the hot stream is set to 1.0 kg/s and 0.43 kg/s. Because each steady-state test has equal sample points and there are no transient effects to consider, it does not matter which admissible input setting is first. The most effective dynamic FDI test is accomplished when the mass flow rate is is set first to 0.1 kg/s followed by a step change to 1 kg/s, as shown in the rightmost corner of the right hand side plot of Figure 3.3. Most importantly, dynamic information increases the output sensitivities with respect to fault and uncertainty, as indicated by the higher values of $|\mathbf{H}_{\xi}|$.

Monte Carlo simulation of 100 runs was performed to compare fault estimates over time with EKF using nominal, optimal steady-state and dynamic test designs, as shown in Figure 3.4. The EKF was used to explore the capability of fouling assessment with a less computationally demanding technique. The initial estimates of fouling resistance

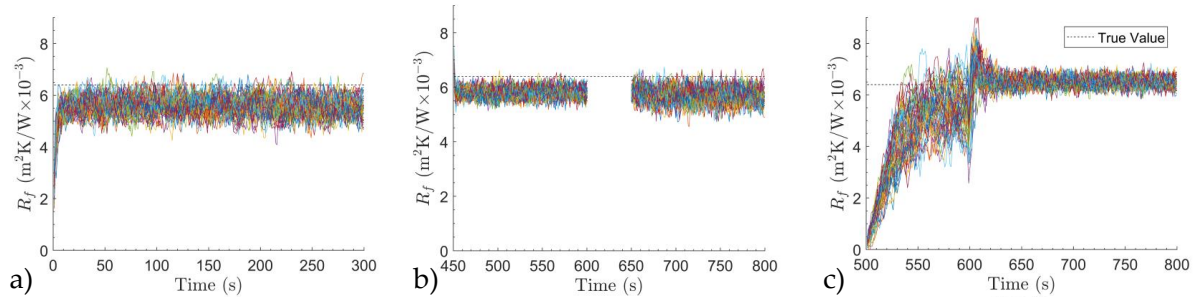

Fig. 3.4: Monte Carlo Simulation of thermal fouling resistance estimation with uncertain moisture content using EKF at (a) nominal, (b) optimal steady-state and (c) optimal dynamic test designs. No data was collected in the optimal steady-state test when in transition to the second steady-state.

and moisture content were set to 0 (m^{2}K/W) and 1.2%, respectively, representing a clean system with nominal moisture in the air. Samples were collected every second and the EKF estimated system states and parameters using the equations shown in Appendix C. The measurement noise of all the samples was variable with time and different in each iteration. In each case study, the initial state estimates used were set to be equal to the mean anticipated states of the heat exchanger at nominal conditions, which are the system initial conditions and were identical for all tests. In the nominal and optimal steady-state tests, the average estimate of thermal fouling resistance by the end of the FDI test was 5.5 and 5.8 (m^{2}K/W $\times 10^{-3}$), respectively. While the range of fouling resistance estimates overlap with the true R_f value during the FDI tests at nominal and optimal steady-state settings,

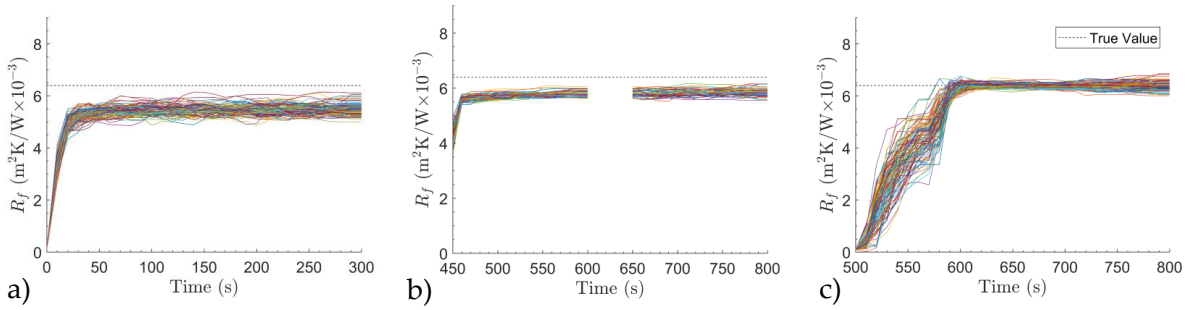

Fig. 3.5: Monte Carlo Simulation of thermal fouling resistance estimation with uncertain moisture content using MHE at (a) nominal, (b) optimal steady-state and (c) optimal dynamic test designs. No data was collected in the optimal steady-state test when in transition to the second steady-state.

only the optimal test with dynamic information consistently led to an accurate estimation of fouling. To test the impact of initial parameter estimates on fouling identification, the EKF was implemented several times using random initial values for the states and parameters estimated. Regardless of the initial parameter estimates, by $t = 50$ s the results were similar, as is shown in Figure 3.4. Measurement noise and the lack of sensitivity of the selected outputs with respect to air moisture led to less accurate fouling resistance estimates at nominal conditions or when the EKF observer was used without transient information.

Another Monte Carlo simulation was performed using MHE to determine its accuracy in fault severity assessment. The results are shown in Figure 3.5, where the same variable measurement noise was injected to each test measurement. The initial estimates were again

set to 0 (m^2K/W) and 1.2%, respectively. The MHE was set so that state and parameter estimations were made for every 10 s in the test, and each moving horizon used 30 samples ($T_N = 30$ s) to update states and parameters. In Figures 3.5a and 3.5b the fouling resistance estimates from the nominal and optimal steady-state tests are seen to be close but do not overlap with the true value of thermal fouling resistance. The additional input step in the optimal steady-state test retains the precision in the estimated range of fouling resistance values from the previous step. The best performance is shown in Figure 3.5c, where after the step change is implemented the dynamic response provides information to improve the fouling resistance estimation consistently. After the system converges to steady-state, the range of estimates increases again. By comparing the estimates from Figures 3.4 and 3.5, it is far more effective to evaluate transient information for FDI and the fault severity assessment with MHE than with EKF, as expected.

Table 3.5: Estimated 95% confidence intervals ($\tilde{\boldsymbol{\xi}} = [R_f, w_{H2O}]$) obtained from MHE at $t = \tau$.

Set of $\tilde{\boldsymbol{\xi}}$	True Values	Nominal		Optimal StS		Optimal Dyn	
		$\hat{\boldsymbol{\xi}}$	95% CI	$\hat{\boldsymbol{\xi}}$	95% CI	$\hat{\boldsymbol{\xi}}$	95% CI
R_f ($m^2K/W \times 10^{-3}$)	6.40	5.48	[5.43,5.52]	5.84	[5.81,5.87]	6.37	[6.34,6.41]
w_{H_2O} (%)	1.20	4.69	[4.60,4.79]	3.74	[3.63,3.85]	1.29	[1.17,1.40]

Table 3.5 presents the estimated values and confidence intervals of the fouling resistance and uncertain parameters with each test design. 95% confidence intervals were generated using nominal, optimal steady-state and optimal dynamic test designs with bootstrapping [94]. The fouling resistance estimates obtained from the nominal and optimal steady-state tests resulted in inaccurate estimates, with the true values outside the 95% confidence intervals. The estimation from the dynamic optimal test design resulted in estimated values and confidence intervals significantly closer to the true values. The moisture content estimation confidence improved as well. Overall, the optimal dynamic test resulted in more accurate and confident parameter estimates of the fouling severity and the uncertain parameter.

3.3.4 Case study II: Identification of heat exchanger fouling with multiple uncertain parameters and inputs

A second case study was explored to assess the capability to estimate fouling severity with transient information in the virtual heat exchanger, with all the parameters and inputs listed in Table 3.4 considered to be uncertain. (3.3) and (3.4) were used to determine the optimal test designs with available steady-state and transient information, respectively. The optimal steady-state FDI inputs for the first and second step were determined to be 1.00 kg/s and 0.29 kg/s, respectively. The optimal dynamic FDI test was the same as in the previous case study; the hot stream flow rate was set initially at the lower bound at 0.1 kg/s that followed by a step change to the upper bound at 1.0 kg/s.

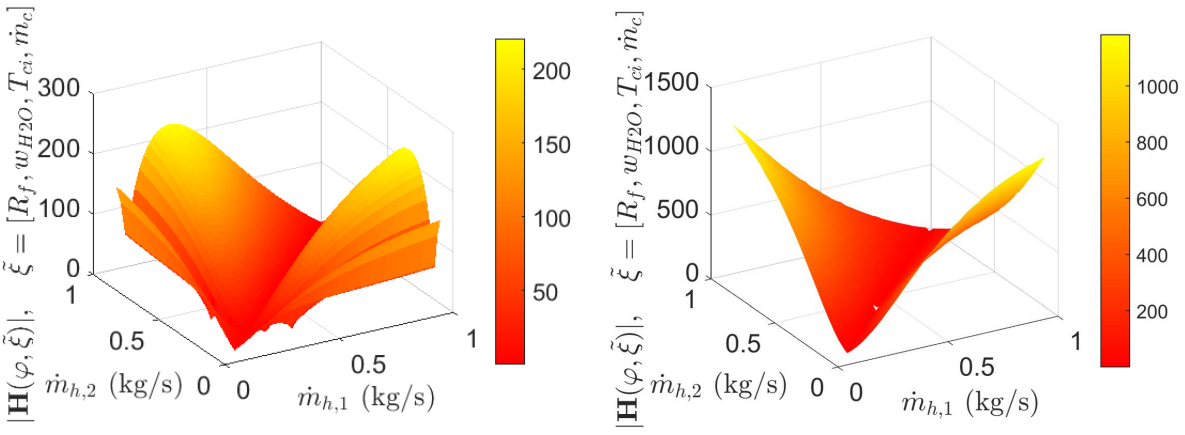

Fig. 3.6: Determinant of the Fisher Information Matrix for the heat exchanger FDI test, over a range of adjustable hot mass flow rates, with test designs consisting of two input settings at steady-state (left, $\boldsymbol{\varphi}^*_{StS} = [\dot{m}_h = [0.29\,\text{kg/s}, 1.0\,\text{kg/s}], N_{test} = 2]$) or with transient response included (right, $\boldsymbol{\varphi}^*_{Dyn} = [\dot{m}_h = [0.1\,\text{kg/s}, 1.0\,\text{kg/s}], N_{test} = 1]$). The uncertain parameters and inputs were the thermal fouling resistance, moisture content, cold mass flow rate and cold inlet temperature.

The calculated test designs were verified by exploring the determinant of the Fisher Information Matrix as a function of the first and second admissible input settings and determining if the test designs were indeed optimal. Figure 3.6 shows the values of the determinant obtained using steady-state (left) and dynamic (right) test information. The highest determinant was found for the steady-state FIM at one input setting at 0.29 kg/s, and another at 1.0 kg/s. The right hand side plot in Figure 3.6 shows that the highest determinant was accomplished with the first input setting at 0.1 kg/s and the second at 1.0 kg/s.

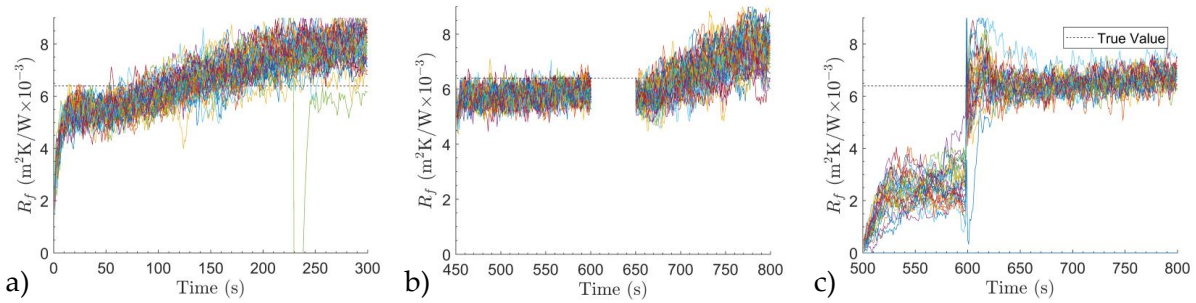

Fig. 3.7: Monte Carlo Simulation of thermal fouling resistance estimation with uncertain moisture content, cold mass flow rate and cold inlet temperature using EKF at (a) nominal, (b) optimal steady-state and (c) optimal dynamic test designs.

Monte Carlo simulation was then performed on the virtual heat exchanger and fouling severity was estimated using EKF on nominal, optimal steady-state and optimal dynamic FDI tests. Figure 3.7 shows 100 iterations of the EKF to estimate fouling at nominal, steady-state and dynamic optimal test designs. Figures 3.7a and 7b indicates that parameter esti-

mation performed with EKF was insufficient with the nominal and optimal steady-state test designs. This is most likely due to the amount of uncertainty included in the simultaneous estimation of states and parameters. In the nominal test, the average value of the fouling resistance estimate was greater than the maximum possible value of R_f by $t = 150$ s. The same occurred with the optimal steady-state value after the second input setting was implemented. The EKF performed on the optimal dynamic test design resulted in the smallest range of fouling resistance estimates, with the average value close to the true R_f value after the step change is complete and the dynamic responses are captured.

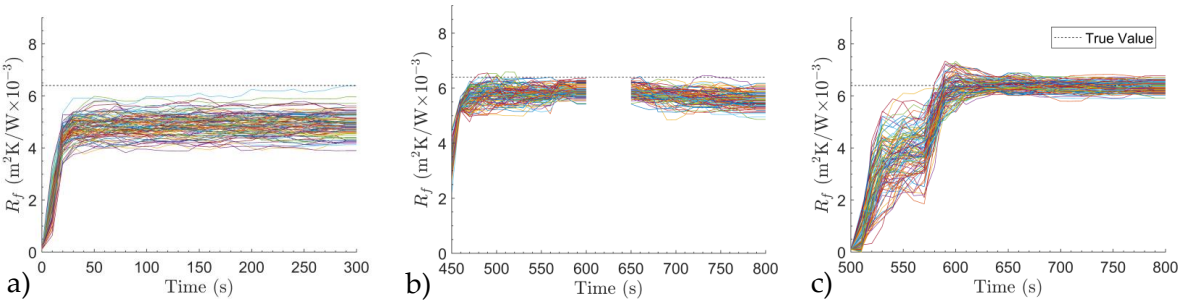

Fig. 3.8: Monte Carlo Simulation of thermal fouling resistance estimation with uncertain moisture content, cold mass flow rate and cold inlet temperature using MHE at (a) nominal, (b) optimal steady-state and (c) optimal dynamic test designs.

Fault severity assessment with MHE was also studied. Figure 3.8 presents the results of the Monte Carlo simulation of 100 runs with variable measurement noise. The nominal and optimal steady-state tests were significantly improved precision as shown in Figure 3.8a

and Figure 3.8b. However, the accuracy and precision of the fouling resistance estimates were lower than in the previous case study due to the increase in system uncertainty. The optimal dynamic test consistently estimated fouling resistance values close to the true value after the step change had been implemented. Before the change in inputs settings, the range of estimated values was greater than in the nominal case, indicating that the first input step was selected solely for data collection during transient. The optimal dynamic FDI test consistently generated accurate fault severity assessment from the available data with the MHE.

Table 3.6: Estimated 95% confidence intervals ($\tilde{\boldsymbol{\xi}} = [R_f, w_{H2O}, \dot{m}_c, T_{ci}]$) obtained from MHE at $t = \tau$.

Set of $\tilde{\boldsymbol{\xi}}$	True Values	Nominal		Optimal StS		Optimal Dyn	
		$\hat{\boldsymbol{\xi}}$	95% CI	$\hat{\boldsymbol{\xi}}$	95% CI	$\hat{\boldsymbol{\xi}}$	95% CI
R_f ($m^2K/W \times 10^3$)	6.40	4.94	[4.85,5.02]	5.56	[5.50,5.66]	6.35	[6.33,6.40]
w_{H_2O} (%)	1.20	4.67	[4.58,4.76]	4.80	[4.76,4.84]	1.33	[1.12,1.44]
$\dot{m}_c$ (kg/s)	1.00	0.90	[0.89,0.92]	1.00	[1.00,1.01]	1.00	[1.00,1.00]
$\dot{T}_{ci}$ (°C)	40.0	37.0	[36.6,37.4]	40.2	[40.2,40.3]	40.5	[40.2,40.7]

The resulting estimates and confidence intervals from the MHE Monte Carlo simulation are presented in Table 3.6. It is shown that the accuracy and precision of the fouling severity estimates decreased significantly when all the parameters and inputs listed in Table 3.4 were

considered uncertain. The optimal steady-state and dynamic tests resulted in more precise estimates of the thermal fouling resistance than the nominal test. There was consistent improvement in the estimation of the remaining uncertain parameters and inputs using dynamic information.

Overall, the inclusion of transient information in active FDI led to significant improvement. Fault severity assessment with EKF (as obtained from the first case study) and with MHE (second case study) indicate that the proposed optimization of the FDI test design improves the fault detectability and identifiability. The case studies presented indicate that the consideration of dynamic responses from changes in inputs in addition to steady-state conditions during test design optimization can lead to more informative tests for FDI. The inclusion of transient information in model-based FDI tests can significantly increase the accuracy of fault diagnosis in systems with known transient behavior. This conclusion is consistent between the assessments performed with EKF and MHE, though the fault estimation is more precise with MHE.

The proposed methodology requires an accurate dynamic model of the system to successfully identify faults using transient information. It should be noted that dynamic system behavior can be difficult to capture and model in certain applications, particularly when the system is at fault. Such models are derivatives of extensive lab-testing in conditions closely representative of field conditions. The generation of test data and accurate models can be quite laborious, but often exists for the verification of a system. In the case studies shown,

the model used for fault identification accurately represents an aerospace heat exchanger system at fault and fault-free conditions, as illustrated in [5]. The transient FDI framework described in this work was deployed in a heat exchanger of a commercial system, as discussed in [95].

3.4 Conclusions

Transient and steady-state model-based information was utilized for active fault detection and severity quantification. Optimal admissible input settings were calculated with the D-optimal design criterion, resulting in different input designs for steady-state and dynamic FDI tests. The importance of dynamic information in FDI test designs was assessed through a series of case studies, dealing with fouling severity estimation in a plate-fin heat exchanger. The results were compared at nominal and optimal test conditions using EKF and MHE for parameter and state estimation. This analysis showed that tests utilizing dynamic output responses to identity faults were consistently more reliable than steady-state tests. Fault severity assessment using EKF was shown to be accurate when only moisture content was considered to be uncertain. When multiple sources of uncertainty were present, only the optimal dynamic test provided enough information to accurately estimate the fault. FDI tests with MHE were successful at identifying anticipated system faults with multiple sources of uncertainty present. The fault severity assessment conducted with MHE was consistently more precise than with EKF.

Chapter 4

Active Fault Identification by Optimization of Test Designs

Abstract

In this chapter, a comprehensive model-based FDI framework is implemented to improve fault identifiability and reduce false alarms during maintenance testing. Maintenance tests are designed and executed followed by false alarm analysis. Each test design is evaluated *a posteriori* using the system model to explore whether false alarms are plausible, given system uncertainty and measurement noise. The proposed framework is applied on two case studies that compare the identifiability of faults at nominal and optimal system test conditions. The first case study focuses on a plate-fin heat exchanger described in Chapters 2 and 3 with various levels of particulate fouling at steady-state and transient conditions. The second case study deals with the same type of fault but in an aircraft environmental control system with multiple sources of uncertainty.

4.1 Introduction

The majority of model-based methods use parameter estimation [14], parity equations [18, 96], state observers [17, 97] or filters [44, 98] that treat faults as unknown or uncertain parameters and states. Typically, model-based FDI algorithms analyze residuals between observed system responses and expected fault-free predictions of physics-based models or correlations based on historical data. If these residuals are sufficiently large, then a fault is detected in the system and an alarm is triggered. FDI methods must be accurate, decisive, and quick in limiting fault propagation to downstream systems [76]. If the cause of an identified fault cannot be found during the FDI test, then the outcome is a false alarm or No-fault-found (NFF) event [99]. False alarms and NFFs are major issues, especially in the automotive and aerospace industries [78, 79], and considerable effort focuses on finding methods to eliminate them, because of their impact on system reliability and maintenance cost [77, 100]. In the case of aircraft systems, the widely variable and uncertain environment is the predominant cause of high rates of NFF events [99]. Therefore, built-in tests are deployed in aircraft maintenance testing to improve fault detection. Common issues in BIT include the uncertainty and wide variability of the inputs, measurement noise and sensor drift, often resulting in false alarms.

A false alarm is the detection of a fault that is not actually present in the system. System uncertainty can affect fault identifiability and increase the rate of false alarms in maintenance testing. Hu and Seiler [26] state that in false alarm analysis there must be a

balance between robustness against uncertainty (to reduce false alarm rates) and sensitivity to disturbances caused by faults. False alarm rate reduction is typically achieved by adjusting FDI test filters and fault detection thresholds, which help compensate for uncertainty. Cui et al. [101] proposed false alarm reduction methods in BIT, based on sensor threshold designs capable of achieving a balance between false alarms and nondetection rates. Nikodem [102] explored sensor locations that reduce false alarms in a boiler system. False alarm reduction techniques have also been proposed to aid data-driven FDI methods, such as principal component analysis (PCA). Mahadevan and Shah [103] used support vector machines to generate a high-dimension input scheme and adjusted it to minimize false alarm rates. Choi et al. [104] used kernel PCA to map data sets and establish patterns to detect faults, by fine-tuning parameters specific to false alarm elimination. Probabilistic models were used by Blough et al. [105] to improve the likelihood of correct diagnosis, leveraging prior information of the distributions of faults and uncertainty in a system. Bayesian networks have also been implemented to incorporate probabilistic model graphically [106].

In addition to adjusting the sensitivity of the fault detection algorithm (e.g. threshold design), another way to reduce false alarm rates is to adjust the system inputs so that the sensitivity of the outputs with respect to faults is increased. These so-called active FDI methods implement an actively configured set (or sequence) of admissible inputs to improve the diagnosis of faults that would otherwise remain undetected at standard system operation [22, 107, 108]. Most approaches of active FDI calculate input settings as continuous or piece-

wise constant variables [97, 109] that lead to separation of the sensed information of the faulty system from the corresponding fault-free prediction. Optimization objectives for active FDI test design include the detection accuracy, robustness against uncertainty, and cost. Real-time selection of control inputs has been expanded to models that use prior input signal information [110]. Esna Ashari et al. [111] incorporated active fault detection in closed-loop systems using linear-feedback control with optimal inputs. Zonotopes were used in Scott et al. [112] to guarantee fault detection based on available signals and output data while improving computational efficiency. Fault detection and optimal control was combined in Šimandl and Punčochá [113] using single objective functions for closed-loop systems. Methods for optimal input designs were developed while also considering model uncertainty using approaches such as maximizing information between hypotheses for a system at known or unknown conditions [114], or for a system with a particular set of faults [115]. In Khandelwal et al. [116], a multi-model scheme for FDI test designs was proposed for self-sensing systems in real time with model uncertainty.

Active FDI techniques such as those reported in Nikoukhah [22] and Andjelkovic et al. [23] require that there exists one set of conditions where there is no overlap between fault and fault-free outputs, and when this set is determined the objective is to minimize the time of detection. In reality, uncertainty and measurement noise do not always allow for complete separation to be feasible. Moreover, many active FDI methods use linear system models [117, 118, 119], which may not accurately capture the relationship between faults

and outputs, particularly in complex non-linear systems. Nonlinear methods have also been proposed in the literature [7, 23], but there are challenges in meeting their computational demands, when deployed in real systems. In particular, on-line methods that calculate inputs for FDI in real-time are difficult to deploy when the system model used is complex or contains multiple inputs and outputs. Active fault detection and identification designed for complex systems requires a robust method of selecting inputs, consideration of system uncertainty and its impact on outputs, and small computational requirements for the deployment of the test. Computing capabilities can be increased by using the system model off-line, thereby allowing for an optimal selection of test conditions to identify system faults in the presence of uncertainty. However, the optimal result may not guarantee a test design that is free of false detections. We present an off-line approach to selecting and assessing test designs intended for use in active FDI. In the method presented, FDI test design is feasible regardless of model structure and the joint confidence between faults and uncertainty in residual data is accounted for. In the approach presented here, the test information in the form of sensitivity of outputs with respect to unknown system faults and uncertain system inputs or parameters is optimized for FDI, after which the test design is evaluated to determine if false alarms have been eliminated in the optimal test.

Well-known, robust methods of information extraction and optimization that are used in parameter estimation and identification can take into account multiple sources of system uncertainty prior to testing [56, 120]. The proposed approach to FDI test selection is based

on OED techniques [53] that use a system model to estimate measurement variances, in response to input trajectories that improve the confidence in the estimation of uncertain or unknown parameters. D-Optimal FDI tests were implemented earlier in Chapter 2, as a method of test design optimization for fault detection, which increases the sensitivity of measurements with respect to faults. It was shown that D-optimal FDI test designs can improve fault detectability and identifiability, where D-optimality targets minimization of the joint confidence regions between unknown or uncertain model parameters representing faults and system uncertainty [58]. The dependence of the temperature of the heat exchanger exit streams on heat exchanger fouling and uncertainty in the inlet stream flow rate and properties was optimized by manipulation of the inlet stream temperature. The method in Chapter 2 is formalized in this paper and it is extended for the determination of false alarms through a method based on parameter identifiability.

Parameter identifiability analysis explores whether the parameters of a model can be uniquely determined from experimental measurements [120, 121, 122]. The identifiability of model parameters is often explored on the basis of the implicit function theorem [123], similarity transformation [124] and local sensitivity analysis [122]. In principle, these methods assess whether different parameter sets can produce similar output trajectories. Translation of identifiability in the field of FDI is conceptually simple. Assume a system model with two different sets of parameters: one representing system faults and another representing system uncertainty. If nearly identical (within some acceptable error) outputs can be generated with

either set of parameters, the system is deemed unidentifiable and can generate false alarms. Therefore, identifiability analyses can be conducted to assess the possibility of false alarms with the system model at the calculated FDI test conditions. The methodology presented herein builds upon the structural global identifiability (SGI) methodology reported in Asprey and Macchietto [125]. SGI calculates the largest distance between all feasible parameter vectors that generate essentially identical output trajectories. As previously reported in Han et al. [31] SGI can be applied at a system state corresponding to D-optimality, which maximizes parameter identifiability. Subsequently, SGI at the D-optimal conditions assesses the false alarm potential of the designed test.

In the following, Section 4.2 presents the FDI framework proposed for the design of BIT of uncertain systems. In Section 4.3, we illustrate the effectiveness of the framework with two open-loop case studies focusing on various aerospace air conditioning subsystems. In the first case study, a plate-fin heat exchanger with accumulated particulate fouling is analyzed, considering uncertainty in its inlet moisture content, cold stream inlet temperature and cold stream mass flow rate. In the second case study, an environmental control system, an aircraft subsystem that regulates cabin air conditions, is studied in order to evaluate the plausibility of false alarms in a steady-state BIT aimed at identifying particulate fouling. The faults in both case studies are assumed to be incipient and deterministic, in that each fault can be accurately quantified as a parameter in the system model. We illustrate the impact of faults in the presence of uncertainty at nominal and optimal test conditions and

the likelihood of false alarms before and after implementing the test design calculated.

4.2 Methods

In the proposed framework, an optimal test design is calculated to maximize robustness for FDI and then analyzed to determine if false alarms are possible with the calculated test design. The overall scheme of the workflow is shown in Fig. 4.1. The first step is to develop a model that accurately represents the system or subsystem of interest. The model must be capable of capturing faults as states or parameters. The system admissible inputs and their allowable range are compiled into the FDI test design vector and comprise the test design space. The uncertainty of inputs, boundary conditions and sensed outputs is assumed to be assessed *a priori* as variability ranges or distributions. These ranges are factored in the calculation of the test design to maximize the information relevant specifically to uncertainty. Equations (3.1a-3.1h,3.3) and (3.2a-3.2h,3.4) were used to formulate the mathematical model and test design optimization for steady-state and dynamic FDI, respectively, in the proposed framework.

If the optimal test fails to provide the necessary precision required to identify faults then other factors such as sensor placement and system design need to be updated in order to improve fault identification. If the test is found to be sufficiently precise, a posterior false alarm analysis is conducted to explore identifiability of faults within the allowable parameter space. This is equivalent to the structural global identifiability of Asprey and

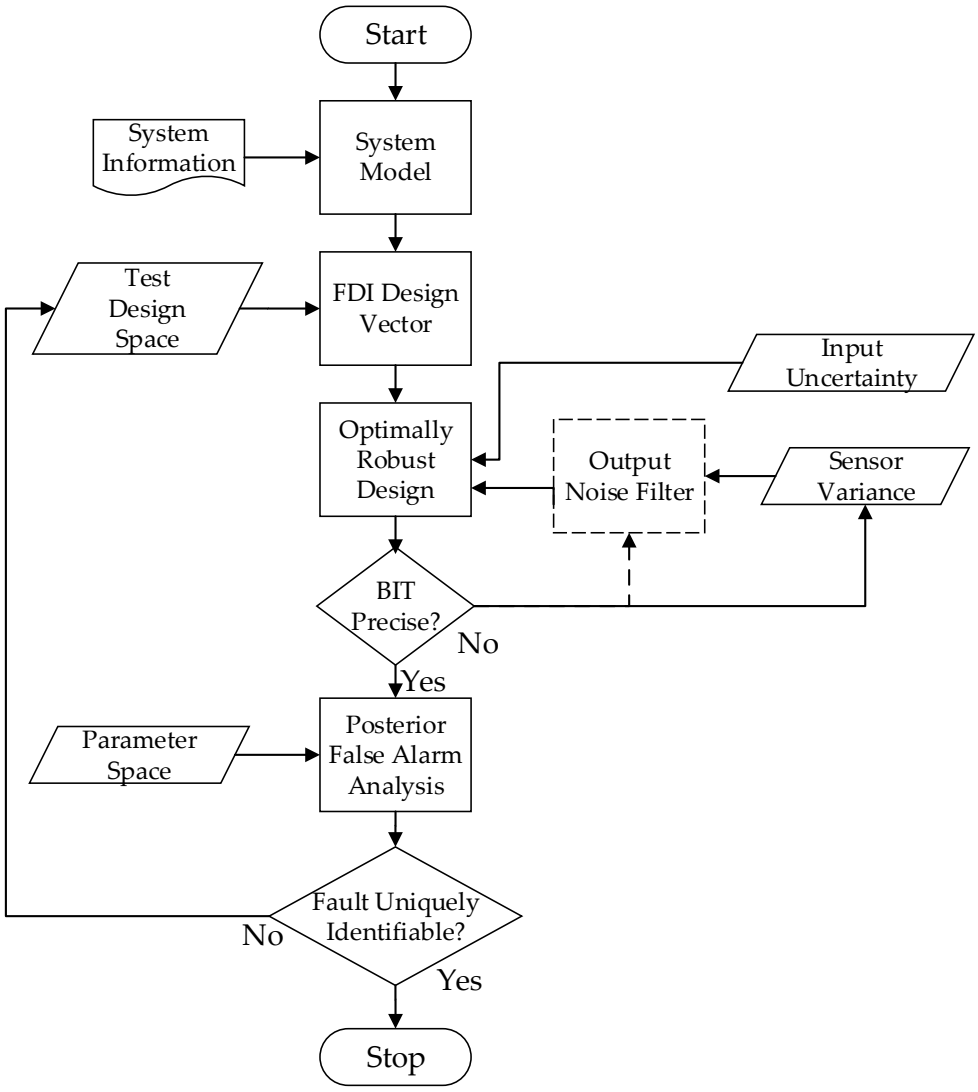

Fig. 4.1: Framework for model-based design and posterior false alarm analysis.

Macchietto [125], in the sense that the entire model input and parameter space is searched at the system state that maximizes the information with respect to the unknown parameters

that represent faults (the D-optimal design). If the faults are uniquely identifiable, in that no other set of faults, uncertain inputs or parameters can produce system outputs similar to those produced by the suspect faults, then the plausibility of false alarms is effectively eliminated and the proposed optimal BIT design is considered robust and deployable. The following sections expand the workflow illustrated in Fig. 4.1 into a complete and generic mathematical formulation.

4.2.1 Optimal test design

The admissible system inputs, $\mathbf{u}_p(t) \in \mathbb{R}^{N_{u_p}}$, are manipulated on the basis of the model of Section 3.2 to optimize fault detection. The process inputs are manipulated by the FDI test as illustrated in Fig. 4.2, which shows how steady-state or dynamic FDI tests manipulate system inputs to generate measurement trajectories. In the steady-state test, measurements are collected and used when the system has settled to steady-state. In the dynamic FDI test, the system starts from a steady-state, and then measurements are collected dynamically.

A measure of the FIM needs to be selected to extract relevant information from the output sensitivities for the purpose of fault identification [126]. Here, the D-optimal design criterion is used to reduce the joint confidence region between estimated faults and uncertain variables [58]. The intent of active fault identification is to determine inputs or input trajectories that result in increased diagnostic accuracy. In ideal (uncertainty-free) systems, this translates to reducing the joint confidence regions between the various different faults

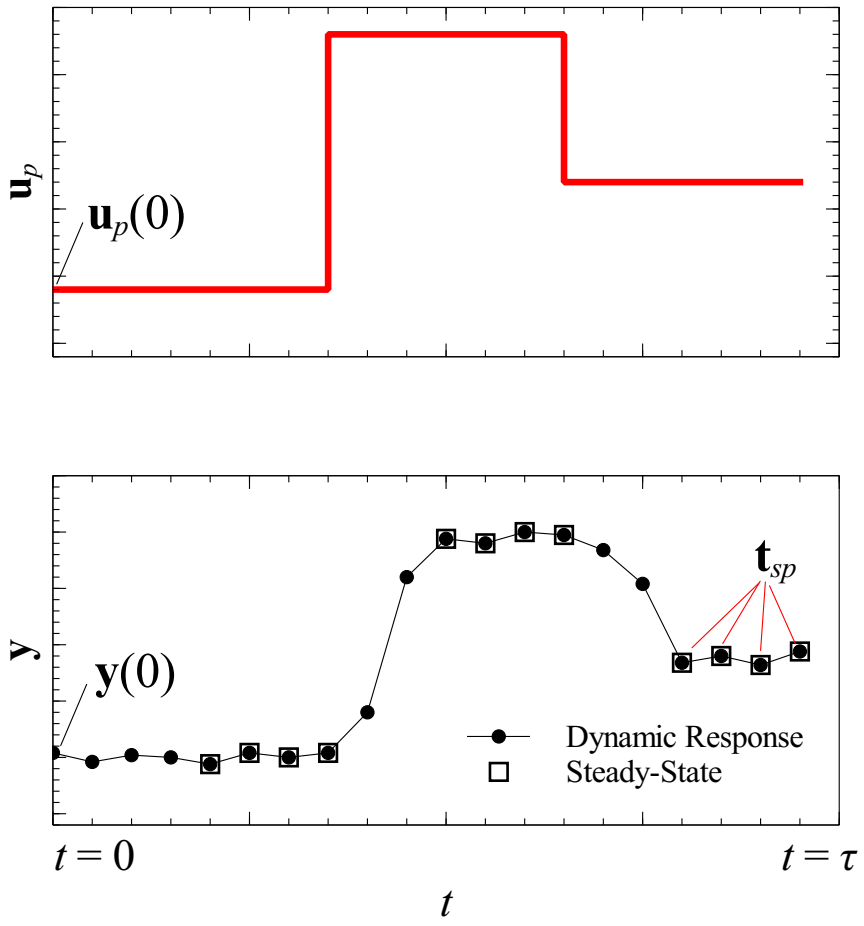

Fig. 4.2: Test design configuration for the FDI framework. The steady-state FDI test considers only steady-state outputs, but the dynamic FDI test includes transient and steady-state information.

a system can exhibit. In systems with uncertainty, the variance between faults and uncertain parameters also needs to be reduced, which translates to reducing the possibility of uncertainty estimated as a fault. As mentioned earlier, the inverse of $\mathbf{H}_\xi$ in (3.1i,3.2i) is

equivalent to the Cramér-Rao lower bound of the variance-covariance matrix. Therefore, the determinant of $\mathbf{H}_{\xi}^{-1}$ can be used to determine a design in which the covariance of the estimated faults or uncertainty is reduced [89]. It should be noted, however, that the FIM is rich in information and other metrics of the FIM could result in useful designs for particular tests. For instance, one could consider excluding the information relevant to the covariance between uncertainty parameters (D_s-Optimal Design) in the objective functions that design the FDI test. Other design criteria might also be of use [89, 126, 127], which is the subject of ongoing work. Nonetheless, the theoretical properties of D-optimality are well suited for FDI test design.

4.2.2 False alarm analysis

After calculating the optimal test design, the next step in the workflow is to determine if false alarms are feasible for this test design. As stated previously, false alarms are considered to be the detection of a particular fault due to uncertainty or other faults when the fault does not exist in the system. In this context, a false alarm is expressed as:

$$\begin{aligned} &\left|\hat{y}_i(\tilde{\mathbf{x}}, \tilde{\mathbf{u}}_u, \tilde{\boldsymbol{\theta}}_f, \tilde{\boldsymbol{\theta}}_u) - \hat{y}_i(\mathbf{x}', \mathbf{u}'_u, \boldsymbol{\theta}'_f, \boldsymbol{\theta}'_u)\right| \leq w_i, \quad i = 1, \ldots, N_y, \\ &\tilde{\mathbf{u}}_u, \mathbf{u}'_u \in \mathbf{U}, \quad \tilde{\boldsymbol{\theta}}_f, \boldsymbol{\theta}'_f \in \boldsymbol{\Theta}, \quad \tilde{\boldsymbol{\theta}}_u, \boldsymbol{\theta}'_u \in \boldsymbol{\Theta}, \end{aligned} \tag{4.1}$$

where $\tilde{\boldsymbol{\theta}}_f$ is the vector of anticipated parameter values representing a fault or set of faults, $\boldsymbol{\theta}'_f$ is the vector of parameter values of a fault-free system or a system with a different set of faults and w_i is the expected measurement noise of the i-th output. The model outputs, $\hat{\mathbf{y}}$,

depend on the uncertain parameter values, $\tilde{\boldsymbol{\theta}}_u$ or $\boldsymbol{\theta}'_u$, and the uncertain inputs, $\tilde{\mathbf{u}}_u$ or $\mathbf{u}'_u$. If the outputs generated with the anticipated set of faults $\tilde{\boldsymbol{\theta}}_f$ is nearly identical to those of a fault-free system with uncertain inputs and parameters $\mathbf{u}'_u$ and $\boldsymbol{\theta}'_u$, respectively or a system containing a different set of faults $\boldsymbol{\theta}'_f$ then the response can trigger a false alarm. False alarms can then be analytically determined by examining the identifiability of faults in the system model used for FDI. This false alarm analysis is based on the structural global identifiability (SGI) methodology developed by Galvanin et al. [128], as applied by Han et al. [31]. In its complete formulation, SGI uses the optimal test design vector, $\boldsymbol{\varphi}^*$, from (3.4) or (3.3), the anticipated values for faults and uncertain parameters and inputs, $\tilde{\boldsymbol{\xi}}(= [\tilde{\boldsymbol{\theta}}_f, \tilde{\boldsymbol{\theta}}_u, \tilde{\mathbf{u}}_u])$, with any other set of values that might give similar $\hat{\mathbf{y}}$ values expressed as $\boldsymbol{\xi}'(= [\boldsymbol{\theta}'_f, \boldsymbol{\theta}'_u, \mathbf{u}'_u])$. The outputs produced by the model with $\tilde{\boldsymbol{\xi}}$ and $\boldsymbol{\xi}'$ at the optimal test design vector, $\boldsymbol{\varphi}^*$, are used in the likelihood function of the residuals between anticipated observed outputs, y_i and any other value of feasible outputs, $\hat{y}_i$, as shown below:

$$L(\boldsymbol{\xi}) = \prod_{k=1}^{N_{sp}} \prod_{i=1}^{N_y} \frac{1}{\sqrt{2\pi\sigma_{ik}^2}} \exp\left(\frac{-\left(y_i(\tilde{\boldsymbol{\xi}}, t_k) - \hat{y}_i(\boldsymbol{\xi}, t_k)\right)^2}{2\sigma_{ik}^2} \right). \tag{4.2}$$

The comparison of likelihood functions is a useful tool for the purpose of evaluating model uncertainty at specific designs, as shown in Rooney and Biegler [129]. The observed outputs, y_i, are the outputs generated using the system model with the addition of measurement noise at each sampling point. The residuals are normalized by the standard deviation of measurement noise, σ_{ik} for the i-th output and k-th sampling point. The likelihood functions

$L(\boldsymbol{\xi}')$ and $L(\tilde{\boldsymbol{\xi}})$ are constrained by ϵ_y as shown in (4.3):

$$-2\log\left[\frac{L(\boldsymbol{\xi}')}{L(\tilde{\boldsymbol{\xi}})}\right] < \epsilon_y. \tag{4.3}$$

The maximum allowable deviation in outputs, ϵ_y, is determined so that the difference between output trajectories is not statistically significant. The method used to determine ϵ_y is described in Appendix D.

A false alarm can occur if a vector, $\boldsymbol{\xi}'$, exists for a a healthy system that leads to similar (per (4.3)) output trajectories to that of a system with faults $\tilde{\boldsymbol{\theta}}_f$. The possibility of false alarms is assessed by finding the maximum distance, Φ_{FA}, between $\tilde{\boldsymbol{\theta}}_f$ and $\boldsymbol{\theta}'_f$ at ϵ_y-similar outputs. This distance is maximized by searching for a vector, $\boldsymbol{\xi}' \in \boldsymbol{\Xi}$, where $\boldsymbol{\Xi}$ is the parameter space that defines the lower and upper bounds for all elements in $\boldsymbol{\xi}$. The analysis is implemented for each anticipated fault to assess the possibility of false alarms. For the steady-state test design, $\Phi_{FA,StS,i}$ that corresponds to fault $\theta_{f,i}$ for $i = 1, ..., N_\theta$ is

calculated according to (4.4):

$$
\begin{aligned}
\Phi_{FA,StS,i} = & \max_{\boldsymbol{\xi}' \in \boldsymbol{\Xi}} \left| \tilde{\theta}_{f,i} - \theta'_{f,i} \right| \\
& \text{s.t.} \\
& -2 \log \left[\frac{L(\boldsymbol{\xi}')}{L(\tilde{\boldsymbol{\xi}})} \right] \leq \epsilon_y, \\
& \text{for} \quad \boldsymbol{\xi} \in \{\tilde{\boldsymbol{\xi}}, \boldsymbol{\xi}'\} : \\
& \mathbf{f}(\mathbf{x}, \mathbf{u}^*_{p,j}, \boldsymbol{\theta}_p, \boldsymbol{\xi}) = \mathbf{0}, \quad \forall j \in [1, N^*_{test}], \\
& \hat{\mathbf{y}} = \mathbf{h}(\mathbf{x}, \mathbf{u}^*_{p,j}, \boldsymbol{\theta}_p, \boldsymbol{\xi}), \quad \forall j \in [1, N^*_{test}], \\
& \boldsymbol{\xi}^L \leq \boldsymbol{\xi} \leq \boldsymbol{\xi}^U,
\end{aligned}
\tag{4.4}
$$

where $\mathbf{u}^*_p$ is calculated in (3.3). The maximum distance, $\Phi_{FA,Dyn,i}$ is calculated for a dynamic

test design according to (4.5):

$$
\begin{aligned}
\Phi_{FA,Dyn,i} = \max_{\boldsymbol{\xi}' \in \boldsymbol{\Xi}} & \left| \tilde{\theta}_{f,i} - \theta'_{f,i} \right| \\
& \text{s.t.} \\
& -2 \log \left[\frac{L(\boldsymbol{\xi}')}{L(\tilde{\boldsymbol{\xi}})} \right] \leq \epsilon_y, \\
& \text{for} \quad \boldsymbol{\xi} \in \{\tilde{\boldsymbol{\xi}}, \boldsymbol{\xi}'\} : \\
& \mathbf{f}(\dot{\mathbf{x}}(t), \mathbf{x}(t), \mathbf{u}_p^*(t), \boldsymbol{\theta}_p, \boldsymbol{\xi}, t) = \mathbf{0}, \\
& \hat{\mathbf{y}}(t) = \mathbf{h}(\mathbf{x}(t), \mathbf{u}_p^*(t), \boldsymbol{\theta}_p, \boldsymbol{\xi}, t), \\
& \forall t \in [t_1, t_{N^*_{test}}], \\
& \mathbf{y}_0 = \begin{cases} \mathbf{f}(\dot{\mathbf{x}}(t_0), \mathbf{x}(t_0), \mathbf{u}_p^*(t_0), \boldsymbol{\theta}_p, \boldsymbol{\xi}, t_0) = \mathbf{0}, \\ \hat{\mathbf{y}}(t_0) = \mathbf{h}(\mathbf{x}(t_0), \mathbf{u}_p^*(t_0), \boldsymbol{\theta}_p, \boldsymbol{\xi}, t_0), \end{cases} \\
& \boldsymbol{\xi}^L \leq \boldsymbol{\xi} \leq \boldsymbol{\xi}^U,
\end{aligned}
\tag{4.5}
$$

where $\mathbf{u}_p^*$ is calculated in (3.4).

If Φ_{FA} is determined to be less than or equal to a false alarm threshold, ϵ_{FA}, then (4.4) or (4.5) (for steady-state and dynamic FDI test design, respectively) is satisfied and the system is not expected to generate false alarms within the given uncertainty in parameters and inputs. This false alarm threshold should correspond to the required precision for fault identification of a particular system. Often this is arbitrarily defined [125, 128], according to system specificity or knowledge. In this work, false alarms are considered to be sufficiently reduced if $\boldsymbol{\theta}'_f$ can be estimated at 10% precision. This corresponds to $\epsilon_{FA} = 0.10$, which

means that FDI is acceptable within 10% error in the estimate of the fault severity (at the worst case scenario of uncertainty).

4.3 Results and discussion

Two aircraft subsystems were used as testbeds for the application of the FDI framework discussed in the Methods section. The first case study is the plate-fin heat exchanger of an environmental control system that extends previous work by Palmer et al. [5]. The second testbed is an aircraft environmental control system described in Warner [6].

4.3.1 Case study I: Plate-fin heat exchanger

Heat exchanger FDI test design

Air-cooled heat exchangers are essential components of aircraft ECS, but are prone to fouling, which is treated as a fault to be quantified in the following. ECS heat exchanger particulate fouling degrades the heat transfer effectiveness of the system and if the fouling is excessive it can block the air passages [36]. The cumulative loss of heat transfer capacity increases the energy required for air to reach the aircraft cabin at the required conditions. Therefore, built-in or maintenance tests are common in heat exchanger fouling identification [87, 130]. Uncertain boundary conditions such as the air moisture, hot and cold side flow rates and inlet stream temperatures affect the accuracy of heat exchanger FDI. Therefore, the framework of Fig. 4.1 was used to generate an FDI test design for improved heat exchanger fouling

quantification. The accuracy of fouling quantification was explored with a heat exchanger model previously developed by Palmer et al. [5] to which low (20% blocked), medium (50% blocked), and high (80% blocked) levels of fouling were injected. Optimal FDI designs were calculated and compared to a nominal scenario of aircraft operation at ground-level operation.

Fig. 4.3 illustrates the inputs and outputs of a typical cross-flow heat exchanger. The nominal inputs of the heat exchanger used for a hypothetical non-optimal FDI are shown in Table 4.1. For illustration purposes, the hot stream mass flow rate was considered as the only admissible input for FDI test design. The hot inlet temperature was assumed to be constant, controlled by the upstream system. The downstream process was assumed to not affect the heat exchanger FDI test. The hot stream mass flow rate was constrained to the range 0.1-1.0 kg/s, which is a reasonable range for the selected heat exchanger geometry. The duration of the test design, τ, was set to 300 s in order to allow time for other system diagnostics [66]. The test was allowed to have up to one stepwise admissible input change, meaning that a maximum of two input settings could be applied. The FDI framework was implemented in two scenarios, one where only outputs from steady-state tests were measured and another where the dynamic responses from step changes were recorded. This was done to evaluate the usefulness of transient information in tests with uncertainty. In the dynamic test designs, the timing of the step change was set to t=100 s. As shown in Fig. 4.3, the heat exchanger studied has temperature sensors at its exits, monitoring the outlet temperatures

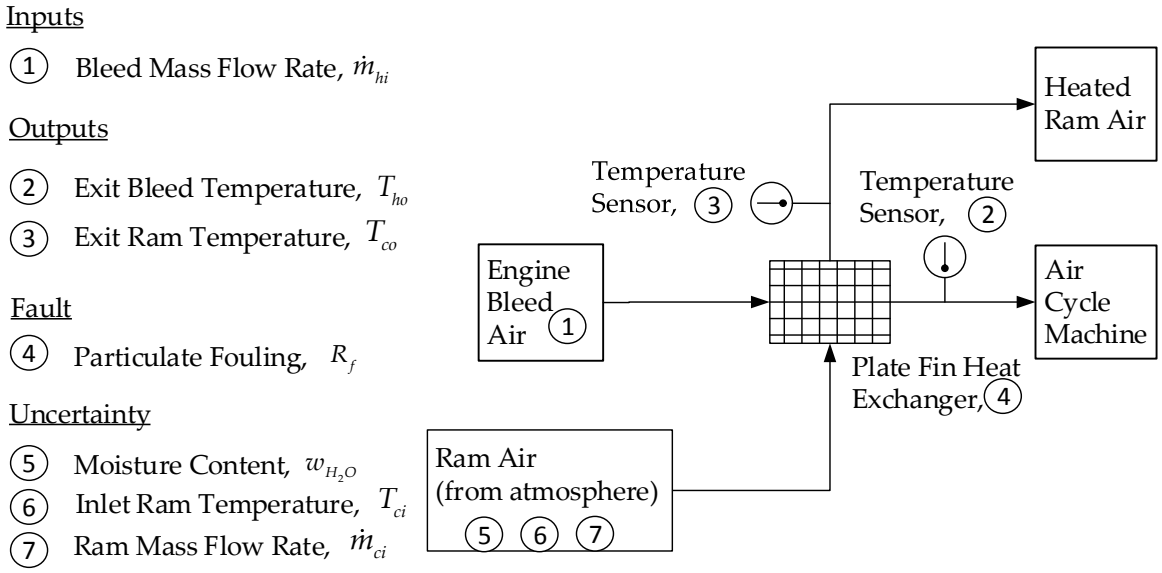

Fig. 4.3: Design scheme of the ECS cross-flow plate-fin heat exchanger [5].

at a default sampling rate of 1 sec^{-1}. For simplicity, the thermocouples were assumed to be error-free, with only white measurement noise at a standard deviation of 0.5 °C.

The anticipated faults and uncertain parameters and inputs considered in this case study are listed in Table 4.2, along with their upper and lower bounds. For the purpose of illustration, we first considered only the thermal fouling resistance, R_f, and moisture content, w_{H_2O}, to be uncertain. Afterwards, we extended the example so that all of the parameters listed in Table 4.2 were considered uncertain or unknown. In each scenario, the optimal designs were calculated using (3.3) or (3.4) at low, medium and high levels of fouling. The test designs were assessed using maximum likelihood estimation to estimate the values of

Table 4.1: Conditions applied in the ECS heat exchanger case studies of fouling estimation.

Flow Condition	Nominal Setting
T_{hi} (°C)	175
T_{ci} (°C)	40
$\dot{m}_{hi}$ (kg/s)	0.30
$\dot{m}_{ci}$ (kg/s)	1.00
p_{hi} (kPa)	150
p_{ci} (kPa)	100

faults and uncertain parameters along with their 95% confidence intervals at the nominal and optimal designs. The estimation function of (4.6) is in accordance with Bard [131] and assumes that all of the sensed outputs have zero-mean normally distributed noise with known standard deviation.

$$\boldsymbol{\xi}^* = \arg\max_{\boldsymbol{\xi}\in\boldsymbol{\Xi}} L(\boldsymbol{\xi}). \tag{4.6}$$

In the assessment that follows, the set of measured outputs, $\mathbf{y}$, was generated with a virtual heat exchanger system which was an instantiation of the heat exchanger model presented in Palmer et al. [5] with normally distributed measurement noise added to the sensed outputs. The heat exchanger model was formulated with the software tool chain detailed in Palmer et al. [5] utilizing the programs Dymola [68] for dynamic simulation, Functional Mock-up

Interface [69] and Modelon FMI-toolbox [71] for model exchange, MATLAB for parameter estimation with the optimization algorithms, NOMAD [73] and IPOPT [132]. Direct multiple shooting methods and optimization performed across multiple initial guesses were implemented to overcome the nonconvexity of the system model. The confidence intervals of the constrained system inputs and model parameters were calculated with bootstrapping [94]. More details about the model, its structure, properties and validation can be found in Palmer et al. [5].

Table 4.2: Lower ($\boldsymbol{\xi}^L$) and upper ($\boldsymbol{\xi}^U$) bounds of the faults and uncertain conditions in the heat exchanger and their anticipated values ($\tilde{\boldsymbol{\xi}}$) for varying levels of fouling blockage.

Uncertain	Lower	Blocked			Upper
Parameter	Bound	20%	50%	80%	Bound
$R_f \times 10^3$ (m^2K/W)	0.00	1.60	4.00	6.40	8.00
w_{H_2O} (%)	0.10	0.10	0.10	0.10	5.00
T_{ci} (°C)	15.0	40.0	40.0	40.0	50.0
$\dot{m}_c$ (kg/s)	0.75	1.00	1.00	1.00	1.25

Fouling identification with uncertainty in one input

The task in this case study was to find optimal steady-state or transient conditions for accurately estimating the thermal fouling resistance in a heat exchanger with uncertain moisture content in its hot and cold streams, and then to analyze these optimal tests to determine if false alarms are possible. Fault and uncertain parameters (R_f and w_{H_2O}, respectively) were injected to the virtual heat exchanger with the values shown in Table 4.2. The nominal and calculated optimal test designs are listed in Table 4.3, along with their upper and lower bounds.

Table 4.3: Nominal and optimal FDI test designs for the plate-fin heat exchanger at low, medium and high fouling levels with uncertain moisture content.

Fouling level	Lower Bound	Upper Bound
20% Blocked	$\dot{m}_h$=[0.10 kg/s], N_{test}=1	$\dot{m}_h$=[1.00 kg/s], N_{test}=2
50% Blocked	$\dot{m}_h$=[0.10 kg/s], N_{test}=1	$\dot{m}_h$=[1.00 kg/s], N_{test}=2
80% Blocked	$\dot{m}_h$=[0.10 kg/s], N_{test}=1	$\dot{m}_h$=[1.00 kg/s], N_{test}=2

The determinant of the FIM calculated from (3.1i) was enumerated over the allowable range of hot mass flow rate values $\dot{m}_{h,1}$ and $\dot{m}_{h,2}$ (corresponding to the setting of $\dot{m}_h$ for tests 1 and 2) and obtained from outputs at steady-state and transient outputs, respectively. Plots of the enumerations performed are shown in Fig. 3.3. The FDI test explored has a

Table 4.4: Nominal and optimal FDI test designs for the plate-fin heat exchanger at low, medium and high fouling levels with uncertain moisture content.

Fouling level	Optimal StS	Optimal Dyn
20% Blocked	$\dot{m}_h$=[0.47 kg/s, 1.00 kg/s], N_{test}=2	$\dot{m}_h$=[0.10 kg/s, 1.00 kg/s], N_{test}=1
50% Blocked	$\dot{m}_h$=[0.45 kg/s, 1.00 kg/s], N_{test}=2	$\dot{m}_h$=[0.10 kg/s, 1.00 kg/s], N_{test}=1
80% Blocked	$\dot{m}_h$=[0.43 kg/s, 1.00 kg/s], N_{test}=2	$\dot{m}_h$=[0.10 kg/s, 1.00 kg/s], N_{test}=1

fixed number of samples ($N_{sp} = 300$) distributed over a maximum of two tests ($N_{test} = 2$, shown as x and y axes). The highest values of $|\mathbf{H}_\xi|$ occur at different hot flow rates in each test, one test at 0.43-0.47 kg/s (depending on fouling level) and one at 1.00 kg/s. The corresponding optimal steady-state test design was estimated to have different hot mass flow rate settings in each test, with one restricted to the upper bound (1.0 kg/s) and the other dependent on the heat exchanger blockage. The most informative tests had the hot flow rate set at the lower bound (0.1 kg/s) followed by a step change at t=100 s to the upper bound of 1.0 kg/s. Dynamic information significantly increases the sensitivity of the outputs with respect to fault and uncertainty, as indicated by the higher values of $|\mathbf{H}_\xi|$. The optimal test design was calculated to be the same at low, medium and high levels of blockage, when

dynamic information was used.

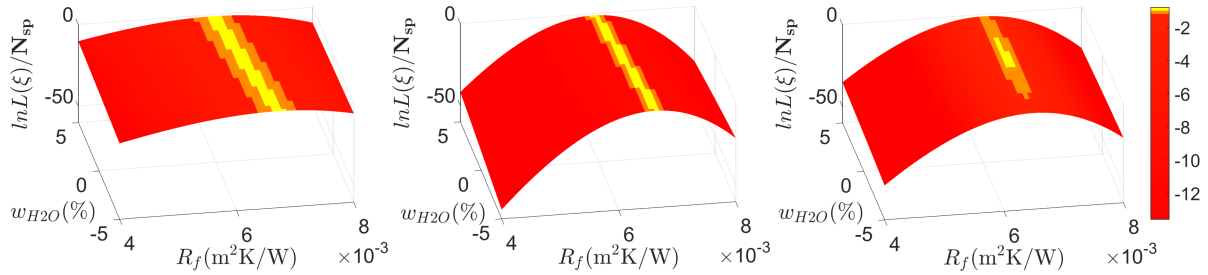

Fig. 4.4: $\log(L(\boldsymbol{\xi}))/N_{sp}$ over a range of system model thermal fouling resistance and moisture content values, using measurements obtained using the nominal test design (a, $\boldsymbol{\varphi}_{Nom} = [\dot{m}_h = [0.3\ \mathrm{kg/s}], N_{test} = 1]$), optimal design for steady-state optimal test design (b, $\boldsymbol{\varphi}^*_{StS} = [\dot{m}_h = [0.43\ \mathrm{kg/s}, 1.0\ \mathrm{kg/s}], N_{test} = 2]$) and dynamic optimal test design (c, $\boldsymbol{\varphi}^*_{Dyn} = [\dot{m}_h = [0.1\ \mathrm{kg/s}, 1.0\ \mathrm{kg/s}], N_{test} = 1]$). The true values of the system are 6.4 $\mathrm{m^2K/W} \times 10^{-3}$ and 0.1%, respectively, that correspond to the virtual heat exchanger that is 80% blocked.

Estimation of the parameters representing fault and uncertainty was performed with data generated by injecting 80% fouling blockage to the virtual heat exchanger. (4.6) was used to estimate heat exchanger fouling and verify the effectiveness of the test design optimization. First, to visually illustrate the estimation confidence, the objective function of (4.6) was enumerated over the allowable range of fault and uncertainty values. Fig. 4.4 shows how the objective function surface $L(\xi)$ changes when (4.6) is solved at nominal and

optimal conditions. In the optimal FDI tests, the objective function surface has sharper contrast and a narrower plateau of values that surround the true values of R_f and w_{H_2O}. At the same number of samples, the neighborhood of likely solutions decreases significantly for the optimal FDI test using transient data, as shown in the right handside plot of Fig. 4.4.

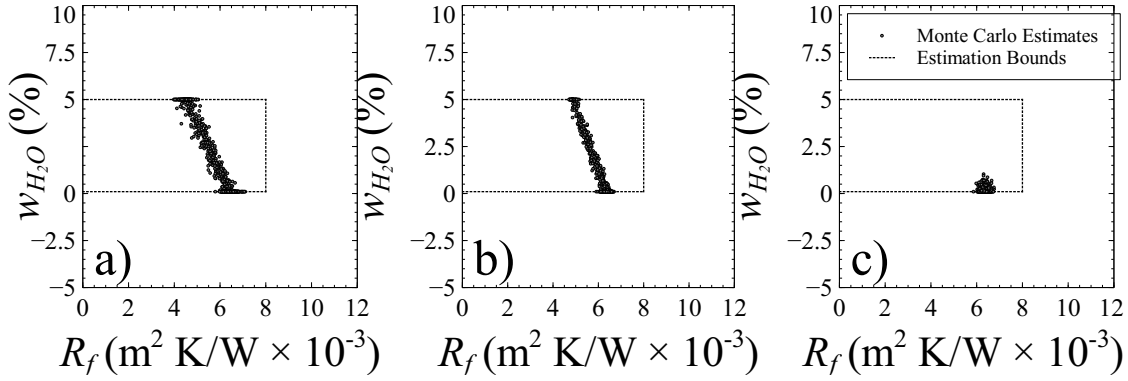

Fig. 4.5: Estimates of thermal fouling resistance and moisture content at high fouling levels at from 1000 FDI tests set to the nominal (a, $\boldsymbol{\varphi}_{Nom}$ =[$\dot{m}_h$ = [0.3 kg/s],N_{test} = 1]), optimal steady-state (b, $\boldsymbol{\varphi}^*_{StS}$ =[$\dot{m}_h$ = [0.43 kg/s,1.0 kg/s], N_{test} = 2]) and optimal dynamic (c, $\boldsymbol{\varphi}^*_{Dyn}$ = [$\dot{m}_h$ = [0.1 kg/s, 1.0 kg/s],N_{test} = 1]) test designs.

The estimates of the thermal fouling resistance and moisture content are shown in Fig. 4.5 at the nominal and optimal steady-state and dynamic test designs. The generation of virtual system outputs was performed using Monte Carlo simulation with 1000 iterations, while the estimation was done with (4.6). The improvement in the confidence region from the nominal test to the steady-state optimal test is small. As shown later, the fault, uncertain

parameters and inputs in this case study are not practically identifiable in a plate-fin heat exchanger with the given measurement noise at steady-state. Assuming that the dynamics of the system model are accurate, the heat exchanger fouling can be confidently estimated at the optimal dynamic test design, as indicated by the respective narrow region of estimates in Fig. 4.5.

To better illustrate false alarms caused by uncertainty, Fig. 4.6 shows the difference between a dry and severely fouled heat exchanger, and a wet and less fouled heat exchanger at nominal and optimal test conditions. The steady-state and dynamic optimal test designs are presented in the left and right handside plots, respectively. The hot stream flow rate is also shown to demonstrate how the outputs correspond to the test configuration. The transient response of the virtual system was included even for the steady-state test to show the smooth transition between tests. It is observed that the heat exchanger with 50% blockage and a moisture content of 5.0% generates similar outputs to a dry heat exchanger fouled at 80% blockage. However, as shown in Fig. 4.6 (e) and (f), the transient responses monitored at the dynamic optimal FDI test have a different profile at dry conditions then at wet conditions, so including dynamic information in the FDI test should decrease the likelihood of false alarms. This is also verified by the false alarm analysis for the steady-state and dynamic FDI test designs conducted using (4.4) and (4.5).

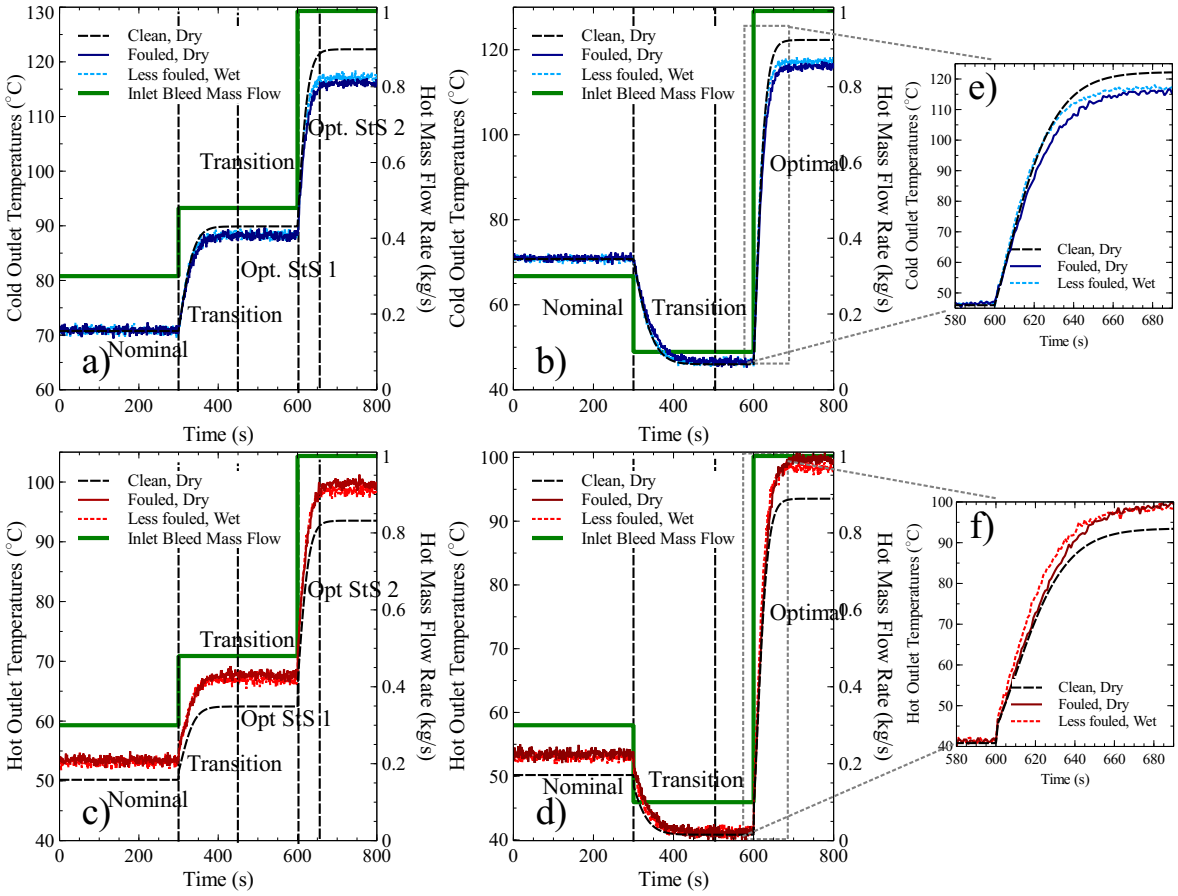

Fig. 4.6: Inlet mass flow rate and predicted cold and hot outlet temperatures of a heat exchanger. The severely fouled and dry conditions examined are at 80% blockage and $w_{H_2O} = 0.1\%$. Less fouled and wet conditions examined are at 50% blockage and $w_{H_2O} = 5.0\%$. Hot and cold outlet temperatures from the nominal and optimal steady-state FDI tests are shown in plots (a) and (c), respectively. The corresponding plots of nominal and optimal dynamic FDI tests are shown in plots (b) and (d). Plots (e) and (f) show the differences in the dynamic response of the cold and hot outlet temperatures for the various scenarios studied.

Next, the false alarm analysis was conducted at the nominal and optimal test designs, as shown in Table 4.5, which displays the maximum distance between parameters representing faults and uncertainty, Φ_{FA}. For ϵ_y-similar sensed outputs, Φ_{FA} is consistently smaller in the steady-state and dynamic optimal test designs than in the nominal test design, meaning that there is smaller likelihood for false alarms to occur. The likelihood for false alarms is also reduced by the increase in % blockage, and this is reflected in the decrease of Φ_{FA} values. In the steady-state tests the maximum distance is larger than the defined threshold, $\epsilon_{FA} = 0.10$ at all fouling levels, so there is not enough confidence in the thermal fouling resistance estimated from the optimal steady-state test. For the dynamic optimal test design, $\Phi_{FA} \ll \epsilon_{FA}$ at all fouling levels. Thus, false alarms are not likely to occur with the optimal dynamic tests designed.

Table 4.5: Φ_{FA} ($\tilde{\boldsymbol{\xi}} = [R_f, w_{H2O}]$) at low, medium and high fouling levels and various N_{sp} values. If $\Phi_{FA} \leq \epsilon_{FA} = 0.10$, FDI test is not expected to trigger false alarms, if all other inputs and parameters are certain.

Fouling level	Nom	Opt StS	Opt Dyn
20% Blocked	0.396	0.165	0.020
50% Blocked	0.308	0.139	0.016
80% Blocked	0.248	0.131	0.014

Fouling identification with multiple uncertain parameters and inputs

The fouling identification problem becomes more realistic (and complex) when we consider the cold mass flow rate and inlet temperature as uncertain variables. In this case, all the variables and parameters listed in Table 4.2 were considered unknown or uncertain, while the hot mass flow rate was still the only admissible input. The determinant of the Fisher Information Matrix, $|\mathbf{H}_\xi|$, was calculated over the allowable range of input values in the test design space for a heat exchanger 80% fouled, as displayed in Fig. 3.6. The increase in the number of uncertain parameters and inputs led $|\mathbf{H}_\xi|$ to become effectively zero for test designs with only one steady-state ($\dot{m}_{h,1} = \dot{m}_{h,2}$). At least two different settings for the admissible input were needed to estimate the faults, uncertain parameters and inputs. The optimal steady-state test design was found to contain two states corresponding to hot flow rates of 0.29 kg/s and 1.0 kg/s. The high flow rate maximizes the sensitivities of the outputs with respect to most of the uncertain conditions, while the low flow rate maximizes the output sensitivity with respect to the inlet cold temperature. The optimal test design in which the output transients were used, set the hot mass flow rates originally at the lower bound and then at the upper bound. This generates rich transient information from the widest allowable dynamic response. The optimal designs were identical at low, medium, and high levels of fouling due to the dilution of the impact of thermal fouling resistance on the test design optimization.

Table 4.6: Estimated 95% confidence intervals ($\tilde{\boldsymbol{\xi}} = [R_f, w_{H2O}, \dot{m}_c, T_{ci}]$) at low, medium and high fouling levels at $N_{sp} = 300$. ($\boldsymbol{\varphi}_{nom} = [\dot{m}_h$=0.3kg/s, N_{test}=1])

Fouling level	Set of $\tilde{\boldsymbol{\xi}}$	True Values	Nominal	
			$\hat{\boldsymbol{\xi}}$	95% CI
20% Blocked	R_f ($m^2K/W \times 10^{-3}$)	1.60	5.14	[0.00,8.00]
	w_{H_2O} (%)	0.10	0.93	[0.10,4.90]
	$\dot{m}_c$ (kg/s)	1.00	0.92	[0.80,1.07]
	$\dot{T}_{ci}$ (°C)	40.0	35.8	[29.2,42.5]
50% Blocked	R_f ($m^2K/W \times 10^{-3}$)	4.00	6.71	[0.23,7.96]
	w_{H_2O} (%)	0.10	1.73	[0.10,4.98]
	$\dot{m}_c$ (kg/s)	1.00	0.98	[0.84,1.05]
	$\dot{T}_{ci}$ (°C)	40.0	35.7	[32.3,42.8]
80% Blocked	R_f ($m^2K/W \times 10^{-3}$)	6.40	3.59	[0.00,8.00]
	w_{H_2O} (%)	0.10	1.10	[0.10,5.00]
	$\dot{m}_c$ (kg/s)	1.00	0.99	[0.88,1.11]
	$\dot{T}_{ci}$ (°C)	40.0	39.5	[34.2,45.1]

The fault, uncertain parameters and inputs were estimated at the nominal test conditions and at steady-state and dynamic optimal test designs using (4.6). Table 4.6 reports the estimates and 95% confidence intervals of the fault, uncertain parameters and inputs, along with the corresponding test design configurations. There is consistent improvement in the estimation accuracy between nominal and optimal test designs for each one of the fouling levels studied. The 95% confidence intervals of the faults and uncertainty are significantly decreased for both the steady-state and dynamic optimal tests for all fouling levels. The lack of confidence in the nominal test indicates that one steady-state condition is insufficient for estimation of fouling with the uncertain parameters and inputs of this case. The inclusion of transient information in the test responses led to significantly smaller confidence intervals.

Table 4.7: Estimated 95% confidence intervals ($\tilde{\boldsymbol{\xi}} = [R_f, w_{H2O}, \dot{m}_c, T_{ci}]$) at low, medium and high fouling levels at $N_{sp} = 300$. ($\boldsymbol{\varphi}^*_{StS} = [\dot{m}_h$=[0.29kg/s, 1.0kg/s], N_{test}=2], $\boldsymbol{\varphi}^*_{Dyn}\dot{m}_h$=[0.10kg/s, 1.0kg/s], N_{test}=1])

Fouling level	Set of $\tilde{\boldsymbol{\xi}}$	True Values	Optimal StS		Optimal Dyn	
			$\hat{\boldsymbol{\xi}}$	95% CI	$\hat{\boldsymbol{\xi}}$	95% CI
20% Blocked	R_f ($m^2K/W \times 10^{-3}$)	1.60	1.19	[0.02,2.40]	1.49	[1.17,1.77]
	w_{H_2O} (%)	0.10	0.55	[0.10,3.33]	0.15	[0.10,0.75]
	$\dot{m}_c$ (kg/s)	1.00	0.99	[0.96,1.01]	0.99	[0.98,1.00]
	$\dot{T}_{ci}$ (°C)	40.0	40.1	[36.0,40.8]	40.1	[39.8,40.3]
50% Blocked	R_f ($m^2K/W \times 10^{-3}$)	4.00	3.74	[3.01,4.22]	3.97	[3.63,4.12]
	w_{H_2O} (%)	0.10	0.87	[0.10,2.65]	0.14	[0.10,0.74]
	$\dot{m}_c$ (kg/s)	1.00	0.99	[0.95,1.01]	1.00	[0.98,1.01]
	$\dot{T}_{ci}$ (°C)	40.0	39.9	[36.1,40.7]	40.0	[39.7,40.2]
80% Blocked	R_f ($m^2K/W \times 10^{-3}$)	6.40	6.03	[5.41,6.73]	6.36	[5.90,6.52]
	w_{H_2O} (%)	0.10	0.71	[0.10,3.51]	0.15	[0.10,2.66]
	$\dot{m}_c$ (kg/s)	1.00	1.00	[0.99,1.01]	0.99	[0.99,1.01]
	$\dot{T}_{ci}$ (°C)	40.0	39.9	[39.5,40.4]	40.0	[39.7,40.7]

Following the framework of Fig. 4.1, a false alarm analysis was executed to determine if the fault at optimal conditions is practically identifiable. The maximum deviation Φ_{FA} was calculated at nominal and optimal test conditions and is shown in Table 4.8. The false alarm threshold, ϵ_{FA} was again 0.10, and the output deviation constraint, ϵ_y, in this scenario was 4.74 according to (D.3). Similar to the previous case study, the optimal test design led to consistently smaller Φ_{FA} values for all the fouling levels studied. At nominal conditions, the false alarm analysis generated Φ_{FA} values that were considerably larger than ϵ_{FA}, while the calculated optimal test designs improved the identifiability of the heat exchanger fault. False alarms were still feasible at the optimal steady-state tests at all fouling levels, but eliminated in all the dynamic tests.

Table 4.8: Φ_{FA} ($\tilde{\boldsymbol{\xi}} = [R_f, w_{H2O}, \dot{m}_c, T_{ci}]$) at low, medium and high fouling levels and N_{sp}=300. If $\Phi_{FA} \leq \epsilon_{FA} = 0.10$, the FDI test is not expected to trigger false alarms, if all other inputs and parameter are certain.

Fouling level	Nom	Opt StS	Opt Dyn
20% Blocked	1.600	0.231	0.030
50% Blocked	1.000	0.262	0.025
80% Blocked	0.309	0.209	0.021

4.3.2 Case study II: Aircraft environmental control system

The heat exchanger fouling identification problem explored in the previous analysis was studied for an integrated environmental control system, to evaluate the implementation of the FDI framework at the system level. A common ECS architecture is shown in Fig. 4.7, which is after the design of [6]. The air supplied from the aircraft engine, referred to as bleed air, has a mass flow rate and temperature determined by upstream subsystems. The bleed air is cooled in a primary heat exchanger by ambient air surrounding the aircraft, referred to as ram air. The bleed air then flows into a compressor to increase its pressure and maintain flow through downstream control systems. This stream flows into the secondary heat exchanger where it is again cooled. That heat exchanger is exposed to ambient air and particulates that cause fouling. Bypass and control valves are in place throughout the ECS, but for simplicity

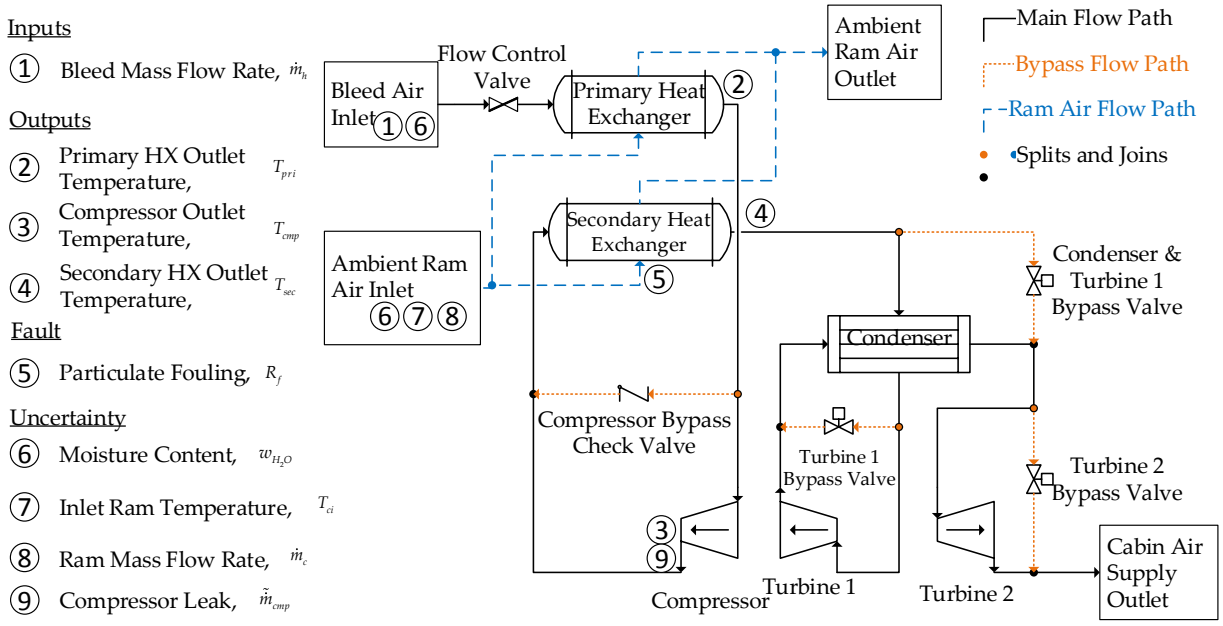

Fig. 4.7: Design scheme of an aircraft ECS subsystem [6].

it is assumed that all bypass valves are closed, during the FDI test.

Similarly to the previous case study the hot mass flow rate was the controllable input and assumed to have an admissible range of 0.1 to 1.0 kg/s. The duration of the test, τ, was restricted to five minutes and $\mathbf{u}_p$ was allowed a maximum of two input settings, N_{test}. Only steady-state tests were considered for FDI, due to the size and complexity of the system. The measured outputs available for fouling detection were the primary heat exchanger bleed exit temperature, T_{pri}, the compressor outlet temperature, T_{cmp}, and the secondary heat exchanger bleed exit temperature, T_{sec}. Each temperature sensor was assigned zero-mean white measurement noise with standard deviation of 0.5 °C. The anticipated faults, uncertain

parameter and inputs, $\tilde{\boldsymbol{\xi}}$, along with their upper and lower bounds are listed in Table 4.9. In addition to the fault, uncertain parameters and inputs considered in the previous analysis in Section 4.3.1, the compressor leak was also considered uncertain. The compressor leak is modeled as the mass flow rate of air leaking from the compressor, due to wear or corrosion, $\tilde{\dot{m}}_{cmp}$, i.e. the deviation from the expected mass flow rate caused by leakage. The compressor leak was assumed to be constant throughout the FDI test. Low, medium and high levels of fouling were considered at 20%, 50% and 80% blockage. For simplicity, the nominal test design was selected to be identical to that of the previous case study.

Table 4.9: Anticipated ($\tilde{\boldsymbol{\xi}}$), lower ($\boldsymbol{\xi}^L$) and upper ($\boldsymbol{\xi}^U$) values of the fault and uncertain conditions in the aircraft ECS for varying levels of fouling severity.

Uncertain	Lower	Blocked			Upper
Parameter	Bound	20%	50%	80%	Bound
$R_f \times 10^3$ (m^2K/W)	0.00	1.60	4.00	6.40	8.00
w_{H_2O} (%)	0.1	0.1	0.1	0.1	5.0
$\dot{m}_c$ (kg/s)	0.75	1.00	1.00	1.00	1.25
T_{ci} ($^\circ$ C)	15	40	40	40	60
$\tilde{\dot{m}}_{cmp}$ (kg/s)	0.00	0.01	0.01	0.01	0.05

Similar to the previous analyses, the hot mass flow rate allowable range was searched for conditions that generate the maximum determinant of $\mathbf{H}_\xi$. Fig. 4.8 shows $|\mathbf{H}_\xi|$ with

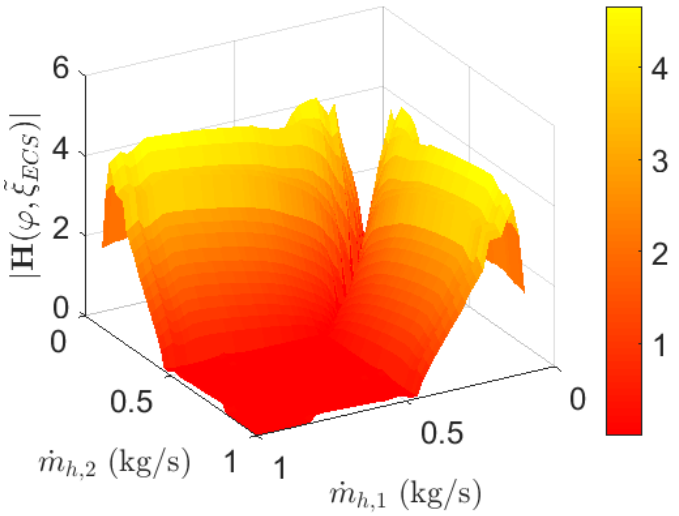

Fig. 4.8: Determinant of the Fisher Information Matrix for the ECS FDI test, over a range of adjustable hot mass flow rates for a test design with two input settings ($\boldsymbol{\varphi}^* = [\dot{m}_h = [0.1\ \text{kg/s}, 0.28\ \text{kg/s}], N_{test} = 2]$). The uncertain parameters and inputs are the thermal fouling resistance (80% Blocked), moisture content, ram mass flow rate, ram inlet temperature and the compressor leak mass flow rate.

respect to the bleed flow rates, $\dot{m}_{h,1}$ and $\dot{m}_{h,2}$, that correspond to the first and second input settings of the FDI test, respectively. One steady-state ($\dot{m}_{h,1} = \dot{m}_{h,2}$) is clearly insufficient to identify fouling with the uncertain parameters and inputs in the environmental control system. The optimal FDI test design was calculated with $\dot{m}_{h,1}$= 0.1 kg/s and $\dot{m}_{h,2}$= 0.18, 0.24 and 0.28 kg/s for the low, medium and high fouling levels, respectively. Then, (4.6) was used to estimate the fault, uncertain parameters and inputs from the temperature sensor

Table 4.10: Estimated 95% confidence intervals ($\tilde{\boldsymbol{\xi}} = [R_f, w_{H2O}, \dot{m}_c, T_{ci}, \tilde{\dot{m}}_{cmp}]$) at low, medium and high fouling blockage at $N_{sp} = 300$.$\dot{m}_h$=0.3kg/s, N_{test}=1.

Fouling level	Set of $\tilde{\boldsymbol{\xi}}$	True Values	Nominal	
			$\hat{\boldsymbol{\xi}}$	95% CI
20% Blocked	R_f ($m^2K/W \times 10^{-3}$)	1.60	2.42	[0.00,6.52]
	w_{H_2O} (%)	0.10	0.47	[0.10,4.87]
	$\dot{m}_c$ (kg/s)	1.00	0.95	[0.87,1.15]
	$\dot{T}_{ci}$ (°C)	40.0	36.7	[34.2,47.6]
	$\tilde{\dot{m}}_{cmp}$ (kg/s)	0.05	0.023	[0.00,0.05]
50% Blocked	R_f ($m^2K/W \times 10^{-3}$)	4.00	3.88	[0.53,7.61]
	w_{H_2O} (%)	0.10	0.62	[0.10,4.91]
	$\dot{m}_c$ (kg/s)	1.00	1.04	[0.90,1.13]
	$\dot{T}_{ci}$ (°C)	40.0	37.4	[35.6,44.7]
	$\tilde{\dot{m}}_{cmp}$ (kg/s)	0.05	0.027	[0.00,0.05]
80% Blocked	R_f ($m^2K/W \times 10^{-3}$)	6.40	5.98	[1.79,8.00]
	w_{H_2O} (%)	0.10	0.42	[0.10,4.86]
	$\dot{m}_c$ (kg/s)	1.00	0.91	[0.89,1.11]
	$\dot{T}_{ci}$ (°C)	40.0	41.4	[35.9,43.1]
	$\tilde{\dot{m}}_{cmp}$ (kg/s)	0.05	0.015	[0.00,0.05]

data generated by the virtual environmental control system, at nominal and optimal steady-state tests. These estimates and their 95% confidence intervals are shown in Table 4.10 along with the test design configurations used in each estimation. There was an increase in confidence using the optimal test design as there was more information generated with two different input settings. Because the sensors in the environmental control system are at different locations than in the heat exchanger case study, the moisture content and ram inlet temperature are more difficult to estimate resulting in slightly larger confidence intervals. On the other hand, the position of the sensors improved the confidence in the estimation of the heat exchanger fouling in the ECS.

As the last step of the FDI framework, a false alarm analysis was performed using

(4.4) to determine the plausibility of false alarms during the test in the aircraft ECS. The maximum deviation, Φ_{FA}, was calculated for all of the faults, uncertain parameters and inputs listed in Table 4.9. The false alarm threshold, ϵ_{FA}, was 0.10 and the output deviation constant, ϵ_y in this case study was 5.54 based on (D.3). The maximum deviation of uncertain faults, parameters and inputs that generated similar outputs at the nominal and optimal test designs are listed in Table 4.11. The maximum distance, Φ_{FA}, is consistently larger than the false alarm threshold, regardless of the test design. This indicates that isolation is not feasible for the fault, uncertain parameters and inputs in the selected design space, meaning that false alarms cannot be eliminated. In this case, the next step to eliminating false alarms should be to update the test design space, include wider input ranges, or reduce the amount of uncertainty by adding more sensors or improving the existing sensors. In response to to this finding, the test design space was expanded to include the inlet bleed temperature as a controllable input. This change provided an optimal test design, free of false alarms at higher fouling levels at steady-state with two distinct input settings at different inlet bleed temperature and mass flow rate values (not shown here).

4.4 Conclusions

A comprehensive framework for fault detection and isolation (FDI) was proposed, focused on minimizing the joint confidence region between faults and uncertain environmental conditions and *a posteriori* assessment of false alarms. Principles of model-based design of experiments

Table 4.11: Φ_{FA} ($\tilde{\boldsymbol{\xi}} = [R_f, w_{H2O}, \dot{m}_c, T_{ci}, \tilde{\dot{m}}_{cmp}]$) at low, medium and high fouling levels. If $\Phi_{FA} \leq \epsilon_{FA} = 0.10$, the FDI test is not expected to trigger false alarms, if all other inputs and parameter are certain.

Fouling level	Nominal	Optimal
20% Blocked	1.736	0.529
50% Blocked	0.903	0.409
80% Blocked	0.989	0.195

and practical parametric identifiability were employed for the objective of robust active FDI. A series of aerospace subsystems were tested using this framework to evaluate its effectiveness. The identifiability of faults was shown to increase significantly through the implementation of the proposed method, with the possibility for false alarms significantly decreasing. In future work, the proposed framework will be expended to include detailed analysis of the anticipated rates of false alarms and nondetections as factors in the selection of optimal FDI tests. Further work is needed to address the challenges inherent in solving the FDI design formulations presented here to global optimality. It would also be useful to assess FDI test design with adjustable time duration, so that the time required to successfully identify faults can be assessed and optimized as well.

Chapter 5

Active Fault Diagnosis for Uncertain Systems using Optimal Test Designs and Detection through Classification

Abstract

An updated methodology is presented for the optimization and assessment of test designs for active fault diagnosis executed via classification techniques. Multiple design criteria are assessed for viability. After the test design is calculated it is implemented with a robust deployment method of low computational cost, based on principal component analysis with k-nearest neighbor algorithm. Two case studies are used to verify the proposed methodology, a three-tank system and a diesel engine.

5.1 Introduction

Methods of information extraction used in parameter estimation such as the work shown in Chis et al. [120] can be used to optimize designs of tests for estimating deterministic sources of uncertainty in a system. When these methods are used for FDI, the selected test design for fault diagnosis can be cast as an optimization problem that maximizes some measure

of the FIM [88]. If we consider system uncertainty that does not correspond to faults as nuisance model parameters, the objective of the test design then becomes a maximization of the sensitivity of outputs with respect to faults and a minimization of the correlation between these faults and the impact of system uncertainty in fault diagnosis. This objective is updated from the previous chapters, in which the objective was to maximize sensitivities and minimize joint confidence between all uncertain parameters, regardless of whether they correspond to faults or system uncertainty. The task of FDI test design then becomes an exercise of determining tests that simultaneously maximize the effect of faults on outputs, minimizes the correlation between multiple faults and uncertainty and minimizes the effect of uncertainty on outputs, for a given model structure. This approach was illustrated in Patan and Patan [133], where the task was to select optimal sensor locations using the FIM such that fault detection capability is improved in passive tests. Here, we expand on these concepts by exploring several design criteria in terms of their effectiveness in FDI of uncertain systems.

In addition to active FDI that reconfigures the system for optimal sensitivity to faults, value exists in leveraging passive FDI techniques (e.g. thresholds, observers, filters). Multi-class classification techniques such as the k-nearest neighbor algorithm (k-NN) and support vector machines are often used for fault isolation, due to their ability to isolate targeted fault patterns [134, 135]. Neural networks can be utilized to generate relations between outputs and fault scenarios [136]. Support vector machines perform linear or nonlinear classification

in complex system fault detection with minimal datasets [137]. k-NN is often preferred for its simplicity and effectiveness in multi-class classification [134]. However, large sets of data can result in training overfit, making it difficult to accurately classify new data points. In this document, k-NN is used because of the relatively small model size. However, when the model used in FDI test design has a large number of states other classification methods would be recommended such as SVM. Principal component analysis (PCA) was thus used as one of the most dominant feature extraction methods because of its versatility, low computational cost and minimal impact on sample information [138, 139, 140]. Combining the proposed test design optimization with PCA and k-NN classifiers results in an active FDI methodology which is deployed using state of the art passive FDI techniques.

The work presented in this document is organized as follows. Section 5.2 presents the framework for calculating and assessing optimal FDI test designs in systems with some anticipation of their faults and uncertainty ranges. The system model formulation, the method for test design optimization, and the classification approach incorporated into the FDI test are discussed in detail. In Section 5.3, the improvements in system FDI by the proposed framework are examined in two separate case studies. The first case study examines the capability to detect and isolate faults in a three-tank system, a common testbed for fault diagnosis and fault tolerant control [7]. The second case study examines a diesel engine exhibiting actuator and component faults. In each case, the system of interest has multiple environmental factors that cause uncertainty in FDI.

5.1.1 Contributions of this chapter

The main contributions of this chapter are as follows: (i) A proposition of many design criteria for FDI test optimization that treat information with respect to faults and with respect to uncertainty differently. (ii) An incorporation of a well-known and robust passive FDI method into active FDI to verify and execute test designs. A comprehensive evaluation of the quality of FDI tests is performed by determining correct classification rates for all anticipated scenarios, via k-NN classification. (iii) A complete framework presented for designing and evaluating active FDI tests based on (i) and (ii). (iv) A comparison of FDI test results obtained with various design criteria in multiple benchmark case studies.

5.2 Methods

5.2.1 Preliminaries: Faults and uncertainty representation

The FDI test designs are generated in this chapter utilizing mathematical models that are formulated as shown in Section 4.2. It is assumed that the system uncertainty, represented as $\boldsymbol{\theta}_u$ and $\mathbf{u}_u$, has a random distribution that is known, bounded and not a function of the test design. $\mathbf{u}_u$ is considered to be time-independent source of system uncertainty during fault diagnosis and does not correlate to $\mathbf{u}_p$. The uncertain parameters and inputs that impact fault detection and isolation are grouped together with the faults as the target vector of the FDI test:

$$\boldsymbol{\xi} = [\boldsymbol{\theta}_f, \boldsymbol{\theta}_u, \mathbf{u}_u]. \tag{5.1}$$

Multiple fault scenarios can occur based on system design and environmental factors. We make the following assumptions regarding the system faults:

- When fault j is present, it is represented by a change in ξ_j, and all other elements in $\boldsymbol{\xi}$ are unaffected (faults are uncorrelated).
- When fault j is present, the corresponding parameter has a value around $\tilde{\xi}_j \in \Xi_j$, where Ξ_j is the range of values possible in fault j (faults are bounded and anticipated).
- When fault j is not present, the parameter corresponding to that fault has a value $\xi_j^0 \in \Xi_j$ (a healthy system condition exists within Ξ_j).

It is possible to have different degrees of fault severity represent different fault scenarios. However, in the case studies presented, a system that is subject to fault j is considered to be under fault scenario j regardless of severity. The test design optimization for FDI is dependent on the parameter and input values assigned to $\boldsymbol{\xi}$. In Bayesian design, tests can be designed that generate information from the entire range of possible values of faults combined with probabilistic weights. To reduce computational complexity, one set of the fault and uncertain parameters is selected that best represents the system at each anticipated fault scenario, denoted as $\tilde{\boldsymbol{\xi}}$, which contains the elements $\tilde{\xi}_j$ for $j = 1, \ldots, N_f$, where N_f is the number of anticipated faults. The values in $\tilde{\boldsymbol{\xi}}$ come from the best estimates obtained *a priori* for each fault parameter and uncertain variable. Chaloner and Verdinelli [141] term this "local optimality" or "approximate Bayesian," as a crude approximation of the expected

utility.

Although faults and system uncertainty are represented as parameters with unknown values, only the fault parameters are the target for diagnosis. Therefore, it is important to separate the elements of $\boldsymbol{\xi}$ that represent faults (i.e. parameters of interest) from the remaining elements (i.e. nuisance parameters). These parameters of interest can be distinguished by partitioning the vector, $\boldsymbol{\xi}$, as shown in (5.2):

$$\boldsymbol{\xi} = \left[\xi_1, \ldots, \xi_{N_f},\ \xi_{N_f+1} \ldots \xi_{N_\xi}\right] = \left[\boldsymbol{\xi}_f,\ \boldsymbol{\xi}_u\right], \tag{5.2}$$

where $\boldsymbol{\xi}_f$ is the vector of N_f parameters representing the faults, and $\boldsymbol{\xi}_u$ is the vector of remaining elements of $\boldsymbol{\xi}$, expressing uncertainty (and as shown later how it impacts system outputs).

5.2.2 Procedure for FDI test design and classification

The workflow for generating an optimal FDI test design and deploying the fault detection tests is illustrated in Fig. 5.1. The test design space defines the available (desirable) range of inputs, sampling times, and time-spans for FDI. The system input-output data is used to determine the variability of noise in each measurement, and impact of faults on outputs. The nominal test design that is considered for FDI is also studied (defined arbitrarily or with heuristic knowledge), to present metrics of the improvement of FDI after its design optimization. The model described in the previous section is used to estimate the values of $\boldsymbol{\xi}$ that correspond to each fault scenario. The anticipated parameters and inputs representing

each fault scenario are used to generate $\tilde{\boldsymbol{\xi}}$, which serves as the basis for calculating the optimal test design vector, $\boldsymbol{\varphi}$, for active FDI. The active FDI test is then implemented for the training and testing the feature extraction and classifiers used in fault diagnosis by running a Monte Carlo simulation for a system model with noise, or in a series of experiments. More details are provided on the training and testing phases in Section 5.2.4.

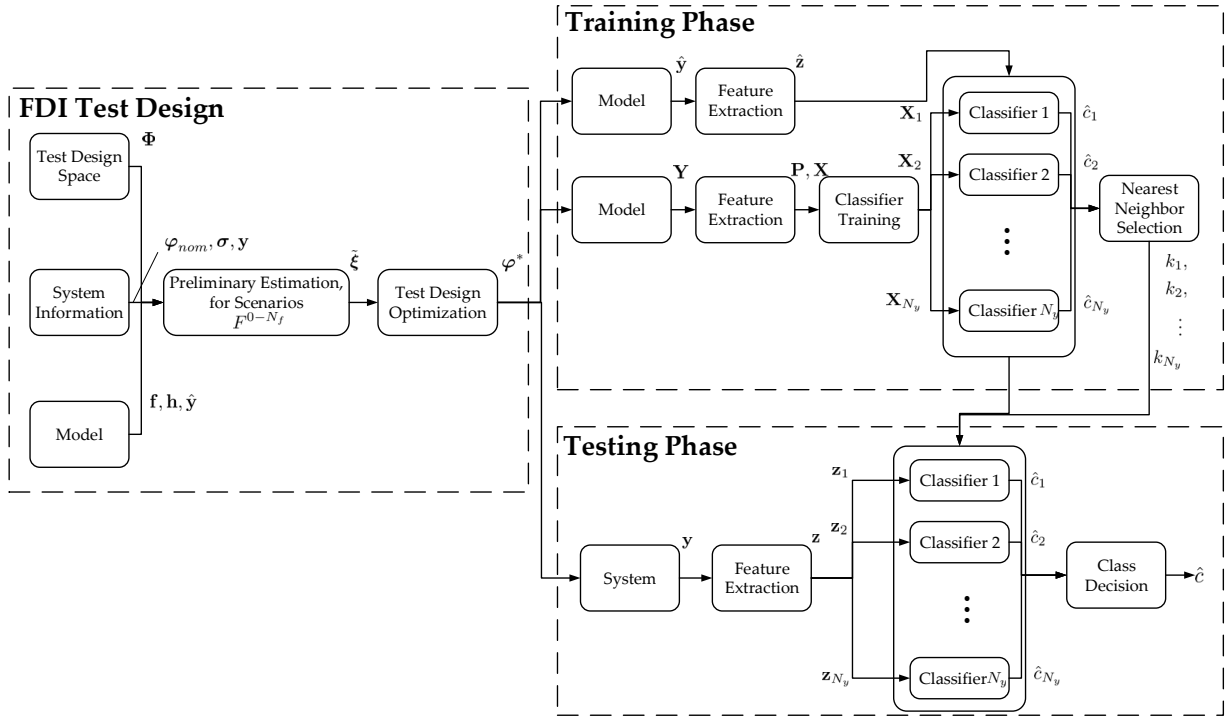

Fig. 5.1: Proposed methodology for the design and execution of FDI.

5.2.3 Design: Test optimization for active FDI

The key concept of the FDI test design method proposed in this work is to manipulate the system configuration to generate system information that leads to accuracy in fault diagnosis and is robust to uncertainty. The output trajectories of the system, $\mathbf{y}$, are observed directly, and measurement noise is considered to be zero-mean, Gaussian and uncorrelated with a known variance of σ^2. Thus, we have a model as expressed in (2.18-2.20), generating system observations $\mathbf{y}(t) \in \mathbb{R}^{N_y}$, which will be used to estimate the severity of faults in each scenario of faults and uncertainty, represented as $\boldsymbol{\xi} \in \mathbb{R}^{N_\xi}$ prior to diagnosis. Because the covariance matrix of the estimated fault values depends significantly on the test design considered, some measure must be selected that quantifies the usefulness of test design configurations. The FIM corresponding to the vector $\boldsymbol{\xi}$, denoted as $\mathbf{H}_\xi$, is widely used to determine such criteria for design selection. As defined by the Cramer-Ráo bound of the covariance matrix, the inverse of the FIM is equal to the minimum error covariance matrix achievable with an unbiased estimator, $\mathbf{V}$ [142]. Sensitivities for the FIM can be obtained through partial derivatives, variance decompositions, and the elementary effects method [143]. Variance decompositions require prior probabilistic knowledge which we assume is not necessarily available, and the intended use of the elementary effects method is for ranking uncertain inputs by order of influence. Therefore, partial derivatives are used to calculate the sensitivity of outputs with respect to faults and uncertainty. In this work, these partial derivatives are normalized and approximated around their anticipated values, $\tilde{\boldsymbol{\xi}}$, with 2^{nd}-order, central

finite differences or forward sensitivity analysis [144] depending on the size and complexity of the system model.

The admissible inputs, $\mathbf{u}_p \in \mathbb{R}^{N_{up}}$, are treated as a piecewise-constant series of discrete inputs at predetermined time points, and adjusted to produce an optimal test design. The test design vector is expressed as (5.3):

$$\boldsymbol{\varphi} = \mathbf{u}_p \in \boldsymbol{\Phi}, \tag{5.3}$$

where $\mathbf{u}_p$ has dimensions $N_{up} \times N_{step}$, where N_{step} is the number of piecewise steps used in the test design vector. The test design space, $\boldsymbol{\Phi}$, specifies the lower and upper bounds of each variable in the test design vector. The test design vector is manipulated to maximize some scalar measure of the FIM, thus $\mathbf{H}_\xi$ is a function of $\boldsymbol{\varphi}$ and $\boldsymbol{\xi}(= \tilde{\boldsymbol{\xi}})$.

The optimization problem is achieved using some scalar measure of the FIM, Ψ, and the formulation of this problem is dependent on whether the output trajectories considered for FDI contain steady-state or dynamic information. Table 5.1 displays the equations for steady-state and dynamic models, (5.4) and (5.5), respectively. Multiple criteria are available for selecting the function, Ψ, to calculate optimal designs [30, 142].

In optimal experimental design, the statistical measure of system information that is optimized is traditionally some functional of the eigenvalues of the FIM, denoted as $\lambda_j, j = 1, \ldots, N_\xi$ [31, 32]. As stated in Franceschini and Macchietto [30], assuming that the estimator used is unbiased, the eigenvalues of the FIM are inversely proportionate to the confidence ellipse axes of the estimated parameters, $\hat{\boldsymbol{\xi}}$. The selection of the statistical measure and

Table 5.1: Mathematical formulations for the optimization of steady-state and dynamic FDI test designs using a function Ψ.

Steady-State FDI	Dynamic FDI
$\boldsymbol{\varphi}^* \in \arg\ \max_{\boldsymbol{\varphi}\in\Phi} \Psi\left(\mathbf{H}_\xi(\tilde{\boldsymbol{\xi}},\varphi)\right)$	$\boldsymbol{\varphi}^* \in \arg\ \max_{\boldsymbol{\varphi}\in\Phi} \Psi\left(\mathbf{H}_\xi(\tilde{\boldsymbol{\xi}},\varphi)\right)$
s.t.	s.t.
$\mathbf{f}(\mathbf{x},\mathbf{u}_p,\boldsymbol{\theta}_p,\tilde{\boldsymbol{\xi}})=\mathbf{0},$	$\mathbf{f}(\dot{\mathbf{x}}(t),\mathbf{x}(t),\mathbf{u}_p(t),\boldsymbol{\theta}_p,\tilde{\boldsymbol{\xi}},t)=\mathbf{0},$
$\hat{\mathbf{y}}=\mathbf{h}(\mathbf{x},\mathbf{u}_p,\boldsymbol{\theta}_p,\tilde{\boldsymbol{\xi}}),$	$\hat{\mathbf{y}}(t)=\mathbf{h}(\mathbf{x}(t),\mathbf{u}_p(t),\boldsymbol{\theta}_p,\tilde{\boldsymbol{\xi}},t),$
$\mathbf{u}_p^L \le \mathbf{u}_p \le \mathbf{u}_p^U,$	$\mathbf{y}_0 = \begin{cases} \mathbf{f}(\dot{\mathbf{x}}(t_0),\mathbf{x}(t_0),\mathbf{u}_p(t_0),\boldsymbol{\theta}_p,\tilde{\boldsymbol{\xi}},t_0)=\mathbf{0}, \\ \hat{\mathbf{y}}(t_0)=\mathbf{h}(\mathbf{x}(t_0),\mathbf{u}_p(t_0),\boldsymbol{\theta}_p,\tilde{\boldsymbol{\xi}},t_0), \end{cases}$
$\mathbf{x}^L \le \mathbf{x} \le \mathbf{x}^U.$ (5.4)	$\mathbf{u}_p^L \le \mathbf{u}_p(t) \le \mathbf{u}_p^U, \quad \forall t\in[0,\tau],$
	$\mathbf{x}^L \le \mathbf{x}(t) \le \mathbf{x}^U, \quad \forall t\in[0,\tau]$ (5.5)

thus which eigenvalues, variances and correlations are targeted for optimization determine how the confidence of the parameter estimates are affected. In the following, we optimize test designs for FDI using four optimality criteria that are known to improve parameter

estimation. The reasoning and implementation of these criteria are as follows. The first criterion considered was implemented to improve the test design by minimizing the volume of the estimate confidence region, resulting in overall enhanced precision in the estimation of multi-parametric systems. Because the volume is the product of the axes of the confidence ellipse, this objective can be met by maximizing the product of the FIM eigenvalues. In statistics, this optimal criterion is referred to as D-optimality [145], as shown in (5.6):

$$\max_{\boldsymbol{\varphi}\in\Phi} \Psi_D\left(\mathbf{H}_\xi\right) = \max_{\boldsymbol{\varphi}\in\Phi} \det\left[\mathbf{H}_\xi\right]. \tag{5.6}$$

The determinant is often replaced with the log determinant for D-optimal criterion as it is numerically easier to solve. D-optimality can be difficult to solve if there is a large number of uncertain parameters. Another objective for the test design optimization can be to optimize the design such that the largest variability between the uncertain parameters is reduced. By maximizing the smallest eigenvalue of the FIM, which is inversely proportionate to the largest axis of the confidence region, the "worst-case" variance of the estimated parameters is minimized. This approach is known as E-optimality [146], as shown in (5.7):

$$\max_{\boldsymbol{\varphi}\in\Phi} \Psi_E\left(\mathbf{H}_\xi\right) = \max_{\boldsymbol{\varphi}\in\Phi} \left[\min_{1\le j\le N_\xi} \lambda_j\left\{\mathbf{H}_\xi\right\}\right], \tag{5.7}$$

In the criteria listed so far, all the elements of $\boldsymbol{\xi}$ are targeted for improved estimation precision. However, when a system contains uncertainty, the vector $\boldsymbol{\xi}$ has elements representing faults and uncertain conditions, as partitioned in (5.2). Estimation of uncertainty is not often of interest and seldom feasible. The information pertaining to correlations between

uncertain parameters should be removed as the estimation of fault-free uncertainty is not the focus of FDI. Therefore, the objective is to minimize the confidence region corresponding specifically to faults while taking into account the impact of uncertainty, which is accomplished using a derivative D-optimality criterion, known as D_s-optimality [147]. To achieve D_s-optimality, the scalar measure of the FIM is expressed as (5.8):

$$\max_{\boldsymbol{\varphi}\in\Phi} \Psi_{Ds}\left(\mathbf{H}_{\xi}\right) = \max_{\boldsymbol{\varphi}\in\Phi} \det\left[H_{ff} - H_{fu}H_{uu}^{-1}H_{fu}^{T}\right], \tag{5.8}$$

where the FIM is partitioned into blocks:

$$\mathbf{H}_{\xi} = \begin{bmatrix} H_{ff} & H_{fu} \\ H_{fu}^{T} & H_{uu}, \end{bmatrix}, \tag{5.9}$$

with:

$$H_{ff} \in \mathbb{R}^{N_f \times N_f}, \quad H_{fu} \in \mathbb{R}^{N_f \times (N_\xi - N_f)}, \quad H_{uu} \in \mathbb{R}^{(N_\xi - N_f)\times(N_\xi - N_f)}. \tag{5.10}$$

The final optimality criterion presented in this document is not a direct measure of the FIM eigenvalues; instead it examines the correlation coefficients between uncertain parameters, $\mathbf{C}$, derived from the variance-covariance matrix, $\mathbf{V}$. A correlation coefficient between two parameters determines the relationship they have on the measurements obtained. The range of correlation coefficients is -1 to 1, where values close to 0 indicate good confidence in the estimated parameters. The coefficients, $C_{i,j}$ for parameters $i, j = 1, \ldots, N_\xi$, are calculated as shown in (5.11):

$$C_{ij} = \frac{V_{ij}}{\sqrt{V_{ii}V_{jj}}}, \quad i \neq j, \tag{5.11}$$

where V_{ij} is the variance between the i-th and j-th elements of $\boldsymbol{\xi}$. Because only the faults are considered to be parameters of interest, the objective is then to minimize the value of correlation coefficients with respect to faults, and between faults and uncertainty. Therefore, the optimal criterion is a selective form of the PAC-optimal criterion reported in [30], and the formulation for the PAC-optimal FDI test design is shown in (5.12):

$$\max_{\boldsymbol{\varphi}\in\Phi} \Psi_{PAC}\left(\mathbf{H}_{\xi}\right) = \max_{\boldsymbol{\varphi}\in\Phi} \left[\sum_{i=1}^{N_f-1} \sum_{j=2}^{N_f} C_{i,j}^2 \Big|_{i\neq j} + \sum_{i=N_f+1}^{N_\xi-1} \sum_{j=N_f+2}^{N_\xi} C_{i,j}^2 \Big|_{i\neq j} \right]^{-1}. \tag{5.12}$$

The criteria described are geometrically interpreted in Fig. 5.2. Each criterion is used to minimize a specific aspect of estimation confidence and is labeled accordingly. The D-optimality criterion aims to minimize the volume of the confidence region. The E-optimal design aims to reduce the length of the major axis of the confidence region, and the PAC-criterion aims to minimize the correlation between parameters, making the confidence ellipse more perpendicular to the axes. Other criteria for test design optimization were assessed for active FDI, but are not shown in this document. In Appendix E, the methods for achieving E_s-optimal, modified E-optimal and G-optimal designs in active FDI are presented as well as the results generated from these FDI test designs.

5.2.4 Training: PCA and k-NN classifiers

After the test design optimization is complete, the calculated design is applied as an active test that is in turn deployed using a k-NN classification problem. A machine learning algorithm for passive FDI, presented by Najjar et al. [148], is leveraged using Principal Com-

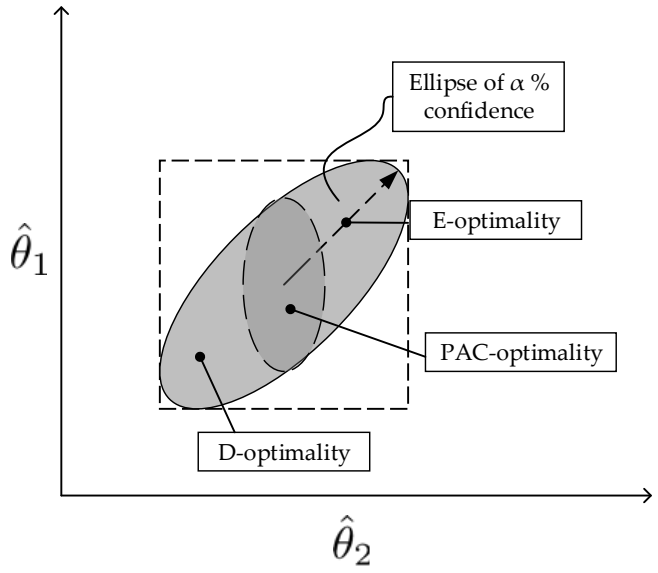

Fig. 5.2: Geometric interpretation of the selected criteria for the FDI test design. The ellipse with the solid outline represents the confidence region of the estimated parameters, with a significance level of α %.

ponent Analysis (PCA) with k-NN classification. As shown in Fig. 5.1, FDI execution has two phases: the training phase and the testing phase. During the training phase, Monte Carlo simulations are performed with randomly generated values for the uncertain parameters and measurement noise (within their allowable range), to create virtual system data. This data is used to determine the range of output responses for all fault scenarios, or classes. After a sufficient amount of training data is collected, it is used to classify future test samples when the presence of faults is unknown. We assess the quality of the FDI test by evaluating

the rate of correct classifications for all scenarios, as discussed in the following.

Feature extraction with PCA

PCA is based on orthogonal decomposition and is often used to consolidate data in classification methods [12]. It is commonly applied in fault detection and diagnosis because of its capacity for quick detection, robust design and ease of on-line implementation [138]. An application of PCA is presented in the following text. After selecting a test design for FDI and performing a Monte Carlo simulation for the training phase, data is compiled into a data matrix $\mathbf{Y}^j$, representing the data collected for fault scenario j, with dimensions $N_{MC} \times N_y N_{test} N_{sp}$:

$$\mathbf{Y}^j = \begin{pmatrix} \mathbf{y}_(\boldsymbol{\xi}_1^j)\Big|_{t=t_1,n=1} & \cdots & \mathbf{y}(\boldsymbol{\xi}_1^j)\Big|_{t=t_{N_{sp}},n=1} & \\ \vdots & \ddots & \vdots & \cdots \\ \mathbf{y}(\boldsymbol{\xi}_{N_{MC}}^j)\Big|_{t=t_1,n=1} & \cdots & \mathbf{y}(\boldsymbol{\xi}_{N_{MC}}^j)\Big|_{t=t_{N_{sp}},n=1} & \end{pmatrix}$$
$$\begin{pmatrix} \mathbf{y}(\boldsymbol{\xi}_1^j)\Big|_{t=t_1,n=2} & \cdots & \mathbf{y}(\boldsymbol{\xi}_1^j)\Big|_{t=t_{N_{sp}},n=N_{test}} \\ \vdots & \ddots & \vdots \\ \mathbf{y}(\boldsymbol{\xi}_{N_{MC}}^j)\Big|_{t=t_1,n=2} & \cdots & \mathbf{y}(\boldsymbol{\xi}_{N_{MC}}^j)\Big|_{t=t_{N_{sp}},n=N_{test}} \end{pmatrix}, \tag{5.13}$$
$$j = 0, \ldots, N_f.$$

The objective of PCA is to transform the data matrix $\mathbf{Y}^j$ into a matrix $\mathbf{T}^j$ of size $N_{MC} \times N'$, where $N' \leq N_y N_{test} N_{sp}$, with the columns of $\mathbf{T}^j$ containing the principal components for

j-th fault scenario. The data matrix $\mathbf{Y}^j$ is linearly transformed:

$$\mathbf{T}^j = \mathbf{Y}^j\mathbf{P}, \tag{5.14}$$

where $\mathbf{P}$ is the transformation orthogonal matrix of size $N_y N_{test} N_{sp} \times N'$, calculated using the Karhunen-Loéve (KL) algorithm [149]. Covariance matrices of each sensor data matrix with size $N_y N_{test} N_{sp} \times N_y N_{test} N_{sp}$, $\mathbf{C_Y}$, are generated from the virtual system at fault-free conditions ($j = 0$). $\mathbf{C_Y}$ is computed according the matrix equality shown in (5.15).

$$\mathbf{C_Y} = \mathbf{E}\left[\left(\mathbf{Y}^0 - \mathbf{E}\left[\mathbf{Y}^0\right]\right)\left(\mathbf{Y}^0 - \mathbf{E}\left[\mathbf{Y}^0\right]\right)^T\right], \tag{5.15}$$

where $\mathbf{E}$ is the expected value of its argument. The orthogonal properties of the transformation matrix, $\mathbf{P}$, ensure that the following equation is true:

$$\mathbf{C_Y}\hat{\mathbf{P}} = \hat{\mathbf{P}}\mathbf{\Lambda}^0, \tag{5.16}$$

where the columns of $\hat{\mathbf{P}}$ are the complete set of eigenvectors relating to $\mathbf{C_Y}$, and the diagonal of the matrix, $\mathbf{\Lambda}^0$, lists the eigenvalues of the sensor data covariance matrix λ_i, $i = 1, \ldots, N_{test} N_{sp}$, with all other terms in $\mathbf{\Lambda}^0$ zero. In mathematical terms:

$$\begin{aligned} \Lambda^0_{ii} &= \lambda_i, \quad i = 1, \ldots, N_y N_{test} N_{sp}, \\ \Lambda^0_{ij} &= 0, \quad i, j = 1, \ldots, N_{test} N_{sp}, \quad i \neq j. \end{aligned} \tag{5.17}$$

To reduce the dimensionality of the data, the principal components of the data matrix are determined by selecting the eigenvectors which consequently become the columns of $\hat{\mathbf{P}}$, related to the highest N' eigenvalues of $\mathbf{C_Y}$:

$$\mathbf{P} = (P_1|P_2|\ldots|P_{N'}), \tag{5.18}$$

where $\mathbf{P}$ is the orthogonal matrix used to transform the data matrix $\mathbf{Y}^j$ to $\mathbf{T}^j$, and P is the eigenvector of the i-th highest λ. The number of principal components must be selected such that the test information is still useful while reducing the number of dimensions of the selected classifier. This approach is applicable to steady-state and dynamic FDI, though it can be computationally demanding for dynamic tests [150].

After the data from the Monte Carlo simulations is transformed, the principal components for all fault and fault-free scenarios are compiled into a matrix $\mathbf{X}$ of size $N_{MC}(N_f + 1) \times N'$,

$$\mathbf{X} = \left[\mathbf{T}^0; \mathbf{T}^1; \ldots; \mathbf{T}^{N_f}\right].$$

The training sets, $\mathbf{X}$, are used in the k-NN algorithm to determine which class best corresponds to any given set of test samples.

k-NN classifier training

After the training data is acquired, the next step is to determine the optimal k. The k value is chosen from possible odd integers $3, 5, 7, 9, \ldots, 21$, that results in the most accurate FDI test. In this work, this is achieved by evaluating which values lead to the highest sum of correct classification rates (CCR) for all anticipated fault scenarios. The CCR corresponding to each fault scenario in the FDI test is determined using additional data acquired from the virtual system. A second Monte Carlo simulation is implemented using N_{MC} runs for each fault scenario. In this Monte Carlo simulation, the fault scenario corresponding to each data

set is not pre-labeled. For each Monte Carlo run of the classifier training phase, the data obtained from the FDI test, $\hat{\mathbf{y}}$, is transformed into the reduced set, $\hat{\mathbf{z}}$:

$$\hat{\mathbf{z}} = \hat{\mathbf{y}}\mathbf{P}. \tag{5.19}$$

In standard k-NN, the test data points are compared with the training points to determine the data sets that generate up to the k-th smallest distance. The euclidean distance between data set points, d, is commonly used for its simplicity, and is calculated as shown below:

$$d\left(\mathbf{X}_l, \hat{\mathbf{z}}\right) = \sqrt{\left(X_{l1} - \hat{z}_1\right)^2 + \left(X_{l2} - \hat{z}_2\right)^2 + \ldots + \left(X_{lN'} - \hat{z}_{N'}\right)^2},$$
$$l = 1, \ldots, N_{MC}.$$

Algorithm 1 Find k-Nearest Neighbors

procedure kNN_Dist($\mathbf{X}, \mathbf{z}, k$) ▷ k= number of neighbors
  for $k' = 1 : k$ **do**
    if $k' = 1$ **then**
      $m^1 \in \arg\min_{1 \le l \le N_{MC}} d\left(\mathbf{X}_l, \mathbf{z}\right)$
    else
      $m^{k'} \in \arg\min_{1 \le l \le N_{MC}, \quad l \neq m^1, \ldots, m^k} d\left(\mathbf{X}_l, \mathbf{z}\right)$
  return $[m^1, m^2, \ldots, m^k]$ ▷ Elements corresponding to the k-nearest neighbors

An algorithm is used to determine which trained data sets have the closest match to the test set. Specifically, Algorithm 1 is used to find the rows of $\mathbf{X}$ that have the smallest distance to $\hat{\mathbf{z}}$. After the rows are determined, the sets are compiled into a matrix that

contains the features corresponding to the nearest neighbors of $\hat{\mathbf{z}}$, denoted as $\mathbf{X}^*$, where

$$\mathbf{X}^* = [\mathbf{X}_{m^1}; \mathbf{X}_{m^2}; \ldots; \mathbf{X}_{m^k}] .$$

The probability of each fault scenario is then approximated with a unit function E, shown below:

$$E(\mathbf{X}_l^*, c^j) = \begin{cases} 1 & \text{if } \mathbf{X}_l^* \text{ belongs to class } c^j, \\ 0 & \text{otherwise.} \end{cases}$$

To determine the probability of each fault scenario, or class, the sum of $E(\mathbf{X}_m^*, c^j)$ is determined for each class, c^j is divided by the number of nearest neighbors considered. The probability of class c^j, $p(c^j)$, is then calculated as shown below:

$$p(c^j) = \sum_{l=1}^{k} \frac{E(\mathbf{X}_l^*, c^j)}{k}, \quad j = 0, \ldots, N_f, \tag{5.20}$$

where k is the number of nearest neighbors. The final step in training the classifiers is to select the k value used in FDI that result in the highest accuracy. The selection of the optimal k is done by predicting the class corresponding to the features extracted from each Monte Carlo run, denoted as $\hat{\mathbf{z}}(\boldsymbol{\xi}_l^j)$ for $l = 1, \ldots, N_{MC}$. The optimal number of nearest neighbors, k^*, should lead to the highest number of correct classifications for all fault scenarios based on the data obtained from the Monte Carlo simulation.

5.2.5 Deployment and assessment: FDI execution

After PCA and classifier training, the FDI test is deployed for several virtual system runs and the proposed test designs are evaluated to determine which criteria result in successful

tests for active FDI. For this assessment, another Monte Carlo simulation is performed using virtual system data for each fault scenario. Though the fault scenarios corresponding to each Monte Carlo iteration are known, the datasets are unlabeled, thus the classes belonging to each dataset need to be declared. The values assigned to the uncertain parameters and measurement noise of each run are randomly generated to determine the classification accuracy of each test for all fault scenarios.

In standard applications of the k-NN algorithm, the label assigned to the system is decided by a discrete "majority vote," thus the class with the largest weighted sum of nearest neighbors is considered to be the predicted class of the system, $\hat{c}_{MV}$:

$$\hat{c}_{MV} \in \arg \max_{c \in \{c^0, c^1, \ldots, c^{N_f}\}} p(c). \tag{5.21}$$

If $\hat{c}_{MV}$ generates a set with more than one selected class, the class from the among that set that contains the point with the shortest euclidean distance to the transformed test dataset is the predicted class. The k-NN algorithm and class decision using (5.19-5.21) and Algorithm 1 is repeated for each Monte Carlo run in the testing phase.

After the predicted classes have been declared for all test samples, the effectiveness of the FDI test design using the majority vote k-NN classification is assessed by confusing the number of correct vs incorrect classifications for each fault scenario. Confusion matrices are used in statistics to compare the accuracy of assigning classes to tests or data. Classifications are tabulated such that the diagonal elements contain the CCR with respect to each class, and off-diagonal elements represent the misclassification rate (MCR) of each decision. Following

(5.21), CCR and MCR values are calculated as shown below:

$$\mathrm{CCR}_j = \frac{1}{N_{MC}^j} \sum_{l=1}^{N_{MC}^j} \begin{cases} 1, & \text{if } \mathbf{z}\left(\boldsymbol{\xi}_l^j\right) \rightarrow \left(\hat{c} = c^j\right) \\ 0, & \text{otherwise} \end{cases},$$

$$\mathrm{MCR}_{j,k} = \frac{1}{N_{MC}^j} \sum_{l=1}^{N_{MC}^j} \begin{cases} 1, & \text{if } \mathbf{z}\left(\boldsymbol{\xi}_l^j\right) \rightarrow \left(\hat{c} = c^k \neq c^j\right) \\ 0, & \text{otherwise} \end{cases},$$

where $N_{MC,j}$ is the total of Monte Carlo runs for fault scenario j. The overall classification accuracy, A_{CCR}, is the number of correct classifications over the total number of FDI tests generated,

$$A_{\mathrm{CCR}} = \frac{\sum_{j=0}^{N_f} \mathrm{CCR}_j}{\sum_{j=0}^{N_f} N_{MC}^j}.$$

To assess the quality of a test, the CCR of each fault scenario and the corresponding A_{CCR} are compared for the nominal test design and the FDI tests generated with the optimality criteria.

Another approach to implementing k-NN is to assign a threshold to the number of neighbors assigned to a particular class. The threshold can be adjusted to change the sensitivity and selectivity of the FDI test, and to satisfy restrictions assigned to either the number of allowable nondetections or false alarms. By assessing the k-NN classification method in this manner the impact of the test design can then be presented in the form of receiver operating characteristic (ROC) plots, which are an effective way to graphically illustrate the ability to diagnose between binary classes across a variable decision threshold. However, implementing a binomial decision threshold for multi-class classification can be

difficult. Therefore, the "one vs all" approach is used by considering the fault-free scenario as the positive class, and all other classes are considered to be negative. For the purpose of generating ROC plots, the class labels are reduced to c^0, representing the fault-free scenario and positive class, and $c^{\emptyset}$, representing all other scenarios that correspond to a system with a fault or set of faults present. The predicted fault detection class using the probabilistic k-NN for ROC plots, c^{FD}, is determined as shown below:

$$\hat{c}_{FD} = \begin{cases} c^0, & \text{if} \quad p(c^0) \geq \delta. \\ c^{\emptyset} \in \{c_1, c_2, \ldots, c_{N_f}\}, & \text{if} \quad p(c^0) < \delta, \end{cases} \tag{5.22}$$

where δ is the assigned threshold to the probability corresponding to the minimum number of neighbors required to consider the system to be without fault.

If $\hat{c}_{FD} = c^{\emptyset}$, then the fault needs to be isolated. The isolated fault class, $\hat{c}_{FI}$, can then be determined by finding the class that results in the largest sum of probabilities. The majority vote approach in (5.21) is then updated for fault isolation, after a fault has been detected using (5.22), as shown below:

$$\hat{c}_{FI} \in \arg \max_{c^{\emptyset} \in \{c_1, c_2, \ldots, c_{N_f}\}} p(c^{\emptyset}). \tag{5.23}$$

Similar to $\hat{c}_{MV}$, the class in $\hat{c}_{FI}$ with the point that has the shortest euclidean distance to the test data is the predicted class. By implementing (5.22) and (5.23) for a threshold range of 0 to 1, the true positive rates (TPR), false positive rates (FPR) and CCR of each fault scenario can be determined to generate ROC plots with the proposed FDI test designs. The quality of the FDI test is reflected in the area under the ROC curve (AUC) of each scenario. AUCs

typically range from 0.5 to 1, where higher AUCs indicate better fault diagnosis with similar test selectivity. Thus, optimizing the test designs used in active FDI with the proposed method results in steeper ROC curves and an improved quality of fault diagnosis.

5.3 Results and discussion

5.3.1 Case study I: Three-tank system

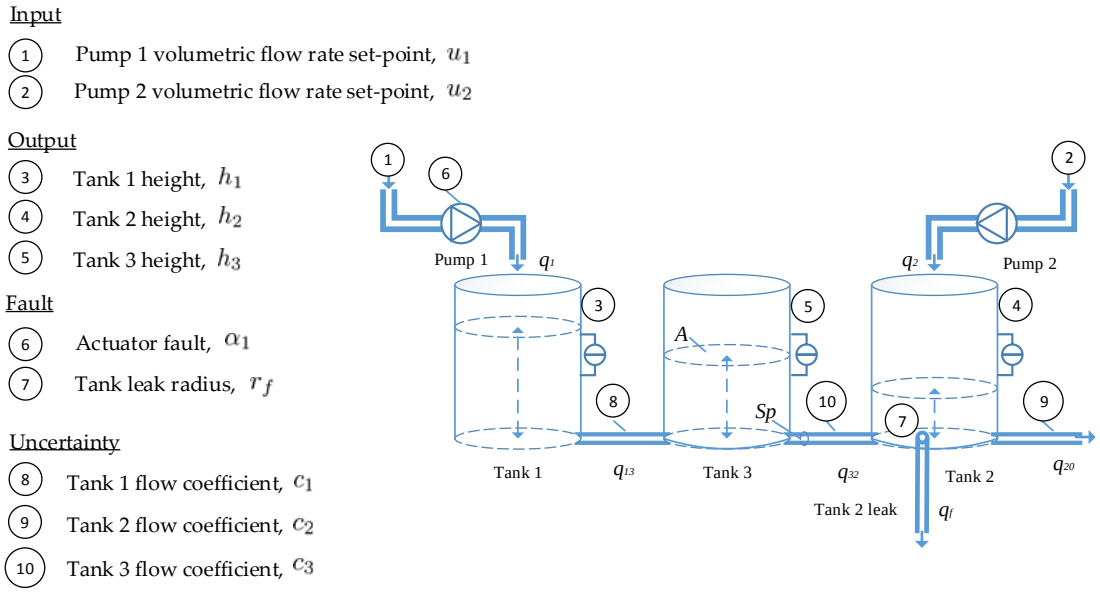

Fig. 5.3: Design schematic of a general three-tank system [7]

In the first case study, we assessed FDI test design options for an open-loop, three-tank system. The three-tank system is a commonly used benchmark for exploring capabilities of fault detection and isolation algorithms [7]. Fig. 5.3 shows the system architecture that

was used, along with the corresponding variables and parameters. In this system, there are three cylindrical tanks with identical cross-sectional areas, A. The system has volumetric flow rates, q_{ij}, which represent the flow from tank i to tank j ($j = 0$ when the stream flows into the fluid sink). The system admissible inputs are the volumetric flow rates assigned to pumps 1 and 2, represented as u_1 and u_2, respectively. The states of the system are the liquid levels in tank 1, 2 and 3, represented as h_1, h_2, and h_3. The pipes connecting each tank have equal cross-sectional areas, S_p. Each pipe has a flow coefficient that affects the tank exiting flow rate, c_1, c_2, and c_3. These variables are considered uncertain so they were included in the faults and uncertain parameters vector, $\boldsymbol{\xi}$, as potential targets in the optimization of FDI test designs.

Two fault scenarios were considered in this case study. The first anticipated fault was a degradation in the pump 1 actuator, characterized by the flow coefficient, α ($\alpha = 1$ at fault-free conditions). The second anticipated fault was a leak that occurs in tank 2, characterized by the leak radius, r_f ($r_f = 0$ at fault-free conditions). The faults and uncertainties are listed in Table 5.2, along with their corresponding Gaussian distributions. The lower and upper bounds of each fault and uncertain parameter was known ($\pm 3\sigma$). The range of every variable in $\boldsymbol{\xi}$ is listed for each fault scenario, c^j, where the system at $j = 0$ is fault-free, $j = 1$ contains a drift in the actuator valve, and $j = 2$ contains a leak in tank 2. The FDI tests designed in the following text consider both fault scenarios and system uncertainty simultaneously.

The three-tank system model utilizes well-known mass balance equations and Torri-

Table 5.2: Faults and uncertain parameters studied in the three-tank system case study, and their normally distributed $\mathcal{N}(\mu, \sigma^2)$ random parameter values with mean, μ, and variance, σ^2.

Set of $\boldsymbol{\xi}$	c^0	c^1	c^2
α	1	$\mathcal{N}(0.6, 0.0025)$	1
r_f (mm)	0	0	$\mathcal{N}(2.0, 1.0)$
c_1	$\mathcal{N}(0.95, 0.0025)$	$\mathcal{N}(0.95, 0.0025)$	$\mathcal{N}(0.95, 0.0025)$
c_2	$\mathcal{N}(0.8, 0.0025)$	$\mathcal{N}(0.8, 0.0025)$	$\mathcal{N}(0.8, 0.0025)$
c_3	$\mathcal{N}(0.95, 0.0025)$	$\mathcal{N}(0.95, 0.0025)$	$\mathcal{N}(0.95, 0.0025)$

celli's law to describe the overall system dynamics, as shown in (5.24):

$$\begin{aligned} A\frac{\partial h_1}{\partial t} &= \alpha u_1 - c_1 S_p \text{sign}(h_1 - h_3)\sqrt{2g|h_1 - h_3|}, \\ A\frac{\partial h_2}{\partial t} &= u_2 + c_3 S_p \text{sign}(h_3 - h_2)\sqrt{2g|h_3 - h_2|} - c_2 S_p \sqrt{2gh_2} - c_2 \pi r_f^2 \sqrt{2gh_2}, \\ A\frac{\partial h_3}{\partial t} &= c_1 S_p \text{sign}(h_3 - h_2)\sqrt{2g|h_1 - h_2|} - c_3 S_p \text{sign}(h_3 - h_2)\sqrt{2g|h_3 - h_2|}. \end{aligned} \tag{5.24}$$

The system states are constrained to 0 m $< h_i \leq$ 0.75 m for i=1,2,3, for any combination of fault and uncertain parameter values within the parameter space. The admissible input range is $0 \leq u_j \leq 10^{-4}$ m^3/s, j=1,2, respectively. It was assumed that all tank heights can be measured ($\mathbf{y} = [h_1, h_2, h_3]$) in the virtual three-tank system. The model was solved and the optimal test was calculated using the program MATLAB [70]. The sensitivities were calculated in this case study using the forward sensitivity analysis, as detailed in Maly and

Petzold [144]. The anticipated fault and uncertainties, $\tilde{\boldsymbol{\xi}} = [0.6, 2.0\text{mm}, 0.95, 0.8, 0.95]$, were injected into the virtual three-tank system. This virtual system is identical to the system model shown in (5.24) with measurement noise added to each output as well as faults and uncertainty injected. The standard deviation of each sensor was assumed to be 0.001 m. The nominal and optimal test designs are detailed in Table 5.3, along with the upper and lower bounds of each admissible input. The values calculated for u_1 and u_2 correspond to one nominal or optimal steady-state test for the detection of faults within system uncertainty as described in Table 5.2. The D-optimal and D_s-optimal test designs are achieved by setting the pump 2 actuator to the lower bound and the pump 1 actuator to the highest possible setting that does not violate output constraints. The D-optimal differs slightly due to the increase in sensitivity of the outputs with respect to the uncertain flow coefficients. The E-optimal test design was calculated to be identical to the D-optimal design. This is improving the confidence of the estimated parameter with the least confidence, which was determined to be one of the fault parameters. Finally, the PAC-optimal test was set to the lower and upper bound of the first and second inputs, respectively, which causes the tank heights to reach similar levels regardless of whether there is a fault present. This design minimizes only the correlations between the faults and uncertain parameters.

The rate of successful diagnosis of each fault using these designs was assessed with Monte Carlo simulation, performed by injecting random distributions to the fault parameters, flow coefficients and measurement noise. 10 steady-state measurement samples were collected

Table 5.3: Nominal and optimal FDI test designs for the three-tank system that contains an actuator fault at tank 1, a leak at tank 2 and uncertain flow coefficients ($\tilde{\boldsymbol{\xi}} = [0.6, 2.0\text{mm}, 0.95, 0.8, 0.95]$).

$\boldsymbol{\varphi}$	Lower Bound	Upper Bound	Nom	D-Opt	D_s-Opt	E-Opt	PAC-Opt
u_1 ($\times 10^{-4}$ m^3/s)	0.10	1.00	0.55	0.76	0.77	0.47	0.10
u_2 ($\times 10^{-4}$ m^3/s)	0.10	1.00	0.55	0.11	0.10	0.65	1.00

for 2000 Monte Carlo runs, at each test design. Histograms of the mean of each steady-state sample set for h_1, h_2 and h_3 at the nominal and D_s-optimal test conditions are shown in Fig. 5.4. The performance of other design criteria is discussed later. As shown in Fig. 5.4, the D_s-optimal test shows significant improvement in the separation between outputs in response to each fault. When comparing the nominal test to the D_s-optimal test, there is small change in the distance between the healthy (c^0) and tank leak (c^2) scenarios, but there is significant improvement in fault isolation (c^1 to c^2).

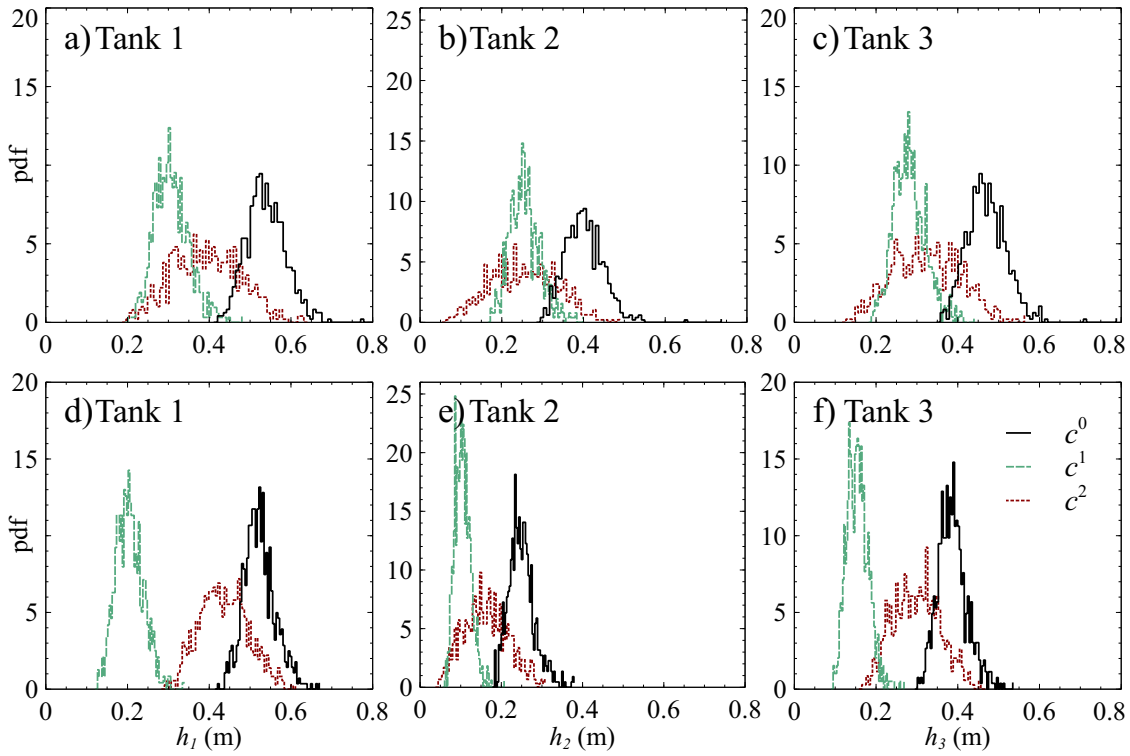

Fig. 5.4: Histograms of Monte Carlo simulations for the heights of tanks 1, 2 and 3 at fault and fault-free conditions, using (a-c) nominal and (d-f) D_s-optimal FDI tests. c^0, c^1 and c^2 were assigned the values or distributions shown in Table 5.2.

Next, PCA was implemented for the training phase of the fault classification method presented in Section 5.2. After testing, the number of reduced dimensions, N', as set to 3. k-NN classifiers were trained, and Monte Carlo samples were generated to determine the rate of correct classifications from each sensor. By fusing the available sensor data, the rates of correct classifications and misclassifications between the predicted and actual classes

Table 5.4: Confusion matrices of a three-tank system FDI with fault scenarios listed in Table 2.

(a) Confusion matrices of FDI executed at nominal, D-optimal and D_s-optimal test designs

		Nominal			D-Optimal			D_s-Optimal		
		Actual			Actual			Actual		
Predicted		c_0	c_1	c_2	c_0	c_1	c_2	c_0	c_1	c_2
	c_0	0.98	0.33	0.10	0.93	0.00	0.32	0.94	0.01	0.32
	c_1	0.01	0.35	0.29	0	1.00	0.00	0	0.99	0.00
	c_2	0.01	0.32	0.61	0.07	0	0.68	0.06	0.00	0.68

(b) Confusion matrices of FDI executed at E-optimal and PAC-optimal test designs

		E-Optimal			PAC-Optimal		
		Actual			Actual		
Predicted		c_0	c_1	c_2	c_0	c_1	c_2
	c_0	0.93	0	0.32	0.64	0.55	0.26
	c_1	0	1.00	0	0.34	0.44	0.21
	c_2	0.07	0	0.68	0.02	0.01	0.53

(c) Classification accuracies of the listed test designs

Test Criterion	A_{CCR}
Nominal	0.65
D-Opt	0.87
D_s-Opt	0.87
E-Opt	0.87
PAC-Opt	0.54

representing each fault scenario were calculated. The corresponding confusion matrices are shown in Table 5.4 for each of the nominal and optimal test designs, for all the design criteria described in Section 5.2.2. The elements contained in the diagonal of the confusion matrices show the number of correct classifications corresponding to each fault scenario (CCR). In the nominal test design, the actuator fault and fault-free scenarios had a correct classification rate greater than 0.85. A three-tank system with a tank leak had a nominal true detection rate greater than 0.75, and a correct classification rate of more than 0.50. In the D-optimal test design, CCRs were consistently greater, and the D_s-optimal test design showed similar improvement with better fault isolation. The objective of the D-optimal design is to reduce

the correlation between all the parameters of interest, with results very similar to those from the D_s-optimal test, because of the small variance in the uncertain parameters of this system. The E-optimal test design was identical to the D-optimal design, therefore the CC and MCR values were the same. This was likely caused by the improvement of the worst-case variance corresponding directly to the confidence of the fault parameter estimates. The PAC-optimal test design resulted in a significant deterioration of the CCRs in all fault scenarios. However, $MCR_{0,2}$ and $MCR_{2,0}$ were reduced to half or more of the nominal test values, caused by reduction of specific parameter correlations. Comparison of the classification accuracies generated from each test (A_{CCR}) indicates that the best test design for active FDI in the three-tank system was produced by D-optimal or D_s-optimal criteria.

For illustration of test performance, ROC plots were generated using k-NN classifiers with a variable threshold for fault detection sensitivity as shown in (5.22). The threshold was assigned a range of 0 to 1, and the rate of false positives vs. true positives, and false positives vs. correct classifications were compared for each threshold setting. The resulting ROC curves are presented in Fig. 5.5 for FDI conducted in the three-tank system at the nominal test design and optimal test designs with different design criteria. The true positive rate (TPR) curves shown in Fig. 5.5a show good fault detection even at high selectivity (low FPR) at all test designs except PAC-Optimal. Almost perfect detection is made possible using D and D_s-optimal test designs. Fig. 5.5b shows that the nominal test has consistently better detection at the same FPR values, a trade-off in some of the test designs in order to

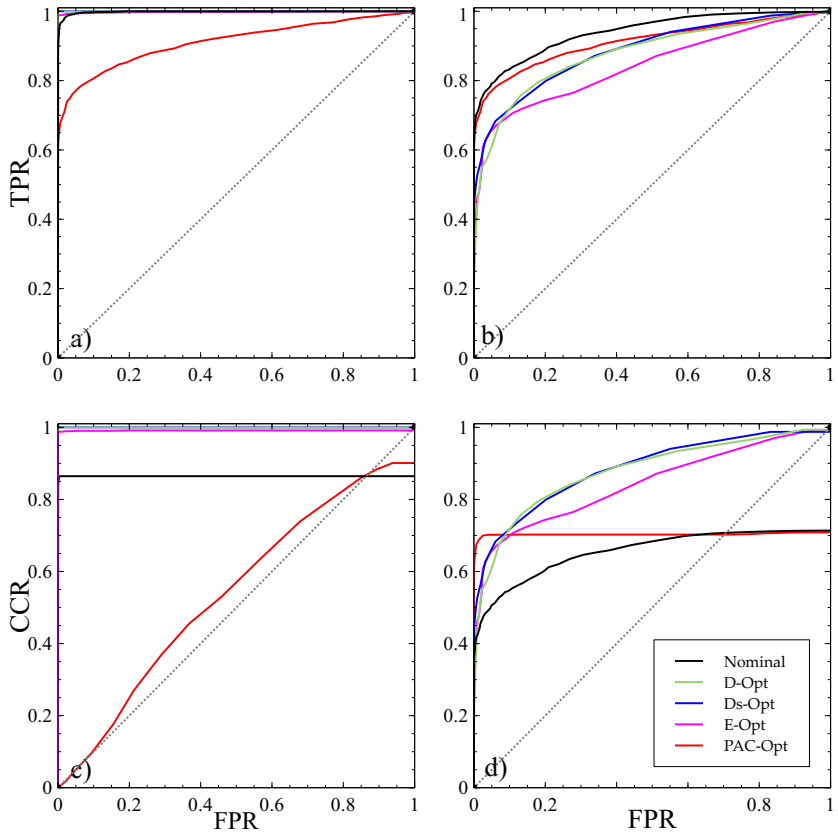

Fig. 5.5: ROC plots of true positive and correct classification rates versus false positive rates with test designs at different optimal criteria. Fault scenarios described in Table 5.2 are presented for a three-tank system with (a,c) actuator fault in tank 1 and (b,d) a leak in tank 2.

meet their respective criteria. Figs. 5.5c and 5.5d, the D and D_s-optimal test designs result in significantly better classification at the same selectivity, compared to other tests. The D_s-optimal test design is shown also to be marginally better for the correct classification of

tank leaks. Overall, the reconfiguration of input trajectories to satisfy D_s-optimality leads to consistent improvement in the diagnosis of faults in lieu of system uncertainty.

Table 5.5: Confusion matrices of a dynamic three-tank system FDI with fault scenarios listed in Table 2.

(a) Confusion matrices of FDI executed at nominal, D-optimal and D_s-optimal test designs

		Nominal			D-Optimal			D_s-Optimal		
		Actual			Actual			Actual		
Predicted		c_0	c_1	c_2	c_0	c_1	c_2	c_0	c_1	c_2
	c_0	0.94	0.01	0.20	0.95	0	0.19	0.95	0	0.18
	c_1	0.00	0.87	0.28	0	1.00	0.00	0	1.00	0
	c_2	0.06	0.12	0.52	0.05	0	0.81	0.05	0	0.82

(b) Classification accuracies of the listed test designs

Test Criterion	A_{CCR}
Nominal	0.78
D-Opt	0.92
D_s-Opt	0.92

The proposed method was found to be effective for dynamic FDI as well. As shown in previous work [151], the use of transient data can improve the detection and identification of system faults so long as the system dynamics are effectively captured in the model used for FDI. For this analysis, the dynamic test designs were implemented as follows. In each Monte Carlo run, the three-tank system was simulated at the nominal test design from $t = 0$ s to $t = 3000$ s. At $t = 3000$ s, the inputs were adjusted to implement the optimal conditions for FDI, and then measurements samples were collected every 300 s from each tank sensor, until $t = 6000$ s. Table 5.5 presents the confusion matrices of the FDI test designs that use

transient information for diagnosing faults. The use of transient information in dynamic FDI increased the sensitivity of the measured outputs to each fault as opposed to the steady-state FDI performed with the same number of samples. Compared to Table 5.4, the overall classification accuracy of the D- and D_s- optimal test designs was improved by 0.03.

5.3.2 Case study II: Diesel engine

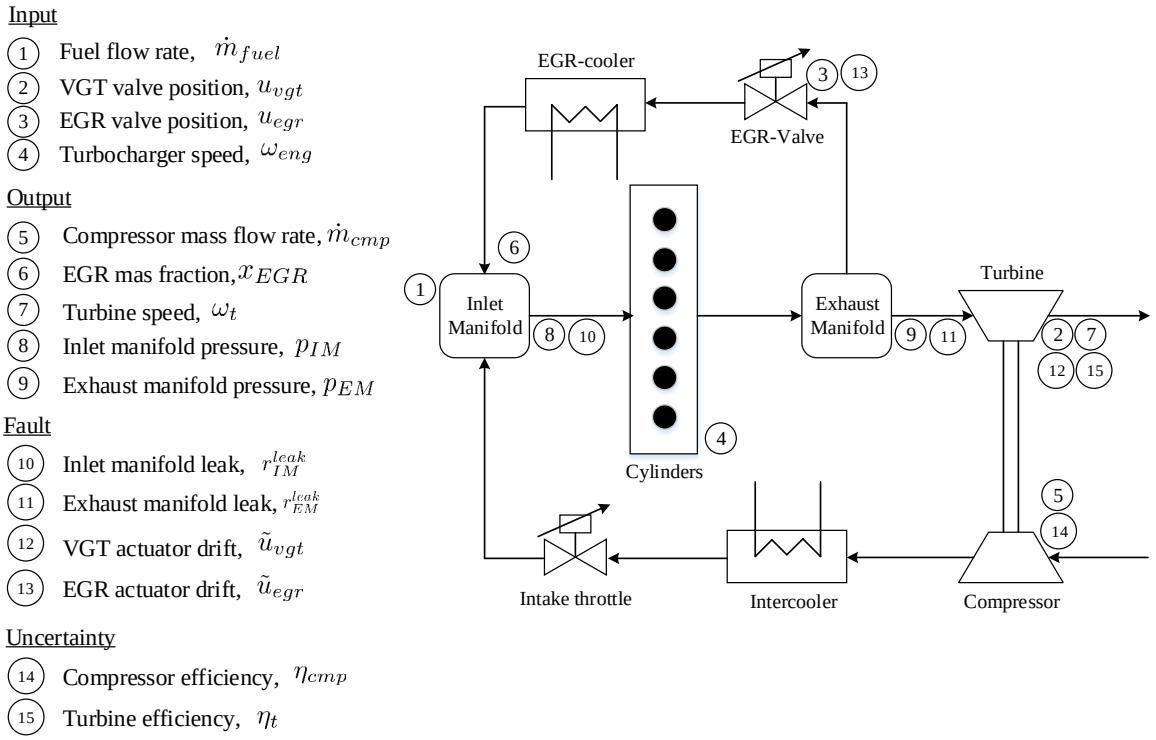

Fig. 5.6: Schematic of a turbocharged air-intake system for a diesel engine [8, 9].

The framework described in the Methods section was also implemented for the opti-

mization and assessment of FDI test designs for the air-intake system inside a diesel engine. Model-based fault diagnosis has been a prominent field of research for diesel engines [9, 152]. The intake system is designed to provide a steady stream of air at desired temperatures and pressures to the diesel engine [152]. Fig. 5.6 shows the air-intake schematic of the system of this case study. Ambient air enters the system through the compressor, which is powered by the exhaust gas flowing through the turbine. The heated air then passes through an intercooler that draws excess heat from the air stream and transfers energy into the liquid coolant. The air stream then passes through a throttle valve into the inlet manifold where it is split into multiple cylinders and reacts with the injected fuel stream. After the fuel combustion, the exhaust gas drives a turbine for power generation. Part of the exhaust stream is recycled to the inlet manifold through an Exhaust Gas Recirculation (EGR) valve.

This system was modeled and the validation of this model is reported in Wahlstrom and Eriksson [153], and was implemented in Simulink [154] for this case study. The system modeled has four adjustable inputs that can be optimized for fault detection; the valve positions in the variable-geometry turbine (VGT), u_{VGT}, and EGR, u_{EGR}, the mass flow rate of the injected diesel fuel, $\dot{m}_{fuel}$, and the speed of the turbocharger, ω_{eng}. The measured system outputs are the pressure at the inlet manifold, p_{IM}, and exhaust manifold, p_{EM}, the rotor speed of the turbine, ω_t, compressor mass flow rate, $\dot{m}_c$, and the mass fraction of the exhaust that is recycled back into the inlet manifold, x_{EGR}. It was assumed that these outputs have normally distributed measurement noise with standard deviation at 5% of their

respective nominal values, as reported by Eriksson et al. [155].

Four time-invariant faults are examined in this case study. The first anticipated fault is a drift in the actuator that determines the VGT valve position, $\tilde{u}_{VGT}$. The second fault is a drift in another actuator that corresponds to the EGR valve, $\tilde{u}_{EGR}$. The last two faults examined are leaks in the inlet and exhaust manifold, r_{IM}^{leak} and r_{EM}^{leak}, respectively. Faults in either actuator affect the performance and costs of the diesel engine operation, while leaks in the manifolds decrease engine efficiency and overtime can lead to a failed manifold. These faults are captured as parameters or inputs in the system model. Moreover, due to the variability in production and the degradation of performance overtime, the system (model) is subject to uncertainty in the compressor maximum efficiency, η_{cmp}, and the turbine maximum efficiency, η_t. These faults and uncertain parameters are compiled together in $\boldsymbol{\xi}$, with distributions as listed in Table 5.6. The anticipated range of every fault parameter in $\boldsymbol{\xi}$ is listed for each fault scenario, c^j, where the system at $j = 0$ is fault-free, $j = 1$ contains a drift in the VGT valve, $j = 2$ contains a drift in the EGR valve, $j = 3$ contains a leak in the inlet manifold, and $j = 4$ contains a leak in the exhaust manifold. The performance of FDI with increased variability in the fault and fault-free conditions ($c \neq c^j$, $\xi_j \geq 0$) is reported in Appendix F of this document. Overall, the change in the range of parameter values reduce the effectiveness of FDI but the optimal test designs improve test performance similarly to the results reported in this section.

Optimal test designs for the detection of actuator faults and manifold leakage in the

Table 5.6: Faults and uncertain parameters, and their normal distributions, ($\mathcal{N}(\mu, \sigma^2)$), with mean, μ, and variance, σ^2.

Set of $\boldsymbol{\xi}$	F^0	F^1	F^2
r_{IM}^{leak} (mm)	0	$\mathcal{N}(6.32, 0.40)$	0
r_{EM}^{leak} (mm)	0	0	$\mathcal{N}(6.32, 0.40)$
$\tilde{u}_{vgt}$	0	0	0
$\tilde{u}_{egr}$	0	0	0
η_{cmp}	$\mathcal{N}(0.736, 1.2e-3)$	$\mathcal{N}(0.736, 1.2e-3)$	$\mathcal{N}(0.736, 1.2e-3)$
η_t	$\mathcal{N}(0.818, 5.8e-4)$	$\mathcal{N}(0.818, 5.8e-4)$	$\mathcal{N}(0.818, 5.8e-4)$

Set of $\boldsymbol{\xi}$	F^3	F^4
r_{IM}^{leak} (mm)	0	0
r_{EM}^{leak} (mm)	0	0
$\tilde{u}_{vgt}$	$\mathcal{N}(0.40, 0.014)$	0
$\tilde{u}_{egr}$	0	$\mathcal{N}(0.40, 0.014)$
η_{cmp}	$\mathcal{N}(0.736, 1.2e-3)$	$\mathcal{N}(0.736, 1.2e-3)$
η_t	$\mathcal{N}(0.818, 5.8e-4)$	$\mathcal{N}(0.818, 5.8e-4)$

diesel engine were calculated based on the optimal criteria of Section 5.2.2. The resulting optimal test designs are listed in Table 5.7, along with the nominal test design reported in Die [154]. Upper and lower bounds for each admissible input are also included in Table 5.6. A safety constraint was implemented during the test design optimization; the pressures of the inlet and exhaust manifold were restricted to a maximum of 2.5 bar and 2.75 bar, respectively. Each design criterion resulted in a unique test design for optimal fault diagnosis. The majority of the proposed test designs kept the relative VGT valve position at roughly 0.50, as that was considered to be the lowest acceptable position that would lead the system states to steady-state. The diesel engine D- and E-Optimal test designs were similar and require high fuel flow to increase separation between the effects caused by faults on the mass fraction of EGR, x_{EGR}. The D_s-optimal test design had consistently low valve positions

for the EGR and VGT, which causes the system outputs to be more sensitive to additive actuator drifts. The PAC-Optimal design had the lowest EGR valve position and engine speed, which make the system more sensitive to the additive EGR actuator drift and the impact of each manifold leak on the turbine speed. The D_s-optimal design also generated the highest engine speed, which significantly increases the changes in manifold pressures and turbine speed caused by all anticipated faults.

Table 5.7: Nominal and optimal FDI test designs for the diesel engine that contains actuator faults in the EGR and VGT, and a leaks in the inlet and exhaust manifolds with the addition compressor and turbine efficiencies ($\tilde{\boldsymbol{\xi}} = [6.32 \text{ mm}, 6.32 \text{ mm}, 0.40, 0.40, 0.736, 0.818]$).

$\boldsymbol{\varphi}$	Lower Bound	Upper Bound	Nom	D-Opt	D_s-Opt	E-Opt	PAC-Opt
$\dot{m}_{fuel}$ (kg/s)	0.0010	0.0189	0.0126	0.0162	0.0048	0.0173	0.0062
u_{EGR} (-)	0.10	1.00	0.82	0.83	0.41	0.63	0.37
u_{VGT} (-)	0.30	1.00	0.55	0.51	0.48	0.54	0.99
ω_{eng} (rpm)	500	2000	1430	1193	1905	982	777

Fault classifiers were trained with data from 2000 Monte Carlo simulations with the diesel engine model at nominal and selected optimal conditions for a diesel engine with no fault, EGR and VDT actuator faults and inlet and exhaust manifold leaks present, c^{0-4}. 10 steady-state samples were collected from each sensor for each Monte Carlo run. PCA transformed this data to extract features for use in the k-NN classification, as described in Section 5.2. FDI performance was assessed with another Monte Carlo simulation with

Table 5.8: Confusion matrices of a diesel engine with fault scenarios listed in Table 6.

(a) Confusion matrices of FDI executed at nominal and D-optimal test designs

		Nominal					D-Optimal				
		Actual					Actual				
		c_0	c_1	c_2	c_3	c_4	c_0	c_1	c_2	c_3	c_4
Predicted	c_0	0.48	0.06	0.05	0.45	0	0.48	0.06	0.05	0.46	0
	c_1	0.06	0.49	0.50	0.04	0	0.04	0.49	0.47	0.04	0
	c_2	0.03	0.42	0.43	0.03	0	0.03	0.42	0.46	0.02	0
	c_3	0.43	0.03	0.02	0.48	0.00	0.45	0.03	0.02	0.48	0
	c_4	0.00	0	0	0	1.00	0	0	0	0	1

(b) Confusion matrices of FDI executed at D_s-optimal and E-optimal test designs

		D_s-Optimal					E-Optimal				
		Actual					Actual				
		c_0	c_1	c_2	c_3	c_4	c_0	c_1	c_2	c_3	c_4
Predicted	c_0	0.77	0.08	0.03	0.16	0	0.48	0.00	0.02	0.49	0
	c_1	0.06	0.49	0.44	0	0	0.00	0.67	0.32	0	0
	c_2	0.02	0.43	0.53	0	0	0.02	0.33	0.65	0.02	0
	c_3	0.15	0.00	0.00	0.84	0	0.50	0.00	0.01	0.49	0
	c_4	0	0	0	0	1	0.00	0	0	0.00	1

(c) Confusion matrices of FDI executed at PAC-optimal test designs

		PAC-Optimal				
		Actual				
		c_0	c_1	c_2	c_3	c_4
Predicted	c_0	0.27	0.20	0.16	0.26	0.13
	c_1	0.19	0.31	0.34	0.18	0.03
	c_2	0.15	0.30	0.34	0.16	0.02
	c_3	0.24	0.15	0.14	0.24	0.12
	c_4	0.15	0.04	0.02	0.16	0.70

(d) Classification accuracy of listed test designs

Test Criterion	A_{CCR}
Nominal	0.58
D-Opt	0.58
D_s-Opt	0.73
E-Opt	0.66
PAC-Opt	0.37

which the PCA/k-NN algorithm was tested in terms of confusion matrices and ROC plots. The corresponding confusion matrices are shown in Table 5.8. Every test design used in this case study resulted in high CCRs for c^4, as the VGT actuator fault in this system is

easy to detect and isolate. However, the remaining faults were difficult to discern and most test designs resulted in less then 0.70 correct classifications. The D-optimal test generated the most correct classifications of exhaust manifold leak, with reduction in the CCR of the EGR valve actuator fault. The estimates of the turbine and compressor efficiencies (i.e. uncertain parameters) lacked confidence in the steady-state model of this case study, therefore the D-optimal and E-optimal test designs were calculated to improve the precision of these parameters in addition to the faults. The drawback of this consideration is the reduction of the EGR actuator drift CCR, which corresponds to c^3. Two test designs gave significant improvement in fault isolation: the D_s-optimal and PAC-optimal tests. Similarly to the previous case study, the D_s-optimal test decreased the variability of the faults while also reducing correlation faults with uncertain parameters. The PAC-optimal test design significantly improved the FDI test as well, but only parameter correlation was considered for optimization, thus fault detection proved to be more difficult than with the D_s-optimal test. This is shown in the overall classification accuracy in Table 5.8c.

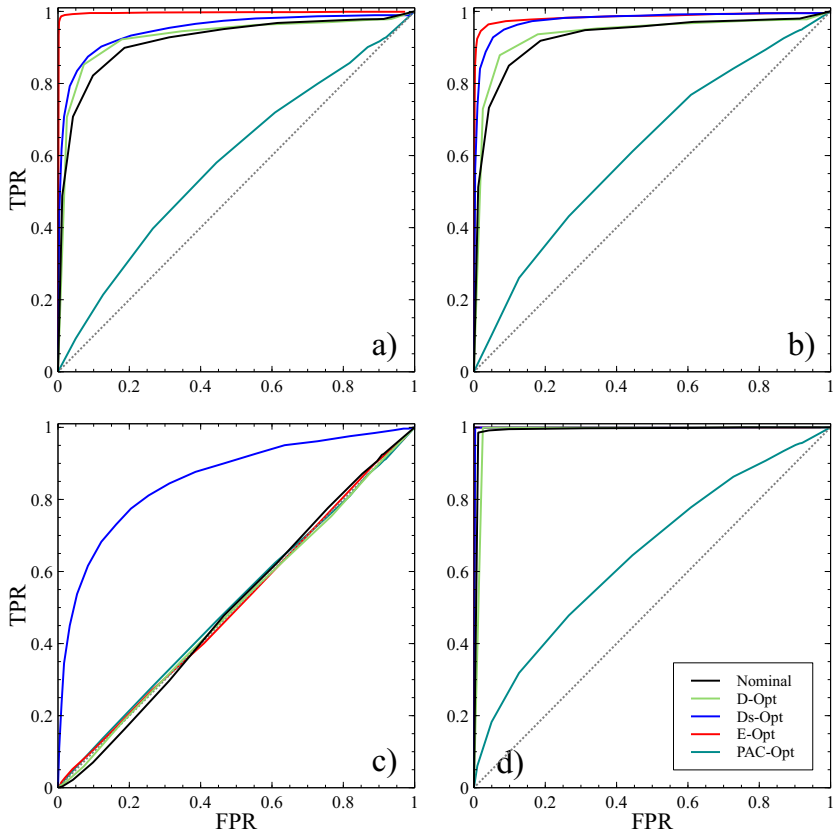

Fig. 5.7: ROC plots of true positive rates versus false positive rates with different optimal criteria. Fault scenarios described in Table 5.6 are presented for a diesel engine with (a) inlet manifold leak, (b) exhaust manifold leak, (c) EGR actuator drift and (d) VGT actuator drift.

Probabilistic k-NN classification was then performed by assigning a decision threshold, representing the minimum allowable probability for a fault to be considered present in the diesel engine. The threshold was assigned a range of 0 to 1, and the relationship between TPR vs. FPR, and CCR vs. FPR are presented in the form of the ROC plots of Fig. 5.7.

Fig. 5.7a presents the ROC plots corresponding to the inlet manifold leak, where the D-optimal and E-optimal generated the steepest curves which indicate a significant likelihood of correct fault detection. The D_s-optimal generates the next best results with acceptable levels of sensitivity at similar selectivity levels. Fig. 5.7b has a similar pattern regarding the exhaust manifold leak, with less sensitivity in the PAC-optimal design to faults than the nominal FDI test. In the EGR actuator fault (Fig. 5.7c) the D_s-optimal test designs generate significantly greater sensitivity than other test designs, with the PAC-optimal test design just under it. The ROC plots generated from the VGT actuator fault (Fig. 5.7d) are consistent with the confusion matrices, in that the detection of faults is very good, with the exception of the PAC-optimal design.

The ROC plots depicting the relationship between the CCR and FPR of each fault scenario in the diesel engine FDI are shown in Fig. 5.8. In the inlet manifold leak scenario, the E-optimal test design generates a significantly higher CCR than the nominal or other optimal test designs. The ROC plots in the exhaust manifold leak and actuator drift scenarios have similar form with the curves in Figs. 5.7b to 5.7d, as shown in Figs. 5.8b to 5.8d. The D- and E-optimal test designs generated the steepest ROC plots in the manifold leak scenarios, making them viable test designs for when the detection and isolation of leaks are the priority for diesel engine FDI. The FDI test with D_s-optimality has a steeper curve in fault scenario 3, and it is almost equal to the true positive curve, meaning that after a fault detection the likelihood of correct fault isolation is very high. The possibility of false alarms

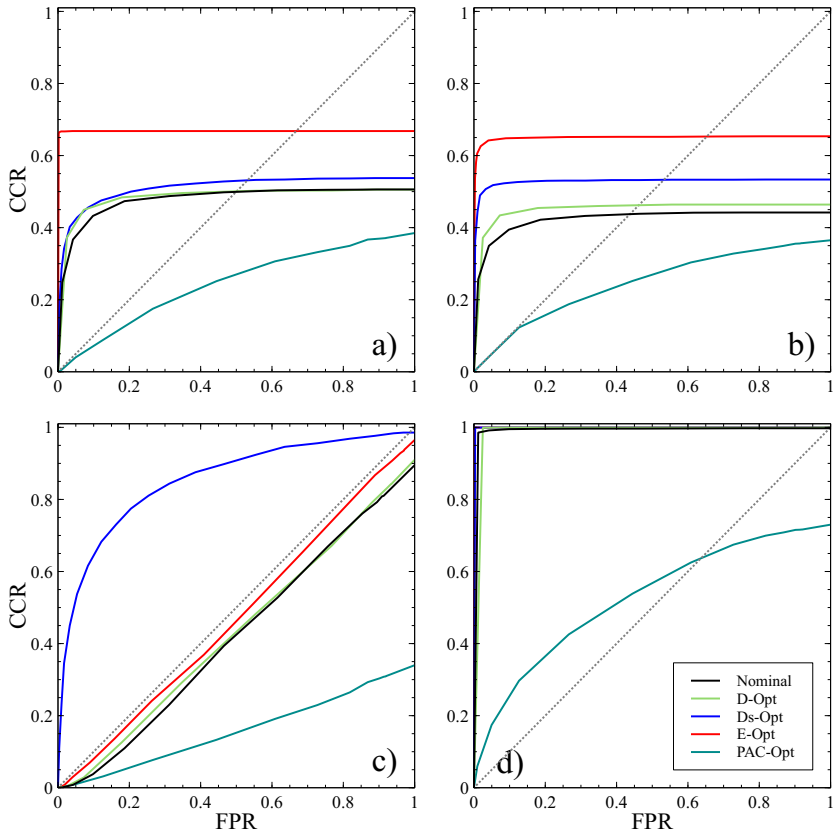

Fig. 5.8: ROC plots of correct classification rates versus false positive rates with different optimal criteria. Fault scenarios described in Table 5.6 are presented for a diesel engine with (a) inlet manifold leak, (b) exhaust manifold leak, (c) EGR actuator drift and (d) VGT actuator drift.

and nondetections in the simulated diesel engine are unavoidable based on selected method and sensors used in fault classification, but through the use of D_s-optimal test designs the probability of misclassification is discernibly lower than with nominal test conditions.

5.4 Conclusion

A complete workflow for active fault detection and isolation was proposed for complex industrial systems. FDI test design was optimized using criteria that relate to the quality and type of information extracted from steady-state or dynamic tests of systems operating under uncertainty. Multiple optimal design criteria were explored in terms of their effectiveness in improving the detectability and isolability of faults. FDI was executed at the calculated test designs by deploying a machine learning algorithm that combines principal components and k-nearest neighbor classification to generate sensitive and robust fault diagnosis triggers. Two case studies, a three-tank system and a diesel engine, were examined using the proposed methodology. Tests that satisfy D_s-optimality criteria were shown to improve the quality of the tests. The PCA/k-NN detection scheme was proven very effective in FDI deployment at extremely small computational footprint. In future work, methods will be implemented to include selection of sensors simultaneously with test design to comprehensively optimize the information extracted in FDI tests.

Chapter 6

Sensor Selection for Active Fault Diagnosis

Abstract

A novel method is presented in this chapter for the simultaneous sensor selection and design of active fault diagnosis tests for complex systems, for which steady state or dynamic models are available. The method assesses all possible sensor combinations for their information with respect to system faults, in the presence of uncertainty and at conditions that maximize information metrics with respect to faults. Sensors are selected for fault detection and isolation (FDI) based on their contribution to information gain. First, normalized Fisher Information in which the sensors participate as binary variables is used to calculate optimal FDI test designs with respect to admissible system inputs. Then, the Kullback-Leibler divergence and the Hellinger distance are used to explore the isolation capability of an FDI test when uncertainty is considered for the system inputs and parameters. FDI tests are deployed using the k-nearest neighbor classification algorithm, which in the case study is used as a verification test for the capability of the method to detect and isolate faults with high correct classification rates and low false alarm rates. The tool-chain proposed is tested

on the benchmark three-tank system, at various levels of measurement noise and uncertainty. The benefits and drawbacks of each step of the proposed method are assessed and discussed along with their computational footprint.

6.1 Introduction

Interest exists in methods that can improve system design to enable health management, and system control algorithms that improve fault detection in the presence of uncertainty. The former can be accomplished by sensor selection during the design or operating stage of a system for the purpose of improving FDI capability, while the latter is the traditional objective of active fault detection methods. However, the simultaneous selection of sensors for optimally designed tests for active FDI is seldom, due to computational complexity and system uncertainty.

The selection of sensors for FDI usually includes metrics or criteria from information theory, which estimate the system error or some relevant information metric of system performance deviation. For instance, the estimation error covariance is minimized in Abdi and Fekri [33] for linear systems while accounting for signal interference. Entropy and mutual information have also been used as objective measures for sensor selection. Najjar et al. [148] used mutual information to maximize relevancy and minimize redundancy for ranking sensors. Tong Zhao and Nehorai [156] developed an energy-efficient method of estimation that selects optimal sensors to reduce communication and processing complexity. Fisher

information functions (such as determinant or trace) have also been used for sensor selection [34, 157]. Because these metrics reflect the confidence in parameter estimates based on system knowledge, they are also suitable for FDI. The optimal selection of sensors for the purpose of fault diagnosis is often intended for use in passive FDI, though methods of active fault diagnosis exist that can improve fault diagnosability. Often, the selection of sensors has to take into account system performance information, which is dependent on the inputs of the system. In passive FDI, this can be resolved using Bayesian inference with prior information of inputs [158]. However, in systems where test settings are configurable and can be actively set to improve FDI, the optimal selection of test settings and sensors can be implemented in unison in the form of active FDI.

In this dissertation, the criterion for selecting external input trajectories for active fault diagnosis must be computationally feasible while taking into consideration the effects of faults and uncertainty on system performance. Thus, it may be more suitable to calculate an optimal set of input trajectories off-line, by treating the FDI test design as a constrained optimization problem, while taking into consideration predetermined safety or performance constraints [5, 159]. We presented a method in Chapter 5 for the calculation of robust off-line test designs for active FDI, using subset D-optimal, or D_s-optimal designs [151, 160]. Faults were considered as parameters of interest, and by solving for D_s-optimality of the Fisher Information Matrix of the output with respect to parameters expressing faults and uncertainty, the joint confidence region between the faults and system uncertainty was

minimized [147]. Here, we consider D_s optimal test designs to improve fault diagnosis by selecting from available test conditions and sensor sets.

Research involving the simultaneous selection of sensors and test design is limited and most sensor selection problems in the literature are restricted to a fixed number of sensors considered for the optimal subset [161]. Patan and Ucinski [35] discretely optimized sensor locations simultaneously with experimental settings for the purpose of parameter identification. In their work, each feasible test setting was represented as a binary variable that was adjusted for test optimization. Building upon their work, this document describes a method where the input trajectories are modeled as a discrete number of steps of bounded continuous variables. Sensed information is described as a boolean decision vector of all the available (or possible) system sensors. The FDI test design problem then becomes a constrained, mixed-integer non-linear optimization problem that maximizes information metrics of the system with respect to faults by manipulating input trajectories and sensors choices. We present a formulation for the nonlinear optimization problem of simultaneous FDI input and sensor selection. Two approaches are introduced to select the number and type of sensors that generate the most informative FDI test, where preference of approach is based on the availability of prior information or on restrictions corresponding to computational footprint.

This paper is organized as follows. The proposed FDI methodology is presented in Section 6.2 for calculating and assessing the optimized FDI test designs with faults and

system uncertainty. Section 6.2 begins with the formulation of the system model as a set of differential algebraic equations (DAEs). It continues with the mathematical formulation of the test design optimization problem for FDI in uncertain systems. The section concludes with two approaches to sensor selection for active FDI set with an adjustable number of sensors. The first approach calculates the optimal FDI test based on normalized Fisher information obtained from model outputs. The second approach is an evaluation of the proposed test designs generated from each sensor set based on Kullback-Leibler divergence and Hellinger distance. In Section 6.4, we demonstrate the effectiveness of each approach with a case study performed on a simulated three-tank system, based on benchmark models reported in [7, 162]. The three-tank system is considered to be prone to multiple tank leaks. Other components are subject to changes that are not caused by faults, representing the system uncertainty. The faults are assumed to be incipient and deterministic, meaning that they are invariant for the duration of the FDI test design which is valid for a small timespan. The system at nominal and optimal conditions are compared with results obtained using PCA and k-NN techniques [20, 163], to determine the improvements generated as a result of the proposed FDI methodology. The selection criterion outputs are determined for the proposed sensor sets, and their effectiveness is compared with the classification accuracy for all fault scenarios. The main results and takeaways of this approach are briefly summarized in the Section 6.5.

6.2 Methods

In the proposed methodology, an optimal test design is calculated to maximize accuracy and robustness for FDI through the manipulation of controllable input trajectories and selection of sensors, and then evaluated for the fault diagnosis success rate. In the first step of the workflow, a model is produced that accurately represents the system or subsystem of interest. System uncertainty that corresponds to inputs, sensed outputs, and boundary conditions is assigned as ranges of distributions that are known *a priori*, and are considered during the test design optimization for active fault diagnosis. The ranges of parameter values corresponding to each fault scenario is considered in the design of the FDI test. The design is optimized using one of two methods proposed in this document to achieve D_s-optimality with sensor selection. The first part of the approach is a single-step optimization problem, where the number and type of sensors and input conditions are solved simultaneously. The second part has two steps. In the first step, the D_s-optimal design corresponding to each assigned number of sensors is solved. In the second step, the sensor set chosen to result in the greatest divergence between different fault scenarios along with the active test design are used to train and test classifiers for FDI execution. The rate of correct classifications are generated from Monte Carlo simulations at the calculated optimal test conditions with respect to each anticipated fault scenario using k-NN classification combined with PCA. More details about the method of fault classification are provided in the previous chapter.

6.2.1 Preliminaries: Active FDI test design and sensor selection optimization

The system model is formulated as shown in Section 3.2. The measurable output vector, $\hat{\mathbf{y}}$, is updated in this chapter as follows. Each variable that is considered as a candidate for observation, i.e. that corresponds to a sensor position and type available in the system, is listed as an output. $\hat{\mathbf{y}}$ is considered to have N_y variables. In the optimization problem, a subset of sensors is chosen from among the potential N_y sensors. This results in a combinatorial problem with respect to sensor selection, where the N_y sensors are split into n_y selected sensors for active fault diagnosis, and $N_y - n_y$ dormant sensors ($n_y \in 1, \ldots, N_y$). These decisions are formulated mathematically by introducing a binary vector, $\mathbf{a}$. Each element in $\mathbf{a}$ activates or deactivates specific measured variable in $\mathbf{y}$; it assigns a value of 0 for when a sensor is dormant, or 1 for when it is active.

The sensitivities of the system outputs with respect to faults and uncertainties are used to calculate the FIM, $\mathbf{H}_\xi$. The information that is available from the system is dependent on the sensors chosen for FDI. In other words, if a sensor is not present then the corresponding output does not generate any information relevant to $\mathbf{H}_\xi$. The expression for calculating $\mathbf{H}_\xi$ takes into account sensor selection by incorporating the sensor binary vector, $\mathbf{a} = [a_1, \ldots, a_{N_y}]$, as is shown in (6.1):

$$\mathbf{H}_\xi(\tilde{\boldsymbol{\xi}}, \boldsymbol{\varphi}) = \sum_{i=1}^{N_y} \sum_{j=1}^{N_y} a_i a_j \sigma_{ij}^{-2} \mathbf{Q}_i{}^T \mathbf{Q}_j, \tag{6.1}$$

where $\mathbf{Q}_i$ is the sensitivity matrix of the i-th output, that contains the sensitivities with respect to the uncertain parameter vector $\boldsymbol{\xi}$ in the neighborhood of $\tilde{\boldsymbol{\xi}}$, for all sampling times.

Each element of $\mathbf{a}$ corresponds to the i-th and j-th outputs, accounting for the sensors included in the FDI test.

The test design vector, $\boldsymbol{\varphi}$, consists solely of the controllable inputs and sensor sets available within the sensor and test design space, $\boldsymbol{\Phi}$, that is considered for fault diagnosis. The designs considered in the following case studies have only one set of inputs, therefore the design vector $\boldsymbol{\varphi}$ has the dimensions $1 \times N_u + N_y$, where N_u is the number of controllable inputs. In FDI tests with multiple steps implemented into the design, the dimensions of $\boldsymbol{\varphi}$ would be $1 \times N_y + N_u * N_{step}$, where N_{step} is the number of discrete steps, and the $\mathbf{u}_p$ is concatenated to a vector. The design vector is expressed as

$$\boldsymbol{\varphi} = [\mathbf{u}_p, \mathbf{a}] \in \boldsymbol{\Phi}. \tag{6.2}$$

The objective is then to solve the mixed-integer non-linear problem and determine a test design $\boldsymbol{\varphi}^*$, that satisfies the selected criteria. The formulation of the problem is dependent on whether dynamic or steady-state information is used. The function used to solve for D_s-optimality, Ψ_{Ds}, is calculated for steady-state FDI as shown in (5.8) in the previous chapter. The conventional approach to sensor selection is to assign a predetermined desired number of sensors, n_y as a constraint to the test design optimization. The problem of the steady-state

D_s-optimal test design is then formulated as expressed in (6.3):

$$\begin{aligned}
&\boldsymbol{\varphi}^* \in \arg \max_{\boldsymbol{\varphi}\in\Phi} \Psi_{Ds}\left(\mathbf{H}_\xi(\tilde{\boldsymbol{\xi}}, \boldsymbol{\varphi})\right) \\
&\text{s.t.} \\
&\mathbf{f}(\mathbf{x}, \mathbf{u}_p, \boldsymbol{\theta}_p, \tilde{\boldsymbol{\xi}}) = \mathbf{0}, \\
&\hat{\mathbf{y}} = \mathbf{h}(\mathbf{x}, \mathbf{u}_p, \boldsymbol{\theta}_p, \tilde{\boldsymbol{\xi}}), \\
&{\mathbf{u}_p}^L \leq \mathbf{u}_p \leq {\mathbf{u}_p}^U, \quad \mathbf{x}^L \leq \mathbf{x} \leq \mathbf{x}^U. \\
&\mathbf{1}^T\mathbf{a} = n_y, \quad a_i \in \{0, 1\}, \quad \forall i = 1, \ldots, N_y.
\end{aligned} \tag{6.3}$$

The solution obtained from (6.3) is the D_s-optimal test design that contains the input trajectories and n_y sensors the maximizes the overall sensitivity of outputs with respect to faults, while minimizes the joint confidence between faults and uncertain parameters, and neglects information with respect to uncertain parameters as shown in (5.4) in the previous chapter.

6.2.2 Test design and sensor selection optimization in the presence of sensor noise and system uncertainty

Sensor selection using normalized Fisher Information

In the first approach to optimal test design, the objective is to maximize the normalized quality of information for all sensors, assuming that all considered sensors have randomly distributed measurement noise that is uncorrelated. The Fisher information matrix is additive, i.e. adding additional sensors will increase or have no effect on the total amount of information [164]. If (6.3) is performed for a steady-state test, and instead of imposing

the first constraint, $\mathbf{1}^T\mathbf{a} = n_y$, where n_y is fixed, the constraint is updated to consider all possible values of n_y. The constraint would be updated to $\mathbf{1}^T\mathbf{a} \in 1, \ldots, N_y$. Because $\mathbf{H}_\xi$ is monotonic with respect to sample size, the constraint will be set to N_y, even though the FDI rate of success may be suboptimal.

Spall [165] states that in the case where samples are independent, the magnitude of the FIM will grow in proportion to the number of samples. Studies have been performed assessing the relationship between the FIM and sample size, particularly for test design efficiency [166, 167]. In this work, the relationship between the FIM and the number of outputs was verified as follows. Suppose an FDI test is performed on a system with n samples collected, $\mathbf{y} = [y_1, y_2, \ldots, y_n]$. Assume the partial derivatives of $\mathbf{y}$ with respect to any parameter in $\boldsymbol{\xi}$ are equal ($\frac{\partial y_i}{\partial \xi_k} = \frac{\partial y_j}{\partial \xi_k} \forall i, j$). This is equivalent to assuming that n identical sensors are used. The sensitivity matrices of generated with available sensor information is formulated as a function of these partial derivatives, using (3.1h) are shown below:

$$\mathbf{Q}_1 = \begin{bmatrix} \frac{\partial y_1}{\partial \xi_1}\Big|_{\tilde{\boldsymbol{\xi}}} & \frac{\partial y_1}{\partial \xi_2}\Big|_{\tilde{\boldsymbol{\xi}}} \end{bmatrix}, \quad \mathbf{Q}_2 = \ldots, \quad \mathbf{Q}_n = \begin{bmatrix} \frac{\partial y_n}{\partial \xi_1}\Big|_{\tilde{\boldsymbol{\xi}}} & \frac{\partial y_n}{\partial \xi_2}\Big|_{\tilde{\boldsymbol{\xi}}} \end{bmatrix}, \quad \Sigma = \text{diag}(\sigma_1^2, \sigma_2^2, \ldots, \sigma_n^2).$$

Because the samples obtained were independent, and sensors are assumed to be identical, the Fisher Information Matrix is $\mathbf{H}_\xi = n\sigma_i^{-2}\mathbf{Q}_i^T\mathbf{Q}_i \forall i$. The linear relationship between the FIM and number of selected sensors is valid for any finite number of outputs. (6.3) is, thus, updated to replace the standard FIM with the normalized FIM in order to weigh the benefit of additional test information with the addition of sensing capability. The normalized FIM is equal to the average Fisher information over all selected sensors, $\bar{\mathbf{H}}_\xi$, and is calculated as

shown below:

$$\bar{\mathbf{H}}_{\xi}(\tilde{\boldsymbol{\xi}}, \boldsymbol{\varphi}) = \left(\mathbf{1}^T\mathbf{a}\right)^{-1} \sum_{i=1}^{N_y} \sum_{j=1}^{N_y} a_i a_j \sigma_{ij}^{-2} \mathbf{Q}_i{}^T \mathbf{Q}_j, \quad \left(\mathbf{1}^T\mathbf{a}\right) \in 1, \ldots, N_y. \tag{6.4}$$

The D_s criterion is then updated to be a function of the average FIM, calculated in (6.5):

$$\max_{\boldsymbol{\varphi}\in\boldsymbol{\Phi}} \Psi_{Ds}\left(\bar{\mathbf{H}}_{\xi}\right) = \max_{\boldsymbol{\varphi}\in\boldsymbol{\Phi}} \left| \left(\mathbf{1}^T\mathbf{a}\right)^{-1} \left(H_{ff} - H_{fu}{H_{uu}}^{-1} H_{fu}^T\right) \right|, \tag{6.5}$$

Equation (6.3) can be updated with (6.5) and the relaxation in the constraint for the number of sensors in the system gives:

$$\begin{aligned}
\boldsymbol{\varphi}^* &= \left[\mathbf{u}_p^*, \mathbf{a}^*\right] \\
&\in \arg \max_{\boldsymbol{\varphi}\in\boldsymbol{\Phi}} \Psi_{Ds}\left(\bar{\mathbf{H}}_{\xi}\left(\tilde{\boldsymbol{\xi}}, \boldsymbol{\varphi}\right)\right) \\
&\quad \text{s.t.} \\
&\quad \mathbf{f}(\mathbf{x}, \mathbf{u}_p, \boldsymbol{\theta}_p, \tilde{\boldsymbol{\xi}}) = \mathbf{0}, \\
&\quad \hat{\mathbf{y}} = \mathbf{h}(\mathbf{x}, \mathbf{u}_p, \boldsymbol{\theta}_p, \tilde{\boldsymbol{\xi}}), \\
&\quad \mathbf{u}_p^L \le \mathbf{u}_p \le \mathbf{u}_p^U, \quad \mathbf{x}^L \le \mathbf{x} \le \mathbf{x}^U, \\
&\quad \mathbf{1}^T\mathbf{a} \in 1, \ldots, N_y, \quad a_i \in \{0, 1\}, \quad \forall i = 1, \ldots, N_y.
\end{aligned} \tag{6.6}$$

By solving for $\Psi_{Ds}\left(\bar{\mathbf{H}}_{\xi}\right)$, an optimal test design is calculated that maximizes the sensitivity of outputs with respect to faults, minimizes the joint confidence between faults and uncertainty and rejects sensors that do not provide new information to the active FDI test.

Sensor selection using fault isolation assessment using divergence

The test design and set of sensors as selected though the method of Section 6.2.2, is optimal for FDI in the neighborhood of $\tilde{\boldsymbol{\xi}}$. The correlation of faults with uncertainty at $\tilde{\boldsymbol{\xi}}$ is minimized per (6.5), but the entire pace of uncertainty is not search for its impact on FDI. Such designs are sufficient when the relationship between outputs $\mathbf{y}$ and parameters $\boldsymbol{\xi}$ is not highly nonlinear and when the range of values in $\boldsymbol{\xi}$ is small. When these conditions are not true, it is feasible to have systems outputs that are affected by uncertainty with different levels of magnitude. A visual illustration of the effect on outputs caused by varying degrees of uncertainty is shown in Fig. 6.1. Histograms of the second output shown in the right-hand side plots (b,d) are virtually unaffected by the increase of system uncertainty, while the range of the first output (plots a and c) have increased significantly, resulting in greater overlap between fault and fault-free scenarios. As shown in Fig. 6.1, uncertainty may impact the sensor information in a way that does not change their mean anticipated values and does not depend on the mean anticipated values, $\bar{\boldsymbol{\xi}}$. It is possible however for one sensor to be more sensitive to uncertainty than another. In this case, system uncertainty and its impact on sensed information may be the dedicating factor for sensor selection. Should prior information be available during the selection of the FDI test design, the method for selecting the optimal FDI test can be updated to include such information, to avoid sensors strongly affected by system uncertainty or to include additional sensors to mitigate the impact of uncertainty.

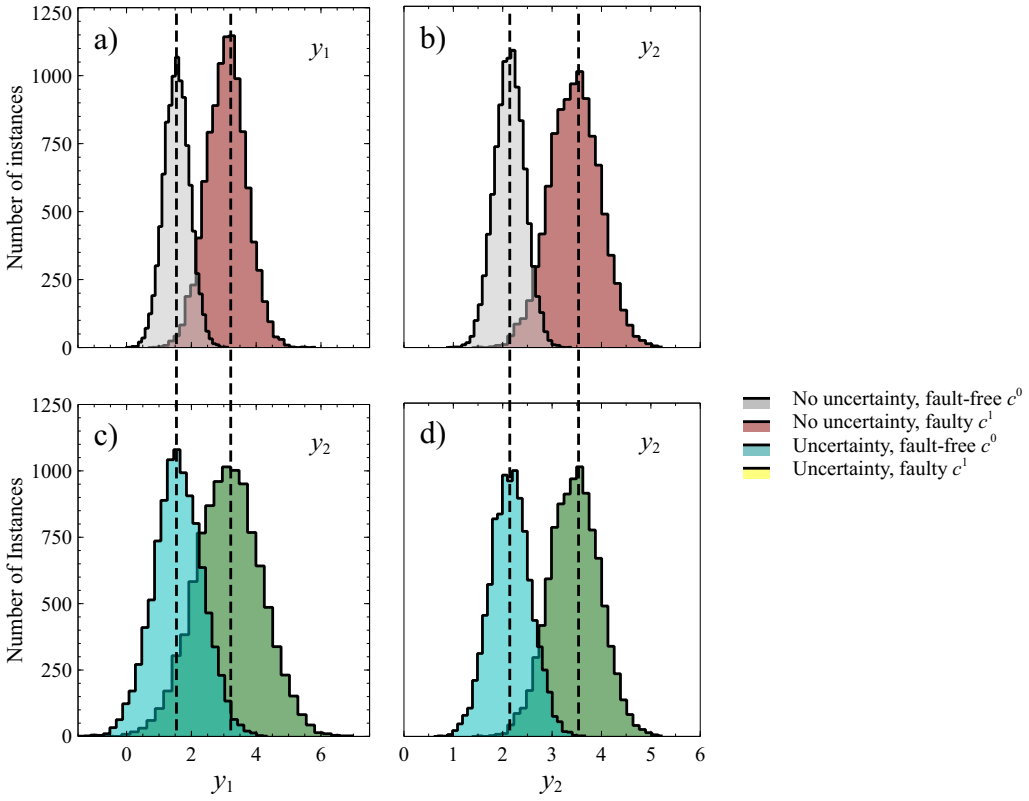

Fig. 6.1: Example histograms of outputs y_1 (a-b) and y_2 (c-d) affected by system uncertainty. The upper and lower plots show the range of outputs with probability densities that are dependent on uncertainty.

Optimal experimental designs have been implemented using Bayesian inference such as in [168, 169]. The drawback of Bayesian designs is the computational load necessary to solve these problems. The approach followed in this paper continues to use frequentist-based optimization for test designs, but it includes the entirety of the *a posteriori* evaluation of the impact of uncertainty, using Monte Carlo simulation data that takes into account

uncertain parameter distributions. The proposed method draws from prior information to solve for an optimal FDI sensor design without relying on Bayesian optimal design, thereby reducing computational footprint. The first step is to perform the test design optimization based on (6.3) for a fixed number of sensors chosen from the entire sensor set. The resulting optimal test design vector is denoted as $\boldsymbol{\varphi}^*_{n_y}$, for n_y predetermined number of sensors. $\boldsymbol{\varphi}^*_{n_y}$ is calculated for all possible integers, $n_y \in 1, \ldots, N_y$, as shown in (6.7):

$$
\begin{aligned}
\boldsymbol{\varphi}^*_{n_y} &= \left[\mathbf{u}^*_p, \mathbf{a}^*\right], \quad n_y \in 1, \ldots, N_y \\
&\in \arg \max_{\boldsymbol{\varphi} \in \boldsymbol{\Phi}} \; \Psi_{Ds}\left(\mathbf{H}_\xi\left(\tilde{\boldsymbol{\xi}}, \boldsymbol{\varphi}\right)\right) \\
&\quad \text{s.t.} \\
&\quad \mathbf{f}(\mathbf{x}, \mathbf{u}_p, \boldsymbol{\theta}_p, \tilde{\boldsymbol{\xi}}) = \mathbf{0}, \\
&\quad \hat{\mathbf{y}} = \mathbf{h}(\mathbf{x}, \mathbf{u}_p, \boldsymbol{\theta}_p, \tilde{\boldsymbol{\xi}}), \\
&\quad \mathbf{u}^L_p \leq \mathbf{u}_p \leq \mathbf{u}^U_p, \quad \mathbf{x}^L \leq \mathbf{x} \leq \mathbf{x}^U, \\
&\quad \mathbf{1}^T \mathbf{a} = n_y, \quad a_i \in \{0, 1\}, \quad \forall i = 1, \ldots, N_y.
\end{aligned}
\tag{6.7}
$$

After $\boldsymbol{\varphi}^*_1, \boldsymbol{\varphi}^*_2, \ldots, \boldsymbol{\varphi}^*_{N_y}$ have been determined, the next step is to generate Monte Carlo simulation data corresponding to each design for all fault scenarios. During this phase, Monte Carlo simulations are performed with random values assigned to uncertain parameters and measurement noise within their predefined range and distribution. This virtual system data is used to evaluate the output responses for all fault scenarios. The data corresponds to each fault scenario as a distribution, and the distance between the distributions of each scenario are compared for the optimal test design. In an ideal situation, the test design

results in no overlap between any of the anticipated fault scenarios. Usually, the objective is to choose sensors that minimize the overlap of these output ranges as much as possible. Synonymous to minimizing the overlap of output distributions is maximizing the divergence between each distribution. Two ways to calculate discrepancies between distributions were used, Kullback-Leibler divergence and Hellinger distance, which are closely related to Fisher information.

The Kullback-Leibler divergence (KLD), or relative entropy, is a well-known method to measuring the divergence between two sets of probability density functions (PDFs) [170]. KLD has been implemented in fault detection and diagnosis [139, 171], as well as sensor placement and selection [172]. It is considered by Bernardo and Smith [173] to be a natural metric in statistics as it stems from maximum likelihood estimation, thus it is a suitable measure for use in test design optimization. The KLD of two continuous PDFs that represent classes c^i and c^j is presented in (6.8), where p is the continuous probability density of the the output vector $\mathbf{y}$ generated from a particular class:

$$D_{KL}^{i,j}(\boldsymbol{\varphi}) = \int p\left(\mathbf{y}|c^i, \boldsymbol{\varphi}\right) \log\left(\frac{p\left(\mathbf{y}|c^i, \boldsymbol{\varphi}\right)}{p\left(\mathbf{y}|c^j, \boldsymbol{\varphi}\right)}\right) d\mathbf{y}. \tag{6.8}$$

The KLD ranges from 0 to ∞, where 0 only occurs when $i = j$. The KLD is not considered to be a formal measure of distance, as it is not symmetric and does not satisfy triangle inequality. Another widely-used metric for measuring distance is the Hellinger distance (HD) [174]. Hellinger distance has been implemented to monitor performance degradation [175], and it is a popular criterion for decision tree splitting [176]. The normalized HD

between two continuous PDFs is defined in (6.9):

$$D_H^{i,j}(\boldsymbol{\varphi}) = \sqrt{\frac{1}{2}\int \left(\sqrt{p(\mathbf{y}|c^i,\boldsymbol{\varphi})} - \sqrt{p(\mathbf{y}|c^j,\boldsymbol{\varphi})}\right)^2 d\mathbf{y}}. \tag{6.9}$$

The HD is more firmly bounded than the KLD in that the only possible values after normalization are between 0 and 1 (without normalization the range is 0 to $\sqrt{2}$), where 0 occurs when the two PDFs are identical and 1 occurs when there is complete separation between the PDFs, the ideal situation when comparing datasets between different fault scenarios.

The KLD and HD measures are calculated in this work with discrete distributions. Monte Carlo simulations are performed for fault scenario i, denoted as c^i for $i = 0, \ldots, N_f$, where N_f is the number of examined faults. At $i = 0$, the system is considered to be free of faults. Approximations to the true PDFs can be made using samples from the Monte Carlo simulations. Histograms are formulated for all fault scenarios to represent fault scenario probabilities via discrete distributions, $P := \left\{P\left(\mathbf{y}^k|c,\boldsymbol{\varphi}\right)\right\}_{k=1,\ldots,N_{part}}$ for any class c and each optimal design $\boldsymbol{\varphi}$, where N_{part} is the number of partitions made in the output space. To ensure that the approximation is valid, (6.10) must hold true for all optimal (N_y) designs, $\boldsymbol{\varphi}^*$:

$$\sum_{k=1}^{N_{part}} P\left(\mathbf{y}^k|c^i,\boldsymbol{\varphi}\right) = 1, \quad i = 0, \ldots, N_f. \tag{6.10}$$

The Kullback-Leibler divergence $D_{KL}^{i,j}$ can be approximated then for all classes i and j calculated according to (6.11):

$$D_{KL}^{i,j}(\boldsymbol{\varphi}) \approx \sum_{k=1}^{N_{part}} P\left(\mathbf{y}^k|c^i,\boldsymbol{\varphi}\right) \log\left(\frac{P\left(\mathbf{y}^k|c^i,\boldsymbol{\varphi}\right)}{P\left(\mathbf{y}^k|c^j,\boldsymbol{\varphi}\right)}\right). \tag{6.11}$$

while the Hellinger distance $D_H^{i,j}$ is calculated as shown in (6.12):

$$D_H^{i,j}(\boldsymbol{\varphi}) \approx \frac{1}{\sqrt{2}} \sqrt{\sum_{k=1}^{N_{part}} \left(\sqrt{P(\mathbf{y}|c^i, \boldsymbol{\varphi})} - \sqrt{P(\mathbf{y}|c^j, \boldsymbol{\varphi})} \right)^2}. \tag{6.12}$$

The optimal test design for active fault diagnosis is considered to have the maximum divergence between all fault and fault-free scenarios. Therefore, the optimal test design $\boldsymbol{\varphi}^*$, is calculated using (6.13):

$$\boldsymbol{\varphi}^* \in \arg \min_{n_y \in 1,\ldots,N_y} \frac{1}{N_f(N_f+1)} \sum_{i=0}^{N_f} \sum_{j=0}^{N_f} D^{i,j} \left(\boldsymbol{\varphi}_{n_y}^* \right), \tag{6.13}$$

where $D \in \{D_{KL}, D_H\}$. Calculating the test design in this approach, though more computationally demanding, provides a more accurate evaluation of optimal sensor sets for reliable fault diagnosis, as shown in the Results.

6.3 Case study description

FDI test designs were calculated for an open-loop, three-tank system. The three-tank system is a commonly used benchmark for testing FDI and control algorithms [7], and is composed of three cylindrical tanks with identical cross-sectional areas, A. The states and potential outputs of the system are the liquid levels in tank 1, 2 and 3, represented as h_1, h_2, and h_3. The flow from tank i to tank j ($j = 0$ when the stream flows into the fluid sink) is represented by the volumetric flow rate, q_{ij}. The admissible inputs of the three-tank system are the volumetric flow rates assigned to pumps 1 and 2, represented as u_1 and u_2, respectively. The pipes connecting each tank have equal cross-sectional areas, S_p. Each pipe

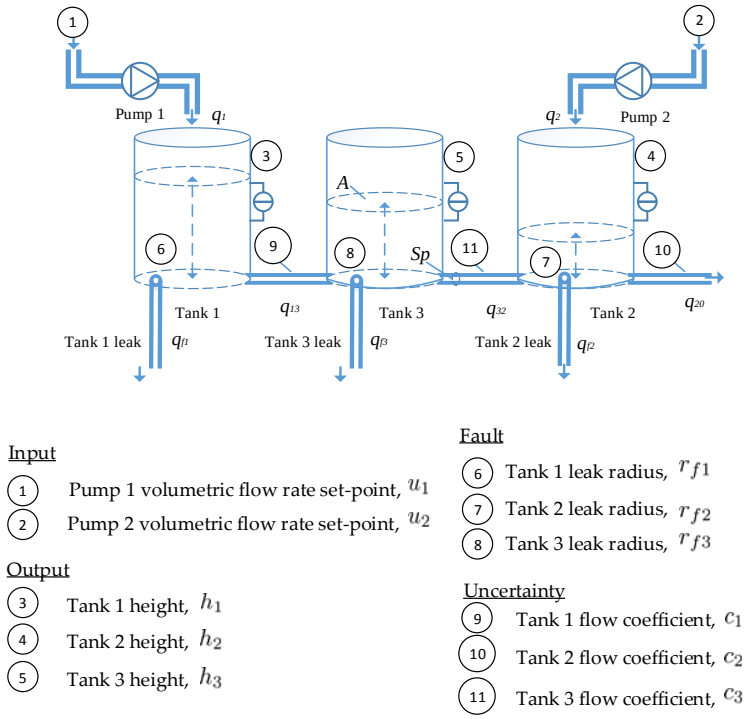

Fig. 6.2: Input-Output architecture of the Three-Tank System, subject to multiple tank leaks and uncertain flow coefficients.

has a flow coefficient that affects the tank exiting flow rate, c_1, c_2, and c_3. These variables are included in the faults and uncertain parameters vector, $\boldsymbol{\xi}$, and are targets in the test design optimization. Fig. 6.2 shows the design architecture of the benchmark system.

Three fault scenarios were considered in this case study. Each anticipated fault was a leak that occurs in one of the tanks, characterized by the leak radii r_{f1}, r_{f2} and r_{f3} for tanks 1, 2 and 3, respectively. When a leak is not present in the i-th tank in the three-tank system, $r_{fi} = 0$. Table 5.2 lists faults and uncertain parameters considered in the case study

along with their corresponding Gaussian distributions. The lower and upper bounds of each fault and uncertain parameter was assumed known at ± 3 times the standard deviation of the distributions. The range of every variable in $\boldsymbol{\xi}$ is listed for each fault scenario, c^j, where the system at $j = 0$ is the fault-free scenario, and $j = 1, 2, 3$ contains a leak in the j-th tank.

Table 6.1: Faults and uncertain parameters studied in the three-tank system case study, and their normally distributed $\mathcal{N}(\mu, \sigma^2)$ random parameter values with mean, μ, and variance, σ^2.

Set of $\boldsymbol{\xi}$	c^0	c^1	c^2	c^3
r_{f1} (mm)	0	$\mathcal{N}(2.0, 0.25)$	0	0
r_{f2} (mm)	0	0	$\mathcal{N}(2.0, 0.25)$	0
r_{f3} (mm)	0	0	0	$\mathcal{N}(2.0, 0.25)$
c_1	$\mathcal{N}(0.95, 0.0025)$	$\mathcal{N}(0.95, 0.0025)$	$\mathcal{N}(0.95, 0.0025)$	$\mathcal{N}(0.95, 0.0025)$
c_2	$\mathcal{N}(0.8, 0.0025)$	$\mathcal{N}(0.8, 0.0025)$	$\mathcal{N}(0.8, 0.0025)$	$\mathcal{N}(0.8, 0.0025)$
c_3	$\mathcal{N}(0.95, 0.0025)$	$\mathcal{N}(0.95, 0.0025)$	$\mathcal{N}(0.95, 0.0025)$	$\mathcal{N}(0.95, 0.0025)$

The three-tank system model utilizes well-known mass balance equations and Torri-

celli's law to describe the overall system dynamics, as shown in (6.14):

$$
\begin{aligned}
A\frac{\partial h_1}{\partial t} &= \alpha u_1 - c_1 S_p \text{sign}(h_1 - h_3)\sqrt{2g|h_1 - h_3|} - c_1 \pi r_{f1}^2 \sqrt{2gh_1}, \\
A\frac{\partial h_2}{\partial t} &= u_2 + c_3 S_p \text{sign}(h_3 - h_2)\sqrt{2g|h_3 - h_2|} - c_2 S_p \sqrt{2gh_2} - c_2 \pi r_{f2}^2 \sqrt{2gh_2}, \\
A\frac{\partial h_3}{\partial t} &= c_1 S_p \text{sign}(h_3 - h_2)\sqrt{2g|h_1 - h_2|} - c_3 S_p \text{sign}(h_3 - h_2)\sqrt{2g|h_3 - h_2|} - c_3 \pi r_{f3}^2 \sqrt{2gh_3}.
\end{aligned}
\tag{6.14}
$$

Constraints were assigned to the three-tank system, in that the tank heights must be within 0 m $< h_i \leq$ 0.50 m for i=1,2,3 for any fault scenario at anticipated flow coefficients. The range of controllable inputs is $0 \leq u_j \leq 10^{-4}$ m^3/s, j=1,2, respectively. The output sensitivities as shown in (3.1h) were calculated in this case study using forward sensitivity analysis. The anticipated fault and uncertainties, $\tilde{\boldsymbol{\xi}} = [2.0\text{mm}, 2.0\text{mm}, 2.0\text{mm}, 0.95, 0.8, 0.95]'$, were injected into the three-tank system. A virtual system was generated that is identical to the system model shown in (6.14), with injected measurement noise and random distributions of uncertainty. The degree of measurement noise and uncertainty in the level sensors was varied in the case study to determine the impact on the proposed optimization approaches. Three scenarios were studied: In the next section, each sensor selection technique is implemented to determine the impact of increasing measurement variance and uncertainty. In Case 1, the three-tank system has three equally precise sensors that can be used in fault diagnosis. In Case 2, the measurement variance in one of the sensors is increased to determine the impact on sensor selection for active fault diagnosis. In Case 3 system uncertainty has a significant effect on sensors, thus depreciating their overall quality of information for detection

Case 1: All three sensors contain normally distributed measurement noise with standard deviation of 0.01 m.

Case 2: Similar to Case 1, except the sensor of Tank 2 level has noise with standard deviation of 0.06 m.

Case 3: The range of uncertainty in the flow coefficients deviates from the values presented in Table 5.2 and the sensors of Tank 2 and 3 levels have noise with standard deviation of 0.06 m.

and isolation of faults. When significant system uncertainty is present (not in the form of measurement noise), the two test design methods can reach different conclusions based on their ability to utilize prior information.

The mixed-integer optimization problems as presented in (6.3-6.7) in this case study were conducted using KNITRO 11.0.1 [177] in MATLAB R2017b [70]. KNITRO's standard branch and bound algorithm was selected for its capacity to solve non-convex, mixed-integer problems, combined with an Interior/Direct solving algorithm for the relaxed subproblems. In the branch and bound method, feasible regions of the mixed-integer problem are partitioned for easier solving (the "branching" aspect). In each iteration, a lower bound is selected based on the current optimal solution of any given branch. This solution is achieved by solving the optimization problem of that particular branch [34]. The integer variables are relaxed into continuous variables, thereby relaxing the MINLP problem. Pseudo-cost

branching was implemented to keep track of and weigh changes in the integer variables. Specifically for the case studies shown, multi-start optimization was implemented along with parallel computing to ensure that the solution is sufficiently close to being globally optimal.

6.4 Results and discussion

The virtual three-tank system detailed in Section 6.3 was used to assess the proposed test design methods of Section 6.2.2. The objective was to find optimal steady-state conditions and combination of sensors that result in the most informative test that is relevant to fault diagnosis. Three cases were evaluated, each containing different levels of measurement noise and uncertainty to evaluate the success of the proposed methods for optimal FDI test design.

In Case 1, the uncertain parameters were assigned the random distributions of Table 5.2 and all sensors had measurement noise with Gaussian distributions ($\sigma_{1-3} = 0.01$ m). The D_s-optimal output of the normalized FIM using the (6.6) is shown in Fig. 6.3, enumerated over the allowable range of input values, u_1 and u_2, for various sensor sets considered for FDI. The left-hand side plot indicates that D_s-optimality is achieved at $\mathbf{u}_p = [0.78,\ 0.06] \times 10^{-4}$ m^3/s, while the center and right-hand side plots show that the highest outputs of $\ln \bar{\Psi}_{Ds}$ are found at $\mathbf{u}_p = [0.80,\ 0.01] \times 10^{-4}$ m^3/s. At $\mathbf{y} = h_1$, the greatest sensitivity to faults and separation in distributions between fault scenario occurs when the flow from pump 1 is maximized. Adding sensor data from h_3 and h_2 resulted in optimal test design to change. Regardless of sensor set, the optimal inputs occur when pumps 1 and 2 are close to or at the

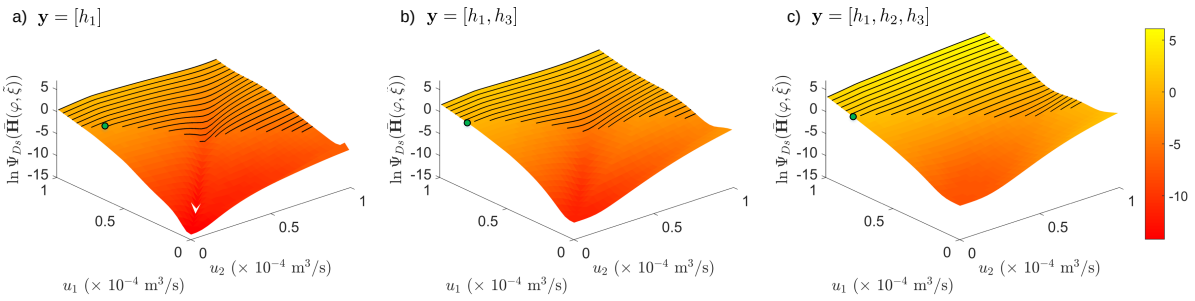

Fig. 6.3: Determinant of the normalized Fisher Information Matrix for the three-tank system over a range of admissible pump flow rates represented as u_1 and u_2, based on the selected sensor sets (a) $\mathbf{y} = [h_1]$, (b) $\mathbf{y} = [h_1, h_3]$ and (c) $\mathbf{y} = [h_1, h_2, h_3]$ of Case 1. Dark regions are the input set that result in violated output constraints, and the green dot is the highest value of $\ln \Psi_{Ds}(\bar{\mathbf{H}}_\xi)$.

upper and lower bounds, respectively, while staying within predefined output constraints. At $\mathbf{y} = h_1$, pump 2 is not set to the lower bound at optimal conditions because the increased pump flow improves the sensitivity of h_1 to possible leaks in tanks 2 and 3. However, when h_3 or h_2 and h_3 are included in the design, the increased pump 2 flow is no longer necessary, and thus better fault isolation occurs at the highest available pump 1 flow rate. The optimal test design was calculated from (6.6) to be $\boldsymbol{\varphi}^* = [u_1^* = 0.80 \times 10^{-4}$ m^3/s, $u_2^* = 0.01 \times 10^{-4}$ m^3/s, $\mathbf{a}^* = [1, 1, 1]]$; all three sensors are relatively precise and together provide the most useful information with respect to faults.

Equations (6.7) and (6.11-6.13) were implemented using KLD and HD measures to

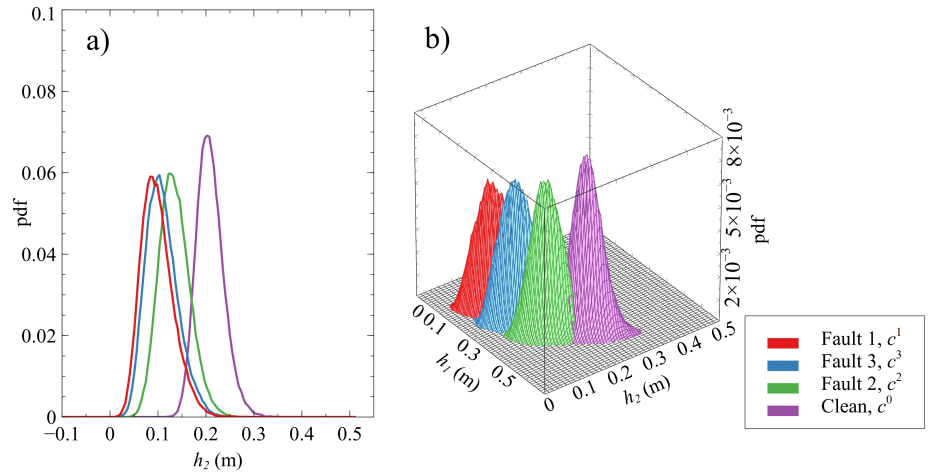

Fig. 6.4: Case 1 probability distributions of the heights of tanks 1, 2 and 3 at fault and fault-free conditions using sensor sets (a) $\mathbf{y} = [h_2]$ and (b) $\mathbf{y} = [h_1, h_2]$. c^{0-3} were assigned the values or distributions listed in Table 6.1.

calculate the optimal test design to compare with the results using (6.6). The first step to this approach is to calculate the optimal test design for the number of sensors considered for FDI ($n_y = 1, 2, 3$). The test designs for each iteration were identical to the optimal points indicated in Fig. 6.3. Monte Carlo simulations were then performed with N_{MC}=10,000 iterations of sample data collected, and the probability distributions of each output were approximated for all fault scenarios. Fig. 6.4 presents the histograms of the joint PDFs of the each scenario with two different sensor sets. The distributions shown in Figs. 6.4a) and 6.4b) are from sensor set $\mathbf{y} = [h_2]$ and $\mathbf{y} = [h_1, h_2]$, respectively. There is overlap between fault scenarios, even at optimal conditions. In Case 1, the amount of total overlap is reduced

by considering the combined probabilities of both sensors in the two-sensor set design. The overlap is reduced further for the joint probability corresponding to all three sensors, but due to high dimensionality those results are not shown in this document.

The FDI test designs were verified using the k-NN classification described in the Appendix based on the data collected from the Monte Carlo simulations. Table 6.2 contains the results of each optimization performed and the classification rate of each proposed test design. The calculated solutions generated from (5.4), (6.6) and (6.7-6.13), i.e. the D_s-optimal measures from the standard and normalized FIM, KLD and HD values are shown in Table 6.2a). The rate of correct classifications and misclassifications of the fault scenarios are presented with respect to the proposed test designs for $n_y = 1, 2, 3$ in Table 6.2b). The standard and normalized D_s-optimal outputs are in agreement that three sensors lead to the most informative FDI tests in Case 1. The KLD and HD outputs follow a similar pattern in that three sensors generate the greatest divergence in joint probabilities between fault scenarios. The classification rates match the pattern shown in all three measures, and the overall classification accuracy is highest at $\mathbf{y} = [h_1, h_2, h_3]$.

The proposed methods for FDI test design optimization must be capable of rejecting sensors with excessive noise. In Case 2, the Tank 2 sensor has more noise, thus the reliability of this sensor in fault diagnosis is reduced. An exhaustive calculation of D_s-optimal outputs were calculated from the normalized FIM over the allowable range of pump flow rates for the same combination of sensor sets, just as in Case 1. The surface plots of these outputs

Table 6.2: Sensor selection measures and confusion matrices of Case 1, with fault scenarios listed in Table 6.1.

(a) Comparison of sensor selection measures from Case 1.

Test Design	$\boldsymbol{\varphi}^*$	$\ln \Psi_{Ds}(\mathbf{H}_\xi)$	$\ln \Psi_{Ds}(\bar{\mathbf{H}}_\xi)$	D_{KL}	D_H	A_{CC}
Opt ($\mathbf{y} = [h_1]$)	[0.78,0.06]	-1.31	-1.31	2.61	0.553	0.74
Opt ($\mathbf{y} = [h_1, h_3]$)	[0.80,0.01]	1.53	0.05	3.32	0.597	0.84
Opt ($\mathbf{y} = [h_1, h_2, h_3]$)	[0.80,0.01]	3.80	1.35	3.51	0.607	0.88

(b) Confusion matrices of Case 1 FDI executed with different sensor sets.

		$\mathbf{y} = [h_2]$				$\mathbf{y} = [h_1, h_2]$				$\mathbf{y} = [h_1, h_2, h_3]$			
		Actual				Actual				Actual			
		c^0	c^1	c^2	c^3	c^0	c^1	c^2	c^3	c^0	c^1	c^2	c^3
Predicted	c^0	0.90	0.00	0.20	0.02	0.89	0.01	0.17	0.02	0.88	0.01	0.12	0.02
	c^1	0.00	0.70	0.00	0.15	0.00	0.90	0.01	0.02	0.00	0.92	0.00	0.03
	c^2	0.10	0.05	0.71	0.19	0.11	0.05	0.74	0.16	0.12	0.01	0.86	0.08
	c^3	0.00	0.25	0.09	0.65	0.00	0.04	0.08	0.80	0.00	0.06	0.02	0.87

are shown in Fig. 6.5. The optimal input values for all sensor sets were found to be identical to Case 1, as the decrease in sensor 2 precision has no direct on sensors 1 and 3, while at

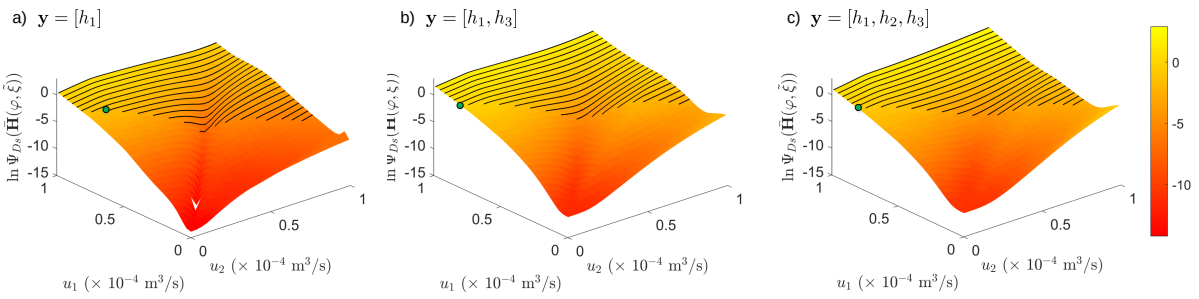

Fig. 6.5: Determinant of the normalized Fisher Information Matrix for the three-tank system over a range of admissible pump flow rates represented as u_1 and u_2, based on the selected sensor sets (a) $\mathbf{y} = [h_1]$, (b) $\mathbf{y} = [h_1, h_3]$ and (c) $\mathbf{y} = [h_1, h_2, h_3]$ in Case 2. Dark regions are the input set that result in violated output constraints, and the green dot is the highest value of $\ln \Psi_{Ds}(\bar{\mathbf{H}}_\xi)$.

$\mathbf{y} = [h_1, h_2, h_3]$ the optimal test design is more dependent on sensors 1 and 3, resulting in an identical optimal test design.

Monte Carlo simulations were performed for Case 2 with random distributions injected into the uncertain parameters according to Table 6.1, with the additional measurement noise into sensor 2. Fig. 6.6 presents the PDFs generated from the anticipated fault scenarios obtained from the optimal test designs for sensor sets, $\mathbf{y} = [h_2]$ and $\mathbf{y} = [h_1, h_2]$. The distribution of the PDFs for each fault scenario in the left plot are significantly wider than in Fig. 6.4a) due to increase measurement noise. There is significant overlap that occurs in fault scenarios c^{1-3}, indicating that fault diagnosis with sensor 2 would be unsuccessful.

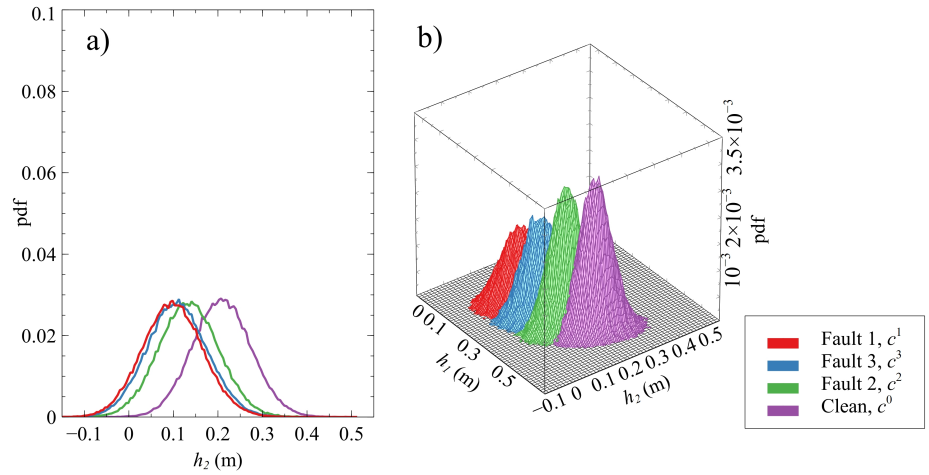

Fig. 6.6: Case 2 probability distributions of the heights of tanks 1, 2 and 3 at fault and fault-free conditions using sensor sets (a) $\mathbf{y} = [h_2]$ and (b) $\mathbf{y} = [h_1, h_2]$. c^{0-3} were assigned the values or distributions listed in Table 6.1.

The joint probabilities in the Fig. 6.6b) have greater overlap caused by the increase in measurement noise in sensor 2. Thus, including sensor 2 would result in a less reliable test design, and false alarms and nondetection are more likely to occur.

k-NN classification was used to classify fault and fault-free conditions from the Monte Carlo simulation generated in Case 2. The classification rates, and optimal test design outputs of selection methods are presented in Table 6.3. The D_s-optimal outputs from the standard FIM increase with additional sensors, regardless of the level of measurement noise. However, the D_s-optimal measure calculated using the normalized FIM decreases with the inclusion of sensor 2, indicating that the average quality of information decreases.

The highest average level of information is generated in Case 1 when $\mathbf{y} = [h_1, h_3]$, thus sensor 2 is rejected to improve FDI. The KLD and HD outputs are in agreement in that the greatest divergence between fault scenarios occurs at $\mathbf{y} = [h_1, h_3]$. The classification rates and overall classification accuracies obtained from the Case 2 Monte Carlo simulations are also in agreement.

Case 3 was then performed to determine the effect of uncertainty on particular outputs and how they are reflected in the proposed methods. The random distributions of the faults and uncertain parameters were adjusted for Case 3 according to the following steps:

1. Flow coefficient c_1 has a Gaussian distribution with a mean value at 0.95 and standard deviation increased to 0.125.

2. Flow coefficients c_2 and c_3 have Gaussian distributions with mean values at 0.8 and 0.95, respectively, and standard deviations decreased to 0.02.

The change in the distributions of the uncertain parameters does not affect the anticipated values of the fault and uncertain parameters, $\tilde{\boldsymbol{\xi}}$. Therefore, the D_s-optimal values that were obtained from $\mathbf{H}_\xi$ and $\bar{\mathbf{H}}_\xi$ are unaffected. Equations (6.7) and (6.11-6.13) utilize prior information to determine the optimal sensor set, therefore the change in distributions will impact the decision of the optimal sensor set. Monte Carlo simulations were performed to determine the effects of the uncertainty described in Case 3 between PDFs generated from the fault scenarios. Fig. 6.6 presents the PDFs generated for single sensor distributions $\mathbf{y} = h_2$ and $\mathbf{y} = h_3$ as well as joint PDFs generated for $\mathbf{y} = [h_1, h_2]$ and $\mathbf{y} = [h_1, h_3]$.

Table 6.3: Sensor selection measures and confusion matrices of Case 2, with fault scenarios listed in Table 6.1.

(a) Comparison of sensor selection measures from Case 2.

Test Design	$\boldsymbol{\varphi}^*$	$\ln \Psi_{Ds}(\mathbf{H}_\xi)$	$\ln \Psi_{Ds}(\bar{\mathbf{H}}_\xi)$	D_{KL}	D_H	A_{CC}
Opt ($\mathbf{y} = [h_1]$)	[0.78,0.06]	-1.31	-1.31	2.61	0.553	0.74
Opt ($\mathbf{y} = [h_1, h_3]$)	[0.80,0.01]	1.53	0.05	3.32	0.597	0.84
Opt ($\mathbf{y} = [h_1, h_2, h_3]$)	[0.80,0.01]	1.72	-0.58	3.09	0.581	0.83

(b) Confusion matrices of Case 2 FDI executed with different sensor sets.

		$\mathbf{y} = [h_1]$				$\mathbf{y} = [h_1, h_3]$				$\mathbf{y} = [h_1, h_2, h_3]$			
		Actual				Actual				Actual			
		c^0	c^1	c^2	c^3	c^0	c^1	c^2	c^3	c^0	c^1	c^2	c^3
Predicted	c^0	0.90	0.00	0.20	0.02	0.89	0.01	0.17	0.02	0.90	0.01	0.17	0.01
	c^1	0.00	0.70	0.00	0.15	0.00	0.90	0.01	0.02	0.00	0.89	0.01	0.04
	c^2	0.10	0.05	0.71	0.19	0.11	0.05	0.74	0.16	0.10	0.05	0.76	0.15
	c^3	0.00	0.25	0.09	0.65	0.00	0.04	0.08	0.80	0.00	0.05	0.07	0.79

Figs. 6.7a) and 6.7c) show significant overlap between the fault scenarios in h_2 and h_3, respectively. Sensor 2 in particular shows overlap between all three fault scenarios, while

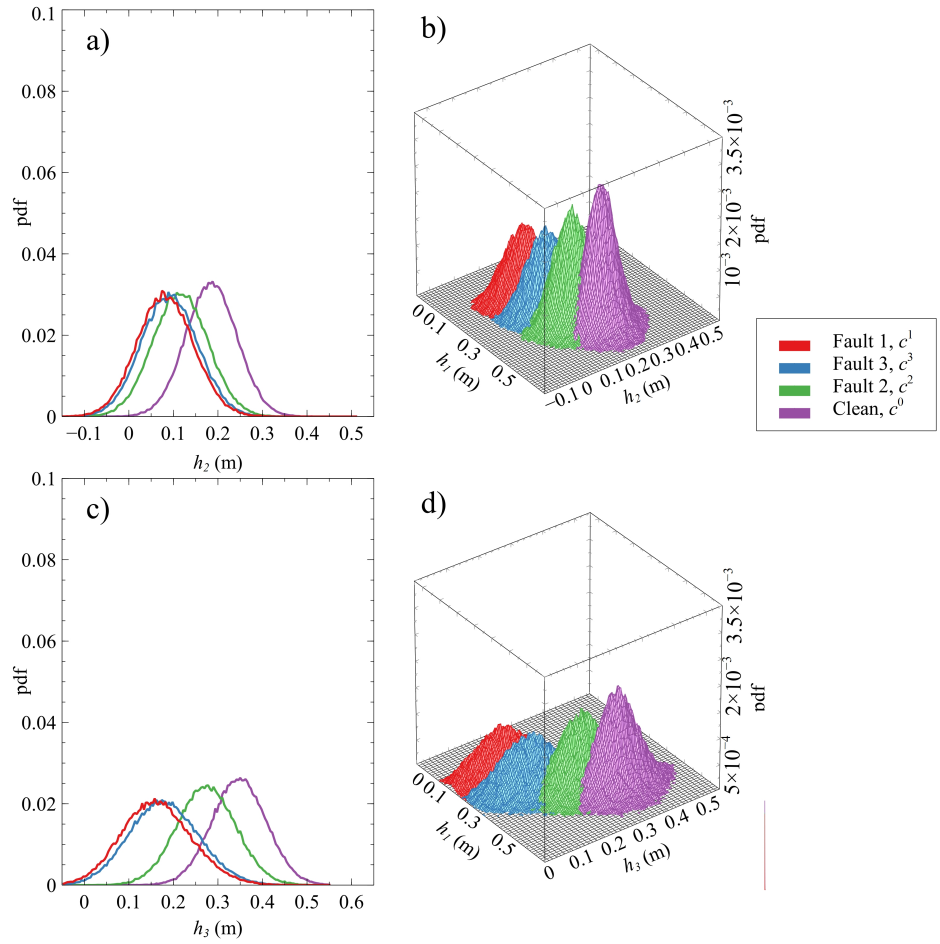

Fig. 6.7: Case 3 probability distributions of the heights of tanks 1, 2 and 3 at fault and fault-free conditions using sensor sets (a) $\mathbf{y} = [h_2]$, (b) $\mathbf{y} = [h_1, h_2]$, (c) $\mathbf{y} = [h_3]$ and (d) $\mathbf{y} = [h_1, h_3]$.

sensor 3 generates similar output distributions for c^1 and c^2. However, the inclusion of the uncertainty in flow coefficient c_1 results in similarly wide distributions as can be seen in Figs. 6.7b) and 6.7d), thus rejecting these sensors will not improve fault diagnosis accuracy.

Table 6.4: Comparison of sensor selection measures from Case 3.

Test Design	$\boldsymbol{\varphi}^*$	$\ln \Psi_{Ds}(\mathbf{H}_\xi)$	$\ln \Psi_{Ds}(\bar{\mathbf{H}}_\xi)$	D_{KL}	D_H	A_{CC}
Opt ($\mathbf{y} = [h_1]$)	[0.78,0.06]	-1.31	-1.31	2.31	0.522	0.67
Opt ($\mathbf{y} = [h_1, h_3]$)	[0.80,0.01]	-0.77	-2.12	2.50	0.540	0.72
Opt ($\mathbf{y} = [h_1, h_2, h_3]$)	[0.80,0.01]	-0.47	-2.64	2.51	0.543	0.73

The sensors sets from the previous cases were used to generate the measures shown in Table 6.4. The distribution of system uncertainty in Case 3 results in KLD and HD values that no longer agree with the normalized D_s-optimal measures. Using (6.6), the optimal test design is considered to be at $\mathbf{y} = h_1$, as the increase in measurement noise in sensors 2 and 3 are considered to be not precise enough to include in the test design compared to sensor 1. However, taking into account how uncertain parameter ranges affect the output distribution from sensor 1, particularly the flow coefficient c_1, sensors 2 and 3 exhibit similar levels of precision and thus are worth including for active fault diagnosis. Therefore, the KLD and HD outputs from (6.11-6.13) indicate that the optimal test design occurs at $\mathbf{y} = [h_1, h_2, h_3]$. The pattern of correct classification accuracies from Case 3 are in agreement with (6.7) and (6.11-6.13).

The methods of sensor selection for active fault diagnosis presented in this document have their respective benefits and drawbacks when applied to nonlinear systems. Because

(6.6) involves a single-step optimization problem for simultaneous input and sensor selection, it requires fewer iterations and is less complex than the second approach, thus the FDI test design can be determined in less time. However, (6.6) does not account for the distribution of faults and uncertainties in calculation of optimal test designs. The approach using (6.7) and (6.11-6.13) is able to use KLD or HD measures to compare proposed optimal sensor sets in uncertainty systems to take into account the range of system uncertainty as prior information. It was found that the second approach would generate the same optimal test design as through (6.6) when the uncertainty was small or unknown. When the system of interest has a significant range of uncertainty it can affect outputs in a manner that is difficult to predict, particularly in nonlinear, complex systems. The test designs generated from (6.6) and (6.11-6.13) are consistently better in terms of accuracy and robustness in systems with uncertainty ranges that were known and significant.

6.5 Conclusions

A methodology was introduced for active FDI in complex systems. Test designs were optimized via D_s-optimality to maximize sensitivity of outputs with respect to faults while accounting for sources of system uncertainty. Controllable inputs for improving FDI were selected concurrently with sensor sets to generate comprehensively optimal test designs. In two approaches to the methodology, each sensor considered was accepted or rejected for active FDI based on the quality of the information provided. The first approach focused

on the evaluation of the D_s-optimal measure of the average FIM generated from proposed sensor sets. The second approach focused on selecting the optimal sensor set from various sensor combinations, comparing the discrepancy between all fault scenarios generated from each output using KLD or HD measures. A case study was examined using both approaches to optimal active FDI via a benchmark three-tank system. While the approaches generated successful test designs that resulted in improved fault diagnosis, their benefits were found to be dependent on the degree of uncertainty present in the system. The first approach with normalized FIM is more efficient in solving for optimal test designs thereby reducing computational load, while the test designs obtained with KLD or HD-based analysis can be used to account for the entire range of system uncertainty when prior information is available. These methods were verified using k-NN classification, and the optimal FDI tests were found to be more accurate and robust against noise and uncertainty.

Chapter 7

Conclusions and Recommendations

7.1 Conclusions

Active fault detection and isolation methods have become increasingly prevalent in improving system costs, safety and reliability. This dissertation was aimed to provide a methodology for the optimal design of active FDI tests prior to their execution, thus increasing the likelihood of successful fault diagnosis. The key aspects of this dissertation were the following: the selection of design criteria that consistently improve fault diagnosis in system with uncertainty present, posterior assessments regarding plausibility of false alarms and nondetections for the proposed designs, and the incorporation of sensor selection for the computationally tractable simultaneous optimization of input design and sensor selection.

In Chapter 1, motivation for model-based fault detection and isolation was discussed as a series of techniques used to improve system costs and reliability. Actively configured FDI design approaches have been implemented in the literature, but the optimal selection of test designs prior to implementation is seldom considered due to computational complexity.

A methodology for the optimally select test designs that improve robustness and accuracy in active FDI was presented in this dissertation. In Chapter 2, a preliminary version of the proposed methodology was applied to a simulated plate-fin heat exchanger that is subject to particulate fouling. A model of the heat exchanger was developed, validated with literature data, and used to determine the optimal conditions for identifying fouling via parameter estimation at steady-state and dynamic conditions with environmental uncertainties present. In Chapter 3, the usefulness of transient information was evaluated for active FDI. A series of case studies were performed to compare the effectiveness of using steady-state and dynamic informationin fault diagnosis, based on the heat exchanger model developed in the previous chapter. Conventional FDI techniques, extended Kalman filtering and moving horizon estimation, were used to verify the benefits of transient data extracted from informative models.

Chapter 4 extends from the work in Chapter 2 to explore the plausibility of false alarms when implementing optimal test designs for active FDI, based on structural global identifiability. Parameter sets were explored at fault and fault-free conditions, respectively, to determine if faults could be declared present from clean system outputs. In addition to the heat exchanger model, the methodology was also applied to a virtual environmental control system to test the applicability of the framework in larger systems. In Chapter 5, multiple design criteria were tested to determine which measure led to consistently improved fault diagnosis. Principal component analysis followed by k-NN classification was used for FDI

execution to test and verify the proposed criteria.. Two virtual case studies were performed to evaluate the criteria: a benchmark three-tank system and the air handling system of a turbocharged diesel engine.

In Chapter 6, the selection of sensors for active detection and isolation of faults was incorporated into the model-based framework for simultaneous optimization. The problem of selecting the best available active FDI test design became a constrained, mixed-integer optimization problem. The D_s-optimal design criterion was chosen to be implemented in this work for its ability to maximize the sensitivity of outputs to faults while taking into account any correlations between faults and uncertainty. Two approaches were presented to assess the overall quality of information provided by selected sensors and to reject sensors that did not improve fault diagnosis. The first approach was based on normalized Fisher information used to generate the average information provided from each sensor in the selected set for a given test design. The second approach included prior information generated from measurement noise and system uncertainty at each fault scenario. The probability densities generated with this information were then used to generate a measure of divergence between all fault scenarios, with the objective of minimizing overlap between scenarios. The divergence measures considered in this chapter were Hellinger distance and Kullback-Leibler divergence. These methods were implemented in several cases using a simulated benchmark three-tank system. Overall, the results show that incorporating the active FDI design methodology consistently improves fault diagnosis accuracy and robustness, particularly with the inclu-

sion of optimal sensor selection. Future work is needed in order to adequately compare this approach to other on-line and off-line approaches, particularly in complex, nonlinear systems with admissible inputs that are prone to uncertainty.

7.2 Recommendations

The conclusions from this work illustrate the ability to consistently improve fault diagnosis, and consequently system costs and reliability, with a systematic optimization of admissible inputs and sensor selection. However, there are limitations in industrial systems that must be considered before implementing the methodology of this dissertation: the availability of models that sufficiently represent how the system interacts with uncertainty and faults, and the test design space and sensor space considered admissible for active FDI. The following recommendations are given in this section regarding future work that further improve the feasibility and effectiveness of the test design selection.

The case studies explored in this dissertation had controllable input trajectories with discrete steps and a range of continuous values with upper and lower boundary conditions. However, real-world applications may have a restricted set of conditions available for FDI implementation due to system complexity or controllability. These finite set of test settings can be represented as integer variables, similar to the work that was done in Chapter 6 for sensor selection. The resulting problem would be considered a combinatorial problem and should be solved accordingly. Active FDI test selection via discrete optimization for a finite

number of available test designs would be beneficial in regards to limited system control capabilities, or to systems with predefined control schedules.

The optimization formulation used in this dissertation was based on frequentist approaches to optimal design. In other words, the optimizations performed were based on the calculation of output sensitivities with respect to targeted parameters based on a single anticipated set of "initial guess" values. The benefit of frequentist approaches is that no additional prior information is necessary for computing the FDI test design, thereby reducing computational costs. However, a more robust method of optimization is available in the literature referred to as Bayesian design. The Bayesian approach to optimization takes into consideration the sensitivities of outputs with respect to uncertain parameters for the entire distribution of the parameter space obtained using prior information. While the computational cost to solve for Bayesian optimal test designs is expensive, the approach would be useful in systems with high nonlinearity when the computational requirements can be met.

Finally, the work shown in this dissertation considered only available sensors and test settings that maximize the accuracy and robustness of fault diagnosis. The choice of optimal sensors and sensor locations is then limited by what is already installed in the system of interest. However, this methodology is also applicable to the selection and placement of sensors prior to system development. A recommendation for improving the methodology for complex systems in development is to incorporate cost and energy factors into the design process. The cost and energy required to install and implement each sensor can vary with

type and location, and should be weighed against the benefits to the quality of information for FDI.

Bibliography

[1] John L. Warner. Environmental control system condensing cycle, 1992.

[2] M.S. Abd-Elhady, T. Zornek, M.R. Malayeri, S. Balestrino, P.G. G. Szymkowicz, and H. Müller-Steinhagen. Influence of gas velocity on particulate fouling of exhaust gas recirculation coolers. *International Journal of Heat and Mass Transfer*, 54(4):838–846, jan 2011.

[3] D.Q. Kern and R.E. Seaton. A Theoretical Analysis of Thermal Surface Fouling. *British Chemical Engineering*, 4(5):258–262, 1959.

[4] Shoaib Ahmed Shah. *Modeling and Fouling Detection of the Aircraft Environmental Control System Heat Exchanger.* PhD thesis, Ryerson University, 2009.

[5] Kyle A. Palmer, William T. Hale, Kyle D. Such, Brian R. Shea, and George M. Bollas. Optimal design of tests for heat exchanger fouling identification. *Applied Thermal Engineering*, 95:382–393, 2016.

[6] J.L. Warner. Environmental control system condensing cycle, March 5 1992. WO Patent App. PCT/US1991/003,529.

[7] Ali Mesbah, Stefan Streif, Rolf Findeisen, and Richard D. Braatz. Active Fault Diagnosis for Nonlinear Systems with Probabilistic Uncertainties. *IFAC Proceedings Volumes*, 47(3):7079–7084, 2014.

[8] Boulaïd Boulkroune, Abdel Aitouche, Vincent Cocquempot, Li Cheng, and Zhijun Peng. Actuator Fault Diagnosis with Application to a Diesel Engine Testbed. *Mathematical Problems in Engineering*, 2015:1–15, 2015.

[9] Mattias Nyberg and Thomas Stutte. Model based diagnosis of the air path of an automotive diesel engine. *Control Engineering Practice*, 12(5):513–525, 2004.

[10] Stephen X. Ding. *Model-based Fault Diagnosis Techniques.* Springer Berlin Heidelberg, Berlin, Heidelberg, 2008.

[11] Venkat Venkatasubramanian, Raghunathan Rengaswamy, Kewen Yin, and Surya N. Kavuri. A review of process fault detection and diagnosis: Part I: Quantitative model-based methods. *Computers & Chemical Engineering*, 27(3):293–311, 2003.

[12] Venkat Venkatasubramanian. A review of process fault detection and diagnosis: Part III: Process history based methods. *Computers and Chemical Engineering*, 27:327–346, 2003.

[13] Venkat Venkatasubramanian, Raghunathan Rengaswamy, and Surya N Kavuri. A review of process fault detection and diagnosis: Part II: Qualitative models and search strategies. *Computers & Chemical Engineering*, 27(3):313–326, 2003.

[14] C. Baskiotis, J. Raymond, and A. Rault. Parameter identification and discriminant analysis for jet engine machanical state diagnosis. In *1979 18th IEEE Conference on Decision and Control including the Symposium on Adaptive Processes*, pages 648–650, Fort Lauderdale, FL, dec 1979. IEEE.

[15] Costas Kravaris, Juergen Hahn, and Yunfei Chu. Advances and selected recent developments in state and parameter estimation. *Computers & Chemical Engineering*, 51: 111–123, apr 2013.

[16] Kris Villez, Babji Srinivasan, Raghunathan Rengaswamy, Shankar Narasimhan, and Venkat Venkatasubramanian. Kalman-based strategies for Fault Detection and Identification (FDI): Extensions and critical evaluation for a buffer tank system. *Computers & Chemical Engineering*, 35(5):806–816, may 2011.

[17] Christopher Edwards, Sarah K Spurgeon, and Ron J Patton. Sliding mode observers for fault detection and isolation. *Electronic Engineering*, 36(4):541–553, 2000.

[18] H. Mohamed Basri, K Lias, W.A. Wan Zainal Abidin, K.M. Tay, and H Zen. Fault Detection using Dynamic Parity Space Approach. In *2012 IEEE International Power Engineering and Optimization Conference*, pages 52–56, Melaka, Malaysia, jun 2012. IEEE.

[19] Sylvain Lalot and Halldór Pálsson. Detection of fouling in a cross-flow heat exchanger using a neural network based technique. *International Journal of Thermal Sciences*, 49:675–679, 2010.

[20] Q. Peter He and Jin Wang. Principal component based k-nearest-neighbor rule for semiconductor process fault detection. In *2008 American Control Conference*, pages 1606–1611. IEEE, 2008.

[21] Zhiwei Gao, Carlo Cecati, and Steven Ding. A Survey of Fault Diagnosis and Fault-Tolerant Techniques Part II: Fault Diagnosis with Knowledge-Based and Hybrid/Active Approaches. *IEEE Transactions on Industrial Electronics*, pages 1–1, 2015.

[22] Ramine Nikoukhah. Guaranteed Active Failure Detection and Isolation for Linear Dynamical Systems. *Automatica*, 34(11):1345–1358, nov 1998.

[23] Ivan Andjelkovic, Kelly Sweetingham, and Stephen L Campbell. Active fault detection in nonlinear systems using auxiliary signals. In *2008 American Control Conference*, pages 2142–2147. IEEE, jun 2008.

[24] Yuncheng Du, Hector Budman, and Thomas A. Duever. Integration of fault diagnosis and control based on a trade-off between fault detectability and closed loop performance. *Journal of Process Control*, 38:42–53, feb 2016.

[25] G. Roberto Marseglia and Davide M. Raimondo. Active fault diagnosis: A multiparametric approach. *Automatica*, 79:223–230, 2017.

[26] Bin Hu and Peter Seiler. Worst-case false alarm analysis of fault detection systems. In *2014 American Control Conference*, pages 654–659. IEEE, jun 2014.

[27] Jafar Zarei and Ehsan Shokri. Robust sensor fault detection based on nonlinear unknown input observer. *Measurement*, 48:355–367, 2014.

[28] Jafar Zarei and Javad Poshtan. Design of nonlinear unknown input observer for process fault detection. *Industrial and Engineering Chemistry Research*, 49(22):11443–11452, 2010.

[29] Yuncheng Du, Thomas A. Duever, and Hector Budman. Fault detection and diagnosis with parametric uncertainty using generalized polynomial chaos. *Computers & Chemical Engineering*, 76:63–75, may 2015.

[30] Gaia Franceschini and Sandro Macchietto. Novel Anticorrelation Criteria for Model-Based Experiment Design: Theory and Formulations. *AIChE Journal*, 54(4):1009–1024, 2008.

[31] Lu Han, Zhiquan Zhou, and George M. Bollas. Model-based analysis of chemical-looping combustion experiments. Part I: Structural identifiability of kinetic models for NiO reduction. *AIChE Journal*, 62(7):2419–2431, jul 2016.

[32] Lu Han, Zhiquan Zhou, and George M. Bollas. Model-based analysis of chemical-looping combustion experiments. Part II: Optimal design of CH4 -NiO reduction experiments. *AIChE Journal*, 62(7):2432–2446, jul 2016.

[33] Afshin Abdi and Faramarz Fekri. Optimal Sensor Selection in the Presence of Noise and Interference. pages 2383–2387, 2017.

[34] Siddharth Joshi and Stephen Boyd. Sensor Selection via Convex Optimization. *IEEE Transactions on Signal Processing*, 57(2):451–462, feb 2009.

[35] Maciej Patan and Dariusz Ucinski. Sensor scheduling with selection of input experimental conditions for identification of distributed systems. In *2010 15th International Conference on Methods and Models in Automation and Robotics*, pages 148–153. IEEE, aug 2010.

[36] Isabel Pérez-Grande and Teresa J. Leo. Optimization of a commercial aircraft environmental control system. *Applied Thermal Engineering*, 22(17):1885–1904, dec 2002.

[37] W. M. Kays and A. L. London. *Compact Heat Exchangers*. McGraw-Hill, New York, NY, USA, 3rd edition, 1984.

[38] Ian Moir and Allan Seabridge. *Aircraft Systems*. John Wiley & Sons, Ltd, West Sussex, England, 3rd edition, 2008.

[39] S. Wright, G. Andrews, and H. Sabir. A review of heat exchanger fouling in the context of aircraft air-conditioning systems, and the potential for electrostatic filtering. *Applied Thermal Engineering*, 29(13):2596–2609, sep 2009.

[40] Ramesh K. Shah and Dusan P. Sekulic. *Fundamentals of Heat Exchanger Design*. John Wiley & Sons, New Jersey, 2003.

[41] S Zubair, A Sheikh, Muhammad Younas, and M Budair. A risk based heat exchanger analysis subject to fouling Part I : Performance evaluation. *Energy*, 25:427–443, 2000.

[42] S Shah, G Liu, and D R Greatrix. Modelling, simulation, and experimental evaluation of a crossflow heat exchanger for an aircraft environmental control system. *Proceedings of the Institution of Mechanical Engineers, Part G: Journal of Aerospace Engineering*, 224(5):613–623, may 2010.

[43] Jonathon S. Litt, Donald L. Simon, Sanjay Garg, Ten-Heui Guo, Carolyn Mercer, Richard Millar, Alireza Behbahani, Anupa Bajwa, and Daniel T. Jensen. A Survey of Intelligent Control and Health Management Technologies for Aircraft Propulsion Systems. *Journal of Aerospace Computing, Information, and Communication*, 1(12): 543–563, 2004.

[44] Lan Shang and Guangjun Liu. Sensor and Actuator Fault Detection and Isolation for a High Performance Aircraft Engine Bleed Air Temperature Control System. *IEEE Transactions on Control Systems Technology*, 19(5):1260–1268, sep 2011.

[45] Oddgeir Gudmundsson, Sylvain Lalot, and J E Thorsen. Comparison of Fouling Detection Methods using Experimental Data. In *Proceedings of International Conference on Heat Exchanger Fouling and Cleaning*, volume 2013, pages 429–436, 2013.

[46] Oddgeir Gudmundsson. *Detection of fouling in heat exchangers.* Thesis, University of Iceland, 2008.

[47] Gudmundur R. Jonsson, Sylvain Lalot, Olafur P. Palsson, and Bernard Desmet. Use of extended Kalman filtering in detecting fouling in heat exchangers. *International Journal of Heat and Mass Transfer*, 50(13-14):2643–2655, jul 2007.

[48] Takahisa Kobayashi and Donald L. Simon. Hybrid Kalman Filter Approach for Aircraft Engine In-Flight Diagnostics: Sensor Fault Detection Case. *Journal of Engineering for Gas Turbines and Power*, 129(3):746, 2007.

[49] François Delmotte, Michel Dambrine, Sabrina Delrot, and Sylvain Lalot. Fouling detection in a heat exchanger: A polynomial fuzzy observer approach. *Control Engineering Practice*, 21(10):1386–1395, oct 2013.

[50] S Lalot and G Mercère. Detection of fouling in heat exhanger using a recursive subspace identification algorithm. In *The 19th International Symposium on Transport Phenomena*, Reykjavik, Iceland, 2008.

[51] Helga Ingimundardóttir and Sylvain Lalot. Detection of Fouling in a Cross-Flow Heat Exchanger Using Wavelets. In H. Muller-Steinhagen, M.R. Malayeri, and A.P. Watkinson, editors, *Heat Exchanger Fouling and Cleaning VIII*, volume 32, pages 349–357, Schladming, Austria, jun 2009. Heat Exchanger Fouling and Cleaning.

[52] H. Al-Asaad and M. Shringi. On-line built-in self-test for operational faults. *2000 IEEE Autotestcon Proceedings. IEEE Systems Readiness Technology Conference. Future Sustainment for Military Aerospace (Cat. No.00CH37057)*, pages 168–174, 2000.

[53] Valerii Fedorov. Optimal experimental design. *Wiley Interdisciplinary Reviews: Computational Statistics*, 2(5):581–589, sep 2010.

[54] Maria Rodriguez-Fernandez, Sergei Kucherenko, Costas Pantelides, and Nilay Shah. Optimal experimental design based on global sensitivity analysis. In *17th European Symposium on Computer Aided Process Engineering*, pages 1–6, 2007.

[55] Mark-John Bruwer and John F. MacGregor. Robust multi-variable identification: Optimal experimental design with constraints. *Journal of Process Control*, 16:581–600, 2006.

[56] Gaia Franceschini and Sandro Macchietto. Model-based design of experiments for parameter precision: State of the art. *Chemical Engineering Science*, 63(19):4846–4872, oct 2008.

[57] Stefan Körkel, Ekaterina Kostina, Hans Georg Bock, and Johannes P. Schlöder. Numerical methods for optimal control problems in design of robust optimal experiments for nonlinear dynamic processes. *Optimization Methods and Software*, 19(3-4):327–338, jun 2004.

[58] Friedrich Pukelsheim. *Optimal Design of Experiments*. John Wiley & Sons, Inc., New York, NY, USA, 1993.

[59] Christos P. Kitsos and Konstantinos G. Kolovos. A Compilation of the D-Optimal Designs in Chemical Kinetics. *Chemical Engineering Communications*, 200(2):185–204, jan 2013.

[60] Tomas Skoglund, Karl-Erik Erik Årzén, and Petr Dejmek. Dynamic object-oriented heat exchanger models for simulation of fluid property transitions. *International Journal of Heat and Mass Transfer*, 49(13-14):2291–2303, jul 2006.

[61] Mihir Sen. *Analytical Heat Transfer*. Department of Aerospace and Mechanical Engineering, University of Notre Dame, Notre Dame, IN, USA, 2008.

[62] R. Bala Sundar Rao, G. Ranganath, and C. Ranganayakulu. Development of colburn j' factor and fanning friction factor f' correlations for compact heat exchanger plain fins by using CFD. *Heat and Mass Transfer*, 49(7):991–1000, mar 2013.

[63] Junqi Dong, Jiangping Chen, Zhijiu Chen, and Yimin Zhou. Air-side thermal hydraulic performance of offset strip fin aluminum heat exchangers. *Applied Thermal Engineering*, 27(2-3):306–313, feb 2007.

[64] R.K. Shah. Compact Heat Exchangers. In *Handbook of Heat Transfer Applications*, pages 4–174. McGraw-Hill, New York, NY, USA, 2nd edition, 1985.

[65] Ning-bo Zhao, Xue-you Wen, and Shu-ying Li. Dynamic Time-Delay Characteristics and Structural Optimization Design of Marine Gas Turbine Intercooler. *Mathematical Problems in Engineering*, 2014:1–14, 2014.

[66] AC-9 Aircraft Environmental Systems Committee. Fault isolation in environmental control systems of commercial transports. Technical report, SAE Aerospace, SAE Aerospace, Warrendale, PA, USA, 2011.

[67] Modelica-Association. "Modelica Language Specification, Version 3.3", 2012.

[68] Dassault Systèmes. Dymola - Dynamic Modeling Library, 2017.

[69] Modelisar. Functional Mock-up Interface for Model Exchange, Version 1.0, 2010.

[70] MATLAB Release 2017b, 2017.

[71] Modelon AB. FMI Toolbox for MATLAB/Simulink, 2014.

[72] Radu Serban and A. C. Hindmarsh. CVODES: the Sensitivity-Enabled ODE Solver in SUNDIALS. *ACM Transactions on Mathematical Software*, 5:1–18, 2003.

[73] S Le Digabel. Algorithm 909: {NOMAD}: Nonlinear optimization with the {MADS} algorithm. *ACM Transactions On Mathematical Software*, 37(4):44:1—-44:15, 2011.

[74] International Civil Aviation Organization. *Manual of the ICAO Standard Atmosphere (extended to 80 kilometres (262 500 feet))*. Montreal, Canada, 3rd edition, 1993.

[75] Richard M. Felder and Ronald W. Rousseau. *Elementary Principles of Chemical Processes*. John Wiley & Sons, Inc, Hoboken, NJ, USA, 3rd edition, 2004.

[76] E. Y. Chow and a. S. Willsky. Analytical redundancy and the design of robust failure detection systems. *IEEE Transaction on Automatic Control*, 29(7):603–614, 1984.

[77] Haiyu Qi, Sanka Ganesan, and Michael Pecht. No-fault-found and intermittent failures in electronic products. *Microelectronics Reliability*, 48(5):663–674, 2008.

[78] Louis Y Ungar. Causes and Costs of No Fault Found Events. In *Proceedings of IPC APEX*, 2015.

[79] Paul Zador and Adrian Lund. Re-Analyses of the Effects of No-Fault Auto Insurance on Fatal Crashes. *The Jounral of Risk and Insurance*, 53(2):226–241, 2016.

[80] Nayeff Najjar, James Hare, Paul D'Orlando, Gregory Leaper, Krishna Pattipati, Andre Silva, Shalabh Gupta, and Rhonda Walthall. Heat Exchanger Fouling Diagnosis for an Aircraft Air-Conditioning System. In *SAE AeroTech Congress and Exhibition*, sep 2013.

[81] Federico Galvanin, Enhong Cao, Noor Al-Rifai, Asterios Gavriilidis, and Vivek Dua. A joint model-based experimental design approach for the identification of kinetic models in continuous flow laboratory reactors. *Computers & Chemical Engineering*, 95:202–215, dec 2016.

[82] Michael Baldea, Nael H. El-Farra, and B. Erik Ydstie. Dynamics and control of chemical process networks: Integrating physics, communication and computation. *Computers & Chemical Engineering*, 51:42–54, apr 2013.

[83] Xiaodian Sun, Li Jin, and Momiao Xiong. Extended Kalman Filter for Estimation of Parameters in Nonlinear State-Space Models of Biochemical Networks. *PLoS ONE*, 3 (11):e3758, nov 2008.

[84] R. E. Kalman. A New Approach to Linear Filtering and Prediction Problems. *Journal of Basic Engineering*, 82(1):35, 1960.

[85] Achim Küpper, Moritz Diehl, Johannes P. Schlöder, Hans Georg Bock, and Sebastian Engell. Efficient Moving Horizon State and Parameter Estimation for the Varicol SMB Process. *IFAC Proceedings Volumes*, 42(11):590–595, 2009.

[86] Eric L Haseltine and James B Rawlings. Critical Evaluation of Extended Kalman Filtering and Moving-Horizon Estimation. *Industrial & Engineering Chemistry Research*, 44(8):2451–2460, apr 2005.

[87] V.R. Radhakrishnan, M. Ramasamy, H. Zabiri, V. Do Thanh, N.M. Tahir, H. Mukhtar, M.R. Hamdi, and N. Ramli. Heat exchanger fouling model and preventive maintenance scheduling tool. *Applied Thermal Engineering*, 27(17):2791 – 2802, 2007.

[88] Kyle A. Palmer, William T. Hale, and George M. Bollas. Active Fault Identification by Optimization of Test Designs. *IEEE Transactions on Control Systems Technology*, pages 1–15, 2018.

[89] Raman K Mehra. Optimal Input Signals for Parameter Estimation in Dynamic Systems-Survey and New Results. *IEEE Transactions on Automatic Control*, 19(6): 753–768, 1974.

[90] Simon J. Julier and Jeffrey K. Uhlmann. New extension of the Kalman filter to nonlinear systems. page 182, jul 1997.

[91] P. Li, V. Kadirkamanathan, and R. Goodall. Estimation of parameters in a linear state space model using a Rao-Blackwellised particle filter. *IEE Proceedings - Control Theory and Applications*, 151(6):727–738, nov 2004.

[92] Peter Kühl, Moritz Diehl, Tom Kraus, Johannes P. Schlöder, and Hans Georg Bock. A real-time algorithm for moving horizon state and parameter estimation. *Computers & Chemical Engineering*, 35(1):71–83, jan 2011.

[93] Kyle A Palmer, William T Hale, Lu Han, Clas A Jacobson, and George M Bollas. Built-in Test Design for Fault Detection and Isolation in an Aircraft Environmental Control System*. *IFAC-PapersOnLine*, 49(7):7–12, 2016.

[94] A.M. Zoubir and B. Boashash. The bootstrap and its application in signal processing. *IEEE Signal Processing Magazine*, 15(1):56–76, 1998.

[95] G.M. Bollas, K. Palmer, D. Prasad, C.A. Jacobson, J.M. Maljanian, R.A. Poisson, and Y.K. Park. Plate-fin heat exchanger fouling identification, December 8 2016. US Patent App. 15/168,741.

[96] J. Gertler. Fault Detection and Isolation using Parity Relations. *Control Engineering Practice*, 5(5):653–661, 1997.

[97] Linlin Li, Steven X. Ding, Jianbin Qiu, Kaixiang Peng, and Ying Yang. An optimal fault detection approach for piecewise affine systems via diagnostic observers. *Automatica*, 85:256 – 263, 2017.

[98] Shunyi Zhao, Biao Huang, and Fei Liu. Detection and Diagnosis of Multiple Faults With Uncertain Modeling Parameters. *IEEE Transactions on Control Systems Technology*, 25(5):1873–1881, sep 2017.

[99] Peter Söderholm. A system view of the No Fault Found (NFF) phenomenon. *Reliability Engineering & System Safety*, 92(1):1–14, 2007.

[100] John Ahmet Erkoyuncu, Samir Khan, Syed Mohammed Fazal Hussain, and Rajkumar Roy. A framework to estimate the cost of No-Fault Found events. *International Journal of Production Economics*, 173:207–222, 2016.

[101] Yiqian Cui, Junyou Shi, and Zili Wang. Intermittent failure process and false alarm interaction modelling of threshold-based monitoring built-in tests (BITs). *International Journal of Production Research*, 54(6):1610–1626, mar 2016.

[102] Mateusz Nikodem. False Alarms in Fault-Tolerant Dominating Sets in Graphs. *IET Control Theory & Applications*, 32(4):751–760, 2012.

[103] Sankar Mahadevan and Sirish L. Shah. Fault detection and diagnosis in process data using one-class support vector machines. *Journal of Process Control*, 19(10):1627–1639, 2009.

[104] Sang Wook Choi, Changkyu Lee, Jong-Min Lee, Jin Hyun Park, and In-Beum Lee. Fault detection and identification of nonlinear processes based on kernel PCA. *Chemometrics and Intelligent Laboratory Systems*, 75(1):55–67, jan 2005.

[105] Douglas M. Blough, Gregory F. Sullivan, and Gerald M. Masson. Efficient Diagnosis of Multiprocessor Systems under Probabilistic Models. *IEEE Transactions on Computers*, 41(9):1126–1136, 1992.

[106] Baoping Cai, Lei Huang, and Min Xie. Bayesian Networks in Fault Diagnosis. *IEEE Transactions on Industrial Informatics*, 13(5):2227–2240, 2017.

[107] Xue Jun Zhang. *Auxiliary signal design in fault detection and diagnosis*. Springer, Berlin Heidelberg New York, 1989.

[108] Sandra Vasquez, Michel Kinnaert, and Rik Pintelon. Active Fault Diagnosis on a Hydraulic Pitch System Based on Frequency-Domain Identification. *IEEE Transactions on Control Systems Technology*, pages 1–16, 2017.

[109] D. Choe, S.L. Campbell, and R. Nikoukhah. Optimal piecewise-constant signal design for active fault detection. *International Journal of Control*, 82(1):130–146, jan 2009.

[110] Ramine Nikoukhah and Stephen L. Campbell. Auxiliary signal design for active failure detection in uncertain linear systems with a priori information. *Automatica*, 42(2):219–228, feb 2006.

[111] Alireza Esna Ashari, Ramine Nikoukhah, and Stephen L. Campbell. Active Robust Fault Detection in Closed-Loop Systems: Quadratic Optimization Approach. *IEEE Transactions on Automatic Control*, 57(10):2532–2544, oct 2012.

[112] Joseph K. Scott, Rolf Findeisen, Richard D. Braatz, and Davide M. Raimondo. Input design for guaranteed fault diagnosis using zonotopes. *Automatica*, 50(6):1580–1589, jun 2014.

[113] Miroslav Šimandl and Ivo Punčochá. Active fault detection and control: Unified formulation and optimal design. *Automatica*, 45(9):2052–2059, 2009.

[114] F. Keresteciolu and I. Çetin. Optimal input design for the detection of changes towards unknown hypotheses. *International Journal of Systems Science*, 35(7):435–444, jun 2004.

[115] Toshiharu Hatanaka and Katsuji Uosaki. Optimal Auxiliary Input Design for Fault Detection of Systems with Model Uncertainty. *IFAC Proceedings Volumes*, 33(15): 487–492, jun 2000.

[116] Dhruv Khandelwal, Siep Weiland, and Amol Khalate. Robust Fault Diagnosis by Optimal Input Design for Self-sensing Systems. *IFAC-PapersOnLine*, 50(1):1031–1036, 2017.

[117] Miroslav Šimandl, Ivo Punčochá, and Jakub Královec. Rolling horizon for active fault detection. *Proceedings of the 44th IEEE Conference on Decision and Control, and the European Control Conference, CDC-ECC '05*, 2005:3789–3794, 2005.

[118] Seyed Mojtaba Tabatabaeipour. Active fault detection and isolation of discrete-time linear time-varying systems: A set-membership approach. *International Journal of Systems Science*, 46(11):1917–1933, 2015.

[119] Davide M. Raimondo, Richard D. Braatz, and Joseph K. Scott. Active Fault Diagnosis using Moving Horizon Input Design. In *Proceedings of the 2013 European Control Conference*, pages 3131–3136, Zürich, Switzerland, 2013.

[120] Oana-Teodora Chis, Julio R Banga, and Eva Balsa-Canto. Structural Identifiability of Systems Biology Models: A Critical Comparison of Methods. *PLoS ONE*, 6(11): e27755, jan 2011.

[121] C Cobelli and J J DiStefano. Parameter and structural identifiability concepts and ambiguities: a critical review and analysis. *The American journal of physiology*, 239: R7–R24, 1980.

[122] Roland Brun, Peter Reichert, and Hans R. Künsch. Practical identifiability analysis of large environmental simulation models. *Water Resources Research*, 37(4):1015–1030, 2001.

[123] X Xia and C H Moog. Identifiability of Nonlinear Systems With Application to HIV/AIDS Models. *IEEE Transactions on Automatic Control*, 48(2):330–336, 2003.

[124] Sandor Vajda, Keith R Godfrey, and Herschel Rabitz. Similarity transformation approach to identifiability analysis of nonlinear compartmental models. *Mathematical Biosciences*, 93(2):217–248, apr 1989.

[125] S P Asprey and S Macchietto. Statistical tools for optimal dynamic model building. *Computers & Chemical Engineering*, 24(2-7):1261–1267, 2000.

[126] G.C. Goodwin and L.R. Payne. *Dynamic System Identification: Experiment Design and Data Analysis*. Academic Press, New York, 1977.

[127] Holger Dette, Viatcheslav B. Melas, and Andrey Pepelyshev. Locally e-optimal designs for exponential regression models. Technical Report 37, Dortmund, Germany, 2003.

[128] Federico Galvanin, Carlo C. Ballan, Massimiliano Barolo, and Fabrizio Bezzo. A general model-based design of experiments approach to achieve practical identifiability of pharmacokinetic and pharmacodynamic models. *Journal of Pharmacokinetics and Pharmacodynamics*, 40(4):451–467, aug 2013.

[129] William C. Rooney and Lorenz T. Biegler. Design for model parameter uncertainty using nonlinear confidence regions. *AIChE Journal*, 47(8):1794–1804.

[130] David P Yuill and James E Braun. Evaluating the performance of fault detection and diagnostics protocols applied to air-cooled unitary air-conditioning equipment. *HVAC&R Research*, 19(6):882–891, 2013.

[131] Yonathan Bard. *Nonlinear Parameter Estimation*. Academic Press, 1974.

[132] Andreas Wächter and Lorenz T. Biegler. On the implementation of a primal-dual interior point filter line search algorithm for large-scale nonlinear programming. *Mathematical Programming*, 106(1):25–57, 2006.

[133] M. Patan and K. Patan. Optimal observation strategies for model-based fault detection in distributed systems. *International Journal of Control*, 78(18):1497–1510, 2005.

[134] A. Moosavian, H. Ahmadi, A. Tabatabaeefar, and M. Khazaee. Comparison of two classifiers; K-nearest neighbor and artificial neural network, for fault diagnosis on a main engine journal-bearing. *Shock and Vibration*, 20(2):263–272, 2013.

[135] Payman Hajihosseini, Mohammad Mousavi Anzehaee, and Behzad Behnam. Fault detection and isolation in the challenging Tennessee Eastman process by using image processing techniques. *ISA Transactions*, 79:137–146, 2018.

[136] Pramod Bangalore and Lina Bertling Tjernberg. An Artificial Neural Network Approach for Early Fault Detection of Gearbox Bearings. *IEEE Transactions on Smart Grid*, 6(2):980–987, 2015.

[137] Shen Yin, Xiangping Zhu, and Chen Jing. Fault detection based on a robust one class support vector machine. *Neurocomputing*, 145:263–268, 2014.

[138] Masayuki Tamura and Shinsuke Tsujita. A study on the number of principal components and sensitivity of fault detection using PCA. *Computers & Chemical Engineering*, 31(9):1035–1046, sep 2007.

[139] Hongtian Chen, Bin Jiang, and Ningyun Lu. An improved incipient fault detection method based on Kullback-Leibler divergence. *ISA Transactions*, 79:127–136, aug 2018.

[140] Xiaogang Deng and Lei Wang. Modified kernel principal component analysis using double-weighted local outlier factor and its application to nonlinear process monitoring. *ISA Transactions*, 72:218–228, jan 2018.

[141] Kathryn Chaloner and Isabella Verdinelli. Bayesian Experimental Design: A Review. *Statistical Science*, 10(3):273–304, 1995.

[142] Friedrich Pukelshiem and William J. Studden. E-Optimal Designs for Polynomial Regression. *Annals of Statistics*, 21(1):402–415, 1993.

[143] Andrea Saltelli, Marco Ratto, Francesca Campolongo, Jessica Cariboni, and Debora Gatelli. *Global Sensitivity Analysis: The Primer*. John Wiley & Sons, 2008.

[144] Timothy Maly and Linda R. Petzold. Numerical methods and software for sensitivity analysis of differential-algebraic systems. *Applied Numerical Mathematics*, 20(1-2): 57–79, 1996.

[145] E. Walter and L. Pronzato. Qualitative and quantitative experiment design for phenomenological modelsA survey. *Automatica*, 26(2):195–213, 1990.

[146] Holger Dette and Weng Kee Wong. E-optimal designs for the MichaelisMenten model. *Statistics & Probability Letters*, 44(4):405–408, 1999.

[147] Susan M. Parker and Chris Gennings. Penalized locally optimal experimental designs for nonlinear models. *Journal of Agricultural, Biological, and Environmental Statistics*, 13(3):334–354, 2008.

[148] Nayeff Najjar, Shalabh Gupta, James Hare, Sherif Kandil, and Rhonda Walthall. Optimal sensor selection and fusion for heat exchanger fouling diagnosis in aerospace systems. *IEEE Sensors Journal*, 16(12):4866–4881, 2016.

[149] H. Hotelling. Analysis of a complex of statistical variables into principal components. *Journal of Educational Psychology*, 24(6):417–441, 1933.

[150] Erik Vanhatalo, Murat Kulahci, and Bjarne Bergquist. On the structure of dynamic principal component analysis used in statistical process monitoring. *Chemometrics and Intelligent Laboratory Systems*, 167:1–11, 2017.

[151] Kyle A Palmer and George M Bollas. Analysis of transient data in test designs for active fault detection and identification. *Computers & Chemical Engineering*, jun 2018.

[152] Tomáš Polóni, Boris Roha-Ilkiv, and Tor Arne Johansen. Mass flow estimation with model bias correction for a turbocharged Diesel engine. *Control Engineering Practice*, 23(1):22–31, feb 2014.

[153] J. Wahlstrom and L Eriksson. Modelling diesel engines with a variable-geometry turbocharger and exhaust gas recirculation by optimization of model parameters for capturing non-linear system dynamics. *Proceedings of the Institution of Mechanical Engineers, Part D: Journal of Automobile Engineering*, 225(7):960–986, 2011.

[154] Software packages from Vehicular Systems. "`http://www.fs.isy.liu.se/Software.`", 2010 (accessed March 23, 2017).

[155] Daniel Eriksson, Erik Frisk, and Mattias Krysander. A method for quantitative fault diagnosability analysis of stochastic linear descriptor models. *Automatica*, 49(6):1591–1600, 2013.

[156] Tong Zhao and Arye Nehorai. Information-Driven Distributed Maximum Likelihood Estimation Based on Gauss-Newton Method in Wireless Sensor Networks. *IEEE Transactions on Signal Processing*, 55(9):4669–4682, sep 2007.

[157] Xiuhua Liu, Xianwen Gao, and Jian Han. Robust unknown input observer based fault detection for high-order multi-agent systems with disturbances. *ISA Transactions*, 61: 15 – 28, 2016.

[158] R. Garnett, M. A. Osborne, and S. J. Roberts. Bayesian optimization for sensor set selection. In *Proceedings of the 9th ACM/IEEE International Conference on Information Processing in Sensor Networks - IPSN '10*, page 209, New York, New York, USA, 2010. ACM Press.

[159] Kyle A. Palmer, William T. Hale, and George M. Bollas. Active Fault Identification by Optimization of Test Designs. *IEEE Transactions on Control System Technology*, In Press:1–16, 2018.

[160] Kyle A. Palmer and George M. Bollas. Active Fault Diagnosis for Uncertainty Systems using Optimal Test Designs and Detection through Classification. *ISA Transactions*, (In review), 2018.

[161] Juri Ranieri, Amina Chebira, and Martin Vetterli. Near-Optimal Sensor Placement for Linear Inverse Problems. *IEEE Transactions on Signal Processing*, 62(5):1135–1146, mar 2014.

[162] Xiaodong Zhang, Marios M. Polycarpou, and Thomas Parisini. A robust detection and isolation scheme for abrupt and incipient faults in nonlinear systems. *IEEE Transactions on Automatic Control*, 47(4):576–593, 2002.

[163] Daegeun Ha, Usama Ahmed, Hahyung Pyun, Chul-Jin Lee, Kye Hyun Baek, and Chonghun Han. Multi-mode operation of principal component analysis with k-nearest neighbor algorithm to monitor compressors for liquefied natural gas mixed refrigerant processes. *Computers and Chemical Engineering*, 106:96–105, 2017.

[164] T. M. Cover and J. A. Thomas. *Elements of Information Theory*. Wiley-Interscience, New York, New York, 2nd edition, 2006.

[165] James C. Spall. Monte Carlo Computation of the Fisher Information Matrix in Nonstandard Settings. *Journal of Computational and Graphical Statistics*, 14(4):889–909, dec 2005.

[166] Milan Stehlík, Juan M. Rodríguez-Díaz, Werner G. Müller, and Jesús López-Fidalgo. Optimal allocation of bioassays in the case of parametrized covariance functions: an application to Lung's retention of radioactive particles. *TEST*, 17(1):56–68, may 2008.

[167] Tim Holland-Letz and Annette Kopp-Schneider. Optimal experimental designs for doseresponse studies with continuous endpoints. *Archives of Toxicology*, 89(11):2059–2068, nov 2015.

[168] Kwang-Ki K. Kim, Davide M. Raimondo, and Richard D. Braatz. Optimum Input Design for Fault Detection and Diagnosis: Model-based Prediction and Statistical Distance Measures. *Proceedings of the 2013 European Control Conference*, pages 1940–1945, 2013.

[169] Xun Huan and Youssef M. Marzouk. Simulation-based optimal Bayesian experimental design for nonlinear systems. *Journal of Computational Physics*, 232(1):288–317, jan 2013.

[170] S. Kullback and R. A. Leibler. On Information and Sufficiency. *The Annals of Mathematical Statistics*, 22(1):79–86, mar 1951.

[171] Lei Xie, Jiusun Zeng, Uwe Kruger, Xun Wang, and Jaap Geluk. Fault detection in dynamic systems using the Kullback-Leibler divergence. *Control Engineering Practice*, 43:39–48, 2015.

[172] Dragana Bajovic, Bruno Sinopoli, and Joao Xavier. Sensor selection for hypothesis testing in wireless sensor networks: a Kullback-Leibler based approach. In *Proceedings of the 48h IEEE Conference on Decision and Control (CDC) held jointly with 2009 28th Chinese Control Conference*, pages 1659–1664. IEEE, dec 2009.

[173] Jos M. Bernardo and Adrian F. M. Smith, editors. *Bayesian Theory*. Wiley Series in Probability and Statistics. John Wiley & Sons, Inc., Hoboken, NJ, USA, may 1994.

[174] T. Kailath. The Divergence and Bhattacharyya Distance Measures in Signal Selection. *IEEE Transactions on Communications*, 15(1):52–60, feb 1967.

[175] Ryan N. Lichtenwalter and Nitesh V. Chawla. Adaptive Methods for Classification in Arbitratily Imbalanced and Drifting Data Streams. In Nitesh V. Chawla, Nathalie Japkowicz, and Zhi-Hua Zhou, editors, *Proceedings of the Workshop on Data Mining When Classes are Imbalanced and Errors Have Costs (ICEC)*, pages 87–98, Bangkok, Thailand, 2010.

[176] David A. Cieslak, T. Ryan Hoens, Nitesh V. Chawla, and W. Philip Kegelmeyer. Hellinger distance decision trees are robust and skew-insensitive. *Data Mining and Knowledge Discovery*, 24(1):136–158, jan 2012.

[177] Richard H. Byrd, Jorge Nocedal, and Richard A. Waltz. Knitro: An Integrated Package for Nonlinear Optimization. pages 35–59. 2006.

[178] William Q Meeker and Luis A Escobar. Teaching about Approximate Confidence Regions Based on Maximum Likelihood Estimation. *The American Statistician*, 49(1): 48–53, feb 1995.

[179] Thomas R. Fears, Jacques Benichou, and Mitchell H. Gail. A reminder of the fallibility of the wald statistic. *The American Statistician*, 50(3):226–227, 1996.

Appendix A

Nomenclature

A.1 Abbreviations

3TS	Three-Tank System
AUC	Area under the curve
BIT	Built-in Test
CCR	Correct Classification Rate
DAE	Differential Algebraic Equations
DEKF	Dual Extended Kalman Filter
ECS	Environmental Control System
EGR	Exhaust Gas Recirculator
EKF	Extended Kalman Filter
FAR	False Alarm Rate
FDD	Fault Detection and Diagnosis
FDI	Fault Detection and Isolation
FIM	Fisher Information Matrix
FMI	Functional Mock-up Interface
FPR	False Positive Rate
HD	Hellinger Distance
HX	Heat Exchanger
iBIT	initiated Built-in Test
KLD	Kullback-Liebler Divergence
MCS	Monte Carlo Simulation
MHE	Maximum Horizon Estimation
MLE	Maximum Likelihood Estimation
NFF	No-Fault Found
NPR	Non-positive Rate
OED	Optimal Experimental Design
PCA	Principal Component Analysis
PFHE	Plate Fin Heat Exchanger

ROC	Receiver Operating Characteristics
SGI	Structural Global Identifiability
SLI	Structural Local Identifiability
SVM	Support Vector Machine
TPR	True Positive Rate
VGT	Variable Geometry Turbine

A.2 General Symbols

A	Area [m^2]
$A_{s,g}$	Effective heat transfer area [m^2]
$C_{p,g}$	Fluid specific heat capacity [J/kg K]
$C_{p,w}$	Wall specific heat capacity [J/kg K]
c_f	Foulant concentration [kg/m^3]
d	Hydraulic diameter [m]
F_w	Friction loss [Pa/m]
f	Friction factor [-]
G	Fluid mass velocity [kg/m^2 s]
H_f	Fin height [m]
h_g	Fluid heat transfer coefficient [W/m^2 K]
h_f	Fouled fluid heat transfer coefficient [W/m^2 K]
j	Colburn factor [-]
K_c	Entrance loss coefficient [-]
K_e	Exit loss coefficient [-]
k_f	Foulant thermal conductivity [W/m K]
k_w	Wall thermal conductivity [W/m K]
L	Likelihood function
M_w	Foulant mass per unit area [kg/m^2]
$\dot{m}_c$	Cold mass flow rate [kg/s]
$\tilde{\dot{m}}_{cmp}$	Compressor mass flow leak [kg/s]
$\dot{m}_h$	Hot mass flow rate [kg/s]
m_w	Heat exchanger wall mass [kg]
N_f	Number of faults
N_{sp}	Number of sampling times
N_{test}	Number of tests
N_u	Number of inputs
N_{u_p}	Number of controllable design inputs
N_{u_u}	Number of uncertain inputs

N_x	Number of states
N_y	Number of outputs
N_θ	Number of parameters
N_{θ_f}	Number of fault parameters
N_{θ_p}	Number of design parameters
N_{θ_u}	Number of uncertain parameters
N_ξ	Number of faults, uncertain parameters and inputs
n_s	Number of steps
p_c	Cold stream exiting pressure [Pa]
p_{ci}	Cold stream entering pressure [Pa]
p_h	Hot stream exiting pressure [Pa]
p_{hi}	Hot stream entering pressure [Pa]
Pe	Peclet number [-]
Pr	Prandtl number [-]
Re	Reynolds number [-]
R_f	Thermal fouling resistance [m^2 K/W]
s_f	Fin spacing [m]
T_c	Cold stream exiting temperature [°C]
T_{ci}	Cold stream entering temperature [°C]
T_{cmp}	Compressor temperature [°C]
T_g	Fluid temperature [°C]
T_h	Hot stream exiting temperature [°C]
T_{hi}	Hot stream entering temperature [°C]
T_{pri}	Primary heat exchanger temperature [°C]
T_{sec}	Secondary heat exchanger temperature [°C]
T_w	Heat exchanger wall temperature [°C]
t	Time
t_f	Fin thickness [m]
t_0	Initial time
u_g	Fluid velocity [m/s]
u_p	Controllable process input
u_u	Uncertain input
V	Volume [m^3]
V_g	Fluid volume [m^3]
V_w	Plate volume [m^3]
w_{H_2O}	Moisture content [%]
x	State variable
y	Measure output
$\hat{y}$	Estimated output

A.3 Greek Letters

α	Fouling coefficient
β	Fouling coefficient
Δp_{core}	Core heat exchanger pressure [Pa]
$\Delta p_{entrance}$	Entering heat exchanger pressure [Pa]
Δp_{exit}	Exiting heat exchanger pressure [Pa]
Δp_{total}	Total pressure loss [Pa]
δ_f	Foulant thickness [m]
ϵ_y	Output threshold
ϵ_{FA}	False alarm threshold
μ_g	Fluid dynamic viscosity [kg/m s]
θ	System parameters
θ_f	Fault parameters
θ_p	Design parameters
θ_u	Uncertain parameters
ρ_g	Fluid density [kg/m^3]
τ	Test duration [s]
τ_s	shear rate

A.4 Vectors and Matrices

$\mathbf{F}$	State Jacobian matrix
$\mathbf{f}$	Governing system equations
$\mathbf{h}$	Output function
$\mathbf{H}$	Output Jacobian matrix
$\mathbf{H}_\xi$	Fisher Information matrix
$\bar{\mathbf{H}}_\xi$	Normalized Fisher Information matrix
$\mathbf{K}$	Kalman gain matrix
$\mathbf{P}$	Prediction and Estimation covariance matrix
$\mathbf{Q}$	Sensitivity matrix
$\mathbf{R}$	Measurement covariance matrix
$\mathbf{t}_{sp}$	Sampling time vector
$\mathbf{u}$	Input vector
$\mathbf{u}_p$	Controllable input vector
$\mathbf{w}$	Measurement noise vector
$\mathbf{V}_\xi$	Variance-covariance matrix
$\mathbf{x}$	State vector
$\mathbf{y}$	Measured output vector
$\hat{\mathbf{y}}$	Estimated output vector

$\mathbf{\Phi}$	Test design space
$\mathbf{\Psi}$	Process noise covariance matrix
$\boldsymbol{\varphi}$	Test design vector
$\boldsymbol{\varphi}^*$	Optimal test design vector
$\boldsymbol{\theta}_f$	Fault parameters
$\boldsymbol{\theta}_p$	Design parameters
$\boldsymbol{\theta}_u$	Uncertain parameters
σ	Standard deviation of measurement noise
$\boldsymbol{\xi}$	Uncertain parameters and inputs
$\tilde{\boldsymbol{\xi}}$	Anticipated values for uncertain parameters and inputs
$\boldsymbol{\xi}_f$	Fault parameters for test design
$\boldsymbol{\xi}_u$	Uncertain parameters and inputs for test design

A.5 Subscript

c	Cold stream
f	Fault
ff	Corresponding faults
fu, uf	Corresponding faults and uncertain parameters
h	Hot stream
u	Uncertain parameter
uu	Corresponding uncertain parameters

Appendix B

Heat Transfer Correlations used in Heat Exchanger Model

This information consists of correlations for the thermal properties of air, correlations for the Colburn and Fanning friction factors, and the method for calculating effective heat transfer area.

B.1 Air thermal property correlations

Note that all temperatures are in unites of Kelvin.

Thermal conductivity

$$k_{air} = 0.0181 \left(\frac{T_{air}}{200}\right)^{0.9} \tag{B.1}$$

Dynamic viscosity

$$\mu_{air} = \left(1.458 \times 10^{-6}\right) \left(\frac{T_{air}^{1.5}}{T_{air} + 110.4}\right) \tag{B.2}$$

Specific heat capacity

$$C_{p,air} = R\left(3.355 + (5.75 \times 10^{-4})T_{air} + (-1.6 \times 10^{-3})T_{air}^{-2}\right) \tag{B.3}$$

Dimensionless quantities

$$\mathrm{Pe} = \mathrm{RePr} \tag{B.4}$$

$$\mathrm{Pr} = \frac{C_{p,g}u_g}{k_g} \tag{B.5}$$

$$\mathrm{Re} = \frac{\rho_g u_g d}{\mu} \tag{B.6}$$

B.2 Fanning friction factor and Colburn factor correlations

For plain fins [62]:

For Re<1000

$$f = 12.892\mathrm{Re}^{-1.229}\left(\frac{H_f}{S_f}\right)^{0.452}\left(\frac{t_f}{S_f}\right)^{-0.198} \tag{B.7}$$

$$j = 0.454\mathrm{Re}^{-0.997}\left(\frac{H_f}{S_f}\right)^{0.435}\left(\frac{t_f}{S_f}\right)^{-0.227} \tag{B.8}$$

For Re≥1000

$$f = 3.133\mathrm{Re}^{-1.285}\left(\frac{H_f}{S_f}\right)^{0.247}\left(\frac{t_f}{S_f}\right)^{-0.181} \tag{B.9}$$

$$j = 0.166\mathrm{Re}^{-1.011}\left(\frac{H_f}{S_f}\right)^{0.228}\left(\frac{t_f}{S_f}\right)^{-0.336} \tag{B.10}$$

For offset strip fins [63]:

$$f = 2.092\mathrm{Re}^{-0.281}\left(\frac{S_f}{H_f}\right)^{-0.739}\left(\frac{t_f}{l}\right)^{0.972}\left(\frac{t_f}{S_f}\right)^{-0.78}\left(\frac{L}{l}\right)^{-0.497} \tag{B.11}$$

$$j = 0.101\mathrm{Re}^{-0.189}\left(\frac{S_f}{H_f}\right)^{-0.488}\left(\frac{t_f}{l}\right)^{0.479}\left(\frac{t_f}{S_f}\right)^{-0.297}\left(\frac{L}{l}\right)^{-0.315} \tag{B.12}$$

B.3 Effective heat transfer perimeter

The effective heat transfer perimeter along the system is calculated as

$$A_s = 2nWL\left[\frac{(S_f - t_f) + \eta_f\,(H_f - t_f)}{S_f}\right], \tag{B.13}$$

The fin efficiency of the system can be obtained from a number of literary sources. The following efficiency comes from heat exchanger analysis performed by Shah for rectangular fins [42]:

$$\eta_f = \frac{\tanh\left(m_i l_i\right)}{m_i l_u} \tag{B.14}$$

$$m_i = \sqrt{\frac{2h}{k_w \delta_f}\left(1 + \frac{\delta_f}{l_i}\right)}$$

$$l_i = \frac{H_f}{2} - \delta_f$$

Appendix C

Dual Extended Kalman Filter for FDI

The mathematical formulation of the Extended Kalman Filter (EKF) used in this work for the purpose of fault detection is provided in this Appendix. The EKF method for dual estimation applied to the fault severity assessment is as follows. The system governing equations were converted into discrete ODEs:

$$\begin{aligned} \mathbf{x}_{k+1} &= \mathbf{f}(\mathbf{x}_k, \mathbf{u}_{p,k}, \boldsymbol{\theta}_p, \boldsymbol{\xi}_k) + \mathbf{v}_k, \\ \mathbf{y}_k &= \mathbf{h}(\mathbf{x}_k, \mathbf{u}_{p,k}, \boldsymbol{\theta}_p, \boldsymbol{\xi}_k) + \mathbf{w}_k, \end{aligned} \tag{C.1}$$

where $\mathbf{x}_k = \mathbf{x}(t_k)$, $\mathbf{v}_k$ is the process noise and $\mathbf{w}_k$ is the measurement noise vectors, respectively. The objective was to regularly track and estimate the states, $\hat{\mathbf{x}}_k$, and predicted fault and uncertain parameters, $\hat{\boldsymbol{\xi}}$, which are treated as additional states. Let $\mathbf{z}$ be the vector of augmented states, where:

$$\mathbf{z}_{k+1} = \begin{bmatrix} \mathbf{x}_{k+1} \\ \boldsymbol{\xi}_{k+1} \end{bmatrix} = \begin{bmatrix} \mathbf{f}(\mathbf{x}_k, \mathbf{u}_{p,k}, \boldsymbol{\theta}_p, \boldsymbol{\xi}_k) \\ \boldsymbol{\xi}_k \end{bmatrix} + \begin{bmatrix} \mathbf{v}_k \\ \boldsymbol{\eta}_k \end{bmatrix},$$

where $\boldsymbol{\eta}_k$ is the uncorrelated Gaussian noise with covariance matrix, $\boldsymbol{\Psi}_\eta$. At each time point, t_k, the estimated set of states, $\hat{\mathbf{z}}_{k|k} = [\hat{\mathbf{x}}_{k|k}^T, \hat{\boldsymbol{\xi}}_{k|k}^T]^T$, take into account the predicted states from previous estimates, $\hat{\mathbf{z}}_{k|k-1} = [\hat{\mathbf{x}}_{k|k-1}^T, \hat{\boldsymbol{\xi}}_{k|k-1}^T]^T$. The matrices, $\mathbf{F}$ and $\mathbf{H}$, are compiled as sets of partial derivatives (calculated with central finite differences) as shown below:

$$\mathbf{F}_k = \begin{bmatrix} \frac{\partial \mathbf{f}}{\partial \mathbf{x}^T} & \frac{\partial \mathbf{f}}{\partial \boldsymbol{\xi}^T} \\ 0 & \mathbf{I} \end{bmatrix}_{\hat{\mathbf{x}}_{k|k}, \hat{\boldsymbol{\xi}}_{k|k}},$$

$$\mathbf{H}_{k+1} = \begin{bmatrix} \frac{\partial \mathbf{h}}{\partial \mathbf{x}^T} & \frac{\partial \mathbf{h}}{\partial \boldsymbol{\xi}^T} \end{bmatrix}_{\hat{\mathbf{x}}_{k+1|k}, \hat{\boldsymbol{\xi}}_{k+1|k}}.$$

Two stages are implemented for the extended Kalman filter, the prediction and filtering stages. The predicted states are calculated based on the previous state estimates, $\hat{\mathbf{z}}_{k+1|k} = [\hat{\mathbf{x}}_{k+1|k}^T, \hat{\boldsymbol{\xi}}_{k+1|k}^T]^T$, as shown in (C.2):

$$\mathbf{z}_{k+1|k} = \begin{bmatrix} \mathbf{x}_{k+1|k} \\ \boldsymbol{\xi}_{k+1|k} \end{bmatrix} = \begin{bmatrix} \mathbf{f}(\mathbf{x}_{k|k}, \mathbf{u}_{p,k|k}, \boldsymbol{\theta}_p, \boldsymbol{\xi}_{k|k}) \\ \boldsymbol{\xi}_{k|k} \end{bmatrix}. \tag{C.2}$$

The covariance matrix of the prediction error is calculated as shown in (C.3):

$$\mathbf{P}_{k+1|k} = F_k P_{k|k} F_k^T + \mathbf{\Psi}, \tag{C.3}$$

where $\mathbf{P}_{k|k}$ is the estimation covariance matrix of the estimated states at time t_k, and $\mathbf{\Psi}$ is the Gaussian noise covariance matrix of the states, a compilation of the process noise covariance matrices of the states and parameters, $\mathbf{\Psi}_v$ and $\mathbf{\Psi}_\eta$, respectively:

$$\mathbf{\Psi} = \begin{bmatrix} \mathbf{\Psi}_v & 0 \\ 0 & \mathbf{\Psi}_\eta \end{bmatrix}.$$

At the filtering stage, the measurements, $\mathbf{y}_{k+1}$, at sampling time point, t_{k+1}, are used to update the predicted state and parameters. The difference between the measurements and the predicted measurements update the state estimation:

$$\hat{\mathbf{z}}_{k+1|k+1} = \hat{\mathbf{z}}_{k+1|k} + \mathbf{K}_{k+1}\left[\mathbf{y}_{k+1} - \mathbf{h}(\hat{\mathbf{x}}_{k+1|k}, \mathbf{u}_{p,k+1|k}, \boldsymbol{\theta}_p, \hat{\boldsymbol{\xi}}_{k+1|k})\right], \tag{C.4}$$

where $\mathbf{K}$ is the Kalman gain matrix defined as

$$\mathbf{K} = \mathbf{P}_{k+1|k}\mathbf{H}_{k+1}^T\left[\mathbf{H}_{k+1}\mathbf{P}_{k+1|k}\mathbf{H}_{k+1}^T + \mathbf{R}\right]^{-1},$$

which is a function dependent on the measurement noise covariance matrix, $\mathbf{R}$. The updated estimation covariance matrix is then defined as shown in (C.5):

$$\mathbf{P}_{k+1|k+1} = \left[\mathbf{I} - \mathbf{K}_{k+1}\mathbf{H}_{k+1}\right]\mathbf{P}_{k+1|k}. \tag{C.5}$$

It was assumed that the process noise is negligible, measurement noise is bounded and known at each time step, and model uncertainty is captured as uncertainty in the model parameters.

Appendix D

Output Deviation Constraint Calculation

The objective of the false alarm analysis is to determine whether the faulty system of interest can generate output trajectories that are essentially identical to the outputs of a system that is fault-free or contains a different fault. The output deviation constraint, ϵ_y, for the false alarm analysis is used to compare two sets of residuals: the first set is generated between the observed outputs, $\mathbf{y}(\boldsymbol{\xi})$, and the expected outputs of the system with its anticipated fault and uncertain parameters and inputs, $\hat{\mathbf{y}}(\tilde{\boldsymbol{\xi}})$, and the second set is generated between the same observed outputs and the expected outputs of a fault-free system or system with different faults, $\hat{\mathbf{y}}(\boldsymbol{\xi}')$. In the case studies tested, we assume that $\boldsymbol{\xi} = \tilde{\boldsymbol{\xi}}$ (the system contains the fault of interest) and that the system model accurately represents the evaluated system. Therefore, the model is used as a virtual system to collect "observed" outputs that are calculated as shown below:

$$\begin{aligned} y_i(\tilde{\boldsymbol{\xi}}, t_k) &= \hat{y}_i(\tilde{\boldsymbol{\xi}}, t_k) + w_{ik}; \\ k &= 1, \ldots, N_{sp}, \quad i = 1, \ldots, N_y, \end{aligned} \tag{D.1}$$

where w_{ik} is the normally distributed observation noise ($\sim \mathcal{N}(0, \sigma_{ij}^2)\ \forall i, j$).

Each set of residuals between the observed and expected outputs are compiled into the likelihood function of (4.2), as described by [131], which is based on the probability density function of each observation. As there are no nuisance parameters considered in this work, the profile likelihood for $\boldsymbol{\xi}'$ is then defined as:

$$R(\boldsymbol{\xi}') = \frac{L(\boldsymbol{\xi}')}{L(\tilde{\boldsymbol{\xi}})}, \tag{D.2}$$

which compares the likelihoods generated with $\boldsymbol{\xi} = \tilde{\boldsymbol{\xi}}$ and $\boldsymbol{\xi} = \boldsymbol{\xi}'$. Assuming that $\tilde{\boldsymbol{\xi}}$ is the vector of true values for the faults, uncertain parameters and inputs, then according to [178] as the test sampling size approaches infinity, the function $-2\log[R(\boldsymbol{\xi}')]$ follows a chi-squared distribution with N_ξ degrees of freedom. A $100(1-\alpha)\%$ likelihood-based confidence region can be generated for $\boldsymbol{\xi}'$ with the set of $\boldsymbol{\xi}$ values such that

$$-2\log[R(\boldsymbol{\xi}')] < \chi^2_{1-\alpha, N_\xi}. \tag{D.3}$$

Therefore, the constraint for this problem, ϵ_y, is set equal to $\chi^2_{1-\alpha,N_\xi}$. It was decided in this work that the analysis should use a default significance level of α=0.05. As a result, ϵ_y ranges from 3.00 to 5.54 based on the value of N_ξ. This constraint is applied to (4.4) and (4.5) to conduct the false alarm analysis for steady-state and dynamic test designs, respectively. Other statistical tests can be used to assign constraints to (4.4) and (4.5), such as the simpler Wald test [179] . Likelihood ratios were used despite the time required to calculate them for any given $\boldsymbol{\xi}$ as their calculation is relatively straightforward and generates a more accurate and reliable constraint than that of the Wald test, resulting in more generalized false alarm assessments (in terms of application and model or parameter requirements).

Appendix E

Additional Optimality Criteria for Active FDI Test Designs

Test design optimization is a crucial decision for active FDI configuration. In control and statistics, a series of criteria are commonly used to calculate or select tests that improve the estimation confidence of targeted parameters, known as the "alphabet optimality" criteria [30]. Multiple criteria were selected from the literature as objectives for the optimization of active FDI test designs:

1. D-optimal
2. E-optimal
3. G-optimal
4. D_s-optimal
5. E_s-optimal
6. modified E-optimal
7. PAC-optimal

In the main document, the D-, D_s-, E- and PAC-optimal criteria (which were considered to be the most relevant and well-known) are detailed and the resulting test designs are used for FDI and compared with the nominal test in each case study. The remaining criteria are solved and used to execute FDI in the supplementary work.

In each of the test design criteria considered, the Fisher Information Matrix (FIM) is used to quantifiably determine the amount of information that can be obtained from the output trajectories of an FDI test regarding uncertain parameters. It is considered to be equal to the Cramer-Ráo lower bound of the variance-covariance matrix of the uncertain parameters. The equation for the FIM as shown in the Methods Section of the main document is restated here:

$$\mathbf{H}_\xi = \sum_{i=1}^{N_y} \sum_{j=1}^{N_y} \sigma_{ij}^{-2} \mathbf{Q}_i^T \mathbf{Q}_j, \tag{E.1}$$

where $\mathbf{Q}_i$ is the sensitivity matrix of the i-th output with respect to the parameters for all tests and sampling times. It is assumed that the measurement noise of each output has a zero-mean, uncorrelated Gaussian distribution with standard deviation of σ_{ij}^2 between the i-th and j-th outputs.

The test design is optimized based on some measure of the FIM so that the system outputs are more sensitive to changes in fault parameters. It is important then to determine which measure is desirable for the problem at hand. A common objective in optimal experimental design is to select a test such that the "worst-case" variance is minimized. Minimizing only the largest variance between parameters reduces the complexity of the optimization problem as it does not have to consider all correlations between parameters simultaneously, such as with D-optimal design. Thus, the optimal solution is obtained by maximizing the smallest eigenvalue, λ_i, which is proportional to the worst-case variability of the parameters. This method is referred to as E-optimal design, which is used to generate data in the main document. However, there are cases where a system has only a subset of uncertain parameters that are of interest, which makes the remaining parameters another subset referred to as nuisance parameters. The Fisher Information Matrix should then be partitioned such that only the parameters of interest are targeted for optimal precision. Thus, the subset E-optimal criterion, or E_s-optimal criterion, is achieved by solving the problem below:

$$\max_{\varphi} \Psi_{Es}(\mathbf{H}_\xi) = \max_{\varphi} \min_{1\leq i\leq N_f} \lambda_i \left\{ H_{ff} - H_{fu} H_{uu}^{-1} H_{fu}^T \right\}, \tag{E.2}$$

where the FIM is partitioned into blocks:

$$\mathbf{H}_\xi = \begin{bmatrix} H_{ff} & H_{fu} \\ H_{fu}^T & H_{uu}, \end{bmatrix}, \tag{E.3}$$

with:

$$H_{ff} \in \mathbb{R}^{N_f \times N_f}, \quad H_{fu} \in \mathbb{R}^{N_f \times (N_\xi - N_f)}, \quad H_{uu} \in \mathbb{R}^{(N_\xi - N_f)\times(N_\xi - N_f)}. \tag{E.4}$$

Instead of focusing solely on the worst-case variance of the system, another approach is to instead compare the best-case and worst-case variance. The result is a test design with similar variability between uncertain parameters that allows for overall increase in confidence, though not to the extent of the D-optimal design. Minimizing the ratio between the largest eigenvalue (best-case variance) and smallest eigenvalue (worst-case variance) is a more robust optimality criteria than the standard E-optimal criteria. This modified E-optimal criteria is calculated as shown below:

$$\max_{\boldsymbol{\varphi}\in\Phi} \Psi_{modE}(\mathbf{H}_\xi) = \max_{\boldsymbol{\varphi}\in\Phi} \frac{\max_{1\leq i\leq N_f} \lambda_i \{\mathbf{H}_\xi\}}{\min_{1\leq i\leq N_f} \lambda_i \{\mathbf{H}_\xi\}} \tag{E.5}$$

In the supplementary material, the basis for formulating the modified E-optimal design was also used to generate a modified E_s-optimal design with parameters corresponding to faults considered to be parameters of interest.

The last test design criteria considered in the supplementary material places emphasis on minimizing the variance of the output predictions instead of the uncertain parameters. The objective must then be to minimize the effect that the worst-case changes in the states can have on the system to minimize the variability of the output predictions. This becomes a min-max problem where the variance of each output sensitivity is minimized by the test design and maximized by the state within the state space. Fisher Information generated from the predicted outputs and anticipated parameters should then be used to normalize this diagonal sum. Suppose the desired outcome of the test design is to ensure that the predicted outputs from a fault scenario are correct, then the test design should be optimized according to G-optimality, which is achieved using the formulation below:

$$\max_{\boldsymbol{\varphi}\in\Phi} \Psi_G(\mathbf{H}_\xi) = \max_{\boldsymbol{\varphi}\in\Phi} \min_{\mathbf{x}\in\mathbf{X}} \operatorname{diag}\left(\mathbf{Q}(\mathbf{x})\mathbf{H}_\xi^{-1}(\tilde{\boldsymbol{\xi}})\mathbf{Q}(\mathbf{x})^T\right)^{-1}, \tag{E.6}$$

where $\mathbf{Q}$ is the comprehensive sensitivity matrix of the FDI test for all measurement samples with each sensitivity dependent on the states selected. This updated matrix is formulated as:

$$\mathbf{Q}(\mathbf{x}) = \begin{bmatrix} \left.\frac{\partial y_1(\mathbf{x})}{\partial \xi_1}\right|_{t=t_1,\boldsymbol{\xi}=\tilde{\boldsymbol{\xi}}} & \cdots & \left.\frac{\partial y_1(\mathbf{x})}{\partial \xi_{N_\xi}}\right|_{t=t_1,\boldsymbol{\xi}=\tilde{\boldsymbol{\xi}}} \\ \vdots & \ddots & \vdots \\ \left.\frac{\partial y_1(\mathbf{x})}{\partial \xi_1}\right|_{t=t_{N_{sp}},\boldsymbol{\xi}=\tilde{\boldsymbol{\xi}}} & \cdots & \left.\frac{\partial y_1(\mathbf{x})}{\partial \xi_{N_\xi}}\right|_{t=t_{N_{sp}},\boldsymbol{\xi}=\tilde{\boldsymbol{\xi}}} \\ \left.\frac{\partial y_2(\mathbf{x})}{\partial \xi_1}\right|_{t=t_1,\boldsymbol{\xi}=\tilde{\boldsymbol{\xi}}} & \cdots & \left.\frac{\partial y_2(\mathbf{x})}{\partial \xi_{N_\xi}}\right|_{t=t_1,\boldsymbol{\xi}=\tilde{\boldsymbol{\xi}}} \\ \vdots & \ddots & \vdots \\ \left.\frac{\partial y_{N_y}(\mathbf{x})}{\partial \xi_1}\right|_{t=t_{N_{sp}},\boldsymbol{\xi}=\tilde{\boldsymbol{\xi}}} & \cdots & \left.\frac{\partial y_{N_y}(\mathbf{x})}{\partial \xi_{N_\xi}}\right|_{t=t_{N_{sp}},\boldsymbol{\xi}=\tilde{\boldsymbol{\xi}}} \end{bmatrix}. \tag{E.7}$$

Because of the computational efforts needed to achieve G-optimal design, this problem is not commonly used or recommended for FDI in nonlinear or dynamic models. However, it is included in the supplementary work as part of a comprehensive examination of the optimal test designs considered for active FDI.

The three-tank case study from the main document is implemented with the additional test designs. The fault scenarios are described in detail in the Results Section and listed in Table 2 of the main document. The test designs that were calculated using the proposed optimal criteria in this document are listed in Table E.1. The modified E-optimal, modified E_s-optimal and G-optimal designs were found to be identical and are achieved with all inputs at upper or lower bounds. The E_s-optimal test design was determined to be unique from all other test designs, including the designs listed in the main document.

Table E.1: Nominal and optimal FDI test designs for the three-tank system that contains an actuator fault at tank 1, a leak at tank 2 and uncertain flow coefficients ($\tilde{\boldsymbol{\xi}} = [0.6, 2.0\text{mm}, 0.95, 0.8, 0.95]'$).

$\boldsymbol{\varphi}$	Lower Bound	Upper Bound	Nom	E_s-Opt	mod. E-Opt	mod. E_s-Opt	G-Opt
u_1 ($\times 10^{-4}$ m^3/s)	0.10	1.00	0.55	0.20	0.10	0.10	0.10
u_2 ($\times 10^{-4}$ m^3/s)	0.10	1.00	0.55	0.91	0.10	1.00	1.00

After the test design optimization was performed for each criterion, the FDI was executed using a combination of PCA and k-NN algorithms as described in the main document. Following the procedures described in the Methods Section, a Monte Carlo simulation of 2000 runs was performed to train classifiers with each test design, and 10 steady-state samples were collected in each run. The trained classifiers were used to classify unlabeled datasets and to determine the success rate of the fault classification. The confusion matrices generated using k-NN for all testing phase samples is presented in Table E.2 along with the overall classification accuracy of each test design. The E_s-optimal criterion was unsuccessful in improving CCRs in any fault scenario, though it reduces the rate of false alarms and nondetections associated with tank leaks, as well as misclassifications between each fault scenario. The results from the modified E-optimal design were similar to that of the E-optimal design, and did not significantly change the CCRs and MCRs from each scenario, even though the test design has the inputs located at the lower bounds. The G-optimal (and modified E_s-optimal) design resulted in greater output prediction confidence, with the drawback of increased correlation between the actuator fault and the uncertain flow coefficients. The CCRs corresponding to the tank leak scenario increased considerably, but overall the G-optimal design resulted in lowest classification accuracy.

Table E.2: Confusion matrices of a three-tank system FDI with fault scenarios listed in Table 2.

(a) Confusion matrices of FDI executed at nominal, E_s-optimal and modified E-optimal test designs

		Nominal			E_s-Optimal			mod. E-Optimal		
		Actual			Actual			Actual		
		c_0	c_1	c_2	c_0	c_1	c_2	c_0	c_1	c_2
Predicted	c_0	0.94	0.01	0.20	0.79	0.25	0.13	0.93	0.00	0.23
	c_1	0	0.87	0.28	0.21	0.69	0.27	0.00	0.88	0.30
	c_2	0.06	0.12	0.52	0.00	0.06	0.60	0.07	0.12	0.48

(b) Confusion matrices of FDI executed at E-optimal and PAC-optimal test designs

		G-Optimal		
		Actual		
		c_0	c_1	c_2
Predicted	c_0	0.67	0.39	0.11
	c_1	0.31	0.55	0.20
	c_2	0.02	0.06	0.70

(c) Classification accuracies of the listed test designs

Test Criterion	A_{CCR}
Nominal	0.78
E_s-Opt	0.69
mod. E-Opt	0.76
G-Opt	0.64

A decision threshold was assigned to a probabilistic k-NN algorithm as described in the Methods section of the main document. The objective is the determine the rate of successful fault diagnoses with each test design based on assigned classification selectivity. Fig. E.1 shows the ROC curves of each fault scenario, comparing the true positive rate (TPR) vs false positive rate (FPR) and the CCR vs FPR. The nominal and modified E-optimal designs generate the best detection and classification of actuator fault as expected based on from the results shown in Table 5.4. The E_s-optimal and and G-optimal designs lead to similar detection rates and slightly better classification rates than the nominal and modified E-optimal test designs. Compared to the results shown in the primary document, the D-optimal and D_s-optimal tests are concluded to be the most effective choices in the diagnosis of faults in a three-tank system.

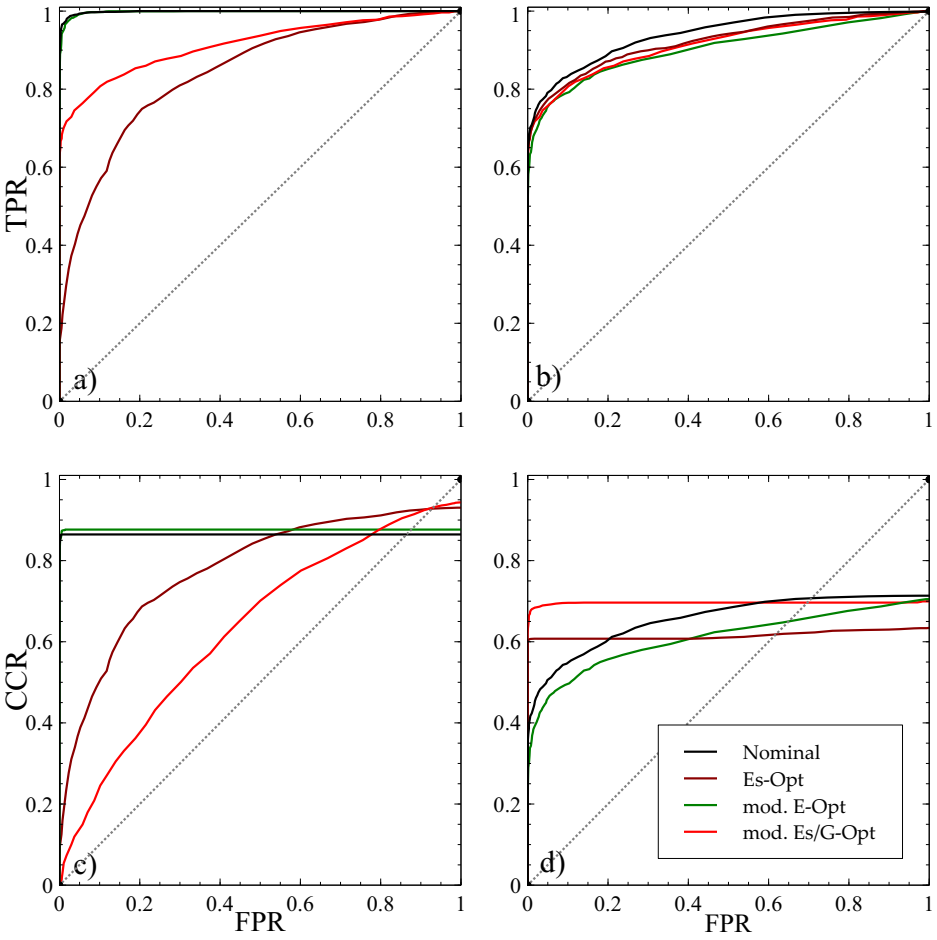

Fig. E.1: ROC plots of true positive and correct classification rates versus false positive rates with test designs at different optimal criteria. Fault scenarios described in Table 2 of the main document are presented for a three-tank system with (a,c) an actuator fault in tank 1 and (b,d) a leak in tank 2.

Appendix F

Increased Parameter Value Ranges in Diesel Engine Fault and Fault-free Scenarios

An evaluation of the FDI test designs was performed for the diesel engine case study considering a range of fault-free conditions that are feasible in the system. The parameters that represent nominal system uncertainty, η_{cmp} and η_t, have identical probabilistic ranges to the previous analysis. The faults are assumed to have a uniform distribution of values that can occur at fault and fault-free conditions. The range of faults and uncertain parameters that can occur in the diesel engine in this evaluation are presented in Table F.1. In the leak-based fault scenarios, if the radius of the hole is greater than 20 % of the allowed maximum radius, the system is considered to be at fault. In the actuator fault scenarios, is the drift that occurs is greater 20 %, the system is considered to be at fault.

The vector $\boldsymbol{\xi}$ does not change, therefore the test designs remain the same for the optimal criteria considered. The k-NN classifiers are retrained to account for the increased range of uncertainty and determine the rate of correct classifications and misclassifications. Confusion matrices of these updated values are listed in Table F.2. As expected, the CCRs of each scenario are considerably less than in the previous confusion matrices due to the increased range of allowable fault-free conditions. In each test design, the CCR of fault scenario 4 is greater than 0.75, indicating the uncertainty does not significantly affect the identification of c^4. The majority of the correct classifications are less than 0.50, indicating the tests are not as reliable for isolation though they are still viable for detection. FDI conducted D_s-optimal test results in a significant increase in the CCR for fault scenario 3, similar to the results in the main document. The overall classification accuracy is the highest with D_s-optimal design, which is the only design with an average classification accuracy greater than 0.50.

Table F.1: Faults and uncertain parameters, and their random distributions. Normal distributions are represented as ($\mathcal{N}(\mu, \sigma^2)$), with mean, μ, and variance, σ^2, and uniform distributions are represented as ($\mathcal{U}(a, b)$), where a and b are the lower and upper bounds, respectively.

Set of $\boldsymbol{\xi}$	c^0	c^1	c^2
r_{IM}^{leak} (mm)	$\mathcal{U}(0, 0.13)$	$\mathcal{U}(0.14, 6.32)$	$\mathcal{U}(0, 0.13)$
r_{EM}^{leak} (mm)	$\mathcal{U}(0, 0.13)$	$\mathcal{U}(0, 0.13)$	$\mathcal{U}(0.14, 6.32)$
$\tilde{u}_{vgt}$	$\mathcal{U}(0, 0.20)$	$\mathcal{U}(0, 0.20)$	$\mathcal{U}(0, 0.20)$
$\tilde{u}_{egr}$	$\mathcal{U}(0, 0.20)$	$\mathcal{U}(0, 0.20)$	$\mathcal{U}(0, 0.20)$
η_c	$\mathcal{N}(0.736, 1.2e-3)$	$\mathcal{N}(0.736, 1.2e-3)$	$\mathcal{N}(0.736, 1.2e-3)$
η_t	$\mathcal{N}(0.818, 5.8e-4)$	$\mathcal{N}(0.818, 5.8e-4)$	$\mathcal{N}(0.818, 5.8e-4)$

Set of $\boldsymbol{\xi}$	c^3	c^4
r_{IM}^{leak} (mm)	$\mathcal{U}(0, 0.13)$	$\mathcal{U}(0, 0.13)$
r_{EM}^{leak} (mm)	$\mathcal{U}(0, 0.13)$	$\mathcal{U}(0, 0.13)$
$\tilde{u}_{vgt}$	$\mathcal{U}(0.21, 0.60)$	$\mathcal{U}(0, 0.20)$
$\tilde{u}_{egr}$	$\mathcal{U}(0, 0.20)$	$\mathcal{U}(0.21, 0.60)$
η_c	$\mathcal{N}(0.736, 1.2e-3)$	$\mathcal{N}(0.736, 1.2e-3)$
η_t	$\mathcal{N}(0.818, 5.8e-4)$	$\mathcal{N}(0.818, 5.8e-4)$

The ROC curves of the relationship between the rate of true positives and false positives is shown in Fig. F.1. The increase in uncertainty in the fault-free parameters, and the resulting reduction in sensitivity to system faults generated a loss in area under the ROC curves. The detection of faults in scenarios 1 and 2 was the highest with D-optimal design, similar to the previous work but with less uncertainty. However, the order of which test designs are better for each fault scenario changes with more uncertainty. Regardless, D_s-optimal shows the steepest curve in fault scenarios 3 and 4, with good performance in fault detection.

Table F.2: Confusion matrices and of a diesel engine with fault scenarios listed in Table 6

(a) Confusion matrices of FDI executed at nominal and D-optimal test designs

		Nominal					D-Optimal				
		Actual					Actual				
		c_0	c_1	c_2	c_3	c_4	c_0	c_1	c_2	c_3	c_4
Predicted	c_0	0.30	0.14	0.13	0.29	0.04	0.34	0.13	0.15	0.36	0.05
	c_1	0.13	0.40	0.37	0.09	0.01	0.09	0.44	0.35	0.08	0.02
	c_2	0.15	0.32	0.34	0.10	0.01	0.14	0.29	0.32	0.13	0.01
	c_3	0.42	0.14	0.16	0.50	0.04	0.42	0.14	0.17	0.43	0.04
	c_4	0.00	0.00	0.00	0.02	0.90	0.01	0.01	0.00	0.00	0.87

(b) Confusion matrices of FDI executed at D_s-optimal and E-optimal test designs

		D_s-Optimal					E-Optimal				
		Actual					Actual				
		c_0	c_1	c_2	c_3	c_4	c_0	c_1	c_2	c_3	c_4
Predicted	c_0	0.47	0.25	0.20	0.15	0.05	0.34	0.13	0.17	0.35	0.03
	c_1	0.20	0.33	0.33	0.03	0.00	0.10	0.44	0.35	0.10	0
	c_2	0.14	0.39	0.43	0.02	0.00	0.16	0.28	0.29	0.16	0.00
	c_3	0.19	0.03	0.17	0.78	0.07	0.32	0.14	0.18	0.32	0.02
	c_4	0.00	0.00	0.00	0.02	0.87	0.08	0.00	0.01	0.07	0.95

(c) Confusion matrices of FDI executed at PAC-optimal test designs

		PAC-Optimal				
		Actual				
		c_0	c_1	c_2	c_3	c_4
Predicted	c_0	0.36	0.23	0.21	0.18	0.06
	c_1	0.22	0.29	0.30	0.10	0.06
	c_2	0.18	0.32	0.34	0.08	0.06
	c_3	0.18	0.11	0.10	0.60	0.03
	c_4	0.06	0.04	0.05	0.04	0.79

(d) Classification accuracy of listed test designs

Test Criterion	A_{CCR}
Nominal	0.49
D-Opt	0.48
D_s-Opt	0.56
E-Opt	0.47
PAC-Opt	0.48

The ROC curves describing the relationship between the rate of correct classifications and false positives is presented in Fig. F.2. The D_s-optimal design has the steepest ROC curves in faults scenarios 2 and 3, and is close to having the steepest curve in fault scenario 4. E-optimal design results in the best CCR of fault scenario 4, but the performance in fault scenario 3 significantly reduces the usefulness of this test. Even with the increase in range of uncertain parameter values for the system as fault-free conditions, the optimization of test designs for active FDI significantly improves the overall success of fault diagnosis in the diesel engine.

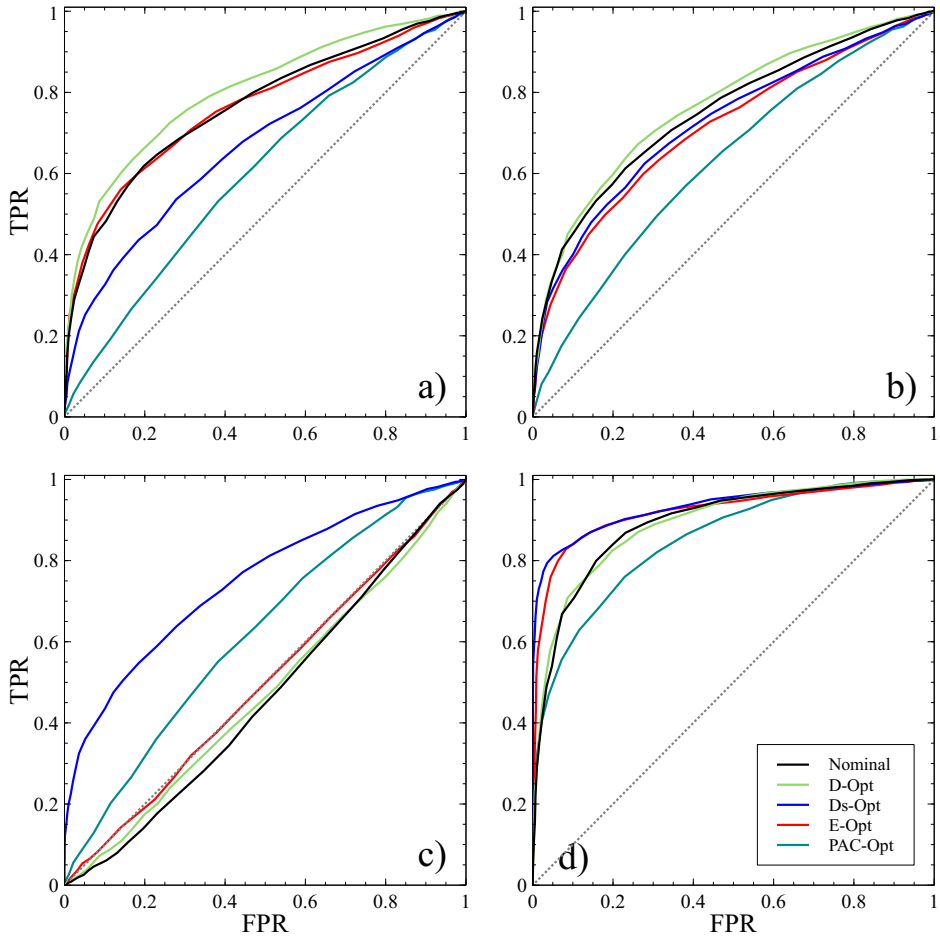

Fig. F.1: ROC plots of true positive rates versus false positive rates with different optimal criteria. Fault scenarios described in Table 2 are presented for a diesel engine with (a) inlet manifold leak, (b) exhaust manifold leak, (c) EGR actuator drift and (d) VGT actuator drift.

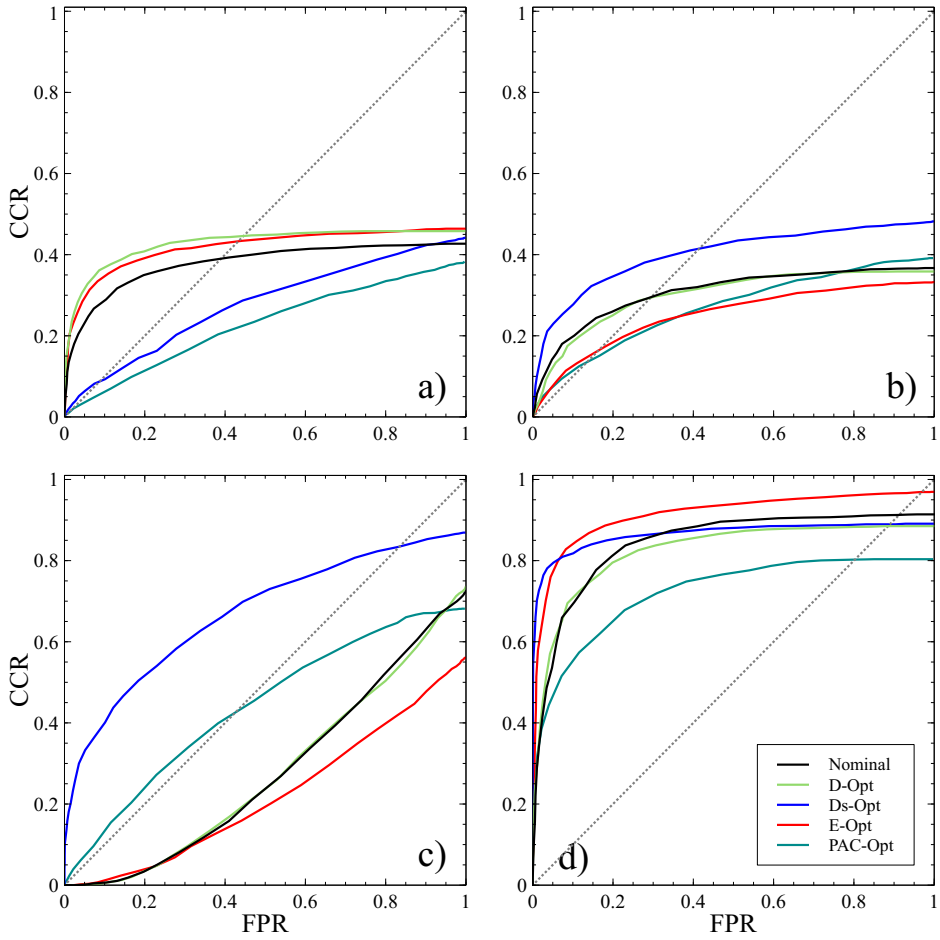

Fig. F.2: ROC plots of correct classification rates versus false positive rates with different optimal criteria. Fault scenarios described in Table 2 are presented for a diesel engine with (a) inlet manifold leak, (b) exhaust manifold leak, (c) EGR actuator drift and (d) VGT actuator drift.